# Far-From-Equilibrium Quantum Many-Body Systems

## From Universal Dynamics to Statistical Mechanics

**Sebastian Anton Erne**

Department of Physics and Astronomy
University Heidelberg

This dissertation is submitted for the degree of
*Doctor of Natural Sciences*

April 2018

Dissertation
submitted to the
Combined Faculties of the Natural Sciences and Mathematics
of the Ruperto-Carola-University of Heidelberg. Germany
for the degree of
Doctor of Natural Sciences

Put forward by

**Sebastian Erne**

born in: Wangen im Allgäu
Oral examination: 11.07.2018

**Far-From-Equilibrium Quantum Many-Body Systems**
**From Universal Dynamics to Statistical Mechanics**

Referees: Prof. Dr. Thomas Gasenzer
Prof. Dr. Selim Jochim

**Far-From-Equilibrium Quantum Many-Body Systems: From Universal Dynamics to Statistical Mechanics**

This thesis examines, along side a series of experiments, the far-from-equilibrium dynamics of isolated quantum many-body systems. As a model example we study the relaxation of a single and two linearly coupled one-dimensional Bose gases, brought out-off-equilibrium through a rapid change in the system parameters. For the single Bose gas this quench is a rapid cooling of the system to the one-dimensional regime, leading to a far-from-equilibrium state. In the subsequent relaxation towards thermal equilibrium we find direct experimental evidence for a scaling evolution in space and time, signaling the approach of a non-thermal fixed point and universality far-from-equilibrium. For the two linearly coupled gases we demonstrate how the analysis of higher-order correlations and their factorization properties can be used to determine the validity of effective field theories. In thermal equilibrium we find the system is described by the sine-Gordon model up to $10^{\text{th}}$-order correlations. Lastly, the relaxation of two independent condensates, initialized in a strongly phase correlated state, is studied in the context of prethermalization, generalized statistical ensembles, and quantum recurrences. Our work paves the way for future studies of universality far from equilibrium.

**Quanten-Vielteilchensysteme fern ab vom Gleichgewicht: Von universeller dynamic zu statistischer Mechanik**

Diese Arbeit thematisiert anhand einer Reihe von Experimenten die Dynamik von isolierten Quanten-Vielteilchen-Systemen fernab vom thermischen Gleichgewicht. Als Modell wird die Relaxation eines einzelnen sowie zweier linear gekoppelter, eindimensionaler Bose-Gase untersucht. Durch eine plötzliche Änderung der Systemparameter wird das Gas in einen Zustand fern vom thermischen Gleichgewicht gebracht. Diese Änderung wird für das einzelne Bose-Gas durch schnelles Kühlen in das eindimensionale System realisiert. In der darauf folgenden Zeitentwicklung hin zum thermischen Gleichgewicht wird eine Skalierungsentwicklung in Raum und Zeit direkt experimentell bestätigt. Dies deutet auf die Annäherung des Systems an einen nichtthermischen Fixpunkt hin und zeigt eine universelle Dynamik fernab vom thermischen Gleichgewicht. Für die linear gekoppelten Kondensate wird aufgezeigt, dass durch die Analyse von Korrelationsfunktionen höher Ordnung und deren Faktorisierungseigenschaften die Validität von effektiven Feldtheorien überprüft werden kann. Im thermischen Gleichgewicht kann das System bis zu Korrelationen 10-ter Ordnung durch das Sine-Gordon-Modell beschrieben werden. Daraufhin wird die Relaxationsdynamik zweier unabhängiger Kondensate, welche zu Anfang in einem stark phasenkorrelierten Zustand präpariert werden, im Kontext von Präthermalisierung, verallgemeinerten statistischen Gesamtheiten und der periodischen Rückkehr eines Quantensystems zurück zu seinem Anfangszustand untersucht. Diese Arbeit ebnet den Weg zur Untersuchung universeller Beschreibungen fern ab vom thermischen Gleichgewicht.

# Declaration

I hereby declare that except where specific reference is made to the work of others, the contents of this dissertation is my original work and has not been submitted in whole or in part for consideration for any other degree or qualification in this, or any other university. I have clearly stated the contribution by other authors and jointly-authored works that I included in my thesis. The content of this thesis is the result of work carried out since the commencement of my graduate studies at the Heidelberg Graduate School of Fundamental Physics, Institute of Theoretical Physics, University Heidelberg.

Sebastian Anton Erne
April 2018

*to my parents for their constant and loving support*

# Table of contents

# Chapter 1

# Introduction

The relaxation of isolated quantum many-body systems lies at the heart of our understanding of the emergence of statistical mechanics from the reversible microscopic dynamics governing the systems evolution. Scientific consensus, drawn from numerous experimental observations, dictates that a sufficiently complex, macroscopic system will eventually reach some kind of stationary state, which, despite its complexity, can be described by only a few macroscopic quantities. The most frequently encountered example thereof are states of thermal equilibrium, which lead to the undoubted success for the foundations of statistical mechanics [1]. However, while quantum many-body systems face a plurality of challenges in practical calculations, the evolution of an isolated system is formally known to follow an energy conserving Hamiltonian flow. This unitary time evolution, while practically incalculable exactly, reveals the paradox of how an isolated system can ever reach a steady state.

This conundrum is beautifully demonstrated by the concept of recurrences in the evolution of an isolated, finite size system. First formulated for classical systems [2, 3], the reconciliation of these seemingly contradictory statements lies at the heart of the emergence of irreversible processes from reversible microscopic mechanics [4]. The concept of such a Poincaré recurrence, and their contradiction to the quantum ergodic theorem formulated by von Neumann [5], were transferred to the quantum regime [6, 7]. The exact unitary evolution of the system in the energy eigenbasis is a simple rotation of each eigenstate with a frequency determined by the energy eigenvalue. Since for a finite size system these eigenvalues are discrete, results for the evolution of quasi-periodic functions immediately dictate that the system in the course of its evolution will return arbitrarily close to its initial configuration at some finite time $t_{\mathrm{rec}}$. While in the thermodynamic limit these arguments do not strictly hold as the spectrum becomes continuous, experimental systems necessarily have a finite extent. This presents us with the question as to how it will be ever possible to observe a steady state in an isolated many-body system.

A possibility to resolve this paradox is presented by the immense complexity of the Hilbert space. Since it scales exponentially with the number of constituents, the time $t_{\text{rec}}$ for such recurrences quickly approaches astronomical scales if no regularities in the spectrum are present [8]. Further, not only the computational complexity but also the amount of information contained in the system grows at this enormous rate, and even determination of the exact microscopic state of the system is shifted to the point of elusiveness. Therefore, as in the foundation of classical statistical mechanics, it is more sensible to concentrate on observable, universal features rather than the exact microscopic evolution. The concept of statistical inference [9, 10] thereby provides a formulation which interpolates between the microscopic and macroscopic properties of the system, and defines emergent statistical ensembles through the inessentiality of the exact microscopic physics for the level of precision the system is probed.

On the level of a dynamical description of the system, this unimportance of the exact microscopic evolution is elegantly phrased in the form of effective field theories. These enable the capture of essential physical properties of the system in terms of effective degrees of freedom, that do not scale as unfavorably with the system size. In addition, these effective theories often allow, due to their simplicity, for a unified description for the low-energy behavior of vastly different systems. The emergence of this universality is connected to a fixed point of the renormalization group [11] which phrases the unimportance of the microscopic details in terms of relevant and irrelevant operators under the renormalization group flow. Through the concept of entropy maximization under the constraints inflicted by the conserved quantities of the effective field theory (see e.g. [12–15]), emergent steady states of the system at different scales can then be phrased in a unified manner.

For a large class of systems and observables the eigenstate thermalization hypotheses (ETH) gives a quantitative description of the thermalization of many-body systems [16, 17]. The validity of the ETH is closely connected to ergodic behavior of the system, and is suggested by various results in quantum chaos theory [18]. The basic principle is, that if the initial state matrix elements of the observable are a sufficiently smooth function of energy, essentially constant over each microcanonical energy shell, the expectation value of the observable in the long time limit relaxes to the predictions of the microcanonical ensemble, independent of the exact configuration in the initial state. ETH has had great success in explaining the emergent thermal properties of complex quantum many-body systems, giving stringent validity criteria connected to alternative theories as e.g. the quantum ergodic theorem by von Neumann [18].

However, not all quantum systems show relaxation to a thermal state and the class of integrable or near-integrable models leads to the breakdown of the ETH [19]. The absence of relaxation in a quantum many-body system was famously demonstrated for the first time in the experiment [20], where colliding clouds of a strongly interacting Bose gas in a one-

dimensional system practically showed no sign of relaxation over the system's lifetime. The reason behind this lack of relaxation is the fact, that the underlying microscopic model is a close realization of the integrable Lieb-Liniger model [21, 22], describing hard-core Bosons in one spatial dimension. While integrability, in contrast to the classical regime [23], is mathematically hard to define in a quantum system [24], it is widely accepted, that therein a large number of dynamically locally conserved quantities strongly restrict the available phase space and hence hinder the equilibration of the system. Alternative definitions include the possibility of an exact solution, by use of the Bethe-Ansatz or similar techniques [25–27], or the absence of diffractive scattering [28] and consequently the fulfillment of the Yang-Baxter equations for scattering matrix [29, 27]. These restrictions on the systems dynamics, however, do not exclude the emergence of a steady state. As argued above, if all constraints inflicted by the integrals of motion are taken into account, a generalized statistical ensemble can be calculated. The approach of an integrable system to such a Generlaized Gibbs Ensemble (GGE) was first put forward by Rigol et al. for a system of hard-core Bosons [30] and was subsequently found in a variety of integrable or near-integrable systems [31–33].

In particular, the emergence of a GGE in near-integrable theories reveals the applicability of emergent statistical descriptions on different time scales during the evolution. The GGE is therein dominated by approximately conserved quantities of the integrable model, which is the effective theory on time scales short as compared to the integrability-breaking contributions [32, 12]. The system therefore, rather than relaxing on a single timescale towards its final steady state, exhibits multiple stages determined by different effective descriptions during its evolution. While here this separation of scales is a result of the near-integrability of the model, the emergence of non-equilibrium quasi-steady states is not bound to near-integrable systems. This brings the notion of universality into the realm of non-equilibrium physics.

A prominent example hereof is the concept of prethermalization [34–37]. Therein initial dephasing of eigenmodes in the system leads to a rapid randomization of the state which becomes independent of the exact initial configuration. During this process certain quantities relax to the an emergent thermal state, determined by the conserved quantities such as energy and particle number but independent of the exact initial configuration. Therefore, while the system in the long term evolution eventually reaches a steady state determined by the microscopic model, the quasi-steady state is determined only by a few universal properties. The emergence of such a prethermalized state was observed in [13, 38], where the theoretically predicted emergence of thermal state in a local light-cone like spread of correlations [14, 39] was connected to the dephasing of eigenmodes of the integrable effective field theory describing the evolution of the system.

It has recently been realized, that a restriction to a quasi-stationary state is in fact not necessary for the definition of universality in far-from-equilibrium situations, and the concept of Non-Thermal Fixed Points [40–42] has been proposed to include time itself as a

dynamical parameter. The idea is that the system in the course of its evolution is attracted to this non-thermal fixed point for a large class of initial conditions. While correlations are non-stationary, their evolution in the vicinity of this attractor solution is determined only by the universal properties of the fixed point. Note especially, that in contrast to equilibrium critical phenomena these non-thermal universality classes are not necessarily related to symmetries in the Hamiltonian, such that systems showing different critical behavior near equilibrium can fall in the same universality class far-from-equilibrium. Numerical evidence of such Non-Thermal Fixed Points was found in systems as diverse as ultracold Bose gases [43–51], relativistic and non-relativistic field theories [52], (non-)abelian gauge theories [53, 54], early universe inflation [55], and in the dynamics of holographically constructed superfluids [56]. Their emergence was often observed together with structure formation, such as vortices, vortex lines, or spin textures. Due to their generic formulation, these non-thermal attractor solutions currently encompass a variety of dynamical critical phenomena, ranging from quantum turbulence [57] to coarsening and phase ordering kinetics [58]. However, the notion of Non-Thermal Fixed Points is deeply connected to the far-from-equilibrium dynamics of an isolated system and hence, while it might share common features, is fundamentally different from near-equilibrium critical phenomena. The question if and how a stringent classification by use of non-thermal universality classes, similar to the classification of Hohenberg and Halperin [59], is possible is a topic of intense ongoing research [60–62].

Ultracold atoms, with the ever increasing possibilities to trap, manipulate, and probe them, present an ideal starting point to investigate these fundamental questions [63]. In this thesis the above described concepts during the non-equilibrium dynamics of far-from-equilibrium quantum many-body systems are studied in the context of a one-dimensional (1D) Bose gas of ultracold $^{87}$Rb atoms trapped on an Atom Chip [64]. In particular we consider two distinct systems: A single 1D Bose gas and a system of two linearly coupled 1D Bose gases, realized in a double well potential. In contrast to their higher dimensional counterparts no transition to a true Bose Einstein condensate is present in these systems [65, 66], which leads, even at the ultracold temperatures necessary to achieve quantum degeneracy, to a rich multi-mode character of the dynamics.

In chapter 2 we give a theoretical introduction to these models, the theoretical approximations, and the effective low-energy description of the systems in terms of the Bogoliubov [67, 68], Luttinger Liquid [69–72], and sine-Gordon [73, 26, 74] model. We further discuss the possible (quasi-)topological excitations present in the system, which in 1D are determined by solitonic waves [67, 75, 76]. These non-dispersive solutions to the classical equations of motion are very stable field configurations expected to emerge during crossing of the phase transition in a finite time [77]. The second part of chapter 2 describes the numerical techniques used in this thesis, namely the truncated Wigner approximation, the stochastic Gross Pitaevskii equation, and the transfer matrix formalism applicable for one dimensional

systems. We conclude chapter 2 by examining explicit solutions for the homogeneous and harmonically trapped system in thermal equilibrium.

In the subsequent chapters we present the combined theoretical and experimental study of a series of experiments[1], which provide comprehensive insight in the relaxation dynamics of isolated, far-from-equilibrium many body systems.

In chapter 3 we investigate the relaxation dynamics of a single Bose gas following a strong cooling quench, which rapidly changes the system from a three-dimensional elongated thermal state to an isolated far-from-equilibrium 1D Bose gas. In accordance with the Kibble-Zureck mechanism [78–81] which predicts the nucleation of topological excitations during the crossing of a phase transition we find the system posterior to the quench to be dominated by solitonic excitations. Due to the limited spatial resolution these are determined through their impact on the momentum distribution of the gas, described by an analytical model of randomly distributed solitonic defects. Changing the speed at which the system is quenched across the transition we find scaling of the defect density in broad accordance with the inhomogeneous Kibble-Zureck predictions. Since our system is likely beyond the Kibble-Zureck regime (as the fastest quench is almost instantaneous) this demonstrates the stability and universality of defect nucleation.

We continue by focusing on the long-term evolution of the system for the fastest quench rate. By comparing the experimental momentum distribution to a thermal quasi-condensate and the predictions of the above random defect model, we find a clear preference of the latter for early times, where the soliton ensemble shows dilution following a power law behavior in time, and complete thermalization of the system on longer time scales. We subsequently analyze the systems dynamics for early times independent of any microscopic model and show that the observed dilution of the soliton ensemble is connected to the approach of a non-thermal fixed point. During the course of this evolution the system is solely determined by a universal function and universal scaling exponents. We identify an emergent conserved quantity in the infrared (IR) which is transported to lower momenta during the evolution and connect this to an emergent condensate peak forming in momentum space.

For the remainder of the thesis we then turn our attention to the Bose gas in a double-well potential. In chapter 4 we first consider the system in and close-to thermal equilibrium. Based on the fundamental principle that quantum many-body systems are fully characterized through their correlations [82, 82, 83] we analyze higher-order correlations of the low-energy effective theory describing the system. The sine-Gordon model, which is a non-Gaussian field theory and hence requires a description beyond the harmonic approximation of free

[1] I am grateful to all the experimentalists I had the great fortune to work with. Due to the close collaboration with the experimental group of Jörg Schmiedmayer at the Technical University in Vienna, all results in this thesis were obtained in direct collaboration with experimentalists. Special thanks go to the collaborators on the projects presented in this thesis, in order of the chapters (3-6): Robert Bücker, Thomas Schweigler, Tim Langen, and Bernhard Rauer

quasiparticle propagation, was proposed to determine the low-energy behavior of two linearly coupled quantum wires realized by our system [84]. Matter-wave interferometry gives direct access to the relative phase between the two condensates, which is the fundamental field described by the sine-Gordon Hamiltonian. Determining the factorization properties of higher-order correlations, we show that the system of two linearly coupled quantum wires (CQW) faithfully describes the sine-Gordon model for correlations up to $10^{\text{th}}$ order. This gives a stringent, statistically significant validation of the approximations performed to arrive at the low-energy description. In particular, the experimental validation of Wick's theorem in case of a Gaussian effective theory allows for a solution of the many-body problem solely through the factorization properties of experimentally measured correlations.

We further extend the presented analysis of higher-order correlations to the situation near thermal equilibrium. Changing the cooling speed in the experiment, non-thermal long lived states are found and connected to the presence of solitonic excitations of the sine-Gordon Hamiltonian. To gain a deeper understanding in the dynamical properties of these topological defects, we study the condensation mechanism theoretically through numerical simulations of the stochastic Gross-Pitaevskii equation (SGPE) [85, 86]. In qualitative accordance with the experiment we find the excitation of solitons during condensation. The results for the full numerical simulations, including in particular interactions between phononic and solitonic excitations, are subsequently compared to a model of statistically independent soltions. This reveals the separated time scales for the thermalization of solitonic and phononic excitations in the sine-Gordon model, which enables us to describe the experimentally measured correlations out-of-equilibrium through a model of randomly distributed non-thermal solitons.

Chapter 5 presents an experiment, in which a single Bose gas is brought out-off equilibrium by rapidly splitting it into two halves. This coherent splitting of the condensates constitutes a quantum quench, which leads to a prethermalized state in the subsequent evolution of the system [13, 38]. We discuss in detail the analytical description of the system in the approximation of a local binomial splitting of the condensate. Of particular interest are harmonically trapped systems, for which we give the first complete solution of the systems dynamics and show that off-diagonal correlations cannot be neglected in the systems evolution. Comparison to numerical simulations of this binomial splitting process in the full non-linear model in the truncated Wigner approximation are found to be in excellent agreement with analytical predictions. Thereafter, we present experimental results, where by changing the splitting protocol the system is shown to relax to a genuine GGE exhibiting multiple temperatures. The evolution and approach of this steady state is explained through quasiparticle dephasing in the integrable low-energy effective theory. Lastly, we give an interpretation of the systems dynamics in terms of emergent conserved quantities. Based on the analytical solution for a binomial splitting and numerical simulations of this instantaneous

splitting process within the SGPE framework we conclude that the emergent prethermalized or GGE state can be understood by dephasing of off-diagonal quasiparticle correlations, which leads to emergent conserved quantities different from the ones imposed onto the integrable system by the splitting process. We conclude by discussing the challenges to a self consistent description of the splitting process and the emergence of the GGE.

In an effort to overcome this challenges we change the splitting protocol in chapter 6 and consider splitting of an initially strongly tunnel coupled system in a double-well potential. Designing the quasiparticle dispersion relation by use of a box-shaped potential, we present the observation of quantum recurrences in the phase coherence between two split condensates. After an initial dephasing of quasiparticles and the approach of a transient thermal like state, correlations of the phase between the two condensates return back close to their initial configuration. Therefore, by implementing an exact recurrence in the effective field theory describing the system, we are able to observe the recurrence of long range order in an interacting many body system containing thousands of interacting particles. Studying the long time evolution we find a significant damping of the recurrence height, which is found to be well described by numerical simulations of the experimental system within the SGPE framework. Exact calculation of the systems dynamics within the harmonic theory, taking into account all experimental imperfections, reveals that the observed damping is caused by higher-order coupling terms, breaking the integrability of the effective field theory.

Finally, a summary and outlook on future perspectives in the study of cold atom systems is presented based on the results and techniques developed in this thesis.

# Chapter 2

# Low-Dimensional Quantum Systems

Low-dimensional quantum systems, for decades, have been a cornerstone of theoretical and mathematical physics [26]. Between exactly solvable and dauntingly incalculable these systems are an ideal field for the investigation of the foundations of quantum many-body physics. Recent developments in the experimental implementation and manipulation of low-dimensional systems enable the detailed study of long standing models of theoretical physics. In the following we introduce the models relevant for this thesis, which is focused on one-dimensional Bose gases.

## 2.1 One-Dimensional Bose Gases

The starting point for the microscopic theory of a Bose gas is the grand-canonical Hamiltonian in second quantized form [68, 67]

$$\hat{H} = \int \mathrm{d}\mathbf{r}\, \hat{\Psi}^\dagger(\mathbf{r},t)\left(-\frac{\hbar^2}{2m}\nabla^2 + V(\mathbf{r}) - \mu\right)\hat{\Psi}(\mathbf{r},t) + \iint \mathrm{d}\mathbf{r}\,\mathrm{d}\mathbf{r}'\, \hat{\Psi}^\dagger(\mathbf{r},t)\hat{\Psi}^\dagger(\mathbf{r}',t)U_{\mathrm{eff}}(\mathbf{r}-\mathbf{r}')\hat{\Psi}(\mathbf{r}',t)\hat{\Psi}(\mathbf{r},t)\,. \tag{2.1}$$

Here $\hat{\Psi}(\mathbf{r},t)$ are the time-dependent field operators in the Heisenberg picture obeying bosonic equal-time commutation relations $[\hat{\Psi}(\mathbf{r}), \hat{\Psi}^\dagger(\mathbf{r})] = \delta(\mathbf{r}-\mathbf{r}')$, the external trapping potential is $V(\mathbf{r})$, and the effective two-body interactions are described by the pseudopotential $U_{\mathrm{eff}}(\mathbf{r}-\mathbf{r}')$. At the temperatures necessary to achieve quantum degeneracy, the low energies and momenta involved reduce the possible scattering events to simple s-wave scattering determined by a single parameter, namely the s-wave scattering length $a_{\mathrm{s}}$ [68, 67]. Interactions are described

to lowest order by an effective contact potential $U_{\text{eff}}(\mathbf{r}-\mathbf{r}') \simeq g_{3\text{D}}\delta(\mathbf{r}-\mathbf{r}')$, where

$$g_{3\text{D}} = \frac{4\pi\hbar^2}{m} a_{\text{s}} \,. \tag{2.2}$$

Depending on the sign of the interaction constant $g_{3\text{D}}$, the Bose gas is either attractive ($a_{\text{s}} < 0$) or repulsive ($a_{\text{s}} > 0$). Since we will consider in the following chapters, a degenerate Bose Gas of $^{87}$Rb with $a_{\text{s}} \simeq 5.24\,\text{nm} > 0$ [87], we focus our discussion on repulsive Bose gases.

The excellent controllability of the external trapping potential $V(\mathbf{r})$ in modern day cold atom experiments enables the study of BECs in highly anisotropic geometries. In the following the potential $V(\mathbf{r}) = V_\perp(x,y) + V(z)$ is chosen harmonic in the radial $V_\perp(x,y) = \frac{1}{2}m\omega_\perp^2(x^2+y^2)$ and generic in the longitudinal direction. To quantify the anisotropy of the system, we define the transverse oscillator length

$$l_\perp = \sqrt{\frac{\hbar}{m\omega_\perp}} \,, \tag{2.3}$$

and the characteristic length scale of the longitudinal confinement $l_\parallel$. For elongated geometries $l_\perp \ll l_\parallel$ one has a separation of energy scales and the density of states for small energies is dominated by excitations in the longitudinal direction. If the energy of the first excited state of the radial trapping potential is greater than the typical energy scales of the system the quasi one-dimensional regime is reached. In thermal equilibrium these are the temperature and chemical potential, so that the conditions can be expressed as

$$k_{\text{B}}T \,,\, \mu \lesssim \hbar\omega_\perp \,. \tag{2.4}$$

Restriction to the transversal ground state freezes out the dynamics in the radial direction. This allows to integrate out the time-independent radial part of the wave function and effectively reduces the dimensionality of the system. The underlying three-dimensional nature of the system is completely encoded in the scattering properties of the effective one-dimensional model [88, 89]. For low momenta, the scattering amplitude can be approximated by a delta potential $U_{\text{eff}}(z-z') \simeq g_{1\text{D}}\delta(z-z')$, where

$$g_{1\text{D}} = 2\hbar a_{\text{s}}\omega_\perp \left(1 - C\frac{a_{\text{s}}}{l_\perp}\right)^{-1} \overset{a_{\text{s}}\ll l_\perp}{\simeq} 2\hbar a_{\text{s}}\omega_\perp \,, \tag{2.5}$$

and $C$ is a constant of order unity[1]. In order to avoid complications due to resonance in the effective 1D scattering we consider in the following the second expression in the limit $a_{\text{s}} \ll l_\perp$, which is fulfilled for all parameters considered in this work.

[1] Note that the definition of the constant $C \approx 1.033$ here differs by a factor of $1/\sqrt{2}$ to the one in [88] due to differences in the definition of $l_\perp$

### 2.1.1 The Lieb-Liniger Model

Taking into account the above simplifications for two-body scattering, the microscopic Hamiltonian (2.1) for low energies and momenta is well approximated by [88]

$$\hat{H}_{\mathrm{LL}} = \int \mathrm{d}z\, \hat{\psi}^\dagger(z,t)\left(-\frac{\hbar^2}{2m}\partial_z^2 + V(z) - \mu + \frac{g_{\mathrm{1D}}}{2}\hat{\psi}^\dagger(z,t)\hat{\psi}(z,t)\right)\hat{\psi}(z,t)\,, \tag{2.6}$$

where for now we consider the one-dimensional regime defined by Eq. (2.4).

The Lieb-Liniger (LL) model [21, 22], which describes a homogeneous 1D Bose gas with $\delta$-potential interactions, is one of the prime examples of a non-relativistic quantum integrable field theory. In the thermodynamic limit, the relevant parameter governing the strength of the interaction is found through scaling of Eq. (2.6) to be

$$\gamma = \frac{m g_{\mathrm{1D}}}{\hbar^2 n_{\mathrm{1D}}}\,, \tag{2.7}$$

where $n_{\mathrm{1D}}$ is the linear density of atoms. In contrast to higher dimensions, interactions in one-dimensional Bose gases become stronger for lower densities. For $\gamma \gg 1$ the system is in the strongly correlated Tonks-Girardeau regime, which, in the limit $\gamma \to \infty$, can be exactly mapped to the spinless free Fermi gas [90]. This correspondence signifies the fundamental principle that quantum statistics play a far less determinant role in 1D systems [71, 72]. This becomes immediately apparent by recognizing that the interchange of two particles in one spatial dimension necessarily leads to interactions between the constituent, and therefore does not allow for a clear distinction between interactions and quantum statistics. For the weakly interacting regime $\gamma \ll 1$ the system is well described by Bogoliubov theory (see Section 2.1.2). An exact solution based on the Bethe Ansatz [25] was found for arbitrary interaction strength by Lieb and Liniger [21, 22] and was extended to finite temperature by Yang and Yang by means of the Thermodynamic Bethe Ansatz [91].

At finite temperature, quantum effects become relevant when the de Broglie wavelength $\lambda_{\mathrm{dB}} = \sqrt{2\pi\hbar/mk_{\mathrm{B}}T}$ is of the order of the mean particle separation $n_{\mathrm{1D}}^{-1}$, which can be used to define the degeneracy temperature [92]

$$T_{\mathrm{d}} = \frac{\hbar^2 n_{\mathrm{1D}}^2}{2mk_{\mathrm{B}}}\,. \tag{2.8}$$

Due to the absence of a true phase transition for the 1D Bose gas, this temperature only defines a broad crossover to the quantum regime. The finite-temperature phase diagram of the LL model is presented in Fig. 2.1 in terms of the dimensionless temperature $T/T_{\mathrm{d}}$ and the LL parameter $\gamma$. Above the degeneracy temperature the system is in the classical ideal gas regime. For lower temperatures, in contrast to the 3D condensate, the 1D Bose gas exhibits

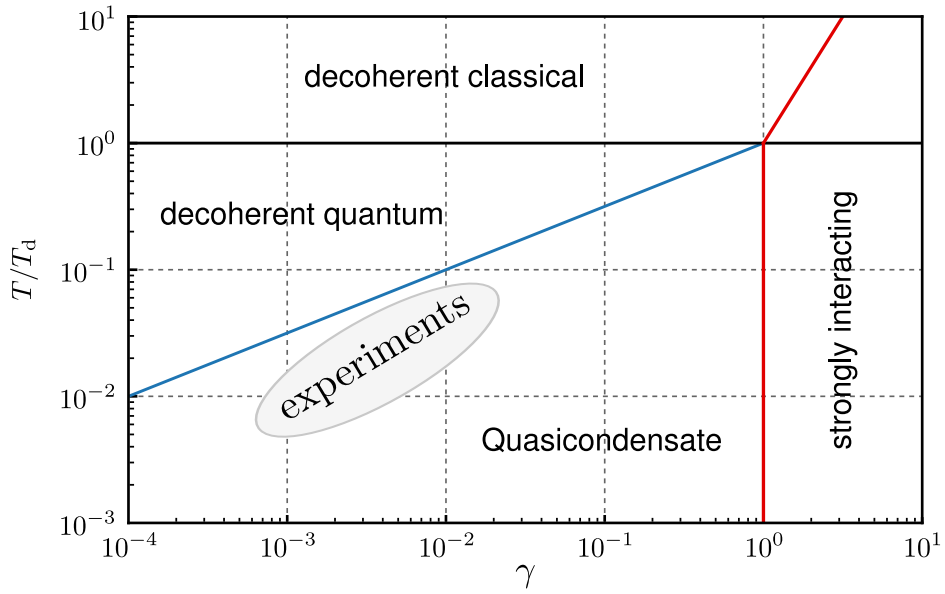


Fig. 2.1 Finite temperature phase diagram of the LL model. In the quantum degenerate regime, several phases exists in the LL model, dependent on the LL parameter $\gamma = mg_{1D}/(\hbar^2 n_{1D})$ and the dimensionless temperature normalized by $T_d = \hbar^2 n_{1D}^2/(2mk_B)$ [92]. The lines mark the crossover between the different regimes and the shaded area depicts typical parameters considered in this thesis.

different phases of quantum degeneracy, which are all loosely connected through a crossover and not a sharp phase transition. For $\gamma \gg 1$ the system is in the strongly correlated Tonks-Girardeau regime. In the quantum decoherent regime, both density and phase fluctuations are large, while for lower temperatures $T/T_d \lesssim \sqrt{\gamma}$ the system enters the quasi-condensate regime, where density fluctuations are highly suppressed. However, in contrast to a true Bose-Einstein condensate, fluctuations of the phase are non-negligible for any temperature and the system regains a multi-mode character. These fluctuations lead to the absence of a true BEC in the thermodynamic limit [65, 66]. However, for a trapped systems long-range order can exceed the size of the atomic cloud, leading to the possibility of a true finite size BEC at low temperatures [93]. For typical experimental parameters considered in this thesis the system is in the weakly-interacting quasi-condensate regime, and thermal fluctuations are typically non-negligible within a single condensate.

### 2.1.2 Bosonization and Tomonaga-Luttinger Liquids

While the exact solution of the LL-model gives valuable insight into the properties of one-dimensional Bose gases, it is not very convenient to calculate its dynamical properties. A more promising approach to describe the dynamics is in the form of an effective field theory[2].

[2]For an excellent review, although not in the context of cold atom systems, see [94]

Before we embark on a detailed discussion of the for our purposes relevant weakly-interacting regime of the LL model, we give some general remarks on effective field theories for one-dimensional systems in the *harmonic fluid approach* [95, 71]. This highlights the importance and especially the generality of this method, whose development culminated in the work of Haldane [69, 70], who introduced the new universality class of *Tomonaga-Luttinger liquids* (TLLs) important for a large number of non-Fermi liquids [26].

It is interesting to first consider why one-dimensional systems require a fundamentally different approach to the formulation of an effective low-energy theory as compared to their higher-dimensional counterparts [71]. Firstly, as evident for the Tonk-Girardeau gas, the distinction between quantum statistics and interaction properties gets blurred. It is therefore desirable to formulate a low-energy theory of the system that is independent of both quantum statistics and the assumption of weak interactions. Secondly, a description of the system in terms of point quasiparticles, as e.g. the dressed fermions in the case of a Fermi-liquid [96], is inadequate because collective excitations arise naturally in one spatial dimension. Due to the inability of particles to freely pass one-another, excitement of a single particle inevitably leads to interactions with its nearest neighbors which quickly converts the disturbance into a collective excitation. Lastly, in bosonic systems no phase transition to the BEC phase occurs at any temperature. Therefore 'traditional' mean-field and Bogoliubov theory, which breaks the $U(1)$-symmetry, cannot be strictly valid in one dimension, and need further justification.

A theoretical framework for this desired unification began with the study of many-Fermion models [97, 98] in the harmonic fluid approach and resulted in the seminal works of Haldane, who generalized the results to what is now known as the TLLs fixed point of renormalization group. The TLL fixed point[3] describes a large class of fermionic and bosonic systems with an algebraic decay of correlations at zero temperature and phononic low-energy excitations, i.e. bosonic quasiparticles with a linear dispersion relation [71]. Strong and weak interactions are treated on the same footing, as the low-energy behavior of the system is described by an effective field theory dependent on phenomenological parameters. These are determined by the microscopic theory but not necessarily defined by a simple perturbative expansion. For bosonic systems the appearance of low-energy phononic excitations is expected from Bogoliubov theory. Note, however, that the TLL is not a mean-field theory and therefore does not break any symmetries. For Fermions, this is an astonishing result which is still reflected in the name *bosonization* often used for the harmonic fluid approach.

In the weakly-interacting regime $\gamma \ll 1$ the TLL Hamiltonian can be derived by a perturbative expansion [99] of the LL Hamiltonian (2.6). Apart from enabling a direct definition of the TLL parameters from the microscopic theory, this has the advantage that it enables the extension of the low-energy approximation beyond the phononic regime and to inhomogeneous systems ($V(z) \neq 0$).

[3] It is actually a line of fixed points characterized by the Tomonaga-Luttinger parameter [72]

For a bosonic system the collective degrees of freedom are the density $\hat{\rho}(z,t)$ and phase $\hat{\theta}(z,t)$, which define the field operators in the Madelung representation

$$\hat{\psi}^\dagger(z,t) = \sqrt{\hat{\rho}(z,t)}\, \mathrm{e}^{-\mathrm{i}\hat{\theta}(z,t)} \,. \tag{2.9}$$

As equality is imposed on the operator level, the quantum fluid approach requires appropriate commutation relations for the collective fields, namely

$$\left[\hat{\rho}(z)\,,\, \hat{\theta}(z')\right] = \mathrm{i}\delta(z-z') \,. \tag{2.10}$$

Strict definition of a hermitian phase operator $\hat{\theta}$ is only possible in a discretized model [99]. As this usually makes the equations rather cumbersome we will immediately consider the continuum limit whenever appropriate. A crucial step in the harmonic fluid approach is to find a suitable low-energy approximation for the density operator $\hat{\rho}(z)$. Since we are interested in the quasi-condensate regime, i.e. low enough temperatures where density fluctuations are highly suppressed, it is sensible to write[4]

$$\hat{\rho}(z) = \rho_0(z) + \delta\hat{\rho}(z) \,, \tag{2.11}$$

where $\rho_0(z)$ is the ground state density profile. The desired low-energy effective theory is now obtained through perturbative expansion of Eq. (2.6) in terms of the small density fluctuations and phase gradients.

To zeroth order in the expansion the Hamiltonian is simply a c-number. This defines the stationary ground state density profile $\rho_0(z)$ through the solution of the time-independent Gross-Pitaevskii equation

$$\left[-\frac{\hbar^2}{2m}\partial_z^2 + V(z) - \mu + g_{1\mathrm{D}}\rho_0(z)\right]\sqrt{\rho_0(z)} = 0 \,. \tag{2.12}$$

For now the geometry of the system is left undefined. Specific solutions will be discussed in Section 2.4. In the following, whenever obvious from the context, we suppress the spatial and temporal dependence of fields to simplify the notation.

[4]This simple form of the density operator is sensible in the weakly-interacting regime, as low-energy fluctuations of the density are correspondent to long wavelengths. In general, the discrete nature of the particles has to be implemented with more care, as short-wavelength low-energy fluctuations are possible. The density operator is therefore approximated by introducing the auxiliary field $\Theta(z)$, defined by $\pi^{-1}\partial_z\Theta(z) = \rho_0(z) + \delta\hat{\rho}(z)$ and takes the form

$$\hat{\rho}(z) = \pi^{-1}\partial_z\Theta(z) \sum_{m=-\infty}^{\infty} \mathrm{e}^{\mathrm{i}m\Theta(z)} \,.$$

For the coarse-grained long-wavelength approximation only the $m = 0$ contribution is taken into account.

The first order correction vanishes, because $\rho_0$ is a stationary solution of Eq. (2.12) and terms containing derivatives of the phase field are at least of second order in the perturbative expansion.

The second order Hamiltonian determines the linearized equations of motion of the density fluctuations $\delta\hat{\rho}$ and the phase $\hat{\theta}$. For later convenience we write it in the form

$$\hat{H}^{(2)} = \int \mathrm{d}z \, \frac{\hbar^2}{4m} \left\{ -\frac{\delta\hat{\rho}}{\sqrt{\rho_0}} \partial_z^2 \left( \frac{\delta\hat{\rho}}{\sqrt{\rho_0}} \right) + \left( \frac{\delta\hat{\rho}^2}{\rho_0^{\frac{3}{2}}} + \sqrt{\rho_0}\hat{\theta}^2 \right) \partial_z^2 \sqrt{\rho_0} - \sqrt{\rho_0}\hat{\theta}\partial_z^2 \left( \sqrt{\rho_0}\hat{\theta} \right) \right\} + g_{1\mathrm{D}} \delta\hat{\rho}^2 \,, \tag{2.13}$$

where from now on we use the rescaled fields

$$\delta\hat{\rho} = \delta\hat{\rho}/\sqrt{\zeta} \,, \qquad \hat{\theta} = \sqrt{\zeta}\hat{\theta} \,. \tag{2.14}$$

For the current case of a single condensate we have $\zeta = 2$. The corresponding Heisenberg equations of motion for the rescaled canonically conjugate fields are

$$\hbar\partial_t \hat{\theta} \sqrt{\rho_0} = \left[ \frac{\hbar^2}{2m} \mathcal{A} - 2\rho_0 g_{1\mathrm{D}} \right] \frac{\delta\hat{\rho}}{\sqrt{\rho_0}} \tag{2.15}$$

$$\hbar\partial_t \frac{\delta\hat{\rho}}{\sqrt{\rho_0}} = -\frac{\hbar^2}{2m} \mathcal{A}\, \hat{\theta} \sqrt{\rho_0} \,. \tag{2.16}$$

where the operator $\mathcal{A} = \partial_z^2 - \rho_0^{-\frac{1}{2}} \left( \partial_z^2 \sqrt{\rho_0} \right)$ is defined to shorten the notation. The equations of motion can be further simplified by eliminating the derivative of the ground state density profile through Eq. (2.12). However, we can make an educated guess for a simple canonical transformation which maps the equations for a quasi-condensate into the usual Bogoliubov equations for a condensate [68, 67]. The new fields

$$B = \frac{1}{\sqrt{2}} \left( \frac{\delta\hat{\rho}}{\sqrt{\rho_0}} + \mathrm{i}\sqrt{\rho_0}\hat{\theta} \right) \quad , \quad B^\dagger = \frac{1}{\sqrt{2}} \left( \frac{\delta\hat{\rho}}{\sqrt{\rho_0}} - \mathrm{i}\sqrt{\rho_0}\hat{\theta} \right) , \tag{2.17}$$

have bosonic commutation relations $\left[ B(z) \,,\, B^\dagger(z') \right] = \delta(z - z')$ and obey the standard Bogoliubov equations

$$\mathrm{i}\hbar\partial_t \begin{pmatrix} B \\ B^\dagger \end{pmatrix} = \begin{pmatrix} -\frac{\hbar^2}{2m}\mathcal{A} + \rho_0 g_{1\mathrm{D}} & \rho_0 g_{1\mathrm{D}} \\ -\rho_0 g_{1\mathrm{D}} & \frac{\hbar^2}{2m}\mathcal{A} - \rho_0 g_{1\mathrm{D}} \end{pmatrix} \begin{pmatrix} B \\ B^\dagger \end{pmatrix} . \tag{2.18}$$

By means of the Bogoluibov expansion of the quadrature field,

$$\begin{pmatrix} B \\ B^\dagger \end{pmatrix} = \sum_m \left[ \begin{pmatrix} u_m \\ v_m \end{pmatrix} \mathrm{e}^{-\mathrm{i}\omega_m t} b_m + \begin{pmatrix} \bar{v}_m \\ \bar{u}_m \end{pmatrix} \mathrm{e}^{\mathrm{i}\omega_m t} b_m^\dagger \right], \tag{2.19}$$

the second order Hamiltonian can be diagonalized within the quasiparticle basis. The dispersion relation of the quasiparticles $\epsilon_m = \hbar\omega_m$ is defined below. Here $\bar{u} \equiv u^*$ is the complex conjugate. The sum is performed over eigenvectors normalized to $\int \mathrm{d}z \left[|u_m|^2 - |v_m|^2\right] = 1$, which exactly cancels the off-diagonal contributions to the Hamiltonian in the modal expansion. The quasiparticle Fock operators obey the usual bosonic commutation relations $[b_m, b_j^\dagger] = \delta_{mj}$, with all other commutators equal to zero. The zero mode ($m = 0$), which is usually considered via the real valued operator for the quantum phase of the field $\hat{Q}$ and its conjugate momentum $\hat{P}$, needs to be included to make the Bogoliubov basis complete and gives rise to phase diffusion [100]. This results in the modal expansion for the density fluctuations and phase operators

$$\delta\hat{\rho} = \sqrt{\frac{\rho_0}{2}} \sum_m \left[ f_m^+ \, \mathrm{e}^{-\mathrm{i}\omega_m t} \, b_m + \mathrm{H.c.} \right] + \hat{P}\partial_{N_0}\rho_0 \tag{2.20}$$

$$\hat{\theta} = \frac{1}{\sqrt{2\rho_0}} \sum_m \left[ -\mathrm{i} f_m^- \, \mathrm{e}^{-\mathrm{i}\omega_m t} \, b_m + \mathrm{H.c.} \right] - \hat{Q} \, . \tag{2.21}$$

We defined the mode functions $f_m^\pm = u_m \pm v_m$, appearing in the expansion of the hydrodynamic variables, normalized to

$$\frac{1}{2} \int \mathrm{d}z \left[ \bar{f}_m^+ f_m^- + f_m^+ \bar{f}_m^- \right] = 1 \, . \tag{2.22}$$

The dispersion relation $\epsilon_m$ and mode functions $f_m^\pm$ are found by inserting the modal expansion into Eq. (2.18) and are given by

$$\epsilon_m \begin{pmatrix} f_m^+ \\ f_m^- \end{pmatrix} = \begin{pmatrix} 0 & -\frac{\hbar^2}{2m}\mathcal{A} \\ -\frac{\hbar^2}{2m}\mathcal{A} + 2g_{1\mathrm{D}}\rho_0 & 0 \end{pmatrix} \begin{pmatrix} f_m^+ \\ f_m^- \end{pmatrix} . \tag{2.23}$$

By construction of the Bogoliubov transformation the second order Hamiltonian (2.13) within the quasiparticle basis is given by a sum of uncoupled harmonic oscillators[5]

$$\hat{H}^{(2)} = \sum_m \epsilon_m b_m^\dagger b_m + \frac{1}{2}\hat{P}^2 \partial_{N_0}\mu_0 \, . \tag{2.24}$$

[5] We neglected an unimportant constant energy functional $E[\rho_0]$ in the definition of $H^{(2)}$ [99]

Due to the inclusion of the so called quantum pressure term $\sim \hbar^2\hat{\rho}^{-\frac{1}{2}}\partial_z^2\sqrt{\hat{\rho}}$ in the equations of motion the above derivation is valid for energies $\epsilon_m > \mu$ and therefore extend beyond the regime of validity of the harmonic fluid approach. Neglecting the quantum pressure term relative to the mean field interaction energy constitutes an important simplification in case of inhomogeneous condensates. This reduces the results obtained in second order perturbation theory to the predictions of the TLL model.

For the ground state $\rho_0$ this simplification is called the Thomas-Fermi approximation, where in Eq. (2.12) the kinetic energy is neglected [101]. Consequently the mean field density profile takes the form of the inverted external potential

$$\rho_0(z) = \frac{1}{g_{1D}}\left[\mu - V(z)\right] \tag{2.25}$$

whereby the chemical potential $\mu$ is defined through the normalization $\int \mathrm{d}z\, \rho_0(z) = N$ to the total atom number $N$.

After neglecting the quantum pressure term Eq. (2.13) reduces to the inhomogeneous Tomonaga-Luttinger-Liquid model [102]

$$\hat{H}_{\mathrm{TLL}} = \frac{\hbar}{2\pi}\int \mathrm{d}z\, \left[v_N(z)(\pi\delta\hat{\rho})^2 + v_J(z)(\partial_z^2\hat{\theta})^2\right] . \tag{2.26}$$

The density stiffness $v_N$ and phase stiffness $v_J$ are defined as [71, 72]

$$v_J(z) = \frac{\pi\hbar\rho_0(z)}{m} \tag{2.27}$$

$$v_N(z) = \frac{1}{\pi\hbar}\partial_{\rho_0}\mu|_{\rho_0=\rho_0(z)} \overset{\gamma\ll 1}{=} \frac{g_{1D}}{\pi\hbar} , \tag{2.28}$$

and are proportional to the superfluid fraction and the inverse compressibility respectively. Note that while we derived the TLL Hamiltonian through an additional approximation within the perturbative expansion, the equations, as discussed at the beginning of this section, describe the long-wavelength physics of a variety of one-dimensional models, in particular the LL model for all values of $\gamma$. It is further common to introduce the local Luttinger parameter $K(z) = \sqrt{v_J/v_N}$, determining the Luttinger-Liquid fixed point [72] and the velocity $c_s(z) = \sqrt{v_J v_N}$, which is the phase velocity of the low-energy excitations, i.e. the speed of sound for the phononic excitations in case of a homogeneous condensate.

Diagonalization of the TLL Hamiltonian proceeds along the same line as before, and can in the weakly interacting regime be directly obtained from Eqs. (2.20)–(2.24) by approximating $\mathcal{A} = \partial_z^2$ and $\mathcal{A} + 2g_{1D}\rho_0 = 2g_{1D}\rho_0$, as well as using the relation $f_m^- = 2g_{1D}\rho_0\epsilon_m^{-1}f_m^+$. Since the TLL model is only valid in the long-wavelength regime, fields and observables are necessarily coarse-grained and all sums are restricted to energies $\epsilon_m \lesssim \mu$.

### 2.1.3 Solitonic Excitations

In the last section we focused on the long-wavelength, small-amplitude oscillations of the field, which can be described by the linearized equations of motion obtained through a perturbative expansion of the many-body Hamiltonian. On the classical level[6], however, it is known the the equations of motion host a variety of non-linear field configurations, minimizing the energy of the system. In the one-dimensional regime, relevant to our study, these quasi-topological excitations are solitonic waves, given by exact analytical solutions in the non-linear regime. These spatially localized, non-dispersive waves have a long history. Solitons have been found to arise in a large number of physical systems [103] ranging from the earths atmosphere [104] to optics [105] and cold-atom systems [106].

The classical non-linear equation of motion for the many-body Hamiltonian (2.6) is the Gross-Pitaevskii equation (GPE) [68, 67]

$$\mathrm{i}\hbar\partial_t\psi(z,t) = \left[-\frac{\hbar^2}{2m}\partial_z^2 + V(z) + g_{1\mathrm{D}}|\psi(z,t)|^2\right]\psi(z,t)\,, \tag{2.29}$$

which to date still represents one of the corner stones in the description of bosonic many-body systems. Exact analytical solutions to Eq. (2.29) can be obtained by use of the inverse scattering method[7] [107] and include exact multi-soliton solutions [108]. In this thesis, we focus on the solution of a single defect [67]

$$\phi_{\mathrm{s}}(z,t) = \sqrt{n_{1\mathrm{D}}}\left[\mathrm{i}\nu + \gamma^{-1}\tanh\left(\frac{z-\nu c_{\mathrm{s}}t}{\sqrt{2}\gamma\xi_{\mathrm{s}}}\right)\right]\mathrm{e}^{\mathrm{i}\mu t}\,, \tag{2.30}$$

in a static homogeneous background $n_{1\mathrm{D}}$ and repulsive interactions[8]. The soliton leads to a localized dip in the density, which is why these defect are referred to as dark solitons. Similar non-dispersive solutions, which show a localized increase in density and are hence called bright solitons [67], are found in case of attractive interactions.

The typical shape of a soliton is depicted in Fig. 2.2 for different soliton velocities $v_{\mathrm{s}} = \nu c_{\mathrm{s}}$, where $c_{\mathrm{s}}$ is the speed of sound in the system. In equilibrium, the width $\xi_{\mathrm{s}}$ of the density suppression is determined by the healing length $\xi_{\mathrm{h}} = \hbar/\sqrt{2mn_{1\mathrm{D}}g_{1\mathrm{D}}}$. This is the typical distance over which the wave function returns to its bulk value when subjected to a local potential perturbation [68, 67]. Since, as we will show explicitly in chapter 3, this is not necessarily the case far from equilibrium, we leave the defect width as a free parameter. For a vanishing soliton velocity $\nu = 0$ the density drops to zero at the center of the soliton. These

[6] Replacing the field operators $\hat{\Psi}^{(\dagger)}$ by classical complex fields $\Psi^{(*)}$

[7] This remarkable chapter of theoretical physics unfortunately lies far beyond the scope of this work. See [27] for a detailed introduction

[8] A more detailed discussion of solitonic defects in spinor Bose gases can be found in [109], whose Masters theses I co-supervised

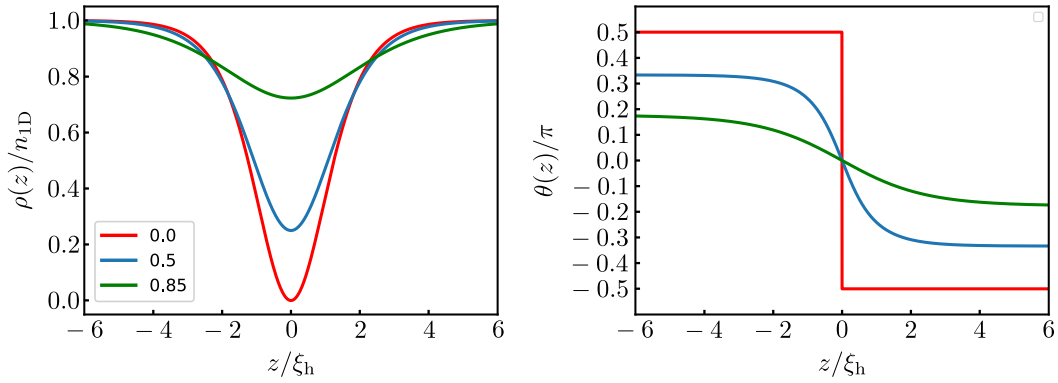


Fig. 2.2 Soliton solution of the LL model. The density suppression (left) and phase modulation (right) for solitons of different velocity $v_s = \nu c_s$, for $\nu = 0, 0.5$, and 0.85. The characteristic width of solitons is the healing length $\xi_h$, scaled by the 'Lorentz'-factor $\gamma^{-1} = \sqrt{1-\nu^2}$. The black soliton ($\nu = 0$) presents a sharp phase kink. Solitons are no topological defects and for increasing velocities get continuously deformed into the unperturbed ground state.

defects are therefore called black, whereas for finite velocities they are referred to as gray solitons, leading to a minimum density $n_{min} = (1-\nu^2)n_{1D}$ with the dimensionless velocity $|\nu| \leq 1$. In addition to the density dip, there is a characteristic phase shift $\Delta\theta = 2\arccos(\nu)$ across a dark soliton. For a black soliton ($\nu = 0$) the phase shows a localized kink with $\Delta\theta = \pi$ where the wave function changes its sign, while for finite velocities ($|\nu| > 0$) the phase changes continuously over the length $\gamma^{-1}\xi_s$, rescaled by the 'Lorentz-factor' $\gamma^{-1} = \sqrt{1-\nu^2}$.

Solitonic excitations represent stable solutions on comparatively long timescales, such that it is possible to adopt, similar to Onsager's picture of point-vortices [110], a particle like representation to describe the dynamics of a solitonic defects [68]. The soliton is thereby, to first order, treated as a particle of negative mass $m_s = -4n_{1D}c_s^{-1}$, representing a hole excitation due to the particles it replaces. Propagation of a solitonic particle is described by Newtonian mechanics, which e.g. allows to determine the movement in an external harmonic confinement, showing a reduced oscillation frequency $\omega_s = \omega_\parallel/\sqrt{2}$ [111, 112]. The dynamics are conveniently described in the extended phase space $(z, \nu, \xi_s)$, where the variable defect width $\xi_s$ is included as an additional parameter.

Multi-soliton states are given, to a first approximation and sufficiently separated defects, as the superposition of single-soliton solutions (2.30). Their interaction properties have to be determined from the solution to the non-linear wave equation [113–116]. For slow moving solitons ($|\nu| < 0.5$) interactions are repulsive on a short length scale. The defects approach each other up to a finite minimal separation during the elastic scattering, before separating again. The minimal distance decreases with increasing velocity, approaching zero for $|\nu| = 0.5$. For higher velocities $|\nu| > 0.5$ a distinction of the defects during the scattering event is no longer possible, revealing their emergent wave character, and only after

the collision for large separations the solitons are again well defined in terms of Eq. (2.30). In both cases, the scattering event after a sufficient separation of the defects leads only to a finite phase shift, resulting in a spatial displacement as compared to the free movement of the defect. As long as the defect ensemble is sufficiently dilute to allow for a clear separation in between scattering events ,this enables a statistical description of the multi-soliton state in terms of particle like excitations. Similar interaction properties are found between solitonic defects and other types of localized density modulations, as e.g. the edges of a trapped condensate [116].

The continuous deformation of a soliton to the ground state of the gas, reached for $|v| \to 1$, shows that solitonic excitations are not topological defects, and hence not connected to a degenerate ground state manifold as a result of symmetries in the underlying microscopic theory. In particular this leads to the possibility of soliton decay[9] as they are not protected by the conservation of any topological charge. Further, the energy of a soliton decreases with increasing velocity $v$, such that any perturbation accelerating the defect may ultimately lead to its decay. In the special case of a harmonic confinement solitonic defects were found to be stable [112], reaching a dynamical equilibrium by constantly emitting and absorbing sound waves during the oscillation. This effect was prominently seen for a slow moving soliton trapped in a shallow harmonic dimple trap [117]. While slow moving solitons are trapped, sound waves are able to leave the system which leads to a constant acceleration of the defect as it cannot reabsorb the emitted phononic excitations. Similarly, interactions with thermal fluctuations were shown to lead to a gradual decay of solitonic excitations [118, 119] and a relaxation of the system back to its equilibrium state. This is in line with the possibility of spontaneous creation, and subsequent decay, of solitonic defects in thermal equilibrium [120], as any temporary large thermal fluctuations of the density or phase field may develop into a transient solitonic excitation. Lastly, since solitons are exact solution to the one-dimensional equations, they are not dynamically stable in elongated three-dimensional condensates, but decay into more stable field configurations like phonons or vortices. This sneaking-instability is however strongly suppressed for condensates in the quasi-one dimensional regime if $g_{1D} n_{1D}/\hbar\omega_\perp \lesssim 2.5$ [119, 121].

### 2.1.4 Bose Gases in the Dimensional Crossover

In some results presented in this thesis the one-dimensional limit for elongated condensates (see Eq. (2.4)) is not completely fulfilled, and radially excited states need to be considered for an accurate description of the system. The dimensional crossover in thermal equilibrium from a one-dimensional to an elongated 3D condensate has recently been studied in [122],

[9] More precisely we mean the decay of a single soliton in a homogeneous system, as compared to the vortex recombinations where at least two vortices are involved.

and good agreement was found with the modified Yang-Yang model [123]. At high densities in the quasi-condensate regime deviations occur due to the transversal swelling of the density profile caused by the atomic repulsion which renormalizes the 1D interaction constant. Within this regime good agreement was found with the equation of state for a quasi-condensate [124, 125]

$$\mu[n_{1\mathrm{D}}] = \hbar\omega_\perp \left( \sqrt{1 + 4n_{1\mathrm{D}}a_\mathrm{s}} - 1 \right) . \tag{2.31}$$

In [125] this was obtained by a variational approach minimizing the chemical potential, and used to obtain a solution for the mean field density profile $\rho_0$ within local density approximation.

Radially excited states also have a significant impact on the dynamics of the system, foremost leading to the breakdown of integrability. This becomes immediately apparent when considering the simplest scattering process allowed by parity conservation; first exciting a single particle to the radially excited state, $\{\phi_{0,0,k_1}, \phi_{0,0,k_2}\} \to \{\phi_{2,0,p}, \phi_{0,0,k_1'}\}$, which subsequently scatters back into the radial ground state, $\{\phi_{2,0,p}, \phi_{0,0,k_3}\} \to \{\phi_{0,0,k_2'}, \phi_{0,0,k_3'}\}$. Adiabatic elimination of the radially excited state is valid as long as the time between the two scattering events is short compared to the dynamics in the longitudinal direction. This leads to an effective three-body interaction $\{k_1, k_2, k_3\} \to \{k_1', k_2', k_3'\}$ where the two sets of momenta are mutually different which contributes to diffractive scattering in the radial ground state and therefore breaks the integrability of the model [126, 127].

Parity conservation enforces the minimum kinetic energy of $2\omega_\perp$ for a collision to transfer particles into a radially excited state. Assuming the kinetic energy of collisions is below this threshold, one is inclined to believe that the system is solely described by the one-dimensional model Eq. (2.6) and retains its integrability. However, due to the time-energy uncertainty the particle number of radially excited states is not conserved and therefore virtual excitations of radially excited states need to be included in perturbative calculations [126]. The above scattering process arises already in second order of perturbation theory (only the two collisions are needed to bring the system back on the energy shell) and gives the dominant contribution to effective three-body collisions. After elimination of the radially excited states the dominant integrability breaking contribution to the Hamiltonian is found to be [126]

$$\hat{H}_\mathrm{ni} = -\frac{\xi}{2} \int \mathrm{d}z \left[ \hbar\omega_\perp a_\mathrm{s}^2 \hat{\psi}^\dagger \hat{\psi}^\dagger \hat{\psi}^\dagger \hat{\psi} \hat{\psi} \hat{\psi} \right] , \tag{2.32}$$

where $\xi = 4\,\mathrm{Ln}\,(4/3) \approx 1.15$ deviates from one due to the inclusion of all radially excited states in the scattering process allowed by parity conservation. The correction (2.32) is negative, and the full Hamiltonian $\hat{H} = \hat{H}_\mathrm{LL} + \hat{H}_\mathrm{ni}$ does not support a stable ground state.

It therefore needs to be considered as a first correction. Nevertheless, $\hat{H}_{\mathrm{ni}}$ represents the dominant contribution to the violation of integrability and the associated relaxation of the system. The full effective one-dimensional Hamiltonian contains higher order interaction terms which stabilize the ground state.

An effective 1D field equation extending beyond the 1D regime can be derived by a variational approach from the classical, or mean-field, equations of a trapped 3D condensate [128]. Therein the transversal wave function is assumed to be a broadened Gaussian with a spatially dependent width $\sigma(z,t)$. Integrating over the radial direction and minimizing the classical action functional with respect to $\sigma$ leads to the relation $\sigma^2 = l_\perp^2 \sqrt{1+2a_\mathrm{s}|\psi|^2}$ between the local radial width and the one-dimensional density. The atomic repulsion broadens the transversal wave function in accordance with [122]. The classical equations of motion for the field take the form of a non-polynomial Schrödinger equation (NPSE)

$$\mathrm{i}\hbar\partial_t\psi(z,t) = \left[-\frac{\hbar^2}{2m}\partial_z^2 + V(z) - \mu + \hbar\omega_\perp \frac{1+3a_\mathrm{s}|\psi(z,t)|^2}{\sqrt{1+2a_\mathrm{s}|\psi(z,t)|^2}}\right]\psi(z,t)\,. \tag{2.33}$$

The NPSE reduces to the GPE[10] (2.29) when expanded to first order in $a_\mathrm{s}n_{1\mathrm{D}}$.

The classical Hamiltonian for the NPSE is given by

$$H_{\mathrm{NPSE}} = \int \mathrm{d}z\, \psi^*(z,t)\left(-\frac{\hbar^2}{2m}\partial_z^2 + V(z) - \mu + \hbar\omega_\perp\sqrt{1+2a_\mathrm{s}|\psi(z,t)|^2}\right)\psi(z,t)\,. \tag{2.34}$$

In second order in $a_\mathrm{s}n_{1\mathrm{D}}$ one recovers the classical analogue of the integrability breaking part $\hat{H}_{\mathrm{ni}}$ with the numerical constant $\xi$ set to one, i.e. only taking into account the lowest radially excited state. In contrast to the perturbative treatment in the full quantum model, the NPSE includes higher order corrections to the Hamiltonian leading to a well defined ground state. The variational approach thereby takes radially excited states into account in an effective, non-simple way.

The equation of state of the NPSE is given by

$$\mu[n_{1\mathrm{D}}] = \hbar\omega_\perp\left(\frac{1+3a_\mathrm{s}n_{1\mathrm{D}}}{\sqrt{1+2a_\mathrm{s}n_{1\mathrm{D}}}} - 1\right) \tag{2.35}$$

and agrees well with Eq. (2.31), showing small deviations for high densities. The transversal swelling of the gas leads to a shift of the speed of sound

$$c_\mathrm{s}^2 = \frac{n_{1\mathrm{D}}}{m}\frac{\mathrm{d}\mu}{\mathrm{d}n} = \frac{\hbar\omega_\perp a_\mathrm{s}n(2+3a_\mathrm{s}n)}{m(1+2a_\mathrm{s}n)^{\frac{3}{2}}}\,. \tag{2.36}$$

[10] with the chemical potential shifted by the radial ground state energy $\hbar\omega_\perp$

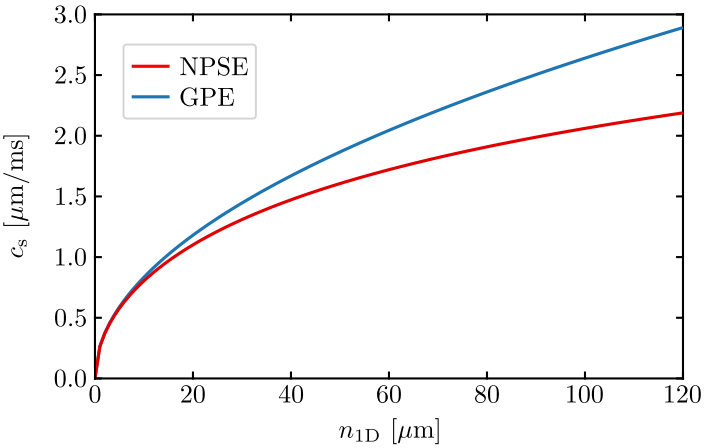


Fig. 2.3 Shift in the speed of sound $c_s$ in the dimensional crossover. Beyond the one-dimensional approximation, swelling of the radial density profile for increasing linear densities $n_{1D}$ leads to a decrease in the propagation speed of phononic excitations along the longitudinal direction. For low densities the GPE and NPSE predictions coincide and the system only occupies the radial ground state.

This effect is faithfully reproduced in a perturbative expansion[11] of the NPSE Hamiltonian (2.34). The inclusion of transversally excited states leads to a renormalization of the effective 1D coupling constant in the harmonic approximation

$$g_{1D} = \hbar\omega_\perp a_s \frac{(2 + 3a_s\rho_0)}{(1 + 2a_s\rho_0)^{\frac{3}{2}}} , \tag{2.37}$$

which, to second order in $a_s$, is in accordance with the perturbative expansion of the full quantum calculation including the non-integrable part $\hat{H}_{ni}$ in the limit $\xi = 1$. In Fig. 2.3 we show the difference in the speed of sound caused by the inclusion of transversally excited states. We will see in chapter 6 that this needs to be considered in comparison to cold atom experiments and demonstrate the validity of the NPSE approach within the semi-classical field approximation for the far-from equilibrium dynamics of elongated condensates within the dimensional crossover.

## 2.2 Coupled Bosonic Quantum Wires

As a second model in this thesis we consider a Bose gas confined to an elongated double-well potential [38, 67]. In the two mode approximation [67, 129] this system is described by two separated one-dimensional condensates, located in the left (L) and right (R) well of the potential, which are linearly coupled by tunneling through the double-well barrier. Due to the spatial separation of the two condensates intra-species interactions are negligible and the

[11] The perturbative expansion is equivalent to the 1D case, except for the interaction term which is obtained to arbitrary order by expanding $\sqrt{1 + 2a_s(\rho_0 + \delta\rho)}$ in a double binomial series and taking advantage of the recurrence relation of the Gamma function $\Gamma(x + 1) = x\Gamma(x)$.

system can be described by two linearly coupled quantum wires [130]

$$\hat{H} = \sum_{j=\mathrm{L,R}} \int \mathrm{d}z\, \hat{\psi}_j^\dagger(z,t) \left( -\frac{\hbar^2}{2m}\partial_z^2 + V(z) + \mu + \frac{g_{1\mathrm{D}}}{2}\hat{\psi}_j^\dagger(z,t)\hat{\psi}_j(z,t) \right) \hat{\psi}_j(z,t) \\ - \hbar J \int \mathrm{d}z\, \hat{\psi}_1^\dagger(z,t)\hat{\psi}_2(z,t) + \hat{\psi}_2^\dagger(z,t)\hat{\psi}_1(z,t)\,. \tag{2.38}$$

The first part describes the dynamics of each condensate, given by the LL Hamiltonian (2.6), while the second hopping term $J$, determined from the overlap integrals of the radial wave function [129], leads to an additional coupling between the two condensates. Due to the absence of intra-species interactions the system, in contrast to the Bose mixture [131, 132], does not have a phase transition or quantum critical point for any value of the coupling $J$. Nonetheless, the hopping term introduces a variety of interesting dynamical phenomena from Josephson oscillations [133, 134, 67], the possibility of matter-wave interference [38] between the two condensates, to a non-trivial low-energy effective theory [84], on which we will focus our attention for the remainder of this section.

### 2.2.1 Perturbative expansion for coupled quantum wires

As in the case of a single condensate, we use the quantum hydrodynamical approach, write the fundamental fields $\hat{\psi}_{\mathrm{L,R}}(z,t)$ in the Madelung representation Eq. (2.9) and a priori assume small density fluctuations $\delta\hat{\rho}_{\mathrm{L,R}}(z,t)$ within each of the condensates. The full Hamiltonian of the coupled system Eq. (2.38) has the form $\hat{H} = \hat{H}_\mathrm{L} + \hat{H}_\mathrm{R} + \hat{H}_\mathrm{J}$. Here $\hat{H}_{\mathrm{L,R}}$ are given by the LL Hamiltonian Eq. (2.6), whose perturbative expansion was already discussed for the case of a single condensate. We therefore refer to Sect. 2.1.2 for details and focus our discussion on the relevant alterations arising from the non-vanishing hopping term $\hat{H}_\mathrm{J}$ coupling the two systems.

Since the coupling depends only on the relative phase $\hat{\theta}_\mathrm{L}(z) - \hat{\theta}_\mathrm{R}(z)$ of the two condensates it is advantageous to introduce the common (c) and relative (r) degrees of freedom

$$\delta\hat{\rho}_\mathrm{c}(z) = \delta\hat{\rho}_\mathrm{L}(z) + \delta\hat{\rho}_\mathrm{R}(z)\,, \qquad \hat{\theta}_\mathrm{c}(z) = \frac{\hat{\theta}_\mathrm{L}(z) + \hat{\theta}_\mathrm{R}(z)}{2}\,, \tag{2.39}$$

$$\delta\hat{\rho}_\mathrm{r}(z) = \frac{\delta\hat{\rho}_\mathrm{L}(z) - \delta\hat{\rho}_\mathrm{R}(z)}{2}\,, \qquad \hat{\theta}_\mathrm{r}(z) = \hat{\theta}_\mathrm{L}(z) - \hat{\theta}_\mathrm{R}(z)\,. \tag{2.40}$$

These fields fulfill canonical commutation relations as well, where the explicit form of the normalization was chosen for later convenience.

In zeroth order in the density and phase fluctuations (c.f. Eq. (2.12)) the coupling $J$ only leads to a shift of the chemical potential $\mu_{\mathrm{L,R}} = \mu_0 - \hbar J$. Here $\mu_0$ is the chemical potential in the limit $J = 0$, chosen to be the same for the left and right condensates. Consequently

we expand the equations of motion of each condensate around the same mean field density profile $\rho_0$. For $\mu_L \neq \mu_R$ the coupled system $J \neq 0$ shows Josephson oscillations between the two wells [67, 134, 133], while for the uncoupled system $J = 0$ the imbalance between the two condensates leads to a coupling of common and relative degrees of freedom in second order perturbation theory due to the difference in the speed of sound in each condensate [135, 136].

Neglecting for the moment the coupling $\hat{H}_J$, the expansion of $\hat{H}_{L,R}$ to second order in the density fluctuations and phase gradients leads for $\mu_L = \mu_R$ to the decoupling of common and relative degrees of freedom

$$\hat{H}_L^{(2)} + \hat{H}_R^{(2)} = \hat{H}_c^{(2)} + \hat{H}_r^{(2)} \,. \tag{2.41}$$

Here $\hat{H}_{L,R,c,r}^{(2)}$ are, in terms of the rescaled fields Eq. (2.14), given by Eq. (2.13) with $\zeta_{L,R} = 2$, $\zeta_c = 4$ and $\zeta_r = 1$.

The contribution of the coupling $\hat{H}_J$ between the two condensates up to second order in the density fluctuations is given by

$$\hat{H}_J^{(2)} = -\hbar J \left[2\rho_0 + \delta\hat{\rho}_c\right]\left(\cos\left(\hat{\theta}_r\right) - 1\right) + \frac{\hbar J}{\rho_0}\delta\hat{\rho}_r^2 \cos\left(\hat{\theta}_r\right) \tag{2.42}$$

$$\overset{\text{eq.}}{\approx} -2\hbar J\rho_0 \cos\left(\hat{\theta}_r\right) + \frac{\hbar J}{\rho_0}\delta\hat{\rho}_r^2 \,. \tag{2.43}$$

While phase gradients are expected to be small for all values of the coupling $J$, the phase field itself needs to be considered non-perturbatively, resulting in the full cosine potential. This couples the common and relative degrees of freedom already at first order in the density fluctuations. In, or near, thermal equilibrium however, it is presumed that the coupling of density and phase fluctuations are negligible and can be neglected in the low-energy regime. In the following we adopt this approximation of the hopping term Eq. (2.43) and confirm its validity in chapter 4. This completely decouples the second order Hamiltonian into an independent sum $\hat{H}^{(2)} \simeq \hat{H}_c + \hat{H}_r$ of common and relative degrees of freedom respectively. The common modes are described by $\hat{H}_c = \hat{H}_c^{(2)}$, i.e. Eq. (2.13) for a single Bose gas, and are hence independent of the coupling $J$ between the two condensates. For the relative modes on the other hand, where $\hat{H}_r = \hat{H}_r^{(2)} + \hat{H}_J^{(2)}$, the linear coupling $J$ introduces new dynamics, on which we focus our discussion for the remainder of this and the following sections.

In order to arrive at an analytically feasible description of the system we neglect the quantum pressure term in $\hat{H}_r^{(2)}$, as we did in the case of a single condensate to reduce it to the inhomogeneous TLL model Eq. (2.26). For the case of two coupled bosonic quantum wires we find a similar reduction to one of the fundamental field theoretical models, namely the

sine-Gordon Hamiltonian [26, 74]

$$\hat{H}_{\mathrm{r}} = \frac{\hbar}{2\pi}\int \mathrm{d}z\, \left[v_N(z)(\pi\delta\hat{\rho}_{\mathrm{r}})^2 + v_J(z)(\partial_z^2\hat{\theta}_{\mathrm{r}})^2 - 4\pi J\rho_0 \cos\left(\hat{\theta}_{\mathrm{r}}\right)\right] . \tag{2.44}$$

The stiffnesses $v_J$ and $v_N$ were defined in Eqs. (2.27) & (2.28) respectively, where the 1D coupling constant $g = g_{1D} + \hbar J/\rho_0$ is rescaled due to the non-vanishing coupling between the two condensates. The rich physics of the sine-Gordon model are discussed in the following Section 2.2.2, but before we continue with a further approximation of the model in case of strong tunnel-coupling $J$.

When the potential energy is dominant compared to the kinetic term, i.e. $J\rho_0/v_J \gg 1$, the field $\hat{\theta}_{\mathrm{r}}$ is restricted close to a single minimum of the cosine potential. Due to the periodicity of the Hamiltonian, i.e. the invariance under a global shift $\hat{\theta}_{\mathrm{r}} \to \hat{\theta}_{\mathrm{r}} + 2\pi n$ for $n \in \mathbb{N}$, this is equivalent to the phase field itself being small and contributing to the same order as its gradient in the perturbative expansion. We can therefore expand the cosine potential to second order in the phase field, to obtain what we will call the massive TLL model

$$\hat{H}_{\mathrm{mTLL}} = \frac{\hbar}{2\pi}\int \mathrm{d}z\, \left[v_N(z)(\pi\delta\hat{\rho}_{\mathrm{r}})^2 + v_J(z)(\partial_z\hat{\theta}_{\mathrm{r}})^2 + 2\pi J\rho_0\hat{\theta}_{\mathrm{r}}^2\right] . \tag{2.45}$$

The homogeneous quadratic model can easily be extended to energies $E > \mu$ by including the quantum pressure term, resulting in the full Bogoliubov spectrum [130]. The diagonalization is equivalent to a single condensate, for $g = g_{1\mathrm{D}}$ and a shift of the kinetic operator $\hbar^2\mathcal{A}/(2m) \to \hbar^2\mathcal{A}/(2m) + 2\hbar J$.

Finally, the model of coupled bosonic quantum wires can be extended into the regime of the dimensional crossover. Starting from the 3D system in a DW-potential this entails calculating the influence of radial swelling on the overlap integrals to determine the quasi 1D parameters of the model. For an inhomogeneous condensate the 1D parameters acquire a non-trivial spatial dependence through the local density, as was the case for the contact interaction $g_{1\mathrm{D}}$ in the NPSE Eq. (2.37). We investigated a spatial modulation of the coupling in numerical simulations but found that it is commonly negligible in comparison to the experiment. We therefore consider the coupling as an exterior parameter. Using, as for the NPSE, a variational approach for the width of the radial wave-function in the classical action the coupling term $\hat{H}_{\mathrm{J}}$ is for $\mu_{\mathrm{L}} = \mu_{\mathrm{R}}$ unchanged by the radial swelling of the condensates. The system close to the 1D regime is therefore described by replacing $\hat{H}_{\mathrm{L,R}}$ with the NPSE Hamiltonian (2.34)[12]. In particular this also leads to a shift of the speed of sound for the relative degrees of freedom.

[12]Note that in the case of non-vanishing intra-species contact interactions the local width of the condensates is determined by a polynomial of higher order and cannot be determined analytically. However by Descartes rule of signs the existence of a unique solution is always ensured.

### 2.2.2 Quantum sine-Gordon model

The sine-Gordon model is one of the prime examples of mathematical physics, and one of only three integrable field theories with an infinite number of higher-order interaction constants [74]. Its applications are ubiquitous ranging from particle and condensed matter physics to the motion of rigid pendula and dislocations in crystals [73, 137, 95, 26].

The sine-Gordon Hamiltonian (2.44) can be written in rescaled form

$$H_{\mathrm{SG}} = \frac{1}{2}\int dz \left[\Pi^2 + (\partial_z\phi)^2 - \Delta\cos\beta\phi\right], \tag{2.46}$$

commonly used in theoretical studies of the SG model [84, 138]. Here we set $\hbar = k_{\mathrm{B}} = 1$, rescaled time $t \to c_s t$, and set $c_s = 1$. Furthermore, we define the conjugate momentum $\Pi = \beta\,\delta\rho$, the rescaled phase field $\phi = \varphi/\beta$, as well as the parameters $\beta = \sqrt{2\pi/K}$ and $\Delta = 8Jm/\beta^2$.

The SG model is an exactly solvable field theory [84, 95, 26]. The spectrum of the Hamiltonian, Eq. (2.46), depends on the value of $\beta$. The system undergoes a Kosterlitz-Thouless transition at the critical point $\beta^2 = 8\pi$ [139]. For larger values, $\beta^2 > 8\pi$, the cosine term becomes irrelevant and the system is in the weakly interacting regime. The Hamiltonian therein reduces to the TLL model. As was shown in [140] for $\beta^2 < 8\pi$ the sine-Gordon model is equivalent to the zero-charge sector of the massive Thirring model, describing massive Dirac fermions with local self-interaction. In this regime, the spectrum can be further divided into two distinct sectors, separated by the Luther-Emery point, $\beta^2 = 4\pi$, at which the model describes non-interacting massive Dirac fermions. For $4\pi < \beta^2 < 8\pi$, the system is described by soliton and anti-soliton excitations, whereas for $0 < \beta^2 < 4\pi$, the spectrum contains additional bound states of (anti-)solitons, called breathers.

These solitonic solutions attracted much attention to the SG model [75]. The single soliton/anti-soliton solution is given by

$$\varphi_{\mathrm{S}}(z) = 4\arctan\left[\pm\exp\frac{z - z_0 - v_{\mathrm{S}}t}{l_J\sqrt{1-(v_{\mathrm{S}}/c_{\mathrm{s}})^2}}\right], \tag{2.47}$$

where $z_0$ is the position and $v_{\mathrm{S}}$ the velocity of the soliton, and $c_{\mathrm{s}} = \sqrt{gn_{1\mathrm{D}}/m}$ the speed of sound (see e.g. [73]). The width of the soliton is given by the length scale $l_J = \sqrt{\hbar/4mJ}$. Motion of the soliton leads to a contraction of this length scale by the 'Lorentz' factor $\sqrt{1-(v_{\mathrm{S}}/c_{\mathrm{s}})^2}$. These topological defects represent a local phase-twist of $2\pi$, connecting adjacent minima of the cosine potential. The parameters applying to our experiment correspond to the weakly interacting regime, $K \gg 1$, typically $K = 63\ldots73$, and hence $\beta^2 = 0.1\ldots0.086$. The sine-Gordon model is hence in the strongly correlated regime, and the cosine potential

can in general not be neglected. This allows for the study of this highly relevant, non-trivial field theory by use of ultracold Bose gases confined in a DW-potential.

## 2.3 Semi-Classical Field Approximation

Semi-classical field approximations, and especially their numerical implementation, has taken a fundamental role in the study of cold-atom systems in theory and experiments alike [141]. One of the underlying principles of these techniques is the fact, that the full quantum dynamics of a many-body system is often well approximated by stochastic simulations of the classical equations of motion. There has also been much progress in numerical simulations aiming to solve the full quantum dynamics, such as multi-configural Hartree-Fock for Bosons (MCTDHB) [142, 143], 2-PI effective action [37, 144], time-dependent density matrix renormalization group (tDMRG) [145], or conformal field theories [56]. However, while the ever increasing level of controllability in cold-atom experiments drives the necessity of a deep understanding of the full quantum dynamics, it also requires an increased understanding for the specifics of the experimental implementation. Numerical techniques based on the semi-classical description present a good approximation to the non-linear quantum dynamics in a highly adaptable framework and hence play an important role in the study of quantum many-body systems.

Since the generalization to a two-component Bose gas is straight forward we consider in Sections 2.3.1 & 2.3.2 for simplicity a single condensate. Details on the numerical implementation are given in Appendix B.

### 2.3.1 Truncated-Wigner Formalism

Probably one of the best known semi-classical approximations is the so called Truncated Wigner Approximation (TWA) [141, 146]. Based on the phase space formulation of quantum mechanics an intricate role is played by the Weyl transformation, which defines a one to one mapping between quantum operators and ordinary functions in phase space [146]. The transformation of the density matrix $\hat{\rho}$ is the so called Wigner function $W(\psi, \psi^*)$, where we immediately adopt the commonly used coherent state representation. In leading order, i.e. to first order in $\hbar$ which is the TWA, quantum corrections do not affect the classical equations of motion. This means that in the semi-classical limit only the time independent Wigner function exhibits corrections due to the quantum nature of the system. Expectation values of observables are subsequently calculated through the averaged of its Weyl symbol weighted by the initial state Wigner function. Corrections beyond the TWA include so called quantum jumps which explicitly add a stochastic noise to the evolution of a single trajectory [146].

These effects are however highly suppressed near the classical limit where the field $\psi$ has large occupation, as it is usually the case for the low energy regime of a Bose gas.

The Wigner function is, while not in general, for many initial states positively defined and can therefore be interpreted as a classical probability distribution. Its time evolution, given by a classical Liouville equation, can be solved by the method of characteristics, where each trajectory evolved according to the classical field equations can be interpreted as a possible realization of the dynamics. Specifically, the procedure is as follows: A single realization of the field is sampled from the initial state Wigner function $W(\psi, \psi^*)$ using direct or Monte Carlo sampling. The field configuration is then evolved according to the classical field equations, in our case the GPE or NPSE equations, up to some time $t$, after which the expectation value of an observable $O(\psi, \psi^*)$ is calculated by averaging many trajectories, i.e.

$$\langle O \rangle = \frac{1}{N} \sum_{i=1}^{N} O(\psi_i, \psi_i^*) \, . \tag{2.48}$$

Important initial state Wigner functions are vacuum and thermal states, for which the Wigner function in the quasiparticle basis is given by a product of uncorrelated complex Gaussian distributions. Their variance is determined by the thermal and quantum occupation of the mode given by the Bose Einstein distribution and an additional $1/2$ of quantum noise (see e.g. [141]).

### 2.3.2 The Stochastic Gross-Pitaevskii Equation

A large part of this thesis is concerned with finite temperature states. Although the sampling of initial conditions in the TWA can be very efficiently implemented it requires the solution to the, in general, inhomogeneous Bogoliubov equations and by construction does not account for higher-order correlation between the quasiparticles.

We therefore consider an alternative approach for finite temperature states of sufficiently high temperature $T$, where the system dynamically thermalizes during the evolution of the so called stochastic Gross-Pitaevskii equation (SGPE) [147–149][13]. Applications of the SGPE, while fewer in number than the TWA, have shown great success in describing the finite temperature dynamics of cold-atom systems [119, 151, 152, 141, 153]. For a comprehensive analysis of the validity range of the SGPE and comparison to other finite temperature approaches see [154].

The derivation of Stoof, which we will adopt here, is based on the Keldysh non-equilibrium formalism [147, 155] and was first numerically implemented in [156]. The

[13] There are two distinct formulations of such a nonlinear Lagevin equation, which arise from different formalisms. For an excellent review see [150]

idea is to separate the system, in a Hartree-Fock-type Ansatz, in a part containing the low-energy, highly occupied modes well approximated in the semi-classical limit by the field $\psi$, and a remainder of high-energy, non-condensed modes described by a quantum Boltzmann equation. In contrast to the Zaremba-Nikuni-Griffin (ZNG) theory [157] the field $\psi$ here describes not only the condensate but contains a number of low-energy modes. For simplicity we will however in the following often refer to $\psi$ simply as the condensate, instead of the low-energy modes described by the SGPE equation. By integrating out the high-energy region, the time evolution of the probability distribution for the condensate $\psi$ is given by a Fokker-Plank equation. The drift coefficient is determined by the unitary evolution of the system plus a complex source term $\mathrm{i}\mathcal{R}$ accounting for scattering between the condensed and non-condensed atoms. The random nature of fluctuations is given by the diffusion coefficient $\hbar\Sigma^{\mathrm{K}}(z,t)$, where $\Sigma^{\mathrm{K}}$ is the Keldysh self-energy. These additional terms depend on the explicit distribution of high-energy particles of energy $\epsilon_{\mathrm{c}}$, which in the Hartree-Fock Ansatz is an operator dependent on the non-vanishing mean-field potential $|\psi|^2$. In general this dependence of the energy on $\psi$ leads to a complicated stochastic equation including multiplicative noise [119].

An important simplification is to assume that the high-energy region of the system is in thermal equilibrium. If thermalization of high-energy particles happens on a time scale much faster than the dynamical processes being modeled, the high-energy region acts as a static heat bath for the condensate. As a consequence, the noise and the dissipative term in the SGPE are connected through the fluctuation-dissipation relation

$$\mathrm{i}\mathcal{R}(z,t) = -\frac{1}{2}\hbar\Sigma^{\mathrm{K}}(z,t)\left(1+n_{\mathrm{BE}}[\epsilon_{\mathrm{c}}]\right)^{-1} \ . \tag{2.49}$$

This allows to map the evolution of the field $\psi$ while being in contact with the thermal cloud to the Langevin equation

$$\mathrm{i}\hbar\partial_t\psi = \Big[U[\psi,\psi^*] - \mathrm{i}\mathcal{R}(z,t) - \mu\Big]\psi + \eta(z,t) \ , \tag{2.50}$$

where the chemical potential $\mu$ defines the total atom number in thermal equilibrium and the operator $U[|\psi,\psi^*]$ determines the unitary evolution of the system, given by either the GPE (2.29) or NPSE (2.33). The dissipative term $\mathcal{R}$ describes particle exchange due to collisions of condensate and non-condensed atoms, while the stochastic "force" $\eta$ represents a noise term due to the random nature of incoherent scattering within the system. Both terms lead to non-conservation of the particle number in the condensate and are essential to ensure that the fluctuation-dissipation theorem is satisfied in the final equilibrium state.

To arrive at a numerically feasible theory the SGPE is commonly further approximated by taking the limit of large-occupation, i.e. approximating the Bose-Einstein distribution

with the Rayleigh-Jeans limit. With the classical form of the fluctuation-dissipation relation (2.49), Eq. (2.50) can be written in closed form

$$i\hbar\partial_t\psi = [1 - i\gamma(z,t)]\Big(U[\psi,\psi^*] - \mu\Big)\psi + \eta(z,t)\,. \tag{2.51}$$

Here $\gamma(z,t) = i\beta\Sigma^K(z,t)/4$, with the inverse temperature $\beta = 1/k_B T$. The stochastic force term $\eta$ is a complex Gaussian white-noise with zero mean and variance[14]

$$\langle\eta(z,t)\eta(z',t')\rangle = 2\gamma(z,t)k_B T\delta(z-z')\delta(t-t')\,. \tag{2.52}$$

Due to the classical form of Eq. (2.49) equilibrium states of the SGPE are stationary states under further unitary evolution of the GPE or NPSE. This is in contrast to the TWA when sampled from the Bose-Einstein distribution, which shows further relaxation to the classical thermal equilibrium state in the long-time evolution. A further common simplification is to choose the parameter $\gamma(z,t)$ independent of time and space. The spatio-temporal dependence can be approximated by direct evaluation in the ergodic approximation or the approximation using Lerch transcendents (for a comparison see [119]). Note that, if one is only interested in creating a thermal state of the system, and not in the dynamics during the condensation, the numerical value of $\gamma$ is arbitrary (within reasonable limits) as it merely rescales the condensation time. However, the value should not be chosen to high in order to avoid the excitation of topological defects during the condensation process which may prevail for a long time, slowing down the approach to thermal equilibrium. Expectation values for observables are calculated equivalent to the truncated Wigner approach, by averaging over many independent realizations.

### 2.3.3 Transfer Matrix Formalism

The TWA and SGPE discussed in the last Sections are applicable for a wide variety of systems, including arbitrary dimensions $d$ and inhomogeneous trapping potentials $V(z)$. However, one-dimensional systems allow for a different approach, based on the Transfer Matrix Formalism (TMF) developed in [158, 76]. Therein, correlation functions of the system at temperature $T$ can be calculated within the classical-field approximation. For two tunnel-coupled superfluids in the harmonic approximation (2.45) this has been analysed in [159]. In particular, the Gaussian fluctuations of the phase along $z$ have been shown to be describable by an Ornstein-Uhlenbeck process[15]. Further developed by I. E. Mazets in the context of the SG model [160] and recently extended to describe the full system of Bose gases in a double well potential [161], this non-perturbative method allows for a direct

[14] More general $\langle\eta(z,t)\eta(z',t')\rangle = \hbar\Sigma^K(z,t)\delta(z-z')\delta(t-t')/2$

[15] Note that we deal with stochastic processes evolving in space, along $z$, but not in time.

sampling of field configuration from the equilibrium distribution for a homogeneous system with arbitrary local interactions[16]. This enables the fast calculation of correlation functions in thermal equilibrium, as no time is needed for the dynamical equilibration of the system. We discuss the explicit solution for the SG model in chapter 4, and outline here the basic principles of this method.

The general model considered in [161, 160] is described by the (classical) Hamiltonian

$$H = \int dz \Big[ \sum_{j=1}^{M} \left( -\frac{\hbar^2}{2m} \psi_j^* \frac{\partial^2}{\partial z^2} \psi_j - \mu \psi_j^* \psi_j \right) + V(\psi_M^*, \ldots, \psi_1^*, \psi_1, \ldots, \psi_M) \Big], \tag{2.53}$$

for the $M$-component Bose field $\psi_j(z)$, $j = 1, \ldots, M$, with an arbitrary local, but not necessarily pairwise interaction potential $V$, conserving the total number of atoms, $N = \int dz \sum_{j=1}^{M} \psi_j^* \psi_j$. The transfer-matrix formalism [158, 76] yields the following expressions for the thermal average and correlation function of operators $O(z)$:

$$\langle O(z_1) \rangle = \langle 0 | O(z_1) | 0 \rangle, \tag{2.54}$$

$$\langle O(z_1) O(z_2) \rangle = \sum_n \langle 0 | O(z_2) | n \rangle \langle n | O(z_1) | 0 \rangle e^{-(\kappa_n - \kappa_0)(z_2 - z_1)} \qquad (z_2 \geq z_1) \,. \tag{2.55}$$

The matrix elements with respect to the eigenstates $|n\rangle$ of the transfer operator $\hat{K}$ (see below), with eigenvalues $\kappa_n$, are defined as:

$$\langle n' | O(z) | n \rangle = \int \prod_j \mathrm{d}q_j \, \Psi_{n'}^* O(z) \Psi_n \,, \tag{2.56}$$

where we define $q_{2j-1} = \mathrm{Re}(\psi_j)$ and $q_{2j} = \mathrm{Im}(\psi_j)$ to shorten the notation. The observables $O(z) = O(q_0, \ldots, q_{2M})|_z$ can be arbitrary functions of the classical field provided the integrals exist. The eigenvalues $\kappa_n$ and orthonormal eigenfunctions $\Psi_n = \Psi_n(q_0, \ldots, q_{2M})$ are given by the Hamiltonian-like hermitian operator [161]

$$\hat{K} = \sum_{j=1}^{2M} \left( -D \frac{\partial^2}{\partial q_j^2} - \beta \mu q_j^2 \right) + \beta V(q_0, \ldots, q_{2M}) \,, \tag{2.57}$$

with $D = m/2\beta\hbar^2$. The operator $\hat{K}$ is directly related to the transfer matrix operator $\hat{T}$ appearing in the calculation of the classical partition function [158, 76, 161, 134], and has the same form as a $2M$-dimensional quantum Hamiltonian for a single particle of mass $\hbar^2/2D$ in an external potential[17]. The equilibrium distribution (c.f. Eq. (2.54)) is determined by the

[16] As long as the system remains dynamically stable

[17] Therefore, as was argued in [161], $\Psi_0$ has all properties of a Hamiltonian ground state function

ground (lowest-eigenvalue) state of the operator $\hat{K}$ [158, 76], via

$$W_{\mathrm{eq}}(q_0, \ldots, q_{2M}) = |\Psi_0(q_0, \ldots, q_{2M})|^2 \,. \tag{2.58}$$

Direct calculation of higher-order correlations (2.55) on the other hand requires the knowledge of the full spectrum of $\hat{K}$.

It is, however, possible to construct a Fokker-Planck equation for the classical probability distribution $W(q_0, \ldots, q_{2M}; z)$ that describes the same stochastic process as the transfer-matrix formalism:

$$\frac{\partial}{\partial z} W = \sum_{j=1}^{2N_f} \left[ D \frac{\partial^2}{\partial q_j^2} W + \frac{\partial}{\partial q_j} (A_{q_j} W) \right] . \tag{2.59}$$

The spatial coordinate $z$ here takes the role of time as compared to the common form of the Fokker-Plank equation. Direct calculation shows that the above stochastic process leads to the same expectation value as the TMF [161]. The stationarity condition of the equilibrium solution $\partial_z W_{\mathrm{eq}} = 0$ determines the drift coefficients $A_{q_j}$, for which from Eq. (2.59) follows

$$A_{q_j} \equiv A_{q_j}(q_1, q_2, q_3, q_4) = -D \frac{\partial}{\partial q_j} \ln W_{\mathrm{eq}} = -2D \frac{\partial}{\partial q_j} \ln |\Psi_0| \,. \tag{2.60}$$

The last step is to realize, that the Fokker-Planck equation is equivalent to a stochastic process described by an Itô equation [162]

$$dq_j = -A_{q_j}\, dz + \sqrt{2D}\, dX_z \,, \tag{2.61}$$

where $dX_z$ is a random term obeying Gaussian statistics with zero mean, $\langle dX_z \rangle = 0$, and variance, $\langle dX_z^2 \rangle = dz$.

Fast sampling of the fields from the full classical equilibrium probability distribution is possible using Eq. (2.60) and Eq. (2.61), after finding only the ground state $\Psi_0$ of the auxiliary operator (2.57) instead of the whole spectrum as Eq. (2.55) requires. Expectation values of an observable $O(z)$, or arbitrary correlations thereof, can subsequently be calculated as in the truncated Wigner or SGPE approach by averaging over many independent realizations (see Eq. (2.48)).

Based on the general discussion, we now give explicit results of the transfer matrix formalism for the sine-Gordon model for a homogeneous condensate $V = 0$ in thermal equilibrium. For two linearly coupled quantum wires ($M = 2$) the interaction potential in

Eq. (2.53) is given by

$$V = \frac{g}{2}\left[(\psi_1^*\psi_1)^2 + (\psi_2^*\psi_2)^2\right] - \hbar J\left[\psi_1^*\psi_2 + \psi_2\psi_1^*\right] , \tag{2.62}$$

with the chemical potential $\mu = gn_{1D} - \hbar J$. For the interaction potential (2.62) we get for the transfer operator $\hat{K}$, using the Madelung representation for the fields, from the general formula (2.57)

$$\hat{K} = \hat{K}_1^{\mathrm{s}} + \hat{K}_2^{\mathrm{s}} + \frac{\hbar J}{k_{\mathrm{B}}T}(\rho_1 + \rho_2) - \frac{2\hbar J}{k_{\mathrm{B}}T}\sqrt{\rho_1\rho_2}\cos(\theta_1 - \theta_2), \tag{2.63}$$

where

$$\hat{K}_j^{\mathrm{s}} = -D\left(\frac{1}{\sqrt{\rho_j}}\frac{\partial}{\partial\sqrt{\rho_j}}\sqrt{\rho_j}\frac{\partial}{\partial\sqrt{\rho_j}} + \frac{1}{\rho_j}\frac{\partial^2}{\partial\theta_j^2}\right) + \frac{g}{2k_{\mathrm{B}}T}\rho_j(\rho_j - 2n_{1\mathrm{D}}) \tag{2.64}$$

is the auxiliary operator for a single superfluid. Note that $\rho_j$ here constitutes the full density field, including perturbations. To reduce the full model to the sine-Gordon Hamiltonian for the relative degrees of freedom we, in accordance with previous approximations, neglect the non-linear coupling of the relative phase $\theta_{\mathrm{r}} = \theta_1 - \theta_2$ and of the densities $\rho_{1,2}$. This completely decouples the relative phase, which is hence fully described by the operator [160]

$$\hat{K}_{\theta_{\mathrm{r}}} = -\frac{2}{\lambda_T}\frac{\partial^2}{\partial\theta_{\mathrm{r}}^2} - \frac{\lambda_T}{4l_J^2}\left(\cos\left(\theta_{\mathrm{r}}\right) - 1\right) . \tag{2.65}$$

Upon further expanding the remainder to quadratic order in the density perturbations the remaining degrees of freedom are determined by the usual Gaussian diffusion and Ornstein-Uhlenbeck processes [159]. The relative phase, however, is calculated from the anharmonic model (2.61) by the Îto equation

$$d\theta_{\mathrm{r}} = -\frac{4}{\lambda_T}\left(\frac{\partial}{\partial\theta_{\mathrm{r}}}\ln|\Psi_0|\right)dz + 2\sqrt{\lambda_T}\,dX_z , \tag{2.66}$$

where $\Psi_0$ is the lowest-eigenvalue solution of the corresponding Mathieu equation [134].

## 2.4 Explicit Results in Thermal Equilibrium

As a last part of this theoretical introduction we discuss the explicit results in thermal equilibrium for the above discussed models. As the remainder of this thesis is concerned with the far-from-equilibrium dynamics of quantum many-body systems and their approach to thermal equilibrium, this forms the basis for the following discussions. We focus here

on results of the mean-field and harmonic approximations for a single condensate and for coupled quantum wires.

### 2.4.1 Mean Field Density

For the homogeneous system the external potential vanishes $V \equiv 0$ and therefore the stationary solution to the mean-field GPE equation (2.12) is simply a constant bulk density $\rho_0(z) = n_0$ with the chemical potential $\mu = n_0 g_{1D}$.

For a harmonically trapped system one commonly considers the Thomas-Fermi (TF) approximation, neglecting the kinetic energy term in Eq. (2.12). This is an excellent approximation in the limit $Na_s/a_\parallel \ll 1$, where $a_\parallel = \sqrt{\hbar/m\omega_\parallel}$ is the harmonic oscillator length of the longitudinal confinement. In the local density approximation (LDA) this approximation can be generalized to Bose gases in the dimensional crossover. The system is, at each point in space, considered to be in the homogeneous equilibrium state, described by the local equilibrium chemical potential $\mu_{\text{l.e.}}[\rho_0(z)]$. The mean field density profile is therefore determined by

$$\mu_{\text{l.e.}}[\rho_0(z)] + \frac{1}{2} m\omega_\parallel^2 z^2 = \mu \,. \tag{2.67}$$

For the one-dimensional GPE the local equilibrium equation of state is $\mu_{\text{l.e.}}[\rho_0(z)] = \rho_0(z) g_{1D}$ leading to the density profile in the Thomas-Fermi approximation (see e.g. Pethick2008a)

$$\rho_0(z) = n_0 \left(1 - \frac{z^2}{R_{\text{TF}}^2}\right) . \tag{2.68}$$

The profile has a peak density $n_0 = \mu/g_{1D}$ and exhibits a sharp cutoff at the Thomas-Fermi radius $R_{\text{TF}}^2 = 2\mu/(m\omega_\parallel^2)$ due to the neglect of the kinetic energy in the mean field GPE (2.12). The chemical potential is fixed by the total particle number and is given by

$$\mu_{\text{TF}} = \left(\frac{3}{4}\sqrt{\frac{m}{2}} g_{1D} \omega_\parallel N\right)^{\frac{2}{3}} . \tag{2.69}$$

Within the dimensional crossover the local equilibrium equation of state is changed due to the inclusion of radially excited states and given by the NPSE result Eq. (2.35). The density profile cannot be given in closed form, but can be reduced to a simple integral determining the only free parameter $R_{\text{NPSE}}^2$ of the NPSE mean field solution. Further simplification is possible by approximating the local chemical potential by Eq. (2.31), for which the integral reduces to a simple algebraic equation [125]. The inclusion of transversally excited states causes a radial swelling of the condensate. This leads to a higher peak density $n_0$ and consequently a

decreased width $R_{\mathrm{NPSE}} \leq R_{\mathrm{TF}}$ of the cloud along the longitudinal direction. The functional form of the density profile however remains rather unchanged and is for a large range of parameters well approximated by the inverted parabola Eq. (2.68) with shifted parameters $n_0$ and $R_{\mathrm{TF}}$.

The exact numerical results can be calculated through evolution of the classical equations of motion after a Wick rotation to imaginary time. This is a convenient method to determine the mean-field density profile and chemical potential for arbitrary external trapping potentials. In imaginary time the evolution is purely dissipative, and each eigenstate of the Hamiltonian is damped at a rate proportional to its energy. Therefore, by constantly rescaling the norm of the wave function, the system relaxes during the evolution to the lowest-energy eigenstate that has a finite overlap with the initially chosen wave function.

### 2.4.2 Harmonic Approximation

#### Homogeneous Condensates

The Bogoliubov-de-Gennes equations (2.23) for a homogeneous background density reduce by choosing the mode function in the plane wave basis $f_m^{\pm} = f_k^{\pm} \sim \exp(\mathrm{i}kz)$ to simple algebraic equations. Together with the normalization condition (2.22) this leads for a system of length $L$ to the well known solutions [68, 67]

$$f_k^{\pm} = \frac{1}{\sqrt{L}} \left( \frac{\epsilon_k}{E_k} \right)^{\mp \frac{1}{2}} \mathrm{e}^{\mathrm{i}kz} \quad , \quad \epsilon_k = \sqrt{E_k(E_k + 2n_0 g_{1\mathrm{D}})} \quad , \quad E_k = \frac{\hbar^2 k^2}{2m} \, , \tag{2.70}$$

where we consider periodic boundary conditions with momenta $k = 2\pi m/L$ and $m \in \mathbb{Z}$. The dispersion relation $\epsilon_k$ shows two distinct regimes, separated approximately by the inverse healing length $k_\xi = \xi_{\mathrm{h}}^{-1} = \sqrt{2m\mu/\hbar^2}$. For high energies $k \gg k_\xi$ the dispersion relation is particle like $\epsilon_k \simeq \hbar^2 k^2/(2m)$ and the quasiparticle excitations are free particles. For low energies $k \ll k_\xi$ the quasiparticles resemble wave-like excitations, showing a phononic dispersion $\epsilon_k \simeq \hbar c_{\mathrm{s}} |k|$ with a common speed of sound $c_{\mathrm{s}} = \sqrt{\mu/m}$. These collective excitations are the only quasiparticles in the coarse-grained TLL model, thereby reducing $\epsilon_k$ to the phononic limit. Note that the solutions remain valid for the NPSE Hamiltonian, leading only to a shift of the chemical potential $\mu$ and interaction constant $g_{1\mathrm{D}}$ according to Eqs. (2.35) & (2.37) respectively.

In thermal equilibrium the distribution function for these non-interacting quasiparticles is given by the usual Bose-Einstein distribution

$$n_k = \langle b_k^\dagger b_k \rangle = \frac{1}{\exp\left(\frac{\epsilon_k}{k_{\mathrm{B}} T}\right) - 1} \, , \tag{2.71}$$

where the chemical potential is set to zero, since adding a quasiparticle to the system does not change the number of real particles. Bose-Einstein condensation of the system is usually associated with off-diagonal long-range order, i.e. a finite value of the one-body density matrix $\rho(z, z')$ for $|z - z'| \to \infty$. Using the Madelung representation and ab initio neglecting the small density perturbations, highly suppressed below the degeneracy temperature [93], the density matrix at low temperatures can be written as

$$\rho(z, z') \approx n_0 \left\langle e^{i\left[\hat{\theta}(z) - \hat{\theta}(z')\right]} \right\rangle \equiv n_0 \, C^{(1)}(z, z') \,, \tag{2.72}$$

where we defined the phase correlation function $C^{(1)}(z, z')$. The appearance of off-diagonal long range order is therefore determined by the long range phase coherence of the condensate. For a Gaussian theory, as is the case for the Bogoliubov approximation, the phase correlation function is $C^{(1)}(z, z') = \exp\left(-\left\langle \left[\hat{\theta}(z) - \hat{\theta}(z')\right]^2 \right\rangle/2\right)$ dependent only on the variance of the phase. By use of the modal expansion (2.21) it is[18]

$$\left\langle \left[\hat{\theta}(z) - \hat{\theta}(z')\right]^2 \right\rangle = \frac{1}{2\zeta n_0 L} \sum_{\epsilon_k \lesssim \mu} \frac{\epsilon_k}{E_k} \left[1 - \cos\left(k\bar{z}\right)\right] (2n_k + 1) \,, \tag{2.73}$$

where we defined the distance $\bar{z} = z - z'$.

For CQW in the limit of vanishing tunneling coupling $J$, discussed in Section 2.2.1, the rescaled fields Eq. (2.14) are described by the same Bogoliubov equations for a single condensate, and thus by Eq. (2.70). The only difference is the rescaling of the fields with $\zeta$, explicitly included in Eq. (2.73) which therefore describes the coherence function for a single condensate as well as the common and relative degrees of freedom for CQW with $J = 0$.

Direct evaluation using the Rayleigh-Jeans approximation $n_k \simeq k_B T/\epsilon_k$, where the equality hold for $n_k \gg 1$, and expressing the sum as an integral extended to infinity gives [163, 99]

$$\left\langle \left[\hat{\theta}(z) - \hat{\theta}(z')\right]^2 \right\rangle \approx 2\frac{|\bar{z}|}{\lambda_T} + \frac{\sqrt{\gamma}}{\pi} \mathrm{Ln}\left(\frac{|\bar{z}|}{\xi_h}\right) . \tag{2.74}$$

The first term on the right hand side stems from the thermal and the second from the quantum fluctuations of the phase field. In accordance with the Mermin-Wagner-Hohenberg theorem [65, 66] the enhanced role of fluctuations in one dimension prohibits a true Bose-Einstein condensate in the thermodynamic limit, and the one-body density matrix shows an algebraic decay even at zero temperature. For $T > 0$, long-wavelength thermal fluctuations dominate the long distance behavior and correlations decay exponentially. The thermal coherence

[18] We now switch back to the un-rescaled fields, see Eq. (2.14), and explicitly write out factors of $\zeta$

length

$$\lambda_T = \frac{2\hbar^2 n_0}{m k_B T} , \tag{2.75}$$

determines the typical length for the randomization of the phase due to temperature.

The single-particle momentum distribution $n(k) = \langle \hat{\psi}^\dagger(k)\hat{\psi}(k)\rangle$ is given by the Fourier-transform of Eq. (2.72) which upon neglecting the minor quantum contributions leads to

$$n(k) = \frac{n_0 \lambda_T^{-1}}{\lambda_T^{-2} + k^2} . \tag{2.76}$$

Extending the above result beyond the phononic approximation reveals a power law decay $n(k) \sim k^{-4}$ for large $k \gg \xi_h^{-1}$ [99].

Development in the realization of flat bottom, box shaped potentials brings the dynamics of homogeneous BECs in the realm of experimental possibility. An experimental realization of such a potential will be discussed in chapter 6 where we also discuss in more detail the influence of boundary conditions on the dynamics of a finite size system.

### Harmonically Trapped System

The Bogoliubov equations (2.23) for a harmonically trapped system reduce after writing $f_m^\pm \sim (1-x^2)^{\mp(1/2)} f_m$ and consistently with the TF approximation for the ground state neglecting the quantum pressure term in second order of perturbation theory to Legendre's differential equation [163]. Neglecting the quantum pressure is equivalent to the TLL approximation of the Hamiltonian[19]. The solution are [163]

$$f_m^\pm(z) = \sqrt{\frac{j+\frac{1}{2}}{R_{TF}}} \left[\frac{2\mu}{\epsilon_m}(1-x^2)\right]^{\mp\frac{1}{2}} P_m(x) , \tag{2.77}$$

where $P_m(x)$ are the Legendre polynomials and the dispersion relation is

$$\epsilon_m = \hbar\omega \sqrt{\frac{m(m+1)}{2}} . \tag{2.78}$$

Density fluctuations are again found to be highly suppressed below the degeneracy temperature [93, 163]. The variance of the phase is given by

$$\left\langle \left[\hat{\theta}(z) - \hat{\theta}(z')\right]^2 \right\rangle = \sum_j^{\epsilon_j<\mu} \frac{(j+1/2)\mu}{2n_0 R_{TF}} \left[P_j(x) - P_j(x')\right]^2 (2n_j + 1) , \tag{2.79}$$

[19] The full Bogoliubov equations however allow for solutions valid for energies beyond $\mu$.

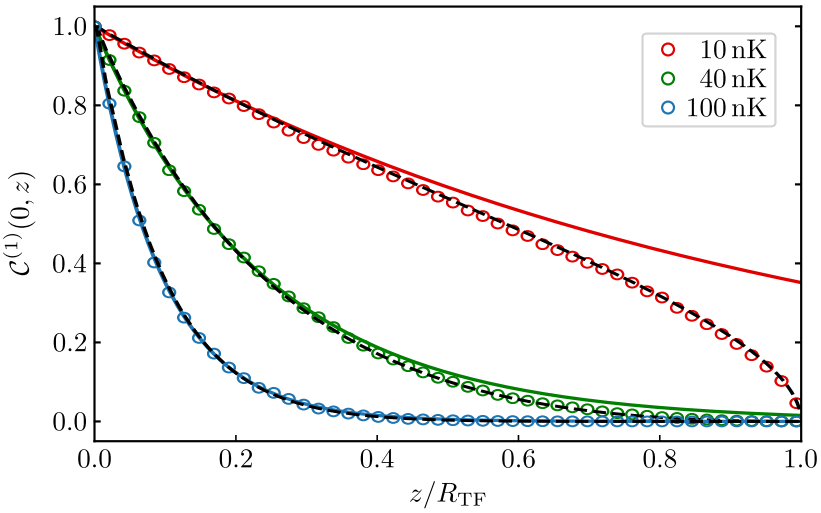


Fig. 2.4 Phase correlation function $C^{(1)}(0,z)$ for a thermal quasi-condensate with $N = 4000$ atoms and $\omega = 7.5\,\mathrm{Hz}$. Dashed lines represent the analytical result for a trapped system (Eq. (2.79)) and solid lines are the homogeneous solution (2.74) for the peak density $n_0$. The dots are the results of sampling of the phase field according to the Îto equation (2.61) of the TMF averaged over $10^5$ realizations. Explicitly Eq. (2.61) reduces to the Ohrnstein-Uhlenbeck process which can be solved in LDA. The central part of the cloud is well described by the homogeneous theory. Deviations occur near the edges of the condensate due to the decreasing density and the finite size of the system. For higher temperatures finite size effects are insignificant due to the fast exponential decay of $C^{(1)}(0,z)$.

where the sum is restricted to $\epsilon_j < \mu$ on account of neglecting the quantum pressure term. The quantum contributions to the phase variances is again negligible at finite temperatures, showing logarithmic dependence of order $\sqrt{\gamma}$ [163]. The formation of a true BEC with off-diagonal long-range order is now possible, since for temperatures $T \lesssim T_\phi = T_\mathrm{d}\hbar\omega_\parallel/\mu$ [163] the decay of the coherence becomes negligible over the size of the cloud. These temperatures are, however, beyond current experimental reach and finite temperature effects commonly dominate, such that the coherence function $C^{(1)}(z,z')$ in the central part of the cloud is well approximated by the homogeneous exponential decay. A comparison of the phase correlation function for the homogeneous (2.74) and harmonically trapped system (2.79) system is presented in Fig. 2.4. For comparison we show the results of the harmonic Ornstein-Uhlenbeck process, for which the spatial dependence of the bulk density is taken into account in LDA.

To calculate the single-particle momentum distribution we rely on the LDA, for which we consider the semi-classical distribution [67]

$$f(k,z) = \rho_0(z)\, n_{\mathrm{hom}}\left[k, \rho_0(z)\right] \ . \tag{2.80}$$

The normalized momentum distribution $n_{\mathrm{hom}}$ for a homogeneous condensate (see Eq. (2.76)) is now a functional of the inhomogeneous mean-field density $\rho_0(z)$, because of the spatial dependence of the thermal coherence length (2.75). The momentum distribution of the harmonically trapped system is given through integration of Eq. (2.80) over the spatial coordinate $z$.

### Coupled Quantum Wires

For non-vanishing tunneling coupling $J$, CQW are considered in the decoupled common and relative degrees of freedom. The common degrees of freedom in the harmonic mTLL approximation (2.45) are independent of the tunneling coupling and thus for any value of $J$ described by the equations for a single condensate (2.70).

The relative degrees of freedom, however, acquire an effective mass, proportional to the tunneling coupling $J$. In case of a homogeneous system the Bogoliubov equations are easily solved [130] by shifting the kinetic energy $E_k \to E_k + 2\hbar J$ (see Eqs. (2.45) & (2.70)). This is possible since the mean field density is simply a constant and the tunneling coupling $J$ therefore does not couple to any spatial coordinates. The functional form of the Bogoliubov mode functions hence remains unchanged and only the dispersion relation is modified to

$$\epsilon_k = \sqrt{(E_k + 2\hbar J)\,(E_k + 2\hbar J + 2n_0 g_{1\mathrm{D}})}\,, \tag{2.81}$$

with $E_k$ defined in Eq. (2.70). In contrast to the phononic dispersion relation $\epsilon_k \sim k$, Eq. (2.81) has a finite gap $\epsilon_{k\to 0} = 2\hbar J\sqrt{1 + n_0 g_{1\mathrm{D}}/\hbar J}$ corresponding to an effective quasiparticle mass.

Because of this finite rest energy, true long-range order is possible for the relative degrees of freedom. In the Rayleigh-Jeans approximation, direct evaluation of Eq. (2.74) gives the first order coherence function [130]

$$C^{(1)}(z, z') = \exp\left[-\frac{2l_J}{\lambda_T}\left(1 - \mathrm{e}^{-\frac{|z-z'|}{l_J}}\right)\right], \tag{2.82}$$

which does not decrease to zero for large separations but approaches the finite value $\mathrm{e}^{-2l_J/\lambda_T}$ for $|z - z'| \to \infty$. The two competing length scales are the thermal coherence length (2.75), describing the randomization of the relative phase $\hat{\theta}_{\mathrm{r}}(z)$ due to temperature, and the length

$$l_J = \sqrt{\frac{\hbar}{4mJ}} \tag{2.83}$$

which sets the scale of the restoration of inter-well coherence due to the finite tunneling coupling $J$. This, however, does not mean that the system is a true BEC. Indeed, fluctuations

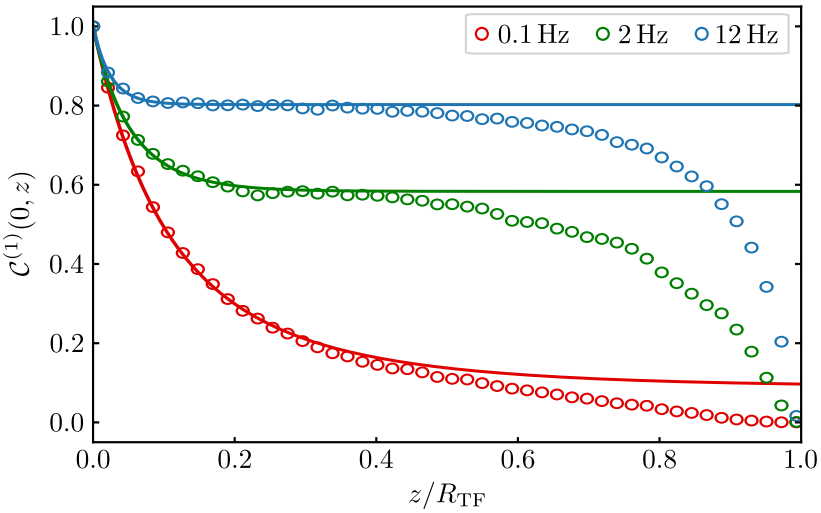


Fig. 2.5 Phase correlation functions $C^{(1)}(0,z)$ for the relative phase $\theta_\mathrm{r}$ of two coupled quantum wires. The solid line is the analytical solution in the homogeneous system (Eq. (2.82)) and the dots are the result of the Ohrnstein-Uhlenbeck process in LDA. The finite tunneling coupling $J$ leads to phase locking between the two condensates and hence a constant value of $C^{(1)}$ for large distances. For the trapped system, the decrease in density leads to an increase in fluctuations (as $\lambda_T \to \infty$) which destroys the long-range order.

in each of the two condensates show unlimited growth of phase fluctuations, due to the influence of the common degrees of freedom, and thus $C^{(1)}(z,z') \to 0$ for $|z-z'| \to \infty$ [134].

The influence of randomization and restoration of phase coherence can explicitly be seen in the stochastic Ornstein-Uhlenbeck process [159], i.e. the harmonic approximation to the TMF discussed in Section 2.3.3. In this approximation, the drift coefficient $A_{q_j}$ (see Eq. (2.60)) for the relative phase degree of freedom is given by $A_{\theta_\mathrm{r}} = 1/l_J$. This acts as a restoring force term in the Itô equation (2.61) counteracting the random diffusion due to temperature[20]. For the common phase, not influence by the finite tunneling coupling $J$ and therefore equivalent to a single condensate, the drift coefficient $A_{\theta_\mathrm{c}}$ vanishes leading to the unlimited growth of fluctuations for any $T > 0$.

For the harmonically trapped system a closed analytical solution is no longer possible due to the spatial dependence of the mean field density profile $\rho_0$ (see Eq. (2.45)). This causes a coupling between the spatial coordinates and the linear tunnel coupling $J$, such that the spatial dependence of the mode functions are modified. Neglecting the quantum pressure term the Bogoliubov equations for the hydrodynamic functions $f^{\pm}(z)$ can be mapped to the differential equation for angular spheroidal wave functions. Since no exact analytical solutions are known, we rely on numerical solutions for inhomogeneous CQW using the SGPE, that is not limited to the harmonic approximation. The homogeneous solutions

[20]The diffusion coefficient $D = \lambda_T^{-1}$, see Eqs. (2.57) & (2.61)

however are a good approximation of the inhomogeneous system within the central part of the cloud, which therefore shows the same qualitative behavior. Significant differences only arise near the edges where the density decreases and coherence is destroyed by the enhanced role of thermal fluctuations (see Fig. 2.5).

# Chapter 3

# Universal Dynamics of a One-Dimensional Bose Gas

It is an in general open question which guiding principles determine the possible paths an isolated quantum many-body system can take starting from a far-from-equilibrium initial state. Of particular interest are situations where the evolution of the system, in close connection to equilibrium critical phenomena, is only determined by a few universal properties, independent of the specifics of the initial state. It has been proposed that such non-thermal attractor solutions are possible during the relaxation of a far-from-equilibrium system [40–42], displaying universal scaling long before any thermalization. In the vicinity of these non-thermal fixed points the evolution of the system is characterized by only a few universal scaling exponents and functions independent of the microscopic details of the system. This opens the possibility for a classification based on universality classes far-from-equilibrium even in the absence of thermal critical points [83, 164]. While there is mounting theoretical and numerical evidence of universality far-from-equilibrium, a direct experimental observation has so far been missing.

In this chapter we present results for the relaxation of a far-from-equilibrium one-dimensional Bose gas[1]. The initial state is created via a rapid cooling quench of a three-dimensional thermal gas to the one-dimensional regime. We characterize the initial state through an ensemble of randomly distributed solitonic defects, which are determined through their impact on the single-particle momentum distribution measured through single-atom resolved measurement of the atomic density in time of flight. By changing the speed at which the system is prepared, we find scaling of the defect density, in broad accordance with the predictions of the inhomogeneous Kibble-Zurek mechanism [165, 77]. The short time evolution is in good accordance with the model of randomly distributed solitonic defects, in particular

[1]The experimental measurements and pre-analysis of the data was performed by R. Bücker. I performed the analysis and interpretation of the data and results presented in this chapter.

revealing the increasing broadening of the density and momentum distribution as well as the damping of the breathing excitation with increasing quench rates. The latter, in accordance with the defect picture, shows a transition from frequency-doubling to no-doubling for the oscillation in momentum space. In the long term evolution the system is found to transition from the defect dominated state to a thermal quasi-condensate for long times.

During this relaxation the system is found to exhibit universal scaling in space and time. In the scaling regime the evolution is determined, independent of the exact initial state, by a single universal function of momentum and a single universal exponent. The non-equilibrium scaling evolution features the transport of an emergent conserved particle number towards the infrared, leading to the build up of a quantum degenerate quasi-condensate. The observed scaling solution is found to be in accordance with the dilution of the soliton ensemble. Our results provide conceptually new access to the time evolution far-from-equilibrium and establish universal scaling dynamics in an isolated many-body system. Finally the observed values for the universal scaling exponents are compared to existing theoretical predictions revealing the possible emergence of a new universality class far-from-equilibrium.

## 3.1 Cooling Quench

Ultra-cold atomic gases have proven to be excellent systems with which to study the physics of quantum many-body systems. The techniques necessary to achieve the ultra-cold temperatures in these systems, although experimentally well established, to date still bare open questions, as to how exactly a system reaches its final equilibrium state [166]. One of the standard procedures used to ultimately cool a system below the critical temperature is evaporative cooling, see e.g. [167–170]. Therein a small fraction of the most energetic particles are removed from the system. As long as the energy of the removed particles is higher than the mean energy per particle in the system, the latter is effectively reduced and elastic collisions lead to a subsequent rethermalization of the system. Repetition of this process, on a time scale slow as compared to the time needed for rethermalization, leads to an increase in phase-space density on account of particle loss, and ultimately in our case to the formation of a Bose-Einstein condensate. Differences in the cooling mechanism occur once the gas reaches the dimensional crossover to a quasi one-dimensional system, where the absence of thermalizing collisions negate the above cooling mechanism. Cooling of a one-dimensional system was considered in [171, 172]. Therein homogeneous particle dissipation and many-body dephasing resulted in a substantial cooling beyond the transition to a one-dimensional system, through a constant squeezing of the rotating Wigner function along the density quadrature.

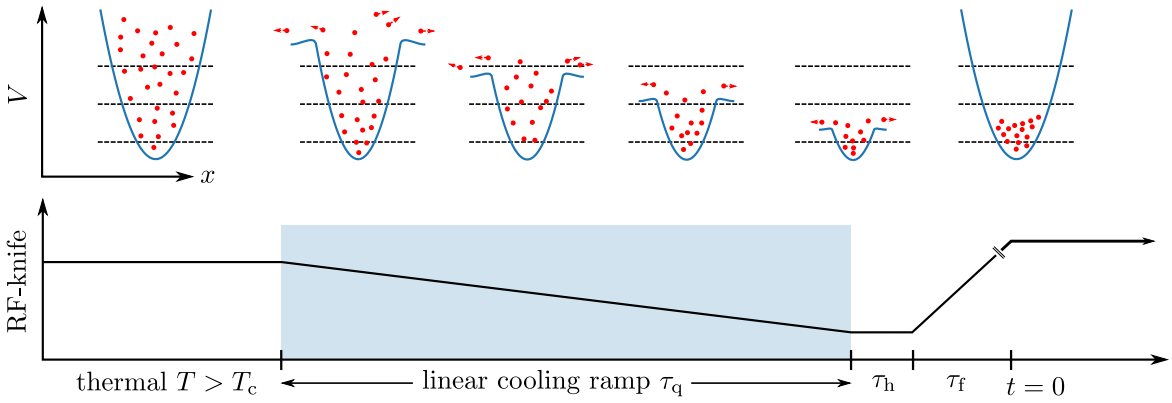


Fig. 3.1 Schematic visualization of the experimental cooling quench procedure. The system is prepared in a deep trapping potential at a temperature $T$, closely above the critical temperature $T_c$ for Bose condensation. During the quench, the RF-knife is linearly ramped to its final value during a variable time $\tau_q$, thereby lowering the trap depth in the radial direction $x$. The final value lies below the first radially excited state (indicated by the dashed lines). The RF-knife is subsequently held at its final position for $\tau_h \approx 0.5\,\mathrm{ms}$ and faded out in $\tau_f \approx 1\,\mathrm{ms}$, thereby raising the trap depth again, leading to a degenerate far-from-equilibrium Bose gas.

In contrast to the cooling mechanisms described above, which all rely on sufficiently slow cooling to allow for a redistribution of energy within the system, we study in the following the relaxation dynamics following a rapid cooling quench. Therein fast removal of high-energy particles[2] constitutes an almost instantaneous quench of the system beyond the dimensional and quasi-condensate crossover, resulting in a far-from equilibrium one-dimensional Bose gas.

The experimental procedure is outlined in Fig. 3.1. The system of $N = 5.5 \cdot 10^4$ atoms is prepared initially in an elongated, $\omega_\parallel = 2\pi \cdot 23\,\mathrm{Hz}$ and $\omega_\perp = 2\pi \cdot 3.3\,\mathrm{kHz}$, deep trapping potential $V_i \approx h \cdot (130 - 160)\,\mathrm{kHz}$ in thermal equilibrium at a temperature $T \approx 780\,\mathrm{nK}$. The thermal cloud is both above the dimensional crossover to an effective one-dimensional system (c.f. Eq. (2.4)) and the critical temperature $T_c$ for the phase-transition to a 3D Bose-Einstein condensate, and therefore has a large excess of particles in transversally excited, high-energy states. During the quench, the trap depth is reduced to its final value $V_f$ at a variable constant rate $R_q = (V_i - V_f)/\tau_q = h \cdot (2 - 25)\,\mathrm{kHz/ms}$, by applying radio-frequency (RF) radiation at a time dependent frequency (RF-knife), leading to an energy-dependent transition of atoms from a trapped to an untrapped spin state [67]. This allows the high-energy particles to leave the trap, on a time scale $\tau_q$, short as compared to the typical collision times needed for re-equilibration of the system. The final trap depth $V_f \approx h \cdot 2\,\mathrm{kHz}$ lies below the first radially excited state of the trapping potential $V_f < \hbar\omega_\perp$. At the end of the cooling ramp, the RF-knife

[2]The removal of particles is fast as compared to the typical collision times needed for re-equilibration of the system

is held at its final position for $\tau_h = 0.5\,\mathrm{ms}$ before it is faded out within $\tau_f \approx 1\,\mathrm{ms}$, thereby raising the trap depth[3] to $V \approx h \cdot 20\,\mathrm{kHz}$. The system is therefore rapidly quenched to the quasi one-dimensional regime, occupying only the transverse ground state. The resultant far-from equilibrium state is held for variables times up to $t \simeq 1\,\mathrm{s}$, during which the universal dynamics develops and takes place.

In order to probe the relaxation dynamics of the system, the cloud is allowed to freely expand, by rapidly switching of the external trapping potentials at a time $t$. Due to the highly elongated trap geometry, the system undergoes a rapid expansion along the tightly confined radial direction leading to a fast dilution of the system and therefore an almost ballistic expansion in the elongated longitudinal direction. The influences of finite interactions between atoms during expansion can be considered within a hydrodynamic approach [67], but lead to no significant differences for the parameters considered here. This enables the time resolved measurement of the longitudinal *in-Situ* (iS) density distribution $\rho(z,t)$ and of the single-particle momentum distribution $n(k,t)$, for short ($t_{\mathrm{tof}} = 1.5\,\mathrm{ms}$) and long ($t_{\mathrm{tof}} = 46\,\mathrm{ms}$) expansion times, respectively. The former is applicable, since the expansion for $t_{\mathrm{tof}} = 1.5\,\mathrm{ms}$ is predominantly along the transversal direction, leaving the longitudinal density distribution unchanged. For the latter, the rapid dilution and consequent ballistic expansion, leads to the conservation of the single-particle momentum distribution during the free expansion. Therefore, the measured density distribution after $t_{\mathrm{tof}} = 46\,\mathrm{ms}$ resembles the original momentum distribution of the gas. The density after $t_{\mathrm{tof}} = 46\,\mathrm{ms}$ time-of-flight is measured with fluorescence imaging [175], which has a high spatial resolution and single-atom sensitivity.

This can be seen explicitly within the semiclassical approximation, for which the discrete set of eigenfunctions of the Hamiltonian is approximated by a smooth density distribution $f(z,k,t)$ in phase-space. The distribution is normalized to the total atom number $\iint \mathrm{d}z\mathrm{d}k/2\pi\, f(z,k,t) = N$. Integration over the position (momentum) variable gives access to the one-particle momentum distribution (density distribution) of the gas. The density after ballistic expansion then takes the form [67]

$$\rho(z_{\mathrm{tof}}) = \alpha^{-1} \int \mathrm{d}z\, f\left(z, k = \alpha^{-1}(z_{\mathrm{tof}} - z), t\right) . \tag{3.1}$$

Here $t$ is the time the gas was released from the trap and $\alpha = \hbar t_{\mathrm{tof}}/m$ stems from the free expansion $\dot{z} = \alpha k$ of a particle with momentum $p = \hbar k$ for a time $t_{\mathrm{tof}}$. From Eq. (3.1) it follows that $\alpha\rho(z_{\mathrm{tof}}) \to n(k = \alpha^{-1} z_{\mathrm{tof}}, t)$ for $t_{\mathrm{tof}} \to \infty$, making the single-particle momentum distribution accessible through measurement of the expanded density profile. We therefore

[3] Additionally, since the RF-knife slightly reduces the radial trapping frequency, this leads to a small interaction quench of the 1D system

define for finite expansion times $t_{\mathrm{tof}}$ the *pulled-back* (pb) momentum distribution

$$n(k,t) \equiv \alpha\rho\left(\alpha^{-1}z_{\mathrm{tof}}\right) = \int \mathrm{d}z\, f\left(z, k-\alpha^{-1}(z+vt_{\mathrm{tof}}), t\right)\,. \tag{3.2}$$

The pb momentum distribution at high $k$-values converges rapidly towards the true momentum distribution of the gas. For low momenta the finite in-Situ size of the cloud does not allow for a clear separation of different momentum modes as atoms of different momenta overlap in the measured density after time-of-flight. This means that for a cloud of size $R$, particles with momentum $k \lesssim k_{\mathrm{iS}} = \alpha^{-1}R$ do not have enough time to propagate sufficiently far outside the in-Situ bulk density to be clearly separated. Therefore the pb momentum distribution for $k \lesssim k_{\mathrm{iS}}$ resembles the in-Situ density profile rather than the actual momentum distribution of the gas. These low-momentum modes can be made accessible in experiments using condensate focusing [176]. Therein a hydrodynamic velocity profile is imposed on the gas which focuses particles with zero momentum to a single point after a finite expansion time $t_{\mathrm{tof}}$ (rather than in the limit $t_{\mathrm{tof}} \to \infty$). We included such a non-vanishing velocity profile $v \equiv v(z,t)$ in Eq. (3.2), which can also e.g. be caused by a breathing excitation [177, 178] of the bulk.

Further simplification of Eq. (3.2) is possible within the local-density approximation, for which the system locally follows the solution for a constant bulk density $n(k, n_{\mathrm{1D}})$, and hence $f(z,k,t) \approx \rho(z,t)n(k,\rho(z,t),t)$. Additionally, to account for the finite imaging resolution in the experiment [179], we include a convolution of the theoretical profiles with a Gaussian point-spread function (PSF), with measured variances $\sigma_{\mathrm{iS}} = 6.8\,\mu$m and $\sigma_{\mathrm{tof}} = 8\,\mu$m for the density profile in-Situ and in time-of-flight, respectively. The latter corresponds to an effective width $\sigma_{\mathrm{pb}} = 0.238\,\mu\mathrm{m}^{-1}$ of the PSF for the pulled-back momentum distribution (3.2). Before comparing the experimental data to explicit theoretical predictions for $f(z,k,t)$, we first give an overview of the experimental results.

### 3.1.1 In-Situ Measurements

As a first step toward characterizing the non-equilibrium state, we investigate the measured density distribution after $t_{\mathrm{tof}} = 1.5\,$ms. The time evolution for the normalized[4] density distribution for different quench rates, measured over the first 27 ms following the quench, is shown in Fig. 3.2a. For low quench rates a strong breathing excitation is visible, leading to an oscillatory compression and expansion of the cloud. For a one-dimensional system the breathing frequency is $\omega_{\mathrm{b}} = \sqrt{3}\omega_{\parallel}$ [67], such that the presented time interval corresponds to

[4]The maximum densities within the time region are $\max[\rho_0(z,t)] = 74, 72, 67, 58, 51, 38, 29, 21\,\mu\mathrm{m}^{-1}$, respectively for increasing quench rates

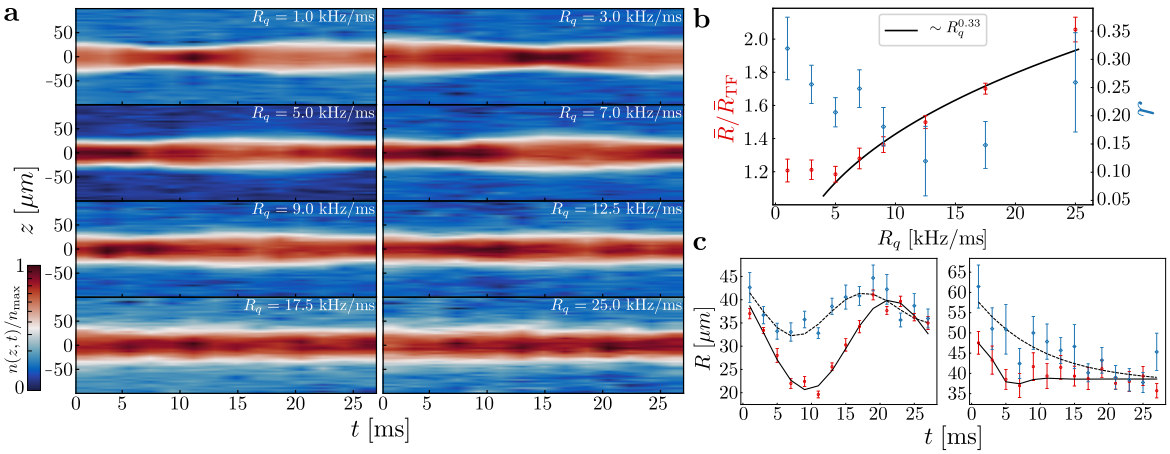


Fig. 3.2 Time evolution of the in Situ density for variable quench rates $R_{\mathrm{q}}$. **a** The atomic density $\rho(z,t)$ is depicted in color, where for each quench rate the density is normalized to its maximum value. Note the non-linear color scale to highlight the spatial extent of the cloud rather than its peak density. The suppression of the breathing excitation for increasing $R_{\mathrm{q}}$ is clearly visible. **b** Mean broadening $\delta R = \bar{R}/\bar{R}_{\mathrm{TF}}$ (red) and breathing amplitude $r = (R_{\max} - R_{\min})/2\bar{R}$ (blue) of the density profile as a function of the quench rate $R_{\mathrm{q}}$. The solid line is a power-law fit, the mean broadening of the cloud increasing with an exponent $\approx 0.33$ while the breathing amplitude decreases. For the highest quench rates $r$ quantifies the exponential decay rather than the oscillation amplitude. **c** Time evolution of the density radius $R$ for exemplary quench rates $R_q = 1\,\mathrm{kHz/ms}$ (left panel, red), $12.5\,\mathrm{kHz/ms}$ (left panel, blue) exhibiting a breathing oscillation and $R_q = 17.5\,\mathrm{kHz/ms}$ (left panel, red), $25\,\mathrm{kHz/ms}$ (left panel, blue) showing exponential decay. The solid and dashed lines are a fit of Eq. (3.4) to the experimental data. Errors denote the standard deviation.

approximately one breathing period. Despite the increasing width of the cloud for higher quench rates, a clear suppression of the breathing excitations is visible.

In order to quantify the broadening of the gas, we compare the experimental results to the analytical predictions for the density of a pure condensate (see Section 2.4). The breathing excitation is taken into account via the scaling Ansatz

$$\rho(z,t) = b(t)^{-1}\rho_0(z/b(t))\,, \tag{3.3}$$

which follows from the hydrodynamic equations for a harmonic confinement of the gas [178, 180]. We fit the experimental density distribution at each time step with the NPSE predictions, using Eq. (3.3) with the scale factor $b(t)$ as the only free parameter. Subsequently, we extract the mean broadening $\delta R = \bar{R}/\bar{R}_{\mathrm{TF}}$ and breathing amplitude $r$ through $R(t) = b(t)\bar{R}_{\mathrm{TF}}$ with

$$b(t) = \delta R\left[1 + r\mathrm{e}^{-\gamma t}\cos(\omega t + \phi_0)\right]\,. \tag{3.4}$$

Because of atom number fluctuations in the experiment we define the scale factor $b(t)$ in relation to the time-averaged, equilibrium Thomas-Fermi radius $\bar{R}_{\mathrm{TF}}$ of the cloud over the first breathing period. The breathing around the broadened mean is quantified by $r = (R_{\max} - R_{\min})/2\bar{R}$ [176], where we included an exponential damping of the amplitude. The initial phase $\phi_0$ and frequency of the breathing oscillation are fitted freely, the latter being in good agreement with the theoretical expectation $\omega = \omega_{\mathrm{b}}$.

The results allow us to identify different regimes where the dynamic properties of the bulk change noticeably (see Fig. 3.2b). For slow quenches $R_q \lesssim 5\,\mathrm{kHz/ms}$ we find a constant broadening $\delta R \approx 1.2$, whereas for higher quench rates the mean extent of the cloud grows compatible[5] with a power-law $\delta R \sim R_q^{0.33}$. The breathing amplitude, however, decreases rapidly with the growing quench rate. Within this regime damping of the oscillations is negligible during the first breathing period. For $R_q \gtrsim 15\,\mathrm{kHz/ms}$ however the cloud ceases to oscillate and shows a rapid decay towards a static broadened density profile with $\delta R \approx 1.4$. For these values $r$ characterizes the amount of decay within the first breathing period rather than the amplitude of the oscillation. The time evolution of $R(t)$ is shown in Fig. 3.2c for $R_q = 1, 12.5\,\mathrm{kHz/ms}$, which marks the edges of the oscillating regime, and $R_q = 17.5, 25\,\mathrm{kHz/ms}$, which exhibit monotone exponential decay.

The breathing oscillation for slow quenches allows us to exploit self-focusing effects to gain access to the momentum distribution at low momenta. The hydrodynamic velocity profile for the breathing excitation is given by $v(z,t) = z\,\dot{b}/b$ (see e.g. [67]). If the focusing-condition

$$\left(1 + \frac{\dot{b}}{b} t_{\mathrm{tof}}\right) = 0 \tag{3.5}$$

is fulfilled, the pb momentum distribution (3.2) converges for all momenta within a finite time $t_{\mathrm{tof}}$.

### 3.1.2 Time-of-Flight Measurements

We now turn to the measurements after $t_{\mathrm{tof}} = 46\,\mathrm{ms}$ time-of-flight. The time evolution of the pb momentum distribution for different quench rates is presented[6] in Fig. 3.3b.

For slow quenches the breathing frequency in momentum space is doubled as compared to the in-Situ oscillation [178]. This is a result of the hydrodynamic velocity imposed by the

[5] Due to the small range of the data the scaling should be taken as a qualitative behavior rather then a quantitative estimate. For this reason we also decided against plotting the data on a log-log scale, as it is usually common for power-law behavior.

[6] As for the in-Situ density, the data for each quench rate is again normalized to its maximum value within the first breathing period $\max[n(k,t)] = 1590, 1880, 1183, 889, 642, 420, 259, 183\,\mu\mathrm{m}$, for increasing quench rates respectively.

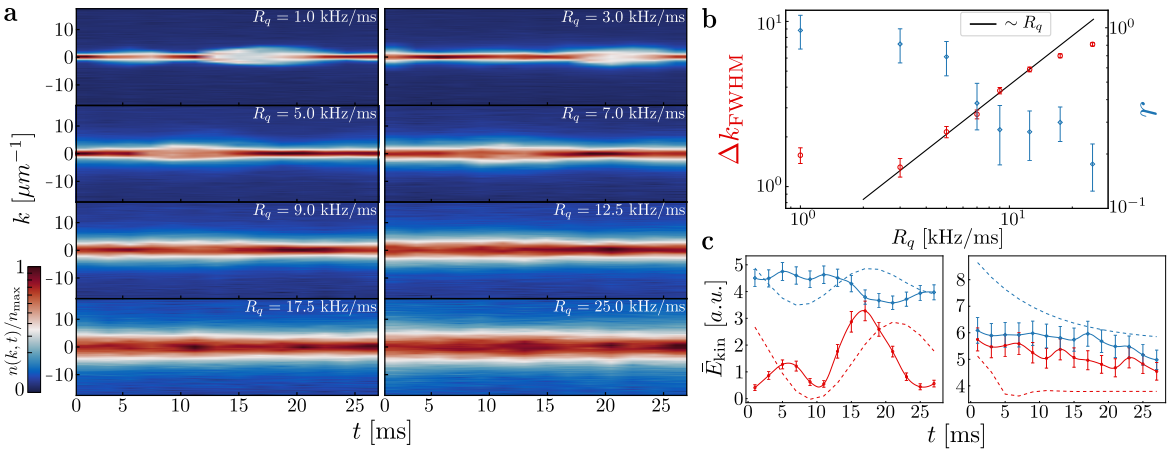


Fig. 3.3 Time evolution of the momentum distribution $n(k,t)$ for variable quench rates $R_q$ **a** Normalized momentum distribution $n(k,t)$ depicted in colors. Note again the non-linear color scale to highlight the extent of the cloud. **b** Full-width-half-maximum $\Delta k_{\mathrm{FWHM}}$ measured at the focus point (red) and breathing amplitude $r = (\Delta k_{\mathrm{max}} - \Delta k_{\mathrm{min}})/2\bar{\Delta} k_{\mathrm{FWHM}}$ (blue) for varying quench rates $R_q$. The solid line is a power-law fit, the FWHM increasing linearly with $R_q$ (note the double logarithmic scale). **c** Mean kinetic energy $\bar{E}_{\mathrm{kin}}$ per particle in the IR ($|k| \leq 5\,\mu\mathrm{m}^{-1}$) for the exemplary quench rates of Fig. 3.2. The dashed lines depicts the respective time evolution of the in Situ radius $R$. The quench rates shown represent the frequency-doubling (left panel, red), no-doubling (left panel, blue), and effectively frozen regime (right panel). Errors denote the standard deviation.

breathing excitation, which broadens the momentum distribution, regardless of a contraction or expansion of the cloud. The breathing in momentum space therefore has a minimum at the positions where the cloud has its maximum or minimum extent and hence shows a frequency-doubling. Note that due to the finite expansion time of the gas the breathing oscillation in the pb momentum space is asymmetric. This can be clearly seen for $R_q = 1\,\mathrm{kHz/ms}$. Firstly, the width of the momentum distribution is not symmetric, but broader for the maximum outwards breathing ($t \approx 16\,\mathrm{ms}$) than the maximum inwards breathing ($t \approx 4\,\mathrm{ms}$) cloud. Secondly, the oscillation period is asymmetric, showing an apparent longer oscillation time for the outward than the inward breathing cycle. This effect is a result of the condensate self-focusing, due to which the pb momentum distribution has a minimum width for a non-vanishing velocity $v(z,t)$. This shifts the minimum of the oscillation in momentum space slightly after (before) the point of maximum (minimum) extent of the cloud in-Situ (c.f. Eq. (3.5)).

Notably, the momentum distribution for the slowest quench rates $R_q = 1,3\,\mathrm{kHz/ms}$ displays a strong double-peak structure, appearing only during the outwards breathing phase ($t \approx 13,18\,\mathrm{ms}$). This might be explained by a slight anharmonicity of the longitudinal trapping potential. While rather negligible for a static cloud, this can lead to the observed double-peak structure for large breathing amplitudes [116]. Further it is unclear if the

hydrodynamic approximation for the collective breathing excitation (3.3) remains valid for the non-equilibrium state in the experiment. In any case, this complicates a quantitative comparison of the experimental data to theoretical predictions and in general leads to large errors in the following analysis.

As the quench rate increases we find a strong damping of the breathing oscillation. We quantify the breathing through the time evolution if the full-width-half-maximum (FWHM) $\Delta k_{\mathrm{FWHM}}$ of the momentum distribution. In Fig. 3.3b we show the breathing amplitude $r = (\Delta k_{\mathrm{max}} - \Delta k_{\mathrm{min}})/2\bar{\Delta} k_{\mathrm{FWHM}}$, where $\bar{\Delta} k_{\mathrm{FWHM}}$ is the time averaged width of the distribution. As for the iS density we find a fast decay of the breathing amplitude for $R_q \lesssim 10\,\mathrm{kHz/ms}$.

Contrary to the iS density, we quantify the mean broadening of the momentum distribution through the FWHM at the focus point, because rather then oscillating around the mean value, the momentum distribution gets broadened twice (during the inwards and outwards breathing phase). Therefore the mean broadening of the distribution is given by the measurement in focus, rather then the time averaged value. Explicitly, to minimize the effect of further dynamics during the first breathing period, we show in Fig. 3.3 the FWHM at the best focus point[7] within the first half of the breathing period. We find a power-law scaling of the width with the quench rate with an exponent $\zeta_{\mathrm{FWHM}} = 0.99(6)$. For $R_q > 12.5\,\mathrm{kHz/ms}$ the experimental data flattens and starts to deviate from the scaling expression.

Closer investigation of the time dependent breathing amplitude shows that the system undergoes a transition from frequency-doubling to no-doubling to a "frozen" momentum distribution. In Fig. 3.3c we present the mean kinetic energy per particle in the IR for $R_q = 1, 12.5\,\mathrm{kHz/ms}$ (left) and $R_q = 17.5, 25\,\mathrm{kHz/ms}$ (right). For slower quench rates a clear transition from frequency doubling to no-doubling is visible. For the latter the momentum distribution oscillates out-of-phase with the iS density. Rather then having its maximum width at the points of maximum in-/outwards velocity, the momentum distribution becomes strongly broadened due to the spatial compression of the gas. For higher quench rates, the momentum distribution becomes effectively frozen and no clear connection to the bulk dynamics is visible. The transition from frequency-doubling to no-doubling for the momentum distribution of a thermal condensate exhibiting a breathing excitation was studied in [178]. Here a similar transition occurs in a far-from equilibrium system, which further exhibits transition to an effectively "frozen" regime.

## 3.2 From Solitonic States to Thermal Equilibrium

Based on the general theoretical understanding of the evolution of systems exhibiting a phase transition, namely the Kibble-Zurek mechanism [165, 77], we expect the nucleation of (quasi-

[7] Meaning at the time, where the discrete data best fulfills the focusing condition Eq. (3.5)

)topological defects within our system. As discussed in Section 2.1.3 the relevant topological defects in one spatial dimension are solitons. Their creation during the phase transition has been studied theoretically, see e.g. [153, 173], and was observed in the experiment [181]. Commonly, the system posterior to the quench is allowed to fully equilibrate which allows the solitonic excitations to fully form before the measurement. In the quasi one-dimensional regime this may be aided through additional slow evaporative cooling. The system hereby redistributes or looses particles in the high energy modes, such that the momentum distribution is determined by the in Situ width of the remaining defects.

Here we consider a cooling quench of the system which is on the order of two orders of magnitude faster than the quenches considered in [181]. Additionally, our system is probed directly following the end of the cooling quench which prevents full equilibration an/or further decay of solitonic defects. Together with the limited experimental resolution, the expected high probability of defect nucleation prevents the direct observation of solitons in the density profile. Therefore the presence of solitonic excitations in the system must be determined through their impact on other observables, as e.g. the single-particle momentum distribution.

### 3.2.1 The Random Defect Model

In the following, we derive an analytical formula of the one-body momentum distribution $n(k,t) = \langle|\hat{\psi}(k,t)|^2\rangle$ for a thermal Bose gas bearing an ensemble of randomly distributed solitonic defects (RDM[8]). The following generalized calculations are based on our previous results on the characterization of solitonic states [116] and their emergence following an interaction quench [182].

We consider the particle-like interpretation of a single solitonic defect and characterize a multi-soliton state through its probability distribution $P_{N_s}(z,v,\xi_s,t) \equiv P_{N_s}(z_1,v_1,\xi_1,\ldots,t)$ in the previously defined extended "phase-space" $(z,v,\xi_s)$. This determines the spectrum at an arbitrary but fixed time $t = t_0$ solely by the distribution $P_{N_s}(z,v,\xi_s,t_0)$, whose time evolution can in principle be calculated by taking into account the elastic scattering of solitons. In many cases however, the dynamics of the soliton ensemble is sufficiently ergodic that the probability distribution can be approximated by its time average $P_{N_s}(z,v,\xi_s,t) \simeq P_{\mathrm{erg}}(z,v,\xi_s)$, at least below the time-span of significant soliton decay.

We first consider a dilute ensemble of solitons on a homogeneous background $\psi_0(z) = \sqrt{n_{1D}}$ at $T = 0$, for which we can write the total wave-function as a product Ansatz

$$\psi(z) = \psi_0(z) \prod_{i=0}^{N_s} \phi_{v_i}(z - z_i) \,, \tag{3.6}$$

[8]Random defect model

over the normalized single soliton solution $\phi_{\nu_i}(z - z_i)$ at position $(z_i, \nu_i)$ in phase-space. As we derived in [182] the finite width $\xi$ of the defects can be considered within a local density approximation. This relates the full one-body momentum distribution for the solitonic state

$$n_{\mathrm{s}}(k) = \left[\frac{k/k_{\xi_{\mathrm{s}}}}{\sinh(k/k_{\xi_{\mathrm{s}}})}\right]^2 n_{\xi_{\mathrm{s}}\to 0}(k)\,, \tag{3.7}$$

to the spectrum for an ensemble of infinitely thin (phase) defects $n_{\xi_{\mathrm{s}}\to 0}(k)$. The second factor is a result of the local density suppression connected to a single solitonic defect and is obtained through the Fourier transform of Eq. (2.30). The momentum $k_{\xi_{\mathrm{s}}} = \sqrt{2}/(\pi\xi_{\mathrm{s}}\gamma)$ is related to the width $\xi_{\mathrm{s}}$ of a single defect, beyond which the local density suppression leads to a sharp decline of the spectrum.

The long-wavelength behavior $n_{\xi_{\mathrm{s}}\to 0}(k)$ is given by the Fourier transform of the first order coherence function $g_1(z_1, z_2)$ calculated in the limit of infinitely thin defects, i.e. for distances $|\bar{z}| = |z_1 - z_2| \gg \xi_{\mathrm{s}}$. The presence of a soliton therefore constitutes only a phase change of the field

$$\psi_0(z_2) = \exp\left(-\mathrm{i}\sum_i \beta(\nu_i)\right)\psi_0(z_1)\,, \tag{3.8}$$

where the sum runs over the number of solitons enclosed in the interval $[z_1, z_2]$. The influence of the soliton ensemble is completely encoded in the probability distribution $P_{N_{\mathrm{s}}}(z, \nu, \xi_{\mathrm{s}})$ and their influence can in principle be determined exactly. However, in order to get an analytically feasible model, we consider the case of an uncorrelated multi-soliton state in accordance with Eq. (3.6). The probability distribution is given by $P_{N_{\mathrm{s}}}(z, \nu, \xi_{\mathrm{s}}, t) = \prod_{i=1}^{N_{\mathrm{s}}} P_i(z_i, \nu_i, \xi_i, t)$ and, assuming ergodicity, completely described by the probability distribution of a single soliton $P(z, \nu, \xi_{\mathrm{s}})$. The first order coherence function then takes the form [116]

$$g_1(z_1, z_2) = n_{1\mathrm{D}}\left[1 - \frac{2}{L}\,\mathcal{I}_L(z_1, z_2)\right]^{N_s}\,, \tag{3.9}$$

where the probability integral $\mathcal{I}_L$ for a system of size $L$ is defined as

$$\mathcal{I}_L = \frac{L}{2}\int_{(z_1,-1)}^{(z_2,+1)} \mathrm{d}z\,\mathrm{d}\nu\, P(z,\nu)\left[1 - \mathrm{e}^{\mathrm{i}\beta(\nu)}\right] = L\,\chi\int_{z_1}^{z_2}\mathrm{d}z\, P_1(z)\,. \tag{3.10}$$

The second form of the integral is given for later convenience and is valid under the assumption of statistical independence of the soliton position and velocity, i.e. $P(z, \nu) = P_1(z)P_2(\nu)$. Therein we defined $\chi = \frac{1}{2}\int \mathrm{d}\nu\, P_2(\nu)\left[1 - \mathrm{e}^{\mathrm{i}\beta(\nu)}\right]$ to shorten the notation, which determines the influence of non-vanishing velocities of the soliton ensemble. Since $\mathcal{I}_L$ is finite in the limit

of an infinitely large system $L \to \infty$, as $P(z, \nu) \sim L^{-1}$, we get

$$g_1(z_1, z_2) = n_{1\mathrm{D}}\, \mathrm{e}^{-2n_s \mathcal{I}_{L\to\infty}(z_1,z_2)}\,, \tag{3.11}$$

for a constant soliton density $n_\mathrm{s} = N_\mathrm{s}/L$. This exponential form of the first-order coherence function is also a good approximation for a finite size system with a sufficiently large number of solitons $N_s$ [116].

As an illustrative example of the typical shape for a soliton dominated Bose gas we give explicit results for a flat distribution in space $P_1(z) = L^{-1}$. Evaluating Eq. (3.10) for a fixed soliton density $n_\mathrm{s}$ and taking into account that $\mathcal{I}_L \geq 0$ results in $\mathcal{I}_L = \chi|z_1 - z_2|$. Explicit evaluation of Eq. (3.9) for a finite size system shows fast convergence towards the exponential form of the first-order coherence function Eq. (3.11) for an increasing number of defects $N_\mathrm{s}$. However, drastic changes can arise for a finite size system containing only a small number of defects which lead to a typical multi-peak structure of the spectrum [116]. Since in the following we are mainly interested in states with $N_\mathrm{s} \gg 1$ we can safely use the exponential form even for a finite size system, for which Eq. (3.7) yields

$$n_\mathrm{s}(k) = \left[\frac{2n_{1\mathrm{D}}k_{n_\mathrm{s}}}{k_{n_\mathrm{s}}^2 + (k-k_0)^2}\right]\left[\frac{k/k_{\xi_\mathrm{s}}}{\sinh(k/k_{\xi_\mathrm{s}})}\right]^2\,, \tag{3.12}$$

Here $k_{n_\mathrm{s}} = 2n_\mathrm{s}\,\mathrm{Re}(\chi) = 2n_\mathrm{s}\bar{\gamma}^{-2}$ and $k_0 = 2n_\mathrm{s}\,\mathrm{Im}(\chi) = -2n_\mathrm{s}\bar{\nu}\bar{\gamma}^{-1}$ correspond to the mean distance between the defects and the mean overall momentum carried by the soliton ensemble and $\chi, \bar{\gamma}, \bar{\nu}$ are averaged variables with respect to $P_2(\nu)$. Apart from an overall shift of the spectrum due to $k_0$, the finite velocity of defects only leads to a rescaling of the relevant scales $k_{n_\mathrm{s}}, k_{\xi_\mathrm{s}}$ with $\bar{\gamma}$.

In the IR the spectrum takes a Lorentzian shape due to the random nature of phase fluctuations and therefore is similar to the thermal quasi-condensate profile Eq. (2.76). Utilizing this similarity we can define the coherence length $\lambda_\mathrm{s}$ and effective temperature $T_s$ of the soliton ensemble

$$\lambda_\mathrm{s} = \frac{\bar{\gamma}}{2n_\mathrm{s}} = \frac{2\hbar^2 n_{1\mathrm{D}}}{mk_\mathrm{B}T_\mathrm{s}}\,. \tag{3.13}$$

In the UV for $k \gg k_{\xi_\mathrm{s}}$ the second parentheses in Eq. (3.12), originating from the local density modulation of the defect, leads to an exponential suppression of high-energy modes $n(k) \sim \exp\left(-2k/k_{\xi_\mathrm{s}}\right)$. The linear exponential decay of the distribution is determined by the defect width and presents a distinct non-thermal feature of the momentum distribution. In between these two scales the system exhibits scaling behavior $n(k) \sim k^{-2}$, which for $\xi_\mathrm{s} \to 0$ extends to infinity.

These results can be extended to inhomogeneous bulk-densities $n_{1D}(z)$ and finite temperatures $T$. Defining the local defect width $\xi_s(z)$ and neglecting correlations between thermal and solitonic fluctuations, we decompose the full field $\psi(z) \simeq \psi_0(z,T)\psi_s(z,P)$, where $\psi_0(z,T)$ is the inhomogeneous background field at finite temperature $T$ and $\psi_s(z,P)$ describes an ensemble of solitonic defects distributed according to the probability distribution $P$ on a homogeneous background. By use of the convolution theorem and the previous results we immediately get the full one-body momentum distribution

$$n(k) = \int \mathrm{d}n_s \; p(n_s) \left[ n_0(k,T) * n_s(k,n_s) \right] \; , \tag{3.14}$$

where $*$ denotes the convolution in Fourier space and we allowed for fluctuations of the soliton density according to the probability distribution $p(n_s)$. Note in particular that deep in the IR, the full spectrum retains its Lorentzian shape, with $\lambda_{T_{\mathrm{eff}}}^{-1} = \lambda_T^{-1} + \lambda_s^{-1}$.

### 3.2.2 Defect Nucleation in Shock Cooled BECs

The relevant scales, $n_s$ and $\xi_s$, are determined through a least-square fit of the RDM to the experimental momentum distribution. In order to take into account the finite expansion time and hydrodynamic velocity profile of the experiment, we use Eq. (3.2) within the LDA with $f(z,k,t) = \rho(z,t)\, n_{\mathrm{RDM}}(k,t)$. Here $n_{\mathrm{RDM}}(k,t)$ is the normalized single-particle momentum distribution of the RDM for a homogeneous system (see Eq. (3.12)) and we consider $\rho(z,t)$ as a pure condensate in the TF-approximation. The effects of a finite velocity of the ensemble are absorbed into the scales $n_s$ and $\xi_s$, which therefore include the constant rescaling due to $\bar{\gamma} \neq 1$. Note especially that any scaling properties remain unaffected and only absolute values are slightly shifted as compared to the effective scales.

The results of the fitting procedure for different quench rates are presented in Fig. 3.4. Depicted are the defect width and density determined at the previously discussed best focus point within the first half of the breathing period (red diamonds). The errors are given by the least-square fit to the experimental data. At these points the density after a finite expansion time best resembles the momentum distribution of the condensate and hence most accurately determines the actual value of the scales $n_s$ and $\xi_s$. For comparison the mean value over the full breathing period (blue dots), its standard deviation (blue shaded region), as well as the minimum and maximum values within the first breathing period (green shaded region) are calculated to quantify the additional defect decay and the expected fluctuations of the relevant scales during the first breathing period.

Concentrating first on the slow quenches $R_q \lesssim 5\,\mathrm{kHz/ms}$, we find large fluctuations of the defect width and density. Notably, for the presented data we already excluded points where the condensate velocity exceeds the threshold $|1 + \tau_{\mathrm{tof}}\dot{b}/b| > 2.5$ (c.f. Eq. (3.5)) above

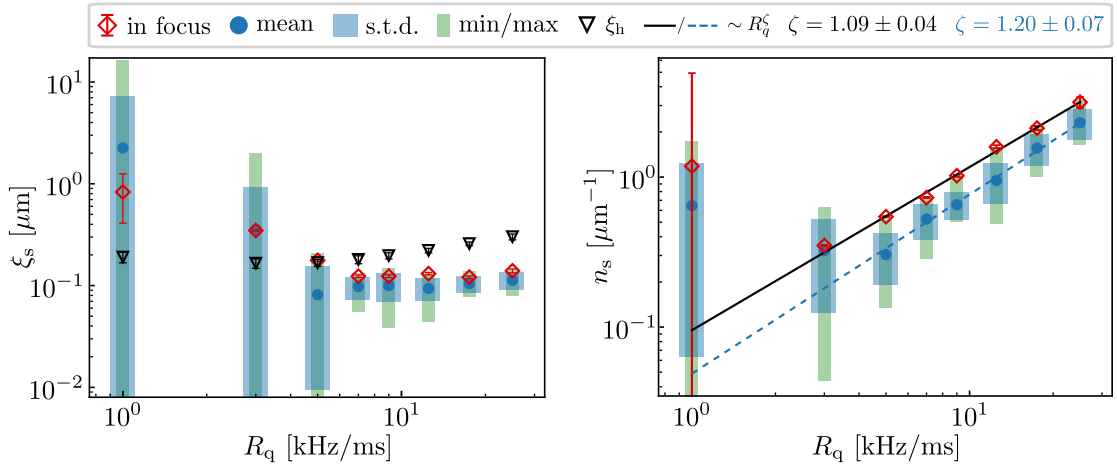


Fig. 3.4 Defect nucleation for varying quench rates $R_q$. Defect width $\xi_s$ (left panel) and density $n_s$ (right panel) determined by the RDM. Red diamonds present measurements at the best focus point within the first half of the breathing period, best resembling the actual values of the scales. The errors denote the std determined from the least-square fit. The mean value over the first breathing period (blue dots), its standard deviation (blue shaded region), and the minimum/maximum values (green shaded region) are depicted for comparison. The defect width deviates for $R_q > 5\,\mathrm{kHz/ms}$ from the expected equilibrium width of solitonic defects (black triangles). The solid black (dashed blue) line is a power-law fit of the defect density in focus (mean) with exponent $\zeta = 1.09 \pm 0.04$ ($1.20 \pm 0.07$).

which the RDM fails to accurately describe the experimental data. This failure is to be expected because, as we already saw in Section 3.1, the system exhibits dynamics beyond the hydrodynamic approximation. Most prominently, the large double-peak structures in the momentum distribution cannot be explained through the hydrodynamic prediction of a scaling solution for the breathing dynamics. The RDM trying to cope with these inaccuracies leads to the observed large fluctuations. While we find the results within their errors to be in accordance with the expected behavior determined for higher quench rates, a statistically significant determination of the relevant scales for the available data is hindered by the absence of a clear separation of the dynamics. Therefore, in this regime, further experiments are needed to determine the cause for the observed deviations from the hydrodynamic solution and to devise an appropriate theoretical description of the systems dynamics.

For increasing quench rates $R_q \gtrsim 5\,\mathrm{kHz/ms}$, due to the suppression of the breathing amplitude, these effects become less pronounced and the system is well described within the hydrodynamic approximation. This allows us to accurately determine the defect width and density for all times, reflected in the decreasing errors in Fig. 3.4.

The defect width is found to converge to a constant value $\xi_s \approx 0.1\,\mu\mathrm{m}$, independent of the quench rate and final atom number. For equilibrated solitons the width is determined by the local healing length $\xi_h \sim n_0^{-1/2}$, and hence it would increase for lower densities (see black

triangles in Fig. 3.4). The observed defect width in the experiment has therefore not yet reached its final equilibrium value for $R_q > 5\,\mathrm{kHz/ms}$, the difference increasing for higher quench rates. The slower exponential decay of the momentum distribution (c.f. Eq. (3.12)) results in an overpopulation of high energy modes. Hence the system is described by an ensemble of randomly distributed defects with an effective width determined by the quench.

Equilibration of the defect width may be prevented because the system is probed immediately after the end of the cooling ramp. Hence, for faster quench rates defects are unable to fully equilibrate before the system becomes isolated. Further, as defect nucleation is expected to take place predominantly near the phase transition, the defect width during creation is determined by the atomic density at the critical point. Any further near homogeneous atom loss of the system leads to a further decrease of the healing length and a re-equilibration of the defect width. Both effects contribute to a defect ensemble in an isolated system for which the defect width has not yet reached its final equilibrium value. The absence of diffractive two-body scattering in an isolated system, however, strongly suppresses the redistribution of particles in momentum space. This leads to the observed discrepancy between the defect width in position and momentum space, as increasing fluctuations of the condensate retain the overpopulation of high energy states as the defect adjusts its width.

The defect density is not influenced by the above non-equilibrium width of the soliton ensemble, and the measurement directly following the quench allows us to test the predictions of defect nucleation unhindered by any possible defect decay posterior to the quench. Turning to the measurement in focus, we find power-law scaling of the defect density with an exponent $\zeta = 1.09 \pm 0.04$. This is in good agreement with the theoretical mean-field prediction of $\zeta_{\mathrm{IKZM}} = 1$ for the inhomogeneous Kibble-Zurek mechanism, and clearly deviates from the predictions $\zeta_{\mathrm{HKZM}} = 1/4$ for a homogeneous condensate. The averaged defect density over the first breathing period shows similar scaling behavior, with a slightly increased exponent $\zeta = 1.20 \pm 0.07$. Despite the influence of the breathing excitation, the decay of defects, and the limited resolution in the IR due to the finite expansion time the averaged results are in reasonable agreement with the predictions in focus.

The approximately linear scaling of the defect density with the quench rate further explains the observed scaling in the in Situ width and the FWHM of the momentum distribution, as discussed in Section 3.1. Considering a soliton to effectively increase the atom number by the particles it displaces, we have $N_{\mathrm{eff}} \sim n_{\mathrm{s}} \sim R_q$. Together with the scaling of the in Situ size of the cloud within the Thomas-Fermi approximation $R_{\mathrm{TF}} \sim \sqrt{\mu} \sim N^{1/3}$, we find scaling of the mean extent of the cloud $R \sim R_q^{1/3}$ as observed in Fig. 3.2. Scaling of the FWHM of the momentum distribution for the RDM is given by Eq. (3.12), which for low defect densities is given by $\Delta k_{\mathrm{FWHM}} \sim n_{\mathrm{s}} \sim R_q$ determined by the Lorentzian distribution. For increasing defect densities, i.e. if $k_{n_{\mathrm{s}}} \approx k_{\xi_{\mathrm{s}}}$, the second factor in Eq. (3.12) stemming from the localized density suppression associated with the defect leads to deviations from the above scaling and for a

fixed defect width to the upper bound $\Delta k_{\mathrm{FWHM}} \simeq 1.49\, k_{\xi_s}$ for $n_s \to \infty$. This is in excellent agreement with the observed scaling and the deviations for fast quench rates in Fig. 3.3.

Lastly the suppression of the breathing amplitude is explained by the increasing density of defects. As discussed in Section 2.1.3 interactions between deep, slow-moving solitons ($\nu < 0.5$) are repulsive. Compression of a gas bearing a random ensemble of defects therefore increases the energy of the system due to the increasing density of the soliton ensemble. This leads to the observed transition from frequency-doubling to no-doubling for the FWHM of the momentum distribution. At the transition, the increase in energy due to compression of the soliton ensemble exceeds the energy at the points of maximum inwards/outwards velocity and the momentum distribution oscillates out-of-phase with the in Situ density. Increasing the density of defects even further results in the observed "stiffness", because further compression of the gas becomes energetically unfavorable [116].

### 3.2.3 Relaxation to Thermal Equilibrium

In the previous section we were mainly concerned with the initial far-from equilibrium state as well as the short term dynamics for variable quench rates $R_q$. We found that the system exhibits a plurality of effects, making it essential to find a comprehensive analysis, which allows us to ascertain and distinguish between the underlying fundamental mechanisms determining the dynamics of the system. To this end we will now focus our attention on the long-term evolution of the system following a fast cooling quench $R_q = 25\,\mathrm{kHz/ms}$. As we described in the last section the system thereby enters a regime, where the density and momentum distribution become "stiff", which separates the additional dynamics caused by a breathing excitation from the fundamental relaxation mechanisms of the system.

The long-term dynamics are determined through a separate measurement of the system, for which the hold time $t$ is chosen at logarithmically equidistant points. This allows to determine the systems evolution for up to $t \approx 1\,\mathrm{s}$. The initial state is prepared by the same cooling mechanism described in the previous section. The system prior to the quench is prepared in thermal equilibrium with $N = 3 \cdot 10^4$ atoms at $T \approx 550\,\mathrm{nK}$. At the end of the cooling ramp the atom number decreased to $N = 1700$. Expectation values are calculated by averaging over different experimental realizations, where the measurement is repeated $\approx 55$ times for each hold time $t$.

The evolution of the in-Situ density $\rho(z,t)$ and the single-particle momentum distribution $n(k,t)$ is depicted in Fig. 3.5. We account for atom loss during the long-term evolution by normalizing the distributions to the total atom number $N(t)$ at each time step. At the end of the evolution $t \approx 1\,\mathrm{s}$ the atom number has dropped by $\approx 60\%$. We find that atom loss becomes significant at $t \approx 100\,\mathrm{ms}$ (c.f. Fig. 3.7). For short times the system shows the previously discussed broadened distributions in position and momentum space. For

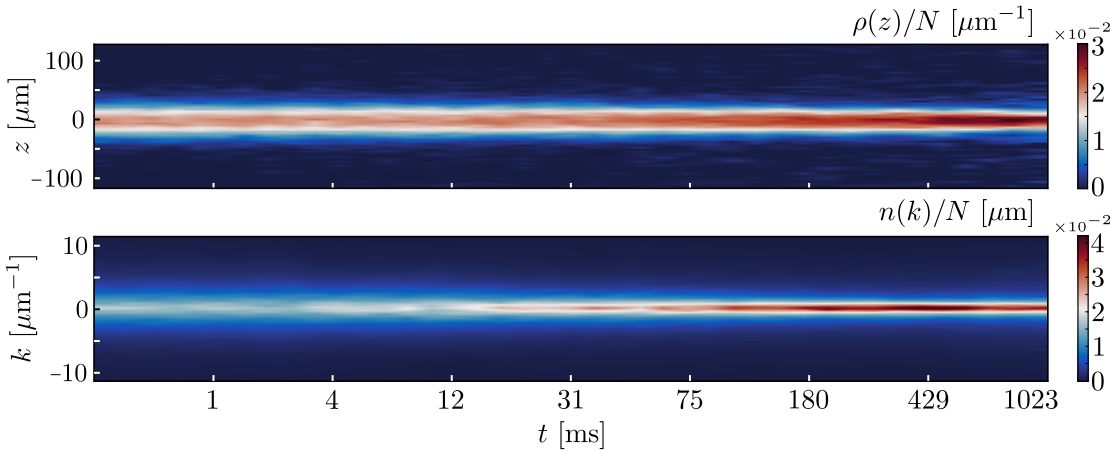


Fig. 3.5 Long-term evolution of the in Situ density $\rho(z,t)$ (upper panel) and momentum distribution $n(k,t)$ (lower panel) for $R_{\mathrm{q}} = 25\,\mathrm{kHz/ms}$. The distributions at each time are normalized by the total atom number $N(t)$ to account for atom loss at late times. Note the linear color scale to highlight the peak density. The emergence of a peak at low momenta in the momentum distribution is clearly visible, signaling the emergence of a quasi-condensed state.

later times however the momentum distribution narrows and a clear peak emerges at low momenta, signifying the condensation of the system. The normalization reveals the effective transference of atoms to the IR, such that the relative occupation of low momentum modes grows significantly. Note that due to the enhanced role of fluctuations in one-dimensional Bose gases, the system retains a multi-mode character in contrast to the formation of a true BEC in higher dimensions.

We quantify the approach to thermal equilibrium by comparing the experimental data at each time $t$ to the theoretical predictions of the momentum distribution (3.2) for the RDM (3.12) as well as a thermal quasi-condensate (2.76). In the RDM we take the density to be a broadened condensate in the TF-regime. The defect width is fixed to $\xi_{\mathrm{s}} = 0.087\,\mu$m, determined by the mean value over the first breathing period. This is done because once the two scales $k_{n_{\mathrm{s}}}$ and $k_{\xi_{\mathrm{s}}}$ are of the same order they become correlated if both scales are fitted freely. We found in the last section that the defect width is rather independent of the quench and conserved in the subsequent evolution. Thereby, by keeping the defect width fixed, we can accurately determine the evolution of the defect density. For the QC the density profile is determined through simulation of the stochastic GPE and we additionally take into account the thermal occupation of radially excited states in the ideal Bose gas approximation [183]. In [184] it was shown that the resultant density distribution describes the system over the full crossover regime from a thermal to a quasi-condensate and is in very good accordance with the modified Yang-Yang model [123, 122]. The chemical potential is determined self-consistently through the experimental atom number. The QC model is

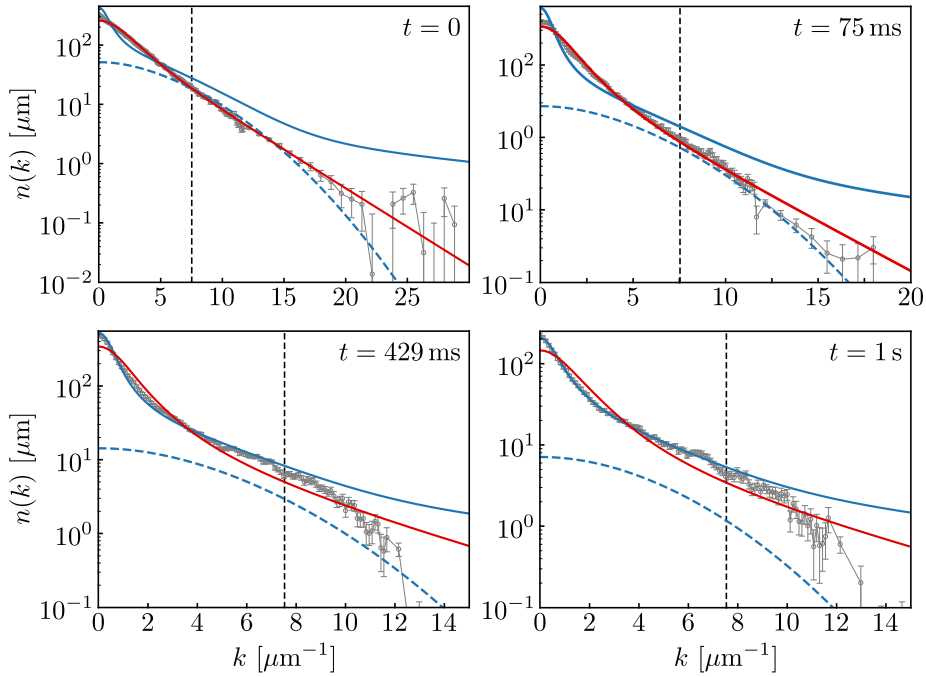


Fig. 3.6 Experimental momentum distribution and model fits. Comparison of the RDM (red) and QC (blue) predictions to the experimental momentum distribution (gray dots) for different times during the evolution. The errors denote the standard deviation of the mean. The experimental data is averaged over $\pm k$ and binned over seven adjacent points in momentum space for $n(k) \lesssim 1$ to reduce fluctuations. The thermal occupation of radially excited states in the QC model is given by the dashed blue line. The vertical line marks the momentum corresponding to the first radially excited state.

expected to only describe the low-energy states of the system and leads to an overestimation for the occupation of high energy particles. We therefore restrict the analysis to energies $E \leq \hbar\omega_\perp$ for which the QC model is expected to accurately describe the system.

The momentum distribution for selective times during the evolution are shown in Fig. 3.6. At high energies the spectrum is binned over 7 adjacent momenta to lower the experimental noise in the regime of low occupation. At early times, $t = 0$ and $t = 75\,\mathrm{ms}$, the system shows excellent agreement with the RDM (solid red line), while the thermal QC fails to describe the data. The observed linear exponential decay of the momentum distribution spanning over two orders of magnitude and extending well beyond the energy of the first radially excited state (dashed vertical line) is a striking confirmation of solitonic defects within the system. For small momenta $k < k_{\mathrm{IS}}$ deviations occur, as the expanded density is not fully converged to the momentum distribution. Differences can be caused by the assumption of ballistic expansion of the gas, since for these highly excited states the free expansion of the gas may become more involved. Further, these momenta probe the system on a length scale comparable to the system size and hence will be influenced by the exact spatial distribution of defects within

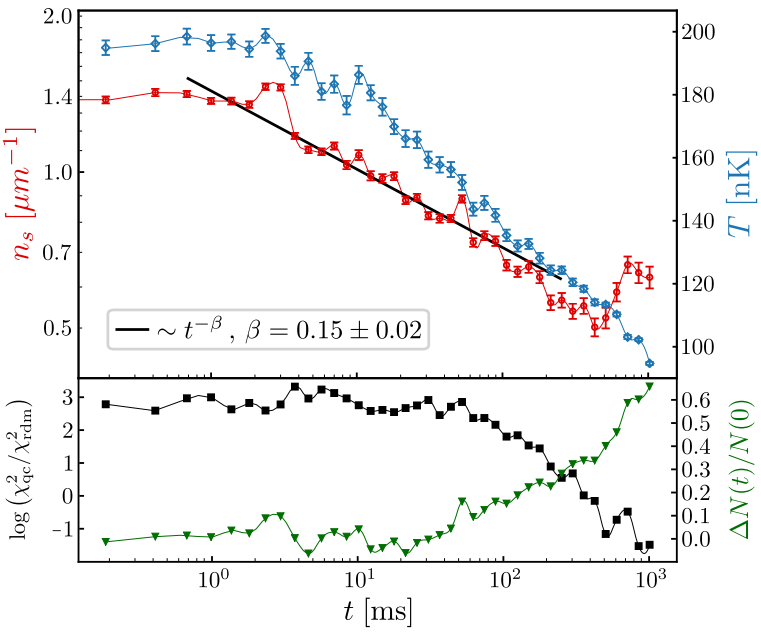


Fig. 3.7 Approach to thermal equilibrium. Time evolution of the characteristic scales for the RDM (red, log-log scale) and QC (blue, log-lin scale) fits (upper panel). The defect width $\xi_s = 0.87\,\mu$m is fixed and determined by the average over the first breathing period. The solid black line is a power-law fit to the defect density, showing dilution of the defect ensemble with an exponent $\beta = 0.15 \pm 0.02$. The quality of the two fits is compared through $\log\left(\chi^2_{qc}/\chi^2_{RDM}\right)$ (lower panel, black squares), showing positive values if the RDM fit is preferred and negative values for the QC. The system clearly deviates from the RDM predictions once atom loss (green triangles) becomes relevant.

the system. A quantitative determination of the probability distribution $P_{N_s}$ describing the defect ensemble is not possible due to the large degree of freedom. However the relevant properties of the system, including the determination of the characteristic scales of the RDM, are well captured by assuming a homogeneous distribution of defects. At late times during the evolution, $t = 429$ ms and $t \approx 1$ s, the reverse happens and the system shows excellent agreement to the QC predictions while the RDM fails to describe the state. This confirms the relaxation of the system to a thermal equilibrium state for late times.

To ascertain the approach of the final equilibrium state we show in Fig. 3.7 the time evolution of the relevant scales $n_s$ and $T$ (upper panel) over the full relaxation period. For early times, the QC model captures the broadening of the density and momentum distribution through a high temperature of $T \approx 200$ nK. The subsequent collapse of the distributions leads to a monotone decrease in temperature which for late times continues due to increasing atom loss in the system. For the latest times the system is fully thermalized at a temperature $T \approx 100$ nK. We compare the quality of the fit for the different models by use of the reduced $\chi^2$ calculated over the momentum range where the models are expected to accurately describe the data. We find $\chi^2_{RDM} \approx 1\,(5)$ and $\chi^2_{QC} \approx 20\,(1)$, for the earliest (latest) times respectively. The transition from a preference of the RDM to the QC model is clearly visible in the

lower panel of Fig. 3.7 showing the time evolution of $\log(\chi^2_{\mathrm{QC}}/\chi^2_{\mathrm{RDM}})$ (black squares). This compares the quality of the two fits, with a positive value preferring the RDM and a negative value preferring the QC fit. We find clear preference of the RDM for $t \lesssim 100\,\mathrm{ms}$ beyond which the system begins to relax towards a thermal QC. Deviation from the RDM become significant beyond the time where atom loss in the system can no longer be neglected (green triangles). This suggests that the thermalization is driven by atom loss leading to an open system. At early times, for which the RDM describes the system, we find significant defect decay of $\approx 50\%$. The defect density, after a short initial period, shows a power-law decay proportional to $t^{-\beta}$ with $\beta = 0.15 \pm 0.02$, spanning approximately two orders of magnitude from $t = 1 \ldots 100\,\mathrm{ms}$. This means that in contrast to the observed exponential decay of solitonic defects [181], the dilution of the ensemble for these highly excited states follows a power-law behavior. This difference in the relaxation mechanism of the system is far more than a singular observation for specific initial conditions, but in fact is connected to fundamental principles of universal dynamics far-from equilibrium.

## 3.3 Universal Dynamics Far-From Equilibrium

In the last sections we found that following a strong cooling quench to the quasi one-dimensional regime the system quickly develops into a far-from equilibrium state, determined by an ensemble of randomly distributed solitonic defects. During the subsequent evolution we determined the coarsening of the soliton ensemble follows a power-law behavior, before, aided by atom loss, the system relaxes to a thermal equilibrium state.

It is an in general open question which relevant guiding principles distinguish the possible paths an isolated quantum many-body system can take, starting from a given far-from equilibrium initial state. Of particular interest are evolutions which, similar to equilibrium critical states, are determined by only a few universal properties. Therein the system, after a transient non-universal evolution, enters a regime where the dynamics of the system is described by a universal scaling function $f_{\mathrm{S}}(x)$, independent of the initial state of the evolution. The universal character of such a non-thermal attractor solution shows up in the form and evolution properties of correlation functions in both space and time [52, 50]. This allows to classify the system, in close connection to equilibrium critical phenomena, by only a few universal scaling exponents and functions. For example, the single-particle momentum distribution $n(k,t)$ of a Bose gas can develop the form

$$n(k,t) = (t/t_0)^{\alpha} f_{\mathrm{S}}\left[(t/t_0)^{\beta} k\right] , \tag{3.15}$$

determined only by the scaling exponents $\alpha$, $\beta$ and the scaling function $f_{\mathrm{S}}(k)$. The reference time $t_0$ is any time that lies within the period where the system shows the universal behavior

(3.15). The possibility to describe the immensely complex microscopic dynamics of thousands of particles through the rather simple scaling relation (3.15) is a truly remarkable result. Similar phenomena are expected to be relevant for a large variety of quantum and classical systems for which only a few symmetry properties determine the far-from equilibrium evolution of the system. We establish in the following the existence of such universal dynamics during the relaxation of our quantum many-body system. This provides direct experimental evidence for a conceptually new access to time evolution far-from equilibrium.

### 3.3.1 Self-Similar Dynamics and Scaling Exponents

Based on the observed power-law dependence of the defect density $n_\mathrm{s} \sim (t/t_0)^{-\beta}$ (see Fig. 3.7) we expect the system to exhibit self-similar scaling dynamics. Extending the RDM momentum distribution (3.12) to include a time dependence of the relevant scales leads in the IR to the scaling solution

$$n\left[k, t, n_\mathrm{s}(t)\right] \sim (t/t_0)^{\beta} n\left[(t/t_0)^{\beta} k, t_0, n_\mathrm{s}(t_0)\right] . \tag{3.16}$$

Here we inserted the observed power-law dependence of $n_\mathrm{s}$ and neglected for $k \ll k_{\xi_\mathrm{s}}$ the second term in Eq. (3.12) caused by the density modulation of the defect.

It is expected that the universal properties change for different inertial ranges [52, 50] due to global particle and energy conservation in the isolated system. This means that the scaling properties in the IR will in general differ from the behavior in the UV, and one does not expect the distributions to be described by a single universal scaling function and/or exponents over the whole momentum range. This is the reason for the limitation of Eq. (3.16) to the IR, which allowed us to eliminate the second, non-universal scale $k_{\xi_\mathrm{s}}$. We therefore expected that the defect width determines the characteristic scale below which the scaling relation Eq. (3.15) is satisfied.

The scaling solution of the RDM has the same form as Eq. (3.15) with $\alpha \equiv \beta > 0$. This relation between the scaling exponents is, in general, determined by the particle conservation within the scaling region[9] [52, 50]. The predicted inverse particle cascade towards the IR is in accordance with the experimental observations (c.f. Fig. 3.5). Thus we expect the two exponents not to be independent and it is advantageous to rather consider the approximately uncorrelated exponents $\beta$ and $\delta_{\alpha\beta} = \alpha - \beta$, i.e. $\alpha = \delta_{\alpha\beta} + \beta$, for the scaling analysis and error estimation.

We now turn to confirming the validity of the scaling dynamics (3.15) in a model-independent way, directly from the time evolution of the experimental data. This has the advantage that the analysis is independent of any theoretical approximations and allows us to

[9] More generally in $d$ spatial dimensions particle conservation the relation is $\alpha = d\beta$

test the systems evolution simply through its universal properties. The scaling exponents are determined using the maximum likelihood function [185]

$$L(\delta_{\alpha\beta},\beta) = \exp\left[-\frac{1}{2}\bar{\chi}^2\left(\delta_{\alpha\beta},\beta\right)\right], \tag{3.17}$$

where

$$\bar{\chi}^2(\delta_{\alpha\beta},\beta) = \frac{1}{N_t^2}\sum_{t,t_0}^{N_t}\frac{\int_{|k|\leq k_0}\mathrm{d}k\,\chi^2(\delta_{\alpha\beta},\beta,k,t,t_0)}{\int_{|k|\leq k_0}\mathrm{d}k}\,. \tag{3.18}$$

The local $\chi^2$ value given by

$$\chi^2(\delta_{\alpha\beta},\beta,k,t,t_0) = \frac{\left((t/t_0)^{\delta_{\alpha\beta}+\beta}n[(t/t_0)^{\beta}k,t_0]-n[k,t]\right)^2}{\sigma((t/t_0)^{\beta}k,t_0)^2+\sigma(k,t)^2}\,, \tag{3.19}$$

where $\sigma(k,t)$ is the standard deviation of the mean for the experimental data. The momentum distributions are normalized by the atom number $N(t)$ to minimize the effect of particle number fluctuations. To assess the discrete momentum distribution for continuous momenta $(t/t_0)^{\beta}k$ we use a linear interpolation of the experimental data and its error for each reference time $t_0$. The local squared residuals (3.19) are integrated over momentum space and averaged over all times $t$ and all reference times $t_0$ within the period where the system exhibits universal behavior. We include a high momentum cutoff $k_0$ in Eq. (3.18), as to only determine the scaling exponents in the IR. For the data presented we find $k_0 \approx 6.5\,\mu\mathrm{m}^{-1}$ which indeed is compatible to the scale $k_{\xi_s} = 5.2\,\mu\mathrm{m}^{-1}$ determined by the defect width.

The maximum of the likelihood function determines the most probable exponents $\delta_{\alpha\beta}$ and $\beta$ which minimize the local residuals (3.19). The global value $\bar{\chi}^2$ hereby determines the quality of the scaling hypotheses over the whole scaling period. The errors are estimated by a Gaussian fit to the marginal likelihood functions[10] given by integrating over one of the exponents, e.g. $L(\delta_{\alpha\beta}) = \int\mathrm{d}\beta\, L(\delta_{\alpha\beta},\beta)$.

The results of the scaling analysis are depicted in Fig. 3.8. The measured (left panel) as well as the scaled momentum distribution according to Eq. (3.15) (right panel) are shown for all times within the scaling region $t \in [0.7, 75]$ ms. We choose the reference time $t_0 = 3.8$ ms, for which the spectrum is given by the solid gray line. For better visibility the data is averaged over seven adjacent points in momentum space (see Fig. A.2 for full resolution). Despite the rather slow dynamics we find clear deviation between $n(k,t_0)$ and $n(k,t)$ giving $\bar{\chi}^2(0,0) = 4$. By drawing the scaled momentum distribution $(t/t_0)^{-\alpha}\,n(k,t)$ as a function of

[10] We find good accordance of the Gaussian fit for all experimental realizations. Therefore the Gaussian estimate is equivalent to the general definition of a decrease of $1/2$ of the likelihood function

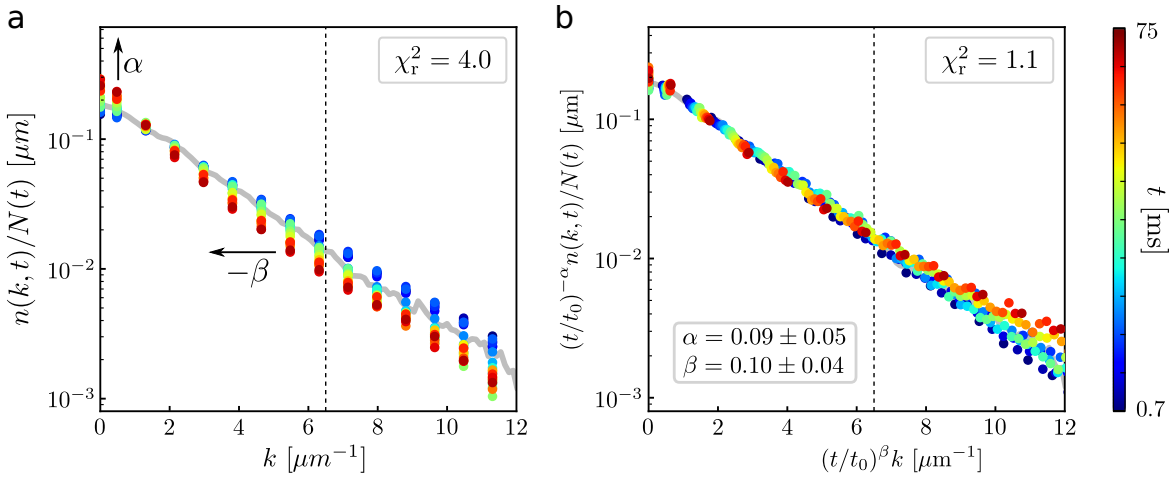


Fig. 3.8 Universal scaling dynamics. Time evolution of the measured (left panel) and momentum distribution scaled according to Eq. (3.15) (right panel). The data is averaged over $\pm k$ and, for better visibility, binned over seven adjacent points in momentum space. The time is encoded in colors (from blue to red). The reduced $\chi^2$ value measuring deviations from the momentum distribution at the reference time $t_0 = 3.8$ ms (gray line, thickness is arbitrary) shows clear deviations within the rescaling region in $k$ (below the dashed vertical line) for the measured data. The exponents $\alpha = 0.09 \pm 0.05$ and $\beta = 0.10 \pm 0.04$ are determined via Eq. (3.17) and show that the scaling evolution is consistent with a conserved particle transport towards the IR. The reduced $\chi^2$ shows perfect agreement for the scaled data.

the scaled momentum $(t/t_0)^{\beta} k$ all times collapse to a single curve. The scaling exponents $\beta = 0.10 \pm 0.04$ and $\delta_{\alpha\beta} = -0.01 \pm 0.03$, giving $\alpha = 0.09 \pm 0.05$, are in good agreement with the expectation $\alpha \equiv \beta$ and are compatible with the exponent determined by the RSM. Considering the theoretical approximations employed this further validates our description of the system by use of the RDM. For the most probable values we get $\tilde{\chi}^2(-0.01, 0.1) = 1.1$ and therefore perfect agreement of the scaled momentum distribution with $n(k, t_0)$ within the experimental errors. The small deviations for the zero-mode $k = 0$ are caused by the finite expansion time, such that the expended density is not fully converged to the momentum distribution. In the UV, for momenta $k > k_0$, the scaled curves show the expected deviation from the universal scaling form.

### 3.3.2 Initial Conditions and Universal Scaling Function

One of the most striking features of universality far-from-equilibrium is the fact that the dynamics are independent of the specifics of the initial state. The universal properties near the fixed-point therefore do not require any fine-tuning of parameters, as it is for example the case in equilibrium critical phenomena where critical scaling only applies near the critical point [59, 164].

Confirming the universality of the observed scaling dynamics we consider three different experiments[11] for varying initial conditions prior and posterior to the quench. The initial thermal cloud of $N = 2.7 \ldots 3.2 \cdot 10^4$ atoms at a temperature $T = 530 \ldots 600\,\mathrm{nK}$ is cooled by the same cooling ramp with $R_q = 25\,\mathrm{kHz/ms}$ resulting in a one-dimensional far-from-equilibrium state of $N \approx 800 \ldots 2800$ atoms. The measurement is repeated $30 \ldots 55$ times for each experimental realization and hold time $t$. We determine the likelihood function and scaling exponents as described in the last section. We find excellent agreement of the scaling exponents for each individual measurement (see Fig. A.2).

This allows us to increase the statistics by averaging the results of the separate measurements. For statistically independent events the combined likelihood function is given by the product of $L(\delta_{\alpha\beta}, \beta)$ calculated for each measurement. The resultant likelihood function as well as the marginal likelihood functions are presented in Fig. 3.9a. We find the statistically significant[12] non-vanishing scaling exponents

$$\beta = 0.10 \pm 0.03 \tag{3.20}$$

$$\delta_{\alpha\beta} = -0.01 \pm 0.02\,, \tag{3.21}$$

fulfilling $\alpha = \beta$ well within the observed errors.

Far-from-equilibrium universal scaling dynamics in isolated Bose gases following a strong cooling quench or for equivalent initial conditions have been studied by means of non-perturbative kinetic equations [52, 50]. A scaling analysis of the kinetic quasiparticle transport yields the exponent $\beta = 1/2$ independent of dimension $d$. This result, however, does not necessarily apply to the case $d = 1$, where due to the kinematic restrictions from energy and momentum conservation the transport is expected to vanish. Furthermore, taking into account that our system is a close realization of the integrable Lieb-Liniger model of a one-dimensional Bose gas with contact interactions, elastic two-body scattering is expected to be absent. As a result, currently, no existing theoretical prediction accounts for the observed non-zero value $\beta \approx 0.1$. An anomalous scaling exponent has been found in [132, 49] for a two-dimensional Bose gas and has been connected to scattering properties of topological excitations in the system, i.e. the dilution of a vortex ensemble. This suggests that a similar connection to quasi-topological excitations could be possible in our system, for which we established the presence of quasi-topological solitonic excitations in the last sections. Additionally the question arises if the system is truely in the 1D regime, or if transversally excited states may contribute to the observed scaling exponents. While the value of the parameter $\beta$ was found to be independent of the spatial dimension, it is an open question if e.g. fractal dimensions $d = 1 + \epsilon$ lead to a smooth interpolation from the finite value in $d = 2$

[11] Including the experimental set discussed in the previous sections

[12] The scaling exponent $\beta$ is non-zero within $3\sigma$ deviation.

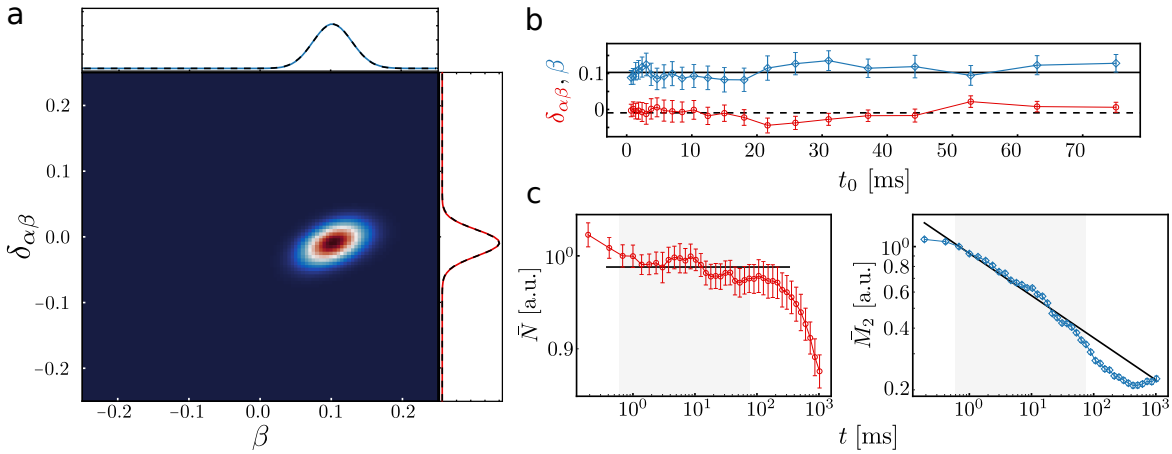


Fig. 3.9 Scaling exponents and global observables. **a** Maximum likelihood function $L(\delta_{\alpha\beta}, \beta)$ averaged over three different initial conditions. At the sides the marginal likelihood functions shown (solid lines) which are in excellent agreement with a Gaussian fit (dashed lines). **b** The averaged scaling exponent determined for each reference time $t_0$ separately agree well with the mean predictions $\beta = 0.1$ and $\delta_{\alpha\beta} = -0.01$ (solid and dashed line). **c** Scaling of the global observables (3.22) and (3.23) (for $n = 2$). The fraction of particles in the scaling region $\bar{N}$ (left panel) becomes approximately conserved (solid line) during the scaling period (gray shaded region). Therein the mean energy per particle in the scaling region $\bar{M}_2$ (right panel) shows the expected power-law behavior $\sim (t/t_0)^{-2\beta}$ (solid line).

to zeros in $d = 1$. Further theoretical studies in a non-perturbative field theoretical description may shed light on the observed scaling exponents in quasi one-dimensional systems.

In addition, we determine the scaling exponents and errors for each reference time $t_0$ separately, by omitting the average over $t_0$ in Eq. (3.17). The exponents for each reference time $t_0$ agree well with the averaged predictions (3.20) (see Fig. 3.9b). This confirms the independence of the scaling relation for different reference times $t_0$.

In order to assess the temporal extent of the scaling regime it is advantageous to determine the validity of the scaling hypotheses by the use of global observables. Assuming a scaling Ansatz according to Eq. (3.15) we find scaling of the averaged observables

$$\bar{N} = \frac{1}{N(t)} \int_{|k| \leq \tilde{t}^{-\beta} k_0} \mathrm{d}k \, n(k,t) \qquad \sim \tilde{t}^{-\delta_{\alpha\beta}} \tag{3.22}$$

$$\bar{M}_{n\geq 1} = \frac{1}{\bar{N} N(t)} \int_{|k| \leq \tilde{t}^{-\beta} k_0} \mathrm{d}k \, |k|^n n(k,t) \quad \sim \tilde{t}^{-n\beta} \, . \tag{3.23}$$

Note the dependence of the integration ranges on the scaling exponent.

Particle number conservation is reflected in Eq. (3.22), which describes the fraction of particles in the region of momentum space where the system shows scaling behavior.

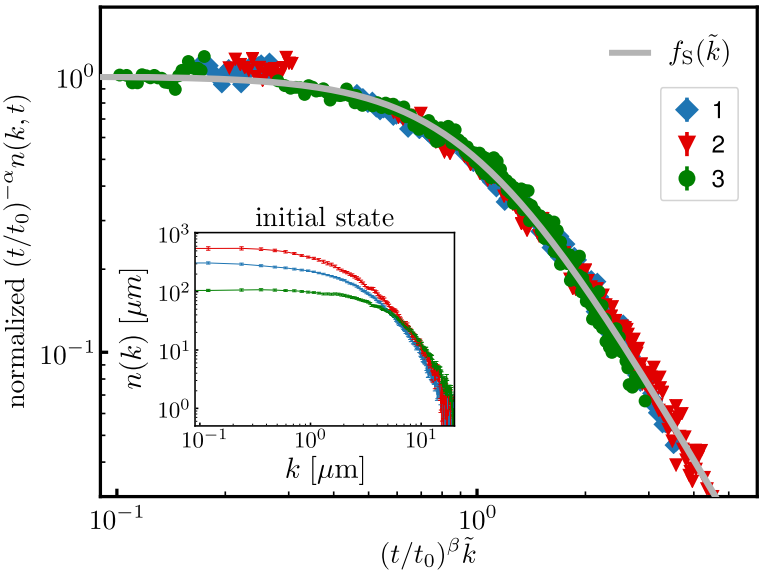


Fig. 3.10 Universal scaling function. The normalized momentum distributions $(t/t_0)^{-\alpha} n(k,t)$ as a function of the dimensionless momentum $(t/t_0)^{\beta} k$ collapse for varying initial conditions (blue, red, green) to a single universal function $f_S = 1/\left(1+\tilde{k}^{\zeta}\right)$ with $\zeta = 2.28 \pm 0.12$ (gray solid line). The experimental data is binned over seven adjacent points in $k$ for clarity. The small deviations for low momenta are due to the finite expansion time of the gas. The inset shows the measured initial momentum distributions at $t = 0$.

A non-vanishing exponent $\delta_{\alpha\beta}$ therein leads to particle transport outside/inside the scaling region and an explicit dependence of $\bar{N}(t)$ on time. The time evolution of $\bar{N}$, averaged over the different measurements, is presented in Fig. 3.9c (left panel) for the full time period up to $t \approx 1s$. After a short non-universal evolution, $\bar{N} \approx$ const within the scaling period (gray shaded region) and decays for late times during the approach of thermal equilibrium. This reveals the emergence of an approximately conserved quantity, which is transported towards the IR during the scaling dynamics, which is another hallmark behavior of the dynamics near a non-thermal fixed point.

For the observables (3.23) the momentum distribution is weighted by a certain power of $|k|$ and normalized by the fraction of atoms in the scaling region. Most importantly $\bar{M}_1$ and $\bar{M}_2$ measure the absolute mean momentum and kinetic energy per particle in the scaling region, respectively. Note that the normalization with $\bar{N}N(t)$ eliminates the dependence of $\bar{M}_n$ on the scaling exponent $\delta_{\alpha\beta}$. This enables the separate measurement of the exponents through the scaling analysis of mean observables. Apart from further validating the scaling dynamics of the system, this allows us to clearly identify the scaling period $t \approx 0.7 - 75$ ms through deviations of the experimental results from the above predicted power-law behavior (see Fig. 3.9c, right panel).

Rescaling the experimental data for each measurement and taking into account the non-universal normalization and momentum scale, all measurements for all times within the scaling period collapse to a single universal function $f_S(\tilde{k})$ (see Fig. 3.10). The dimensionless momentum $\tilde{k} = k/k_{nu}$ is normalized by the non-universal momentum scale $k_{nu}$. This is the only parameter apart from an overall normalization which encodes the specifics of the initial state. In comparison to the RDM $k_{nu}$ is determined by the defect density, which was found to be the relevant non-universal scale in Eq. (3.16). The dependence of this scale on the specifics of the initial state and/or quench is in accordance with the Kibble-Zurek picture of defect nucleation during a phase transition. Therein the absolute number of defects created during the quench depends on the actual values of e.g. the atom number at the point of the transition. We find a similar behavior for the defect density, despite the fact that our system is most likely not in the validity regime of the Kibble-Zurek mechanism. Universality, however, completely determines the scaling evolution of the system through the function $f_S$ and exponents $\alpha$ and $\beta$. To fully characterize the former we fit the generic function $(1 + \tilde{k}^{\zeta})^{-1}$ [52, 50, 49] to the experimental data for which we find $\zeta = 2.28 \pm 0.14$. The observed exponent deviates slightly from the predicted universal function of the RDM $\zeta = 2$ and the general predictions in [50] of $\zeta = d + 1$. Since the universal function is known to depend on the dimensionality of the system, the deviations measured in the experiment might show dynamics beyond the one-dimensional regime.

## 3.4 Summary

In this chapter we studied the relaxation dynamics of a one-dimensional Bose gas following a strong cooling quench. We identified the emergent far-from-equilibrium state of the system as a quasi-condensed gas bearing an ensemble of randomly distributed solitonic defects. This allowed us to describe the systems properties within a model of randomly distributed quasi-topological defects (RDM).

Probing the system immediately at the end of the cooling ramp, which, for the fastest quench rates $R_q$ are approximately two orders of magnitude faster than any previous experimental investigations, we determined the presence of solitonic excitations through their impact on the single-particle momentum distribution. We believe this approach provides a clean setup for the study of defect nucleation during quench dynamics as it enables us to probe the system before any additional defect decay. At early times, we found the system to be characterized by solitonic defects of an approximately constant non-equilibrium width. We attributed this to the absence of equilibration of the defect ensemble, caused by the rapid quench and subsequent isolation of the system.

Varying the rate $R_q$ at which the cooling ramp was performed we found scaling of the defect density $\sim R_q^{1.09}$. Defect nucleation hence closely follows the predictions of the inhomogeneous Kibble-Zurek mechanism [165, 77]. However, for the fastest quench rates considered in the experiment the system, in contrast to the Kibble-Zurek calculations, is at no point during the quench near its thermal equilibrium state. Our observations therefore reveal the perseverance of Kibble-Zurek-type scaling of defect nucleation beyond its strict range of validity. The determined scaling of the defect density allowed us to explain the observed (model-independent) properties of the system, such as scaling for the width of the density and momentum distributions.

We further found that, similar to thermal equilibrium states [178], these solitonic states lead to a transition for the breathing frequency of the gas from frequency-doubling to no-doubling in momentum space. We explained this behavior based on the repulsive interactions of slow-moving solitons, which suppresses compression of the gas for increasing defects densities. Increasing the density of defects even further we observed a transition to a "stiff" condensate, showing an almost stationary, strongly broadened density and momentum distribution. We like to highlight that the observed transition happens entierly in the quasi-condensed phase of the gas and is not connected to the transition of the system to a free Bose gas.

In the second half of this Chapter, we turned our attention to the long-term relaxation of the system, for hold times up to $t \approx 1\,\mathrm{s}$. To minimize the influence of additional dynamics, as e.g. the strong breathing excitations observed for slow quench rates, we focused our attention on the fastest quenches, with $R_q = 25\,\mathrm{kHz/ms}$.

We quantified the approach to a thermal equilibrium state by comparing the momentum distribution for each time during the evolution to the theoretical predictions of the RDM and a thermal quasi-condensate. A $\chi^2$ analysis revealed the preference of the RDM for times $t \lesssim 100\,\mathrm{ms}$, beyond which the system begins to deviate and finally approach a thermal equilibrium state, well described by the quasi-condensate model. During the time that the RDM accurately describes the system, we found a dilution of the defect ensemble leading to a transport of particles towards the IR and the emergence of a quasi-condensed peak in the momentum distribution. The decay of defects hereby followed a power-law behavior $\sim t^{1.50\pm0.02}$, which indicates the emergence of universal behavior in the system.

We therefore investigated in the last Section the emergence of universal dynamics far-from-equilibrium for these strongly quenched systems. These scaling evolutions are characterized by only a few universal scaling exponents and scaling functions, independent of the details of the initial state. We found that the system for varying initial conditions, after a short transient evolution, indeed enters such a scaling regime characterized by the universal function $f_S = (1 + k^\zeta)$ with $\zeta = 2.24 \pm 0.12$ and scaling exponents $\alpha \approx \beta = 0.1$. We connected the evolution to the emergence of a conserved quantity, transported towards the IR. Our

results present striking evidence for the direct experimental observation of non-equilibrium scaling dynamics and the approach of a non-thermal fixed point in an isolated quantum many-body system.

# Chapter 4

# Characterizing Many-Body Systems via Higher-Order Correlations

Quantum many-body systems are fully characterized through their correlations [82, 82]. While this concept forms the basis of the introduction to theoretical studies of Quantum Field Theory its implementation in an experimental system has so far been mostly lacking. Higher-order correlations, and their factorization properties i.e. how they can be decomposed into lower-order correlations, are known to provide important information about the underlying structure of the field theory, its interactions and its complexity [186, 83, 187]. Nonetheless, experimental systems are up to now mostly probed through lower-order correlations. However, with the rapid progress in cold atom experiments [63] measuring higher-order correlations is now within reach [188–190, 15]. Studying their factorization properties gives direct access to highly non-trivial field theoretical calculations. In the limit of equal times, the $N^{\text{th}}$ order correlations of the fundamental fields contain the combined effect of all possible scattering events containing $N$ particles. In theoretical calculations this usually involve an infinite series of Feynman diagrams which need to be evaluated [186, 83, 187]. Determining in experiments up to which order these correlations have a significant contribution to the systems properties, allows for a stringent comparison to theoretical calculations and gives valuable information about the possibly irrelevant operators which renormalize to zero in the low-energy description of the system. In particular, observing complete factorization according to Wick's theorem [191, 83, 187, 186], proves without any further theoretical calculations, that the diagonalizing degrees of freedom are found and the system is described by a quadratic Hamiltonian.

We implement these concepts through a detailed analysis of the factorization properties of the relative phase between two linearly coupled quantum wires, realized in a double-well

potential[1]. Matter-wave interferometry [192] gives direct access to the spatially resolved relative phase, which is described by an effective field theory, the sine-Gordon model [84]. By adjusting the tunneling rate through the double-well barrier, the relevance of higher-order coupling terms in the SG model can be tuned, shifting the model from a Gaussian state to a strongly correlated system. Detailed comparison of the factorization properties of higher-order correlations up to $10^{\text{th}}$ order reveals the validity of the SG model as the low-energy effective theory to an unprecedented accuracy over the whole range of coupling parameters. In limiting cases complete factorization of higher-order correlations is found, proving the validity of the quadratic low-energy approximations commonly employed in the description of ultracold Bose gases.

By changing the speed at which the condensate is cooled into the double-well, we can further study the near-equilibrium properties of correlation functions in the SG model. Analysis of the full distribution functions of phase differences, containing the combined information of all higher-order correlations, solitons are found to prevail in these long lived non-thermal states as remnants of the fast condensation dynamics. Establishing through numerical simulations of the condensation dynamics in the SGPE framework the rapid thermalization of fluctuations around these highly non-linear solutions and the approximate decoupling of phononic and solitonic excitations we explain the observed non-equilibrium higher-order correlations through a model of randomly distributed solitons. Our findings underline the precision higher-order correlations offer in the analysis of quantum many-body system, which therefore are an essential tool for reading, verifying, and characterizing quantum simulators [193].

## 4.1 Parameter Space and Lower-order Correlations

Coupled quantum wires are an excellent starting point for the investigation of non-Gaussian field theories. Their low-energy description, the SG model (2.44), has an infinite number of higher order coupling terms, which cannot be neglected in the description of the system [84, 194].

Examining low-order correlations in thermal equilibrium demonstrates the need for a description beyond the harmonic Bogoliubov approximation. The simplest of these is the

[1]This chapter is based on and contains parts of [160]. I contributed to the theoretical calculations, interpretation of the theoretical results and experimental data, performed numerical simulations, and contributed to writing of the manuscript.

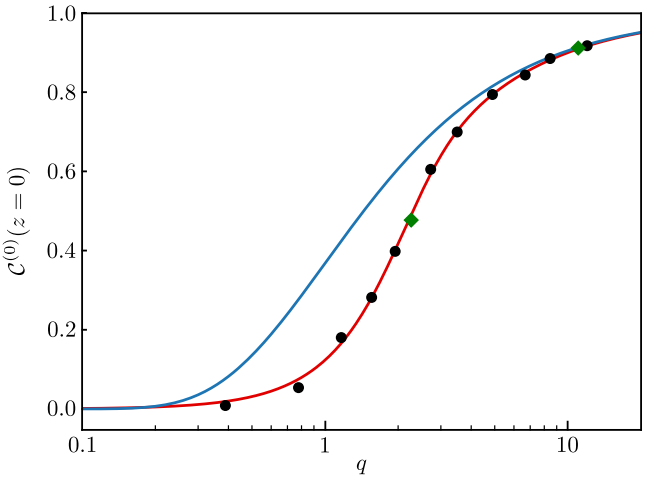


Fig. 4.1 Coherence factor $C^{(0)}(z=0)$ as a function of the parameter $q = \lambda_T/l_J$. The harmonic theory (blue) agrees well with the full SG model (red) for vanishing $q \to 0$ and large $q \gg 1$ tunneling coupling. In the intermediate regime clear deviations signal the relevance of higher-order correlations. Black dots show the result of the SGPE simulation which clearly reproduce the full nonlinear model. The green diamonds are are the parameter discussed in Section 4.4.

coherence factor

$$C^{(0)}(z) = \frac{\langle \hat{\psi}_{\mathrm{L}}^{\dagger}(z)\hat{\psi}_{\mathrm{R}}(z)\rangle}{\sqrt{\langle|\hat{\psi}_{\mathrm{L}}(z)|^2\rangle\langle|\hat{\psi}_{\mathrm{R}}(z)|^2\rangle}} \simeq \left\langle \exp\left(\mathrm{i}\hat{\theta}_{\mathrm{r}}(z)\right)\right\rangle , \tag{4.1}$$

which quantifies the amount of phase locking between the two condensates [130, 194, 38]. For the approximate equality we again neglected the highly suppressed density fluctuations. For a translation invariant system, Eq. (4.1) is independent of the spatial coordinate $z$ and related to the finite value of the first order coherence function at large separations, $C^{(0)} = \sqrt{C^{(1)}(z,z')|_{|z-z'|\to\infty}}$ (see e.g. (2.82)).

The deviations between the Bogoliubov predictions and the exact result obtained through the transfer matrix formalism signal the need for a description of the system beyond the harmonic approximation (see Fig. 4.1). Hereby, he parameter $q = \lambda_T/l_J$ is the only relevant parameter determining the behavior of local observables [194]. For the Bogoliubov theory this is evident from the analytical solution $C^{(0)} = \exp(-l_J/\lambda_T)$ [130]. This remains valid in the TMF since the expectation value of local observables depends only on the ground state wave function $\Psi_0$ (and not its eigenvalue $\kappa_0$), for which the transfer matrix operator (2.65) can be rescaled, leaving $q$ as the only relevant parameter. In the limit $q \to 0$ the coherence factor approaches zero, because for the decoupled system the phase between the two independent condensates is completely random. For $q \gg 1$ the coherence factor approaches unity. Here the strong hopping between the two condensates locks their relative phase, restricting the dynamics close to the minimum of the cosine potential in the SG Hamiltonian. In both these limits the Bogoliubov theory agrees well with the TMF predictions, as expected from the mTLL approximation of the SG Hamiltonian (see Section 2.2.1). For intermediate values, however, clear deviations arise signaling the relevance of higher-order coupling terms in the effective field theory description.

The fact that local observables only depend on a single parameter allows us to greatly decrease the available parameter space. While non-local observables will show dependence on the independent scales $l_J$ and $\lambda_T$, and for the latter will ultimately break into a dependence of $n_{1D}$ and $T$ once the density decreases and density fluctuations are no longer negligible, the relevance of non-Gaussian fluctuations is predominantly determined by $q$. For the question of non-Gaussianity the parameter space is therefore approximately reduced from $(T, n_{1D}, J)$ to $(\lambda_T, l_J)$ and ultimately only determined by $q$. This has a second advantage, as it is therefore possible to classify experimental measurements through the coherence factor (4.1). While an independent measurement of the thermal coherence length is necessary to fully determine the position of a measurement in the parameter space, and especially the explicit dependence of non-local observables, classification in terms of $q$ enables comparison of different measurements solely through the study of correlation functions.

## 4.2 Correlation Functions in the sine-Gordon Model

Although lower-order correlations are able to determine the breakdown of the Gaussian approximation, little information is gained about the relevant parameters that need to be included in the effective description of the system. Higher-order correlation functions thereby allow for a stringent and statistically significant analysis of the structure and validity of such a coarse-grained model. They thus give valuable information about the relevance of coupling terms in the effective field theory as well as the underlying microscopic model, enabling us, in direct connection to quantum field theoretical calculations, to quantify the influence of non-linear couplings in the effective Hamiltonian order by order. Further, an analysis of their factorization properties is not bound to any theoretical predictions and the validity of theoretical approximations can be tested based only on experimental measurements. In the following, we discuss the general properties of higher-order correlations in the SG model and their connection to quasiparticle interactions before giving a detailed description of their factorization properties that form the basis for their detailed analysis in the remainder of this Chapter.

### 4.2.1 Relation to quasiparticle interactions

Expanding the cosine potential we write the SG Hamiltonian (2.44) as

$$\begin{aligned} H_{\mathrm{SG}} &= \int dz : \left[ g\delta\hat{\rho}_{\mathrm{r}}^2 + \frac{\hbar^2 n_{1D}}{4m}\left(\frac{\partial\hat{\theta}_{\mathrm{r}}}{\partial z}\right)^2 + \hbar\tilde{J}n_{1D}\hat{\theta}_{\mathrm{r}}^2 \right] : - \int dz : \left[ 2\hbar\tilde{J}n_{1D}\sum_{n=2}^{\infty}\frac{(-1)^n}{(2n)!}\hat{\theta}_{\mathrm{r}}^{2n} \right] : \\ &= H_0 + V\,, \end{aligned} \tag{4.2}$$

where we split the Hamiltonian into a free part $H_0$, which is quadratic in the fields, and an interaction part $V = V_4 + V_6 + \ldots$, which contains all higher-order terms. We wrote the Hamiltonian in its normal-ordered form (where all creation operators are to the left, denoted by : :) which leads to a multiplicative renormalization of the coupling $J \to \tilde{J}$, and we dropped an irrelevant constant (see e.g. Ref. [140]). All information about the system is contained in correlations of the form

$$\langle \hat{\theta}(t_1, x_1)\hat{\theta}(t_2, x_2) \cdots \hat{\theta}(t_N, x_N)\rangle \equiv \mathrm{Tr}\left\{\rho_D\, \hat{T}\, \hat{\theta}(t_1, x_1)\hat{\theta}(t_2, x_2) \cdots \hat{\theta}(t_N, x_N)\right\}, \tag{4.3}$$

where $\rho_D$ denotes the density operator specifying the system at a given time, and the trace is taken over the time-ordered product of field operators as indicated by the time-ordering operator $\hat{T}$.

The quadratic Hamiltonian $H_0$ is given by the mTLL model (2.45), whose exact diagonalization within the Bogoliubov quasiparticle basis was discussed in Section 2.2.1. There we argued that in the limiting cases of zero or very strong tunneling coupling $J$ the interaction potential $V$ vanishes, for the latter due to smallness of the fluctuations $\hat{\theta}_\mathrm{r}(z)$. In this approximation direct calculation of the trace in the quasiparticle Fock basis leads to factorization of correlations. This is expected for a free theory since, due to the absence of interactions, only quasiparticle propagation contributes to the correlation functions. This result can be generalized to arbitrary order by use of Wick's theorem for thermal states [187].

The calculation of correlation functions becomes increasingly more complicated for a non-vanishing interaction potential $V$, due to the non-vanishing commutator $[H_0, V]$. In thermal equilibrium, the correlation functions of the phase can be calculated in perturbation theory in the imaginary-time (Matsubara) formalism[2]. One defines the time-ordered correlation functions in imaginary time $\tau$ (Matsubara Green's functions)

$$\langle \hat{T}\hat{\theta}_H(\tau_1, z_1) \ldots \hat{\theta}_H(\tau_N, z_N)\rangle \equiv \frac{\mathrm{Tr}\left[\mathrm{e}^{-\beta H_0}\, \hat{T}\, \mathcal{U}(\beta, 0)\hat{\theta}_I(\tau_1, z_1) \ldots \hat{\theta}_I(\tau_N, z_N)\right]}{\mathrm{Tr}\left[\mathrm{e}^{-\beta H_0}\, \mathcal{U}(\beta, 0)\right]}, \tag{4.4}$$

where $\hat{\theta}_H(\tau, z) = \mathrm{e}^{\tau H_\mathrm{SG}}\hat{\theta}_\mathrm{r}(z)\mathrm{e}^{-\tau H_\mathrm{SG}}$ are the Heisenberg field operators in imaginary time $\tau$, and $\hat{\theta}_I(\tau, z) = \mathrm{e}^{\tau H_0}\hat{\theta}_\mathrm{r}(z)\mathrm{e}^{-\tau H_0}$ are the fields in the interaction picture (denoted by the subscript $I$), evolving in imaginary time with the free Hamiltonian $H_0$. The time evolution operator

[2] Be aware that, in this thesis, we do not anticipate to solve the problem using perturbation theory in any way, and hence do not concern ourselves with the inevitable problems of divergencies occurring in the perturbative expansion, and their solutions using well-established field-theoretical tools as resummation, renormalization, and summation of divergent series. For details of the presented methods see any book on (statistical) field theory, e.g. [83, 187].

$\mathcal{U}(\beta, 0)$ fulfills

$$\partial_\tau \mathcal{U}(\tau, 0) = -V_I(\tau)\mathcal{U}(\tau, 0) \,, \tag{4.5}$$

whose solution can, e.g. , be written as the Dyson series [187]

$$\mathcal{U}(\tau, \tau') = \hat{T} \mathrm{e}^{-\int_{\tau'}^{\tau} \mathrm{d}\tau'' V_I(\tau'')} = \sum_{n=0}^{\infty} \frac{(-1)^n}{n!} \int_{\tau'}^{\tau} \mathrm{d}\tau_1 \cdots \int_{\tau'}^{\tau} \mathrm{d}\tau_n \, \hat{T} \, V_I(\tau_1) \dots V_I(\tau_n) \,. \tag{4.6}$$

Therewith correlation functions (4.4), up to any order in $V_I$, are expressed through a diagrammatic expansion in Feynman diagrams [83, 187].

The sine-Gordon Hamiltonian, Eq. (4.2), represents a scalar field theory with an infinite number of polynomial interaction terms. Standard results of quantum field theory allow to distinguish between three distinct types of diagrams. First, all diagrams in which the fields of the interaction potential $V$ are contracted among themselves and are otherwise disconnected (vacuum diagrams). These vacuum diagrams are exactly canceled by the denominator in Eq. (4.4) to all orders in the perturbative expansion. Second, all diagrams which are not fully connected only contribute to the disconnected part of the correlation function, and can be factorized into full, lower-order correlation functions. Third, the fully connected diagrams describe genuine $N$-body quasiparticle interactions and constitute the connected part of the correlation function.

The above time-ordered imaginary-time correlation functions are only directly related to physical observables for equal times $\tau_1 = \cdots = \tau_N$, for which they coincide with the equal time correlation functions discussed in this thesis[3]. However, the Matsubara Green's functions may be analytically continued to the real-time axis to determine the physically relevant real time correlation functions (4.3).

Since the correlation functions in thermal equilibrium become time-translation invariant, employing a Fourier transformation with respect to times, one can represent the $N^{\text{th}}$-order correlation as

$$\langle \hat{\theta}(t_1, x_1) \cdots \hat{\theta}(t_N, x_N) \rangle = \int \frac{d\omega_1}{2\pi} \cdots \frac{d\omega_N}{2\pi} \, e^{i(\omega_1 t_1 + \cdots + \omega_N t_N)} \, 2\pi \, \delta(\omega_1 + \cdots + \omega_N) \\ G^{(N)}(\omega_1, \dots, \omega_{N-1}; x_1, \dots, x_N) \,. \tag{4.7}$$

Here $G^{(N)}(\omega_1, \dots, \omega_{N-1}; x_1, \dots, x_N)$ denotes the $N^{\text{th}}$-order correlation amplitude with external frequencies $\omega_i$ at spatial points $x_i$, for $i = 1, \dots, N$. Diagrammatically, they can be represented

[3] Note that, in general, the limit $\tau_1, \dots, \tau_N \to \tau$ needs to be taken with care as the time-ordered Matsubara Greens-functions might be discontinuous at equal times, due to non-vanishing commutators [187]. Since, for the correlations considered here, the equal-time commutator vanishes no further problems occur in taking the equal-time limit.

as:

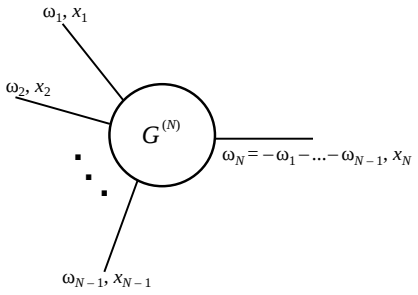


The 4th-order amplitude $G^{(4)}(\omega_1, \omega_2, \omega_3; x_1, x_2, x_3, x_4)$, for instance, describes all possible quantum processes with $|\omega_i|$ injected ($\omega_i > 0$) or taken out ($\omega_i < 0$) at points $x_i$ for $i = 1, 2, 3$ such that the total energy is conserved with $-\omega_1 - \omega_2 - \omega_3$ at $x_4$. For two-body interactions and the case of a real scalar field, this involves standard scattering processes with Feynman diagrams having two incoming and two outgoing lines, but also diagrams with one line in and three lines out, the conjugate process (three in, one out), or even all lines in (or all lines out).

From the Fourier representation (4.7) one observes that an $N^{\text{th}}$-order equal-time correlation function ($t = t_1 = t_2 = \cdots = t_N$) represents the sum over all the different processes with $N$ external lines

$$\langle \hat{\theta}(t, x_1) \cdots \hat{\theta}(t, x_N) \rangle = \int \frac{d\omega_1}{2\pi} \cdots \frac{d\omega_{N-1}}{2\pi} \, G^{(N)}(\omega_1, \ldots, \omega_{N-1}; x_1, \ldots, x_N) \,. \tag{4.8}$$

More precisely, equal-time correlation functions for bosonic fields measure the symmetrized (anti-commutator) part of the time-ordered correlators (4.3). For the real scalar field operator considered here, this can be directly observed from the definition of the time-ordering operator, as e.g. for the 2nd-order correlation:

$$\begin{aligned} \langle \hat{T} \hat{\theta}(t_1, x_1) \hat{\theta}(t_2, x_2) \rangle &= \langle \hat{\theta}(t_1, x_1) \hat{\theta}(t_2, x_2) \rangle \Theta(t_1 - t_2) + \langle \hat{\theta}(t_2, x_2) \hat{\theta}(t_1, x_1) \rangle \Theta(t_2 - t_1) \\ &= \frac{1}{2} \langle \big\{ \hat{\theta}(t_1, x_1), \hat{\theta}(t_2, x_2) \big\} \rangle + \frac{1}{2} \langle \big[ \hat{\theta}(t_1, x_1), \hat{\theta}(t_2, x_2) \big] \rangle \, \mathrm{sgn}(t_1 - t_2) \,. \end{aligned}$$

Here the step function is defined by $\Theta(t > 0) = 1$ and $\Theta(t < 0) = 0$ and the sign function is $\mathrm{sgn}(t) \equiv \Theta(t) - \Theta(-t)$. Since the equal-time commutator vanishes, $[\hat{\theta}(t, x_1), \hat{\theta}(t, x_2)] = 0$ for the real scalar field operator, the symmetrized part is given by the anti-commutator $\{\hat{\theta}(t_1, x_1), \hat{\theta}(t_2, x_2)\} \equiv \hat{\theta}(t_1, x_1)\hat{\theta}(t_2, x_2) + \hat{\theta}(t_2, x_2)\hat{\theta}(t_1, x_1)$ at equal times $t_1 = t_2$.

Since the experimentally measured phase fields are linear in the quasiparticle creation/annihilation operators, $N^{\text{th}}$-order correlation functions are a direct measure of the combined effect of the $N$-body quasiparticle interaction (to all orders in the coupling). This allows for a direct comparison to highly non-trivial field-theoretical calculations, and gives

valuable information about the convergence of the perturbative expansion, the validity of non-perturbative theoretical methods, and the summation of divergent series. Measurements of equal-time correlation functions represent a powerful tool to quantify the combined effect of all possible quantum processes that contribute to an $N^{\text{th}}$-order correlation — no matter how high the order of a process in terms of powers of Planck's constant $h$ may be, or whether the contribution is of non-perturbative origin.

### 4.2.2 Phase Correction and Full Distribution Functions

Since the phase field is defined on a circle $S^1$ care has to be taken when evaluating the path integral where the topological constraints need to be taken into account. The integration over all possible paths on the circle is consequently replaced by a the sum over all paths resulting in the same action [195], for which the phase is smoothly extended to the interval $(-\infty, \infty)$ and the final point is summed over all periodic repetitions in order to ensure the cyclic invariance of the phase correlations.

This phase correction can also be understood by realizing that the phase $\theta_{\text{r}}(z)$ itself is not a uniquely defined physical observable, but is only defined modulo $2\pi$. Consequently, in the experiment, matter-wave interferometry only allows us to determine the phase up to $\pm 2\pi n$, where $n \in \mathbb{Z}$. This corresponds to the degenerate vacuum states of the SG model, where the Hamiltonian is invariant under a shift $\hat{\theta}_{\text{r}} \to \hat{\theta}_{\text{r}} \pm 2\pi n$. The phase differences

$$\varphi(z, z') = \hat{\theta}_{\text{r}}(z) - \hat{\theta}_{\text{r}}(z') \,, \tag{4.9}$$

however, are, after the phase has been smoothly extended to the interval $(-\infty, \infty)$, a well defined observable. The extension of the phase, as was considered in [160], is depicted in Fig. 4.2. The phase field $\theta_{\text{r}}(z)$ is shifted to remove the unphysical jumps across the boundary, which occur when the phase has wrapped once around the circle $S^1$. Practically

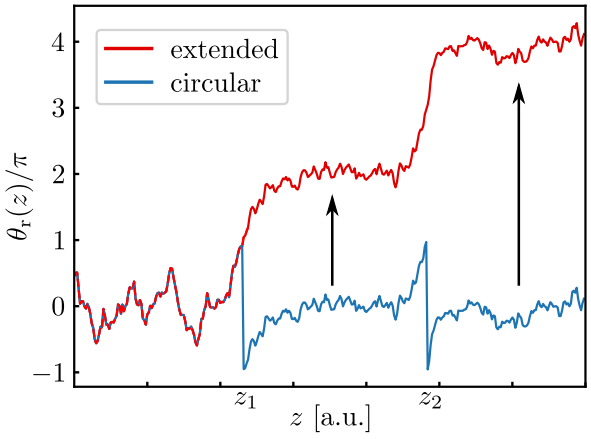


Fig. 4.2 Correction of the phase profile. Depicted is the correction performed to obtain unbound phase differences. The original phase profile (blue) crosses the boundary twice at $z_1$ and $z_2$, visible in the instantaneous jump of $2\pi$. Shifting the phase by $\theta_{\text{r}}(z) \to \theta_{\text{r}}(z) + 2\pi\,(4\pi)$ for $z > z_1\,(z > z_2)$ leads to the smooth, unbound phase (red) free of any kinks. Solitons are unaffected by the correction, and are clearly visible in the extended phase profile.

this is done by enforcing that neighboring points on the spatial grid have a phase difference $|\theta_\mathrm{r}(z) - \theta_\mathrm{r}(z + \Delta z)| \leq \pi$. This leads to a well defined hydrodynamic velocity field $v \sim \partial_z \theta_\mathrm{r}$, free of any poles. By considering phase differences the remaining global ambiguity of $2\pi n$ for the phase field is eliminated.

The advantage of this extended phase scheme is two-fold and is best illustrated by considering the full distribution functions (FDFs) of phase differences. These probability distributions contain all information about the higher order correlation functions, and are given by the Boltzmann weight $\exp(-\beta H)$ after integrating out the remaining, completely decoupled degrees of freedom. The difference of the FDFs before and after the smooth extension of the phase profile is shown for two distinct cases in Fig. 4.3.

The distribution function for the uncorrected phase differences is, as the phase itself, only defined on the circle $S^1$. In case of a free field theory it takes the form of a wrapped normal distribution [196]. Expectation values are only well defined for periodic (circular) observables, which, as we will explicitly show below, has disadvantages when considering the factorization properties of higher-order correlations. The FDF of phase differences calculated from the corrected phase field, are not limited by the periodicity of the observables and reveal the Gaussian distribution expected for a free field theory.

Further, as discussed in Section 2.2.2, the SG model has solitonic solutions, which represent a localized rotation of the phase by $2\pi$. The wrapped distribution of the uncorrected phase profile is only sensitive to the localized rotation of the phase, and not the absolute change of $2\pi$ due to the connection of two minima in the SG potential. Circular observables are hence far less sensitive to these highly non-linear field configurations, as they cannot distinguish between the degenerate vacuum states of the SG model. In the presented example of three shifted Gaussian distributions the wrapped distribution is approximately Gaussian, masking the highly non-Gaussian fluctuations of the phase. In the FDFs for the corrected phase profiles the degenerate vacuum states become clearly separable, due to the removal of unphysical jumps[4].

FDFs present a powerful method to compare the combined results of higher-order correlations. They contain valuable information of the shot-to-shot fluctuations. FDFs have previously been used in the context of full counting statistics of the measured contrast of interference fringes in the interference of two one-dimensional Bose gases [197–199] and were used to determine the relaxation of the system to a prethermalized state [13, 200]. While all information about the state is contained in the FDFs, studying its correlations and especially their factorization properties reveals, order by order and independent of any theoretical predictions, the relevance of contributions that drive the system beyond the harmonic regime.

[4]Note that solitons always have a finite width and hence are not removed in the phase correction as long as their width is larger than the spatial resolution.

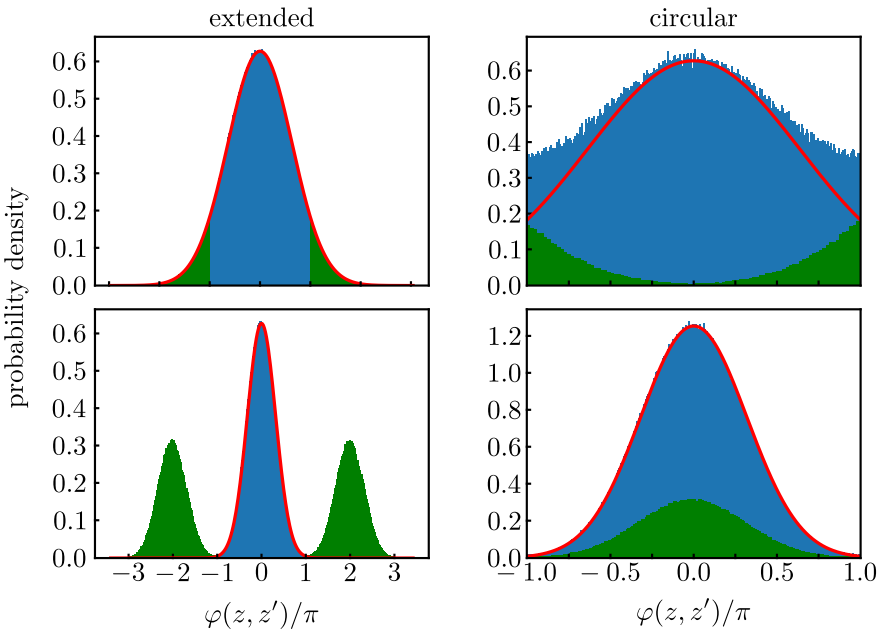


Fig. 4.3 Schematic comparison of full distribution functions for phase differences of the circular and corrected phase profiles. The green area depicts fluctuations outside the bound interval $[-\pi, \pi)$ which for the circular distributions are folded back in the central region. Upper row: For large Gaussian fluctuations of the unbound phase field (left) representing a free field theory the circular distributions (right) are distinctly non-Gaussian. Lower row: In case of a mixture distribution of the unbound phase field representing solitonic excitations, the circular distribution is approximately Gaussian. The two examples clearly show, how FDFs of the circular phase distort the notion of Gaussian phase fluctuations and hence the direct connection to quasiparticle interactions.

### 4.2.3 Phase Correlation Functions

We define the $N^{\text{th}}$-order[5] phase correlation function for the corrected phase differences

$$\mathcal{G}^{(N)}(\mathbf{z}, \mathbf{z}') = \langle \varphi(z_1, z_1') \dots \varphi(z_N, z_N') \rangle \,, \tag{4.10}$$

with coordinates $\mathbf{z} = (z_1, \dots, z_N)$ and $\mathbf{z}' = (z_1', \dots, z_N')$ along the length of the system. The first-order correlation function, as well as all other correlation functions where $N$ is an odd positive integer, vanish by symmetry. While all information is contained in the $N^{\text{th}}$-order correlation function it is more insightful to consider their decomposition in connected and disconnected parts

$$\mathcal{G}^{(N)}(\mathbf{z}, \mathbf{z}') = \mathcal{G}^{(N)}_{\text{con}}(\mathbf{z}, \mathbf{z}') + \mathcal{G}^{(N)}_{\text{dis}}(\mathbf{z}, \mathbf{z}') \,. \tag{4.11}$$

[5]The correlation function is actually dependent on $2N$ spatial points, however still of $N^{\text{th}}$ order in the field operators $\varphi$ and/or $\hat{\theta}_{\text{r}}$

This separates the genuine new information at this order $\mathcal{G}^{(N)}_{\text{con}}$ from the redundant information contained in lower-order correlations $\mathcal{G}^{(N)}_{\text{dis}}$. We introduced the disconnected correlation functions as the sum over all possible combinations of correlations with a total of $N$ external lines containing at least two completely disconnected Feynman diagrams. This defines, through Eq. (4.11) and simple combinatorics, the general formula for the connected part [196]

$$\mathcal{G}^{(N)}_{\text{con}}(\mathbf{z},\mathbf{z}') = \sum_{\pi} (|\pi|-1)!\,(-1)^{|\pi|-1} \prod_{B\in\pi} \left\langle \prod_{i\in B} \varphi(z_i, z_i') \right\rangle. \tag{4.12}$$

Here, the sum runs over all possible partitions $\pi$ of $\{1,\ldots,N\}$ with $|\pi|$ the number of parts in the partition, the first product runs over all blocks $B$ of the partition and the second product over all elements $i$ of the block. It is possible to simplify Eq. (4.12) by using central moments, i.e. shifting $\varphi \to \varphi - \langle\varphi\rangle$, thereby eliminating all terms containing the first-order correlation function. Connected correlation functions are also called cumulants or, in a generalized form, semi-invariants [196]. For our system the sum is further simplified as only correlation functions where $N$ is an even positive integer contribute, which leads to $\mathcal{G}^{(2)}_{\text{con}}(\mathbf{z},\mathbf{z}') = \mathcal{G}^{(2)}(\mathbf{z},\mathbf{z}')$ and, e.g., for the 4$^{\text{th}}$-order connected correlation function:

$$\begin{aligned}\mathcal{G}^{(4)}_{\text{con}}(\mathbf{z},\mathbf{z}') = \mathcal{G}^{(4)}(\mathbf{z},\mathbf{z}') &- \langle\varphi(z_1,z_1')\varphi(z_2,z_2')\rangle\langle\varphi(z_3,z_3')\varphi(z_4,z_4')\rangle \\ &- \langle\varphi(z_1,z_1')\varphi(z_3,z_3')\rangle\langle\varphi(z_2,z_2')\varphi(z_4,z_4')\rangle \\ &- \langle\varphi(z_1,z_1')\varphi(z_4,z_4')\rangle\langle\varphi(z_2,z_2')\varphi(z_3,z_3')\rangle\,.\end{aligned} \tag{4.13}$$

Whenever not explicitly stated otherwise, we will in this thesis always assume vanishing odd-order correlation functions in the decomposition into connected and disconnected parts[6]. Higher-order connected correlation functions are easily obtained through Eq. (4.12), since they become rather cumbersome we will not show their explicit form here.

For Gaussian states, all higher-order connected correlation functions ($N > 2$) vanish, i.e. $G^{(N>2)}_{\text{con}}(\mathbf{z},\mathbf{z}') \equiv 0$. Hence, all correlation functions factorize and one recovers Wick's theorem [83] stating that, for a Gaussian state, all correlation functions with ($N > 2$) are determined by second-order correlations. Explicitly, the Wick decomposition is given by

$$G^{(N)}_{\text{wick}}(\mathbf{z},\mathbf{z}') = \sum_{\pi_2} \left[ \prod_{B\in\pi_2} \langle\varphi(z_{B_1}, z'_{B_1})\varphi(z_{B_2}, z'_{B_2})\rangle \right]. \tag{4.14}$$

[6]Note however that in the numerical evaluation of connected correlation functions we always use the general formula Eq. (4.12) containing all orders of correlation functions. This is especially advantageous if odd-order correlation retain a finite, but always small, value due to limited statistics or experimental noise

Here the sum runs over all possible partitions $\pi_2$ of $\{1,\dots,N\}$ into blocks of size 2. The product again runs over all blocks $B$ of the partition (see [196]).

Choosing coordinates $z \equiv z_1 = z_2 = \ldots = z_N$ and $z' \equiv z'_1 = z'_2 = \ldots = z'_N$, the above formulas simplify as we are considering only correlations which are powers of a single random variable $\varphi = \varphi(z, z')$. Here we suppress the spatial argument to shorten the notation, as we will do in the following whenever all spatial arguments are the same. In this case, the $N^{\text{th}}$-order connected correlation function can be determined by the recursion formula

$$\mathcal{G}^{(N)}_{\text{con}}(z,z') = \mathcal{G}^{(N)}(z,z') - \sum_{m=1}^{N-1} \binom{N-1}{m-1} \mathcal{G}^{(m)}_{\text{con}}(z,z')\mathcal{G}^{(N-m)}(z,z') \,. \tag{4.15}$$

Specifically for the lowest orders we get

$$\begin{aligned} \mathcal{G}^{(2)}_{\text{con}}(z,z') =& \langle\varphi^2\rangle \,, \\ \mathcal{G}^{(4)}_{\text{con}}(z,z') =& \langle\varphi^4\rangle - 3\langle\varphi^2\rangle^2 \,, \\ \mathcal{G}^{(6)}_{\text{con}}(z,z') =& \langle\varphi^6\rangle - 15\langle\varphi^4\rangle\langle\varphi^2\rangle + 30\langle\varphi^2\rangle^3 \,. \end{aligned} \tag{4.16}$$

For a Gaussian state, we get from Wick's theorem

$$G^{(N)}_{\text{wick}}(z,z') = \langle\varphi^2\rangle^{N/2}(N-1)!! \,, \tag{4.17}$$

where $(\dots)!!$ is the double factorial. These simplified formulas will be helpful in the next section, where we discuss the factorization properties of commonly used periodic observables.

### 4.2.4 Periodic Correlation Functions

We extend upon the previously defined coherence factor $C^{(0)}$ and first order coherence function $C^{(1)}$ by defining the general $N^{\text{th}}$-order periodic correlation function [15]

$$C^{(N)}(\mathbf{z},\mathbf{z}') = \frac{\langle \hat{\psi}_{\text{L}}(z_1)\hat{\psi}^\dagger_{\text{R}}(z_1)\hat{\psi}^\dagger_{\text{L}}(z'_1)\hat{\psi}_{\text{R}}(z'_1)\dots\hat{\psi}_{\text{L}}(z_N)\hat{\psi}^\dagger_{\text{R}}(z_N)\hat{\psi}^\dagger_{\text{L}}(z'_N)\hat{\psi}_{\text{R}}(z'_N)\rangle}{\sum_{n=1}^{N}\sqrt{\langle|\hat{\psi}_{\text{L}}(z_n)|^2\rangle\langle|\hat{\psi}_{\text{R}}(z_n)|^2\rangle\langle|\hat{\psi}_{\text{L}}(z'_n)|^2\rangle\langle|\hat{\psi}_{\text{L}}(z'_n)|^2\rangle}} \,. \tag{4.18}$$

These correlations do not rely on the correction of the phase profile and are therefore simpler to calculate from experimental or numerical data.

In order to isolate the contributions of $N$-body quasiparticle interactions to $C^{(N)}$ we seek a functional relation to the connected correlation functions of the relative phase $\mathcal{G}^{(N)}$, extending beyond the commonly used harmonic approximation. Defining the random variable

$\Phi_N(\mathbf{z},\mathbf{z}') = \sum_{i=1}^{N} \varphi(z_i, z_i')$ the $N^{\text{th}}$-order periodic correlation function can be written as

$$C^{(N)}(\mathbf{z},\mathbf{z}') \simeq \left\langle \exp\left(\mathrm{i}\Phi_N(\mathbf{z},\mathbf{z}')\right)\right\rangle . \tag{4.19}$$

We again neglected the highly suppressed density fluctuations, for which the correlations (4.19) are equivalent to vertex operators of the SG model [84]. Using Eq. (4.15) the cumulant generating functional $K_N(\lambda)$ for the random variable $\Phi_N$ is

$$K_N(\lambda) = \mathrm{Ln}\left(\left\langle \mathrm{e}^{\mathrm{i}\lambda\Phi_N}\right\rangle\right) = \exp\left(\sum_{m=1}^{\infty} \frac{(-\lambda)^m}{(2m)!}\left\langle \Phi_N^{2m}\right\rangle_{\text{con}}\right) . \tag{4.20}$$

Realizing that $K_N(1) \equiv C^{(N)}$ determines, by use of the multi-linearity of joint cumulants[7], the desired connection between the periodic correlation functions and $\mathcal{G}^{(N)}$. As again the formulas get increasingly cumbersome with the number of spatial coordinates, we give here only the explicit formula for the first-order coherence function

$$C^{(1)}(\mathbf{z},\mathbf{z}') = \exp\left(\sum_{m=1}^{\infty} \frac{(-1)^m}{(2m)!}\mathcal{G}_{\text{con}}^{(2m)}(\mathbf{z},\mathbf{z}')\right) . \tag{4.21}$$

Periodic correlation functions are not directly related to $N$-body interactions of quasiparticles and even the first-order correlation function contains contributions arising from $N$-body quasiparticle interaction up to arbitrary order $N$ in a non-simple way.

Corresponding to free quasiparticle propagation the harmonic approximation truncates the above sum at $m = 1$,

$$C_{\text{wick}}^{(1)}(\mathbf{z},\mathbf{z}') = \exp\left[-\frac{1}{2}\left\langle \varphi(\mathbf{z},\mathbf{z}')^2\right\rangle\right] , \tag{4.22}$$

[7] The general formula

$$\left\langle (X+Y)^n \right\rangle_{\text{con}} = \sum_{j=0}^{n} \binom{n}{j} \left\langle \underbrace{X,\ldots,X}_{j}, \underbrace{Y,\ldots,Y}_{n-j} \right\rangle_{\text{con}}$$

is easily extended to an arbitrary sum of random variables $X, Y, \ldots$. For $\Phi_N = \sum_{i=1}^{N} \varphi(z_i, z_i')$ this relates $\langle \Phi^n \rangle_{\text{con}}$ to the correlations of the phase $\mathcal{G}^{(N\leq n)}$

Due to the periodicity and the resulting restricted (finite) domain of these correlation functions the correct Wick decomposition of periodic higher-order correlations thereby takes the form

$$C^{(N)}_{\mathrm{wick}}(\mathbf{z},\mathbf{z}') = \frac{\prod_{m,n=1}^{N} C^{(1)}_{\mathrm{wick}}(z_m, z'_n)}{\prod_{1\le m,n\le N}^{m<n} C^{(1)}_{\mathrm{wick}}(z_m, z_n) C^{(1)}_{\mathrm{wick}}(z'_m, z'_n)} \,. \tag{4.23}$$

## 4.3 Equilibrium Results and Factorization

We begin our analysis of higher-order correlation functions in the thermal equilibrium state for two coupled quantum wires. Our system is a Bose gas of $^{87}$Rb atoms, cooled in a static double well potential with an adjustable barrier (see Section 2.2). Tunneling through the barrier leads to a linear coupling $J$ between the two 1D systems. This allows us to tune the coupling constant of the cosine potential entering the SG Hamiltonian, and therewith the relevance of non-Gaussian fluctuations. Matter wave interferometry gives direct access to the spatially resolved relative phase between the two condensates. This corresponds to the fundamental field $\hat{\theta}_{\mathrm{r}}(z)$ of the effective field theory, which allows us to directly calculate higher-order correlation functions in analogy to theoretical calculations in quantum field theory. The expectation value is calculated by averaging over 290 . . . 2800 (typically 1000) experimental measurements. By adjusting the double-well barrier we explore different regimes of the SG model and determine the relevance of higher-order connected correlation functions.

We show in Fig. 4.4 the 4$^{\mathrm{th}}$ order correlation function $\mathcal{G}^{(4)}(\mathbf{z},\mathbf{z}')$ as well as its decomposition into disconnected $\mathcal{G}^{(4)}_{\mathrm{dis}}(\mathbf{z},\mathbf{z}')$ and connected $\mathcal{G}^{(4)}_{\mathrm{con}}(\mathbf{z},\mathbf{z}')$ parts for different values of the phase locking strength $q$. For uncoupled ($q = 0$) and strongly coupled ($q = 6.1$) condensates we find complete factorization of the correlation function according to Eq. (4.11). The connected part completely vanishes and all information is contained in the second-order correlation functions, determining the disconnected part $\mathcal{G}^{(4)}_{\mathrm{dis}}(\mathbf{z},\mathbf{z}')$ of the correlation function.

This means that the system is well described by a set of non-interacting quasiparticles and higher-order couplings in the Hamiltonian become irrelevant. For vanishing tunneling coupling $J$ the factorization would be expected on the level of the effective field theory, as the SG model reduces to the quadratic TLL model. However, even in this regime, we neglected an infinite series of higher-order coupling terms in the perturbative expansion of the microscopic Hamiltonian (2.38) to arrive at the TLL model. The validity of these approximations is confirmed by the observed factorization of higher-order correlations. The factorization for large $q$ is a non-trivial result even on the level of the effective field theory itself and explicitly confirms the irrelevance of higher-order couplings in the SG Hamiltonian.

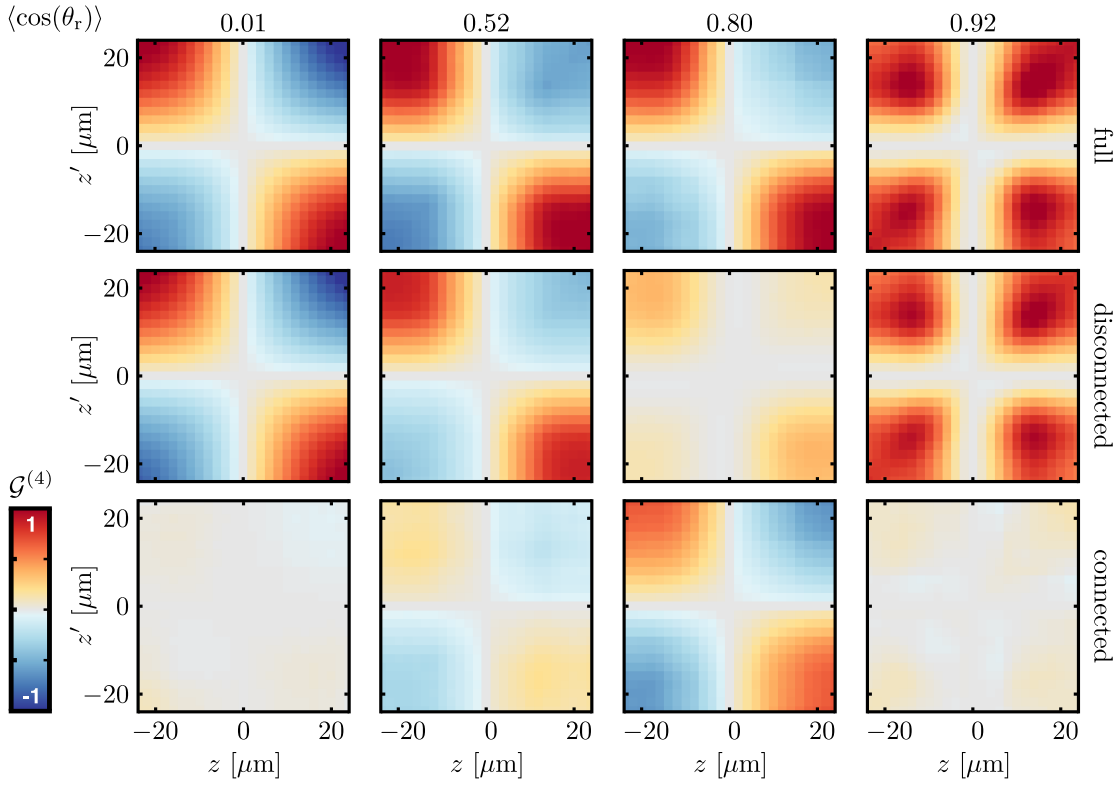


Fig. 4.4 Experimental factorization of the 4th-order correlation $\mathcal{G}^{(4)}(\mathbf{z}, \mathbf{z}')$ into connected and disconnected parts. The increase in the tunneling coupling is quantified through the increasing coherence factor $\langle\cos(\theta_r)\rangle$. We randomly chose $z_3 = -z_4 = 14\,\mu$m and $\mathbf{z}' = 0$ to visualize the high dimensional data. For vanishing and strong tunneling ($\langle\cos(\theta_r)\rangle = 0.01, 0.92$) the connected part $\mathcal{G}^{(4)}_{\text{con}}$ vanishes and all information is contained in the lower order correlations. The system is therefore in a Gaussian state, described by non-interacting quasiparticles. We hence found the degrees of freedom that diagonalize the Hamiltonian. For intermediate tunneling coupling a significant connected part remains, revealing the non-Gaussian fluctuations of the relative phase field. Figure adapted from [160].

The complete factorization of higher-order correlation functions, even without knowledge about the underlying theoretical model, shows that we have found the degrees of freedom within which the system can be described by a free field theory. Therefore, based only on factorization properties of experimental correlation functions, the structure of the effective Hamiltonian is determined to take the form of the mTLL model. This explicitly shows that a vast number of possibly irrelevant operators renormalize to zero in the low-energy theory describing thermal equilibrium.

When the tunneling coupling is tuned to an intermediate regime, a significant connected part remains and the relative phase field in thermal equilibrium exhibits non-Gaussian fluctuations. The system is therefore no longer solely described by free quasiparticle propagation. The observed connected part of the 4th order correlation function is a direct result of the

combined effect of two-body quasiparticle interactions, which therefore remains a relevant coupling and hence cannot be neglected in the low-energy description of the system.

For a quantitative comparison of the relevance of higher-order connected correlation functions, we turn to spatially averaged observables, taking into account the full $4^{\text{th}}$ order connected correlations. The relevance of the connected correlation function is usually measured by comparing its local value to the disconnected part of the correlation function. Due to experimental noise it is however advantageous to determine the relevance of connected higher-order correlation in comparison to the full correlation and compare global, i.e. spatially integrated, values rather than a local comparison of $\mathcal{G}^{(N)}_{\text{con}}$ and $\mathcal{G}^{(N)}$. To mitigate this problem, we therefore define the measure

$$M^{(N)} = \frac{\sum_{\mathbf{z}} |\mathcal{G}^{(N)}_{\text{con}}(\mathbf{z}, \mathbf{0})|}{\sum_{\mathbf{z}} |\mathcal{G}^{(N)}(\mathbf{z}, \mathbf{0})|} \,. \tag{4.24}$$

The absolute value is introduced because for phase differences of the extended phase the sign of the correlation function depends on the fixed coordinates (see the cross structure in Fig. 4.4). While a locally defined measure $\mathcal{G}^{(N)}_{\text{con}}(\mathbf{z}, \mathbf{0})/\mathcal{G}^{(N)}(\mathbf{z}, \mathbf{0})$ is always positively defined, positive and negative parts of the correlation cancel one another in Eq. (4.24) since the integration over the connected and full correlation is performed separately. Note that due to the absolute value in Eq. (4.24), the measure is not an unbiased estimator of the connected correlation function calculated from the true probability distribution. Considering, e.g. , a finite random sample drawn from a Gaussian distribution higher-order connected correlations fluctuate around zero and summing over their absolute values leads to a non-zero measure $M^{(N)}$.

We compare the results for the experimental data with predictions of the SG model, solved exactly for a homogeneous system in the classical limit by use of the TMF explained in Section 2.3.3. As we are now interested in non-local observables, the second relevant scale $\lambda_T = 15 \ldots 20\,\mu$m must be determined independently through speckle patterns in time of flight [201]. We determine the solution in the TMF through the stochastic Îto process (2.66), completely defined by the two scales $q$ and $\lambda_T$ and only dependent on the ground state solution of the corresponding Mathieu equation (see Section 2.3.3). We further take into account the finite experimental resolution by convolution of the unbound phase field[8] with a Gaussian PSF of measured standard deviation $\sigma_{\text{PSF}} = 3\,\mu$m.

Practically, a single realization of the phase field is calculated by sampling an initial value of the phase from the equilibrium distribution (2.58), calculating the evolution in space

[8]Note that the correction for unphysical jumps is essential here, as due to the convolution these jumps acquire a finite width. They therefore become fictitious solitons in the phase profile, drastically altering the results.

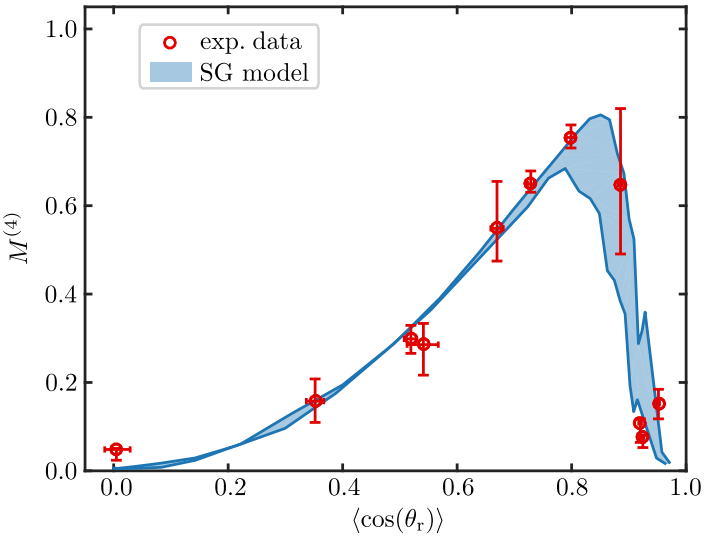


Fig. 4.5 Relative size of the 4th-order connected correlations in thermal equilibrium. Red dots are the integral measure $M^{(4)}$ (Eq. (4.24)) calculated from the experimental data for different phase locking strengths $\langle\cos(\theta_r)\rangle$. The measure quantifies the size of the connected correlations $\mathcal{G}^{(4)}_{\text{con}}$ as compared to the full correlation $\mathcal{G}^{(4)}$. The experimental data is in good agreement with the theoretical predictions of the SG model, calculated using the TMF (2.66). For intermediate phase locking a significant part of the correlation $\mathcal{G}^{(4)}$ is given by the connected part. The shaded area depicts the estimated spread of the experimental parameters. The errorbars represent the 80% confidence interval calculated by bootstrapping [202]. Figure adapted from [160].

according to the Îto equation (2.66) on a discrete spatial grid[9], and finally convolving the phase profile with the Gaussian PSF. The correlation functions are calculated by averaging over typically $10^5$ independently sampled field configurations.

In Fig. 4.5 the dependence of $M^{(4)}$ is shown for increasing tunneling coupling $J$, quantified through the experimentally measured coherence factor $\langle\cos(\theta_r)\rangle$ (c.f. Eq. (4.1) for vanishing odd order correlations) calculated at the center of the longitudinal trapping potential. The theoretical predictions for the SG model are calculated for the measured spread of the thermal coherence length $\lambda_T$, and are in excellent agreement with the experimental observation over the full range of parameters. The finite value for $\langle\cos(\theta_r)\rangle \approx 0$ in the experiment is due to the finite statistics and the above explained bias of the measure (4.24). For the experimental data, only the central, nearly homogeneous[10], part of the cloud is used for the analysis. We can therefore neglect the spatial dependence of $q$ due to the spatially dependent bulk density $\rho_0(z)$.

[9] Depending on the spatial resolution of the grid the stochastic propagation in space is performed on a finer grid to achieve numerical convergence of (2.66)

[10] The density variation within this region is $\approx 25\%$, which is similar to the considered spread in $\lambda_T$

Here, direct comparison of the experimental system to its predicted effective field theory provides stringent proof for the validity of the low-energy description. It is important to remember, that for the presented analysis only one parameter, $\lambda_T$, has to be measured independently. Comparison to the theoretical predictions is otherwise solely performed on the level of measured correlation functions.

Measuring and calculating higher-order connected correlation functions, $N > 4$, is an experimentally and computationally much more challenging task. Firstly, statistically significant results demand an ever increasing number of realizations. Secondly, the computational demand scales enormously with the order of the correlation. The number of partitions in Eq. (4.12) is given by the Bell number[11] [196]. Further the dimension of the $N^{\text{th}}$ order correlation is $n_{\text{g}}^N$ for a given spatial grid of $n_{\text{g}}$ points. These numbers can be reduced by use of central moments, which reduces the Bell number as sets of length one do not contribute, and exploiting the symmetry of the correlation function, which is a fully symmetric tensor and hence has $\binom{n_{\text{g}}+N-1}{N}$ unique elements. Nonetheless, we still had to reduce the number of points considered in the integral measure (4.24), and consider only every second, third, and fourth point for $N = 6, 8$ and 10 respectively.

A comparison of these connected higher-order correlations is shown in Fig. 4.6. For increasing $N$ deviations occur, which are explained by the finite statistics of the experiment and the biased estimator Eq. (4.24). Note that while higher-order correlations become irrelevant for small coherence factors $\langle\cos(\theta_{\text{r}})\rangle \lesssim 0.2$, they retain a significant contribution to the full correlation function in the intermediate regime, such that in terms of the free quasiparticles the system represents a strongly interacting field theory (see Section 4.2.1). We emphasize that the experimentally measured higher-order cumulants give access to information about $N$-particle interactions, within a given basis, beyond perturbation theory, and do not rely on the smallness of the coupling constants.

The commonly used periodic correlations $C^{(N)}$ are not well suited for the presented analysis of higher-order correlations. While for Gaussian fluctuations a form of Wick's theorem can be recovered by use of the correct factorization relation (4.23), in a non-Gaussian theory even the second-order correlation $C^{(2)}$ receives contributions of higher-order connected correlations $\mathcal{G}^{(N)}_{\text{con}}$ up to arbitrary order $N$. The fact that $\mathcal{G}^{(N)}_{\text{con}}$ enters in an alternating series masks the relevance of higher-order corrections, e.g. for the first-order coherence function (4.21) where in the strongly correlated, intermediate coupling regime long-range order is restored through a detailed canceling of higher-order connected correlations. This is in contrast to the Bogoliubov predictions, where the long-range order is connected to the amplitude of two-point correlations of the relative phase.

[11] The first few Bell numbers are $B_N = 2, 15, 203, 4140, 115975, 4213597$ for $N = 2, 4, \ldots 12$

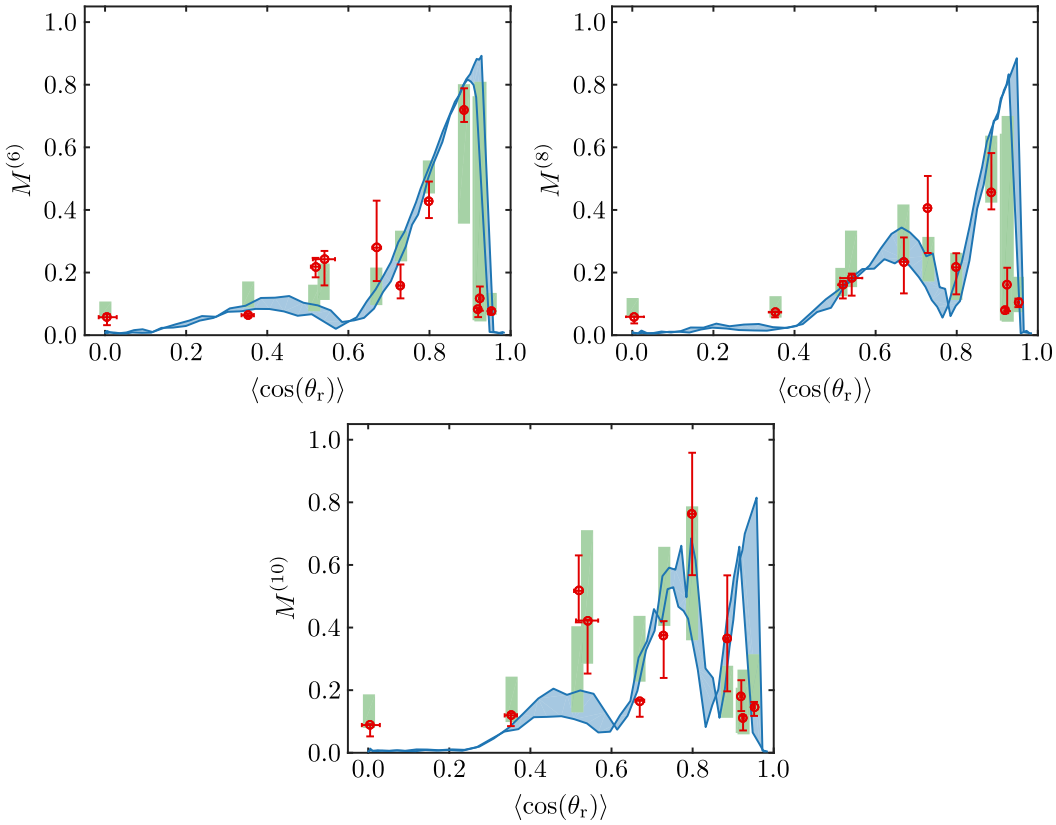


Fig. 4.6 Integral measure $M^{(N)}$ for higher-order correlations $N = 6, 8, 10$. Th experimental data is given by the red dots with the errorbars representing the 80% confidence intervals calculated by using bootstrapping [202]. The theoretical predictions of the SG model for a large sample size ($10^5$ realizations) is given by the blue shaded region, while the green bars represent the results of the TMF for the experimental sample size. The latter are in good agreement with the experimental data up to $10^{\text{th}}$-order correlations. Note, in particular, that the finite values of the measure for zero tunneling coupling are a result of the finite experimental sample size and the bias of the estimator $M^{(N)}$ (see text for details). Figure adapted from [160].

## 4.4 Relaxation Towards Equilibrium

So far we have discussed data that was prepared by very slow cooling, which was fully equilibrated and could be described by the equilibrium predictions of the SG model. We now turn our attention for the remainder of this Chapter to the dynamics during condensation and the near-equilibrium regime of CQW.

Calculating the non-equilibrium evolution of the SG model is a highly non-trivial task and we can no longer rely on the TMF of Section 2.3.3 which is only applicable in thermal

equilibrium. Further, while the SG model is expected to be, to some degree[12], a sensible approximation of the non-equilibrium physics of CQW, e.g. following a quench in the parameters [84, 203], the evolution during the condensation is dominated, at least for some initial time, by the dynamical equations of the fundamental fields $\hat{\psi}_{\mathrm{L,R}}(z)$. The SGPE introduced in Section 2.3.2 allows us to simulate the condensation process of CQW, and hence enables us to describe the approach of thermal equilibrium and the emergence of the low-energy effective description of the system.

### 4.4.1 Fast Cooling and Non-Thermal States of CQW

Experimentally, the need for a description of the system beyond thermal equilibrium is demonstrated by changing the cooling speed with which the system is prepared. We compare the results of the last section with data, produced by increasing the cooling speed by a factor of $10^{13}$.

The FDFs allow us to quantify the combined deviations of the non-thermal state. In Fig. 4.7 we compare for the slow and fast cooled data the FDFs of the relative phase difference $\varphi(z, z')$ for a fixed distance $z = -z' = 20\,\mu$m, chosen symmetrically around the center of the trap. In accordance with the analysis of higher-order correlations in Section 4.3 we find good accordance between the slow cooled data and the equilibrium distribution of the SG model (red lines). In particular, for strong phase locking between the two condensates ($\langle\cos(\theta_{\mathrm{r}})\rangle = 0.92$), as anticipated from the validity of the Wick decomposition, the distribution is Gaussian. For the fast cooled data, however, clear differences are visible. For small tunneling coupling the distribution is broadened and has a lower probability of small phase fluctuations. With increasing tunneling coupling, clear peaks in the FDF emerge, located at $\pm 2\pi$, while the central peak of the distribution shows reasonable agreement with the equilibrium predictions. Note that only the FDFs of the unbound phase differences are capable of distinguishing between these subtle differences, since the circular distributions, as discussed in Section 4.2.2, fold these side-peaks back into the interval $[-\pi, \pi)$, onto the central peak.

The appearance of well separated side-peaks in the FDFs shows that the phase field exhibits a well defined rotation, multiples of $2\pi$. Therefore phase fluctuations do not simply increase, leading to an overall broadening of the distribution, but instead exhibit localized twists. We already encountered such a twist in the soliton solution of the SG model (see Section 2.2.2). Indeed by comparing phase profiles contributing to the central and side peak of the distribution, we find such solitonic excitations to be present in the system (see

[12] Far from equilibrium coupling of the density and phase fluctuations can in general no longer be neglected, driving the system beyond the SG physics. We will discuss these effects in more detail in Chapters 5 & 6

[13] The evaporation rates for the slow cooling in Section 4.3 amount to a few percent per 10 ms at the end of the cooling ramp, and a few 10% for the fast cooled data. See [160]

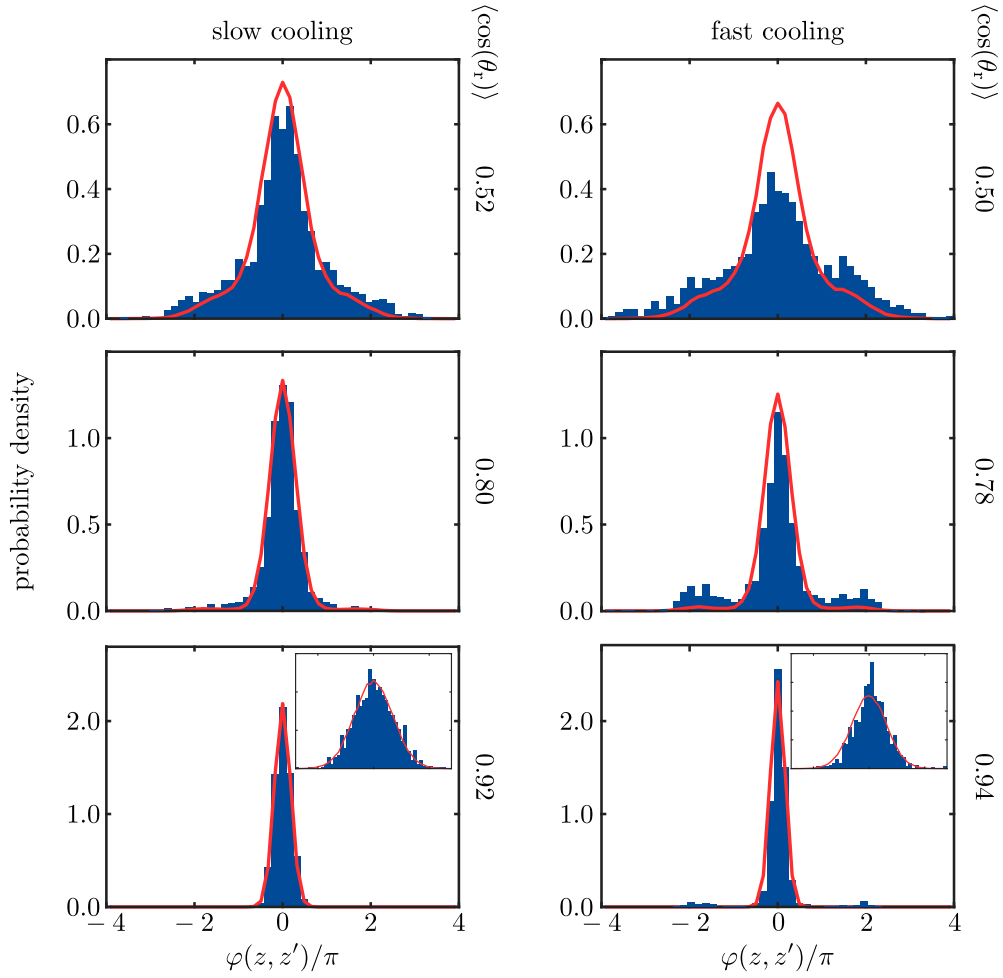


Fig. 4.7 Comparison of FDFs for the unbound phase differences $\varphi(z, z')$ for different cooling speeds in the experiment. The FDF for the slow cooled data (left column) discussed in Section 4.3 are in good agreement with the theoretical predictions of the SG model (red lines). The inset for the largest tunneling coupling clearly shows the Gaussian distribution in accordance with the observed factorization of higher-order correlations. The FDF is displayed for $z = -z' = 20\,\mu$m. Increasing the cooling speed (right column) the system shows clear deviations from the SG equilibrium model. For higher tunneling couplings pronounced peaks at $\pm 2\pi$ emerge. For $\langle\cos(\theta_r)\rangle = 0.94$ the inset reveals reasonable agreement of the central peak to the thermal equilibrium results. Figure adapted from [160].

Fig. 4.8). While these isolated solitons cannot be clearly distinguished from other fluctuations for smaller tunneling couplings, this strongly suggests that the observed broadening of the distribution is connected to additional solitons excited by the fast cooling of the gas.

The excitation of topological excitations during the crossing of a phase transition inevitably brings us back to the discussed Kibble-Zurek mechanism. The nucleation of solitons is a direct consequence of the order parameter locally choosing one of the degenerate vacuum

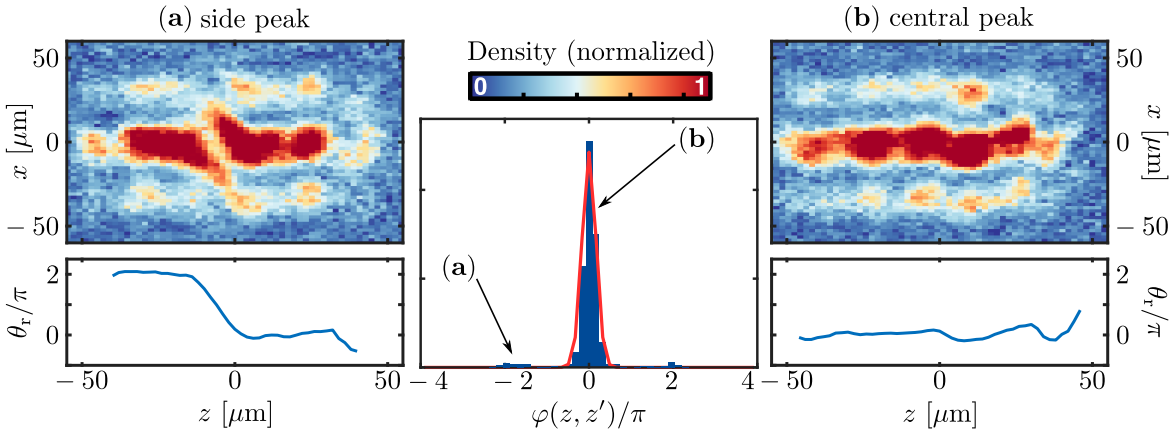


Fig. 4.8 Interference patterns and SG solitons. Studying individual interference patterns (phase profiles) for the fast cooled data reveals solitons as the reason for the side peaks in the FDFs. These defects are clearly visible in the interference patterns and the extracted phase profiles. Figure adapted from [160].

states of the SG Hamiltonian. Causality prevents spatially dislocated parts of the system to adjust to a single value for the order parameter, and at the interface between such uncorrelated vacuum states topological defects are created. The observed side-peaks are therefore a direct visualization of the degenerate minima of the SG Hamiltonian, smoothly connected through solitonic excitations.

### 4.4.2 Solitons and Topological Ordering

Solitons constitute highly non-linear field configurations in terms of these quasiparticle excitations, defined by the quadratic mTLL Hamiltonian. Therefore their presence leads to significant connected higher-order correlations $\mathcal{G}^{(N)}_{\text{con}}$, which can already be inferred by the distinctly non-Gaussian shape of the FDF. This shows that the Hamiltonian is not diagonal within this quasiparticle basis and suggests a highly interacting system, whereas in the soliton basis the only change due to their interactions is an additional shift of their coordinates [75].

We therefore extend the study of higher-order correlations by explicitly separating the influence of statistically independent, non-interacting solitons to the phase field $\theta_{\text{r}}(z)$. Similar to the RDM in Section 3.2.1, the field in this random soliton model (RSM) is defined as

$$\theta_{\text{r}}(z) = \tilde{\theta}_{\text{r}}(z) + \sum_{i=1}^{N_s} \phi_s(z - z_s^i) \,. \tag{4.25}$$

Here $z_s^i$ is the position of a soliton, given by the probability distribution $P_s(z)$. The remaining phase fluctuations $\tilde{\theta}_{\text{r}}$ around the classical solitons also include the breather solutions, which cannot be clearly separated from the fluctuating phase field. Expectation values of phase

correlation functions (4.10) can be expanded as

$$\mathcal{G}^{(N)}(\mathbf{z},\mathbf{z}') = \sum_{i=-N_s}^{N_s} p_i\, \mathcal{G}^{(N)}(\mathbf{z},\mathbf{z}')|_{Q=i}\ . \tag{4.26}$$

The topological charge $Q$ measures the difference of kink and antikink solutions in the volume defined by $\mathbf{z},\mathbf{z}'$, and $p_i$ is the probability of such a state in the ensemble. The decomposition in connected and disconnected correlation functions within each topological sector proceeds as outlined in the last sections. The $N$-th order connected correlation thereby separates into an independent sum of $N$-th order connected correlations for the multi-soliton state and the remaining phase fluctuations[14].

The main contribution of solitonic excitations to $\mathcal{G}^{(N)}_{\text{con}}$ stems from the finite phase difference for large separations $|\phi_s(z) - \phi_s(z')| = 2\pi$ for $|z - z'| \to \infty$. The finite width of the solitons $\sim l_J$ only has minor contributions. In the limit $l_J \to 0$ the full distribution function of phase differences takes the form of a mixture distribution

$$F(\varphi(z,z')) = \sum_{i=-N_s}^{N_s} p_i(z,z') P_i(\tilde{\varphi}(z,z'),\mu_i)\ , \tag{4.27}$$

given by the weighted sum of probability distributions $P_i(\tilde{\varphi},\mu_i)$, defined within each topological sector. These only depend on the remaining phase fluctuations $\tilde{\varphi}$ around the solitons, while each distribution is shifted to a mean value $\mu_i = 2\pi i$ due to the finite value of the topological charge $Q$. This leads to the characteristic multi-peak structure of the full distribution function as observed in Fig. 4.7. The weights are the probability $p_i(z,z')$ of states with a topological charge $Q$ within the ensemble[15], fulfilling $\sum_i p_i(z,z') = 1$. Therefore, excitation of soliton reduces the probability $p_0$ and decreases the central peak of the distribution. This suggests, while not visible in the side peaks of the broad distribution, that the weakly tunnel coupled state $\langle\cos(\theta_{\text{r}})\rangle = 0.5$ has a large number of additional, non-thermal solitons.

Of particular interest is the strong coupling limit ($J \gg 1$), where solitons and phononic fluctuations are well separated. While for a thermal state the probability of exciting a soliton approaches zero, the same is in general not true away from thermal equilibrium. Solitonic excitations may prevail for very long times, as remnants of previous far-from equilibrium dynamics of the system. During the relaxation, the system near thermal equilibrium is described by Eq. (4.27) with Gaussian distributions $P_i(\tilde{\varphi},\mu_i)$ (see Fig. 4.8). Higher-order connected correlations within this model are calculated from Eq. (4.15) and the central

[14] As for statistically independent random variables $X$ and $Y$ the joint cumulants vanish, i.e. $\langle X^n Y^m\rangle_c = 0$

[15] Alternatively one can label the states by the soliton number in the volume rather than the topological charge $Q$. In this case each distribution $P_{i\geq 1}$ itself is a mixture distribution of states $|Q|, |Q|-2, \cdots -|Q|+2, -|Q|$

moments for the Gaussian mixture distribution, given by

$$\langle(\tilde{\varphi}-\mu)^j\rangle = \sum_{i=-N_s}^{N_s}\sum_{k=0}^{j/2}\frac{j!}{2^k k!(j-2k)!}(\mu_i-\mu)^{j-2k}\,p_i\,\sigma_i^{2k}\,. \tag{4.28}$$

Here $\sigma_i = \langle\tilde{\varphi}^2\rangle|_{Q=i}$ is the phase variance in a topological sector. For an equal probability $p_i = p_{-i}$ for kink and antikink solutions the mean value $\mu$ vanishes.

### 4.4.3 Condensation within the SGPE Formalism

To gain deeper understanding of the influence of solitons on higher-order correlations and determine the validity and limitations of the above RSM we study the condensation of CQW within the SGPE framework. The evolution of the system is described in terms of the fundamental fields $\hat{\psi}_{\mathrm{L,R}}(z)$ which evolve according to the coupled Lagevin equations (c.f. Eq. (2.51))

$$\mathrm{i}\hbar\partial_t\begin{pmatrix}\psi_\mathrm{L}\\ \psi_\mathrm{R}\end{pmatrix} = [1-\mathrm{i}\gamma(z,t)]\begin{pmatrix}H(|\psi_\mathrm{L}|^2) & -\hbar J\\ -\hbar J & H(|\psi_\mathrm{R}|^2)\end{pmatrix}\begin{pmatrix}\psi_\mathrm{L}\\ \psi_\mathrm{R}\end{pmatrix}+\begin{pmatrix}\eta_\mathrm{L}\\ \eta_\mathrm{R}\end{pmatrix}, \tag{4.29}$$

where $H(|\psi|)$ defines the unitary evolution of a single condensate according to the GPE (2.29) or NPSE (2.33). We take a single parameter $\gamma = \gamma_{\mathrm{L,R}}$, independent of space and time, corresponding to equal scattering rates between the thermal cloud and each condensate. The variance of the complex Gaussian white noise $\eta_{\mathrm{L,R}}$ is given by Eq. (2.52), for which Eq. (4.29) evolves towards the stationary thermal state.

While the random noise $\eta$ has Gaussian statistics, the unitary evolution is defined by the exact non-linear equations, and hence the system in thermal equilibrium exhibits non-Gaussian fluctuations of the relative phase in accordance with the predictions of the SG model (see Fig. 4.9a). The remaining fields, i.e. the relative density $\rho_\mathrm{r}$ and the common degrees of freedom, in accordance with theoretical assumptions show Gaussian statistics for any value of the tunneling coupling. This confirms the approximations which we a priori assumed in Sections 2.2.1 & 4.3 to arrive at the SG model as the low-energy effective theory. Further, the SGPE extends beyond the TMF as it is applicable for inhomogeneous condensates. The data given corresponds to typical parameters of [160]. We find that the system is well described within the LDA[16]. In particular, the alterations due to the inhomogeneity are small for the central part of the cloud considered in the analysis of the experimental data, which explains the observed accordance with the homogeneous SG model. Near the edges of the cloud differences occur, due to the increasing role of fluctuations for small densities.

[16]This includes a spatial dependence on the linear tunneling coupling $J$ between the two condensates.

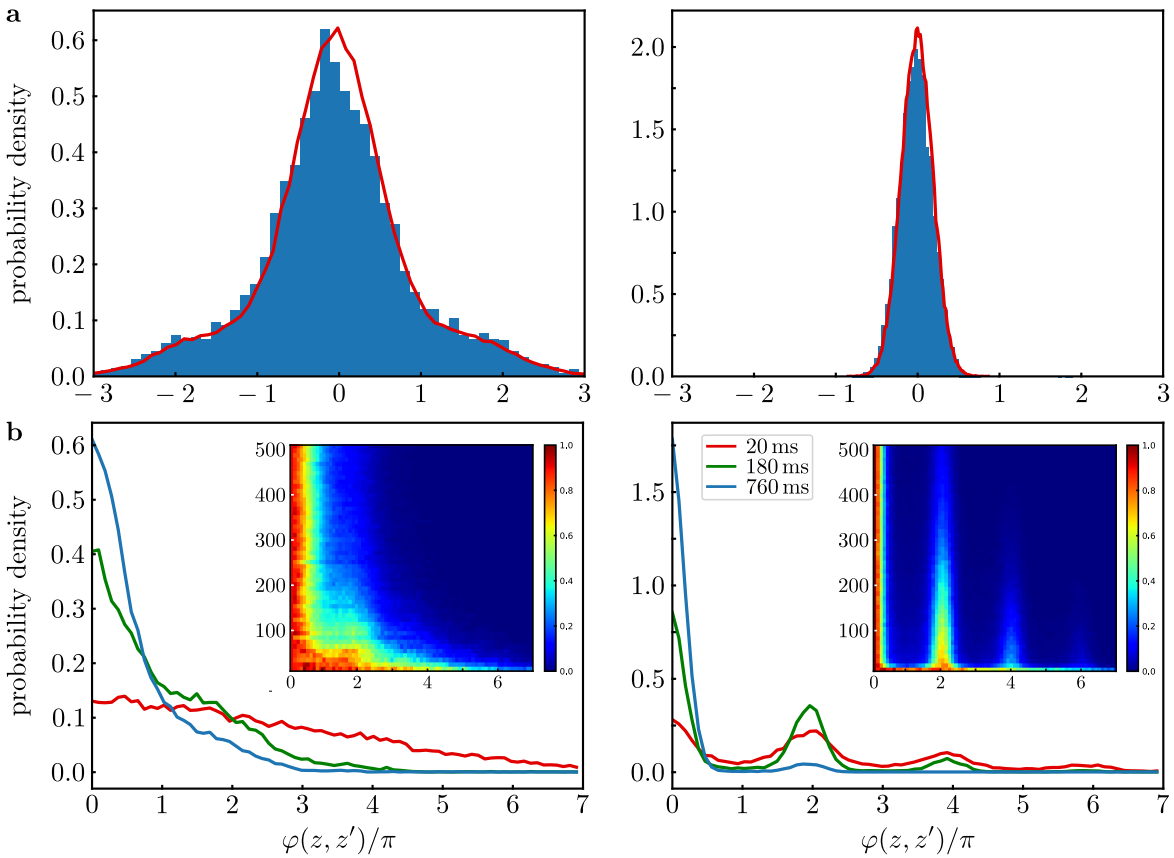


Fig. 4.9 Approach of thermal equilibrium during SGPE evolution. **a** Full distribution function of the relative phase difference for the final equilibrium state reached by the SGPE. The parameters for the evolution are $N = 5000$ atoms per well, $\lambda_T = 15\,\mu$m, and $J = 1,22$ Hz leading to $\langle\cos(\theta_r)\rangle = 0.49, 0.91$. The red line is the predictions of the equilibrium SG model calculated using the TMF, and is in good agreement to the full non-linear model of two CQW. **b** SGPE evolution and approach of thermal equilibrium. The inset shows the time evolution of the FDF (with the probability density depicted in color). For strong tunneling coupling a pronounced mixture distribution emerges and slows down the approach to thermal equilibrium. The FDF for three different times are depicted in the main figures. For low tunneling coupling a clear overpopulation around $\varphi = 2\pi$ remains visible signaling the presence of non-thermal solitons.

The time evolution during the relaxation of the system is presented in Fig. 4.9b for two values of the phase locking $\langle\cos(\theta_r)\rangle = 0.5\,(0.9)$, chosen in the intermediate (strong) coupling regime. The thermal coherence length $\lambda_T = 15\,\mu$m was chosen within the experimental uncertainty. We consider the system initially in the unbroken symmetry phase, obtained through evolution of the SGPE for $\mu < 0$ [153]. At $t = 0$ we instantaneously quench the chemical potential to its final value, determined through imaginary time evolution of the coupled system. The slight shift of $\mu$ with temperature is negligible for our parameters. The

system is subsequently evolved with Eq. (4.29) up to $t = 2\,\mathrm{s}$, for which we found convergence to the final equilibrium state for any parameter $\lambda_T$ and $l_J$.

For strong tunneling coupling the FDF relaxes through soliton decay from a pronounced mixture distribution towards the thermal equilibrium result. The high probability of exciting a soliton at the onset of condensation is due to the dependence of $q$ on the atomic density. While the condensate forms, $q$ rises. Therefore, at early times, excitation of a soliton is energetically easy as the cosine potential in the SG Hamiltonian is very shallow. Once the amplified scattering into the condensate leads to a quick rise of the density, these solitons become frozen because of the increasing depth of the cosine potential. After the condensate has formed these solitons represent very stable field configurations connecting the degenerate minima of the SG Hamiltonian. Their decay happens mostly near the edges of the condensate, where large density and phase fluctuations drive the system beyond the SG model and solitons are no longer topologically protected.

When the tunneling coupling is lowered a clear separation of the side peaks is no longer possible due to the increasing width of solitons ($\sim l_J$) and of the FDF (due to the increased role of thermal fluctuations). Nonetheless, a clear broadening of the distribution and a decrease of the central peak are clearly visible and, in accordance with the experimental observations, show the increase of phase fluctuations away from equilibrium.

Notably, the relaxation times for strong and weak phase locking are significantly different, with the latter showing comparatively fast relaxation towards its thermal equilibrium state. While it is plausible, that the increased role of thermal fluctuations in the weakly coupled system leads to a faster decay of solitons and consequently a faster relaxation time, quantitative estimates of this time scale are hindered by the non-linearity of the problem and the immense parameter space. The latter, while in equilibrium approximately reduced to the parameter $q$, shows explicit dependence on all scales $n_{1\mathrm{D}}$, $T$, and $J$, due to the noise term $\eta$ in the SGPE evolution, which only depends on the temperature $T$. Further, although the final equilibrium state of the SGPE evolution is independent of the parameter $\gamma$, the dynamics during condensation show a highly non-linear dependence. This is to be expected, as $\gamma$ determines the growth and damping of the evolution, and therefore contributes to both defect creation and decay [152]. While the atom number growth still allows for a scaling of time with $\gamma$ [119], the relative phase fluctuations relax on a different time scale due to the nucleation of topological excitations. This leads to additional explicit dependences on the initial state prior to condensation, the rate at which the transition to the quasi-condensate regime is crossed, and the parameter $\gamma$.

The approach of thermal equilibrium for the strongly coupled system is drastically slowed down by the high probability of exciting a soliton during the initial growth of the condensate. Note that this effect is even more pronounced in the homogeneous system, as solitons are unable to decay near the edges of the cloud where they are no longer topologically protected.

In accordance with the experimental observations, prominent side peaks emerge in the FDFs for faster condensation as an increasing number solitons is created during the onset of condensation. However, for a quantitative comparison of the condensation dynamics to the experiment, additional data, such as the initial temperature and the experimental rate of condensation, would be required to match the condensate growth in the SGPE evolution to the experimental observations.

Here it shall suffice, since we are more interested in the influences caused by the presence of solitons than their exact number counting statistics, to choose a constant value $\gamma = 0.05$, keeping in mind that the time in the SGPE evolution does not necessarily correspond to the physical time of the experiment. Nonetheless, interactions between solitons and thermal fluctuations are accurately described in the SGPE formalism, and we can ask the question to what extent the non-equilibrium state can be described by an access of statistically independent, non-thermal solitons.

For the topological ordering of field configurations, we use a soliton detection algorithm. Therein, possible solitons are first detected by scanning the phase profiles for phase differences $|\varphi(z, z')| \geq 1.8\pi$ for increasing distances $|z - z'|$, where the threshold for a possible soliton is slightly lowered from its theoretical value $2\pi$ because of thermal fluctuations of the phase field. If for given values $z, z'$ the threshold is exceeded the local region is labeled to contain a possible soliton, and the remainder of the phase profile is searched accordingly. Thereafter, for each region containing a possible soliton we compare the residuals of a local least-square fit of the full soliton solution (2.47) within this region to a fit using a quadratic polynomial. If the former leads to smaller residuals, the state is labeled a soliton, otherwise the state is considered non-conclusive. Phase profiles can subsequently be ordered into the topological sectors. This gives access to the full counting statistics of solitons, their width, topological charge, and spatial distribution. In case of strong tunneling coupling the detection algorithm gives excellent results, due to the separation of scales for the solitonic and thermal fluctuations, while for decreasing phase locking between the condensates, the detection of solitons becomes less clear, and only well separated solitons can be detected.

Given the full counting statistics of solitons we can test the validity of the RSM through comparison to the out-off-equilibrium results of the SGPE evolution. In Fig. 4.10 we show the FDFs calculated within the RSM and directly from the numerical data, for an early time $t = 180\,\mathrm{ms}$. In the RSM the results of the soliton detection algorithm were used to sample field configurations according to Eq. (4.25), where the remaining fluctuations $\tilde{\theta}_\mathrm{r}$ were sampled from the equilibrium distribution using the TMF. The good agreement between the two models reveals, that fluctuations around the solitons thermalize on a much more rapid time scale. Most notably, for the strongly coupled system, this shows that fluctuations around the solitons are already Gaussian and hence well described by a set of non-interacting quasiparticles. Solitons can therefore be interpreted as false vacua of the phononic excitations

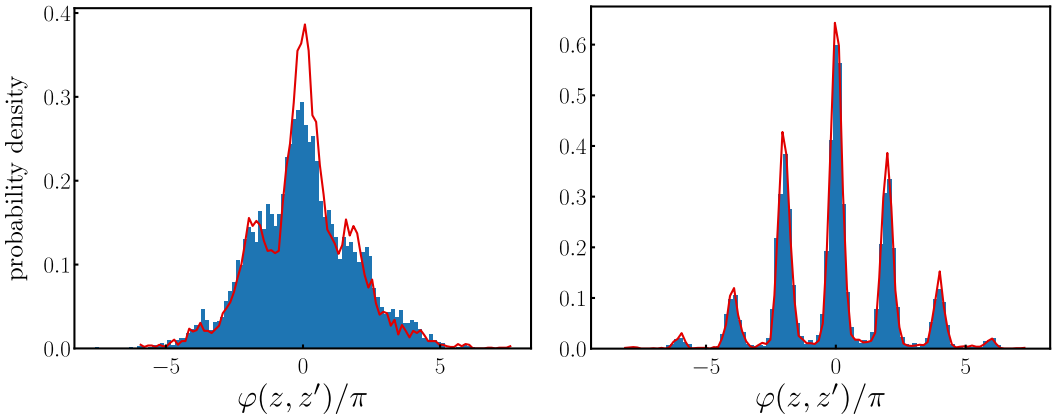


Fig. 4.10 Non-equilibrium FDFs in the random soliton model. Comparison of the SGPE data for $t = 180\,\text{ms}$ to the predictions of the RSM (4.25) shows good agreement. The RSM was calculated imposing additional solitons in a thermal background sampled from the TMF. This shows that the system relaxes on two timescales, while non-thermal solitons are still present, fluctuations around these defects have already thermalized on a much shorter timescale. The slight differences for low tunneling coupling are attributed to the problem of accurately detecting solitons in the increasingly fluctuating background.

[204]. The deviations in the weakly coupled regime are attributed to the increase in non-conclusive fits in the detection algorithm, which makes a clear distinction between solitonic and thermal fluctuations impossible. Nonetheless, the RSM is in reasonable agreement with the non-equilibrium distribution, which shows that clearly separable solitons are the main cause of the broadened FDF.

### 4.4.4 Higher-Order Correlations Out-Of-Equilibrium

Based on the analysis of the last Section, we can ask the question if the experimental non-equilibrium data can be described by an excess of non-interacting solitons and otherwise thermal fluctuations of the phase. Since for the experimental data, excitation of multiple solitons is highly suppressed (see Fig. 4.7) we limit our analysis to the zero- and one-soliton sector and vary the probability $p_\text{s}$ for a soliton within the ensemble. We calculate the measure $M^{(4)}$ for the RSM using phase profiles determined by stochastic sampling from the TMF, adding randomly distributed solitons according to Eq. (4.25).

In the limiting case of a mixture distribution (4.27), analytical insight can be gained by calculating the local measure $M^{(4)}(z, z')$ in the one-soliton sector (see Eq. (4.24) omitting the integration and absolute values). The most striking feature therein is, that dependent on the relative amplitude for the full and connected correlation of the field $\tilde{\theta}_\text{r}$, the local measure in the RSM has a maximum at a finite soliton probability $p_\text{s}$. This leads, in certain regimes, to a

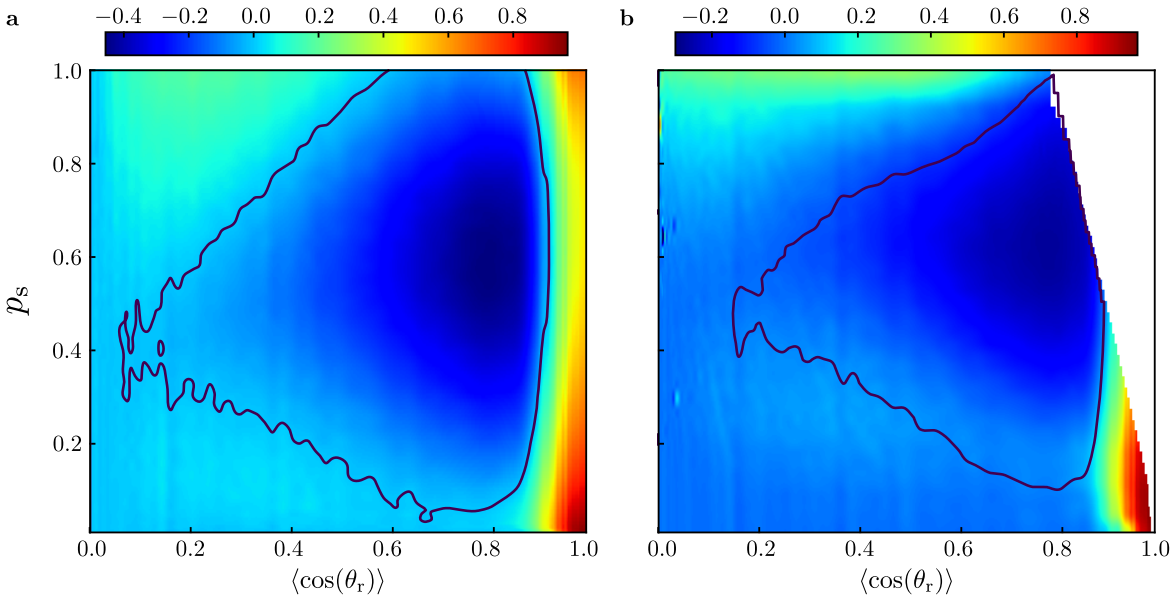


Fig. 4.11 Influence of non-thermal solitons on the integral measure $M^{(4)}$. Comparison of the equilibrium predictions for $\lambda_T = 15\,\mu$m to the results of the RSM as a function of the coherence factor and the soliton probability $p_s$ within the ensemble. The difference $M^{(4)}_{\mathrm{RSM}} - M^{(4)}_{\mathrm{thermal}}$ is depicted in color. Within the black contour line the measure is negative, i.e. additional soliton lower the relevance of higher-order correlations. **a** Difference for the same coherence factor in thermal equilibrium. **b** Difference for the same coherence factor (including the influence of solitons in the RSM). Note, in particular, that the white area is physically undefined as solitons lead to an upper bound of the coherence factor and no numerical artifact.

counterintuitive decrease of higher-order connected correlations due to additional fluctuations caused by non-thermal solitons.

This effect is also visible in the integral measure Fig. 4.11a, where we compare the results of the full RSM to the thermal predictions. A negative value corresponds to a lower value for $M^{(4)}$ caused by non-thermal solitons. For a comparison to the experiment it is important to bare in mind, that solitons also decrease the coherence factor $\langle\cos(\theta_r)\rangle$. Since this is the determining, independently measured factor in the experiment, we also compare in Fig. 4.11b the results for the same value of $\langle\cos(\theta_r)\rangle$, calculated before and after solitons have been imposed, rather than the same value of $q$ in thermal equilibrium. Note especially, that the white area for large coupling and soliton numbers is no numerical artifact, but is physically not defined as the large number of solitons truly limits the phase locking between the two condensates.

A fit of the RSM predictions to the experimental non-equilibrium data shows excellent agreement (see Fig. 4.12). We find two distinct branches for the soliton probability within the intermediately coupled regime $\langle\cos(\theta_r)\rangle \lesssim 0.8$. The soliton probability is either increasing

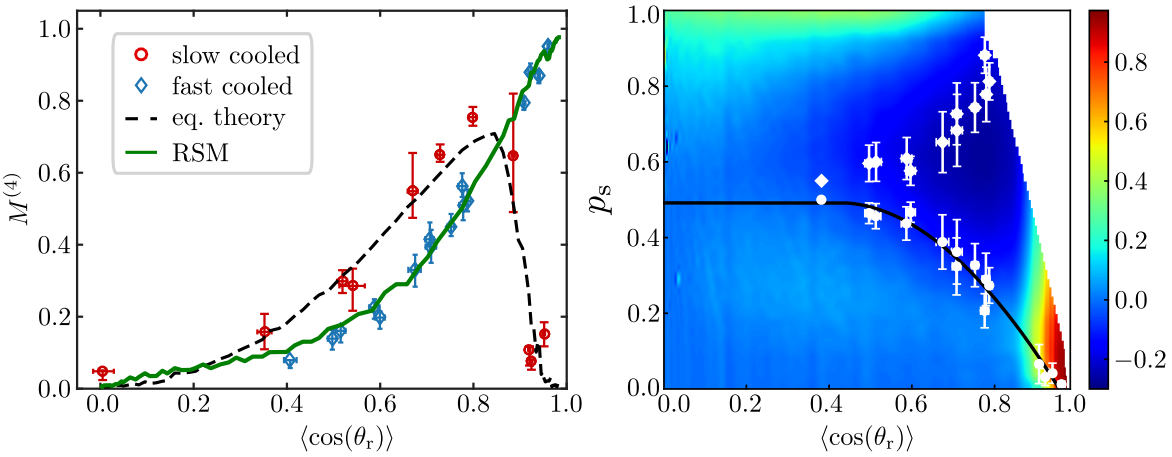


Fig. 4.12 Experimental results for non-equilibrium correlations. The non-equilibrium experimental data obtained by fast cooling (blue diamonds) clearly deviates from the equilibrium experimental data (red dots) and TMF predictions (black dashed line). Fitting the soliton probability in the RSM through comparison of $M^{(4)}$ for the fast cooled experimental data we find good agreement for all values of the coherence factor (green solid line). The thermal fluctuations used in the RSM are given by the black dashed line. The determined soliton probability is depicted in the right panel. We find two distinct branches, with increasing and decreasing soliton probability, for the intermediately phase locked data, where the measure $M^{(4)}$ is lowered as compared to the equilibrium values. In the strongly phase locked regime only a low soliton probability can explain the observed increase in of the connected correlations. Therefore, the soliton probability decreases with increasing phase locking. The black line is a free fit to the determined soliton probabilities, extrapolated with a constant value to $\langle\cos(\theta_r)\rangle = 0$, used for the line in the left panel (green solid line). The errors represent the standard deviation.

or decreasing with $\langle\cos(\theta_r)\rangle$, but both branches show a regular behavior. Within this regime the connected correlation function is lowered as compared to the equilibrium result. At the upper most value ($\langle\cos(\theta_r)\rangle \approx 0.8$) the SG model in thermal equilibrium is almost maximally correlated and any additional fluctuations in the RSM lead to a decrease of the connected correlation function (c.f. Fig. 4.11a). Above this point the situation reverses, and we find an increase of $M^{(4)}$ as compared to equilibrium. Notably, this enormous increase from practically zero to almost one is caused only by a very low probability of solitons and is the result of the narrow Gaussian distribution of thermal fluctuations. This further allows us to determine the preferred branch of the soliton probability, which thereby shows a continuous decrease for an increasing phase locking. This shows the precision and sensitivity higher-order correlations present for the study of many-body systems. Detailed studies of the condensation process are needed to determine the observed difference between the experimental and SGPE results for the soliton probability in the strongly coupled regime. Apart from the discussed need for detailed experimental parameters, comparison to three-dimensional SGPE simulations of the

full double-well potential may shed light on the influence of radially excited states during the condensation process.

## 4.5 Summary

In this Chapter we presented a detailed calculation of the factorization properties of higher order correlations in the SG model. This allowed us to determine the validity of the SG model as the low-energy effective field theory describing the system of two linearly coupled quantum wires in and close-to thermal equilibrium. In certain regimes we found complete factorization of higher-order correlations and therefore the exact solution to the quantum-many body problem solely through the experimental measurement and analysis. This revealed in particular that a large number of possibly irrelevant operators indeed renormalize to zero in the low-energy description and the system in thermal equilibrium approaches the TLL fixed point.

As a consequence of the finite domain of the phase, we argued that a correction of the phase field, in close analogy to the extended zone scheme in the path integral, needs to be performed in order to accurately determine the factorization properties of higher-order correlations. After discussing the general connection to quasiparticle interactions we gave explicit formulas for the factorization into connected and disconnected correlations. We further connected the commonly used periodic correlations and their higher-order generalizations $C^{(N)}$ through a cumulant expansion to the fundamental correlations of the phase field. This explicitly showed, that quasiparticle interactions influence these correlations already at first order in a non-trivial way, which makes them less suited to the study of non-Gaussian field theories. In case of a Gaussian field theory this expansion allowed us to determine the correct form of Wick's theorem for periodic correlations.

Comparing experimentally measured higher-order correlations in thermal equilibrium to predictions of the SG model we were able to determine the validity of the low-energy description for connected correlations up to $10^{\text{th}}$ order. The equilibrium results of the SG model were obtained by sampling of individual field configurations from the Îto equation of the TMF. This non-perturbative method facilitates the fast calculation of higher-order correlations through direct sampling from the equilibrium distribution. The method presented is an important step towards the solution of complex many-body systems by experiment (see also chapter 7) and hold large promise in the unbiased and unambiguous verification of future quantum simulators.

The phase correction further allowed us to define the unbound full distribution functions of phase differences, which unlike the wrapped distributions for the bound phase variable, reveal the connection of distinct vacuum states of the SG model through solitonic excitations.

By changing the speed at which the condensates are cooled into the double-well, we found long lived non-thermal states. The FDFs revealed an excess of non-thermal solitons, which are remnants of the fast condensation process.

Simulation of the cooling process within the SGPE framework confirmed the excitation of these topological defects during the condensation of the system. During the rapid growth of the condensate, the cosine potential in the SG Hamiltonian rises quickly, freezing these excitations in the phase. Their long life time lead to a separation of scales, and fluctuations around these defects are found to decouple and thermalize on a much shorter time scale. Therefore, in the strongly coupled regime where solitons and phonons are clearly separated, solitons can be interpreted as false vacuum states for the remaining phase fluctuations. We found good accordance of the FDFs between the SGPE and a model of randomly distributed solitons in a thermal background, which enabled us to explain the experimentally observed non-equilibrium higher-order correlations for any value of the coupling through this random soliton model. As a striking result we confirmed the experimentally observed decrease (increase) of the fourth-order connected correlation function within the regime of intermediate (strong) phase locking for the non-equilibrium SG model.

# Chapter 5

# Prethermalization and Generalized Gibbs Ensemble

The connection between the microscopic dynamics of an isolated quantum many-body system and the foundation and emergence of a statistical mechanics is a fundamental open problem. Of particular interest are systems, that during their course of evolution approach an intermediate long-lived state and do not simply relax to thermal equilibrium on a single timescale. Therein, an important role is played by integrable models, where a large number of locally conserved quantities strongly inhibits the thermalization of the system. Instead of relaxing to thermal equilibrium, described by the usual thermodynamic ensembles, it was proposed that these systems relax to a so called Generalized Gibbs Ensemble (GGE) [30]. Based on the fundamental principle of entropy maximization [9, 10] GGEs encompass a large number of commonly used statistical ensembles, including the thermodynamic Gibbs or diagonal ensembles, and allow for the incorporation of the restriction inflicted by non-trivial conserved quantities on the dynamics of the system. This enables a clear definition of emergent statistical descriptions as a form of statistical inference based on the level of precision.

In this chapter we investigate the emergence of such a Generalized Gibbs state during the relaxation of two decoupled one-dimensional Bose gases[1]. By rapidly splitting a single condensate in two halves the system is quenched in a far-from-equilibrium initial state. This leads to an initially almost perfectly correlated phase between the two systems, whose evolution is probed through the full first-order coherence function $C^{(1)}(z, z')$. In the ensuing evolution the emergence of a steady state appears locally, traversing the system in a light cone like fashion [14, 39]. This local spread of correlations is connected to the dephasing

[1] This chapter is based on and contains parts of [15]. I contributed to the theoretical calculations, interpretation of the theoretical results and experimental data, performed numerical simulations, and contributed to writing of the manuscript.

of eigenstates in the integrable effective field theory, the TLL model, which describes the relative degrees of freedom between the two condensates. Based on a model of local binomial splitting we calculate the time evolution within the harmonic theory for the homogeneous and harmonically trapped system. While the former relaxes to a prethermalized state, well described by an effective temperature defined by the splitting process, we find for the latter that off-diagonal quasiparticle correlations prevent the system from reaching a steady state. These off-diagonal correlations, through a second light cone-like dephasing, are found to contribute to the phase correlation function on the same order as the diagonal quasiparticle occupations. In contrast, we find in the experiment relaxation of the system to a steady state determined by the conserved quantities of the integrable model. By changing the splitting protocol, this quasi-steady state can be tuned from a prethermalized state, described by a single temperature, to a genuine GGE, exhibiting at least two distinct temperatures. In the last section we discuss the apparent problems of the binomial splitting model, and propose a solution based on emergent conserved quantities in a finite temperature system, studied within the SGPE framework. Finally we comment on the challenges for a self consistent numerical simulation of the exact dynamics during the splitting of the gas, which is essential for a detailed understanding of the emergence of the observed GGE.

## 5.1 From unitary dynamics to statistical mechanics

Relaxation to a stationary, possibly thermal, state of closed quantum systems is to date still an open and interesting question [32]. The unitary time evolution and the discreteness of states of these systems lead to the conservation of the overlap-coefficients $C_m$ of the initial state with the eigenstates of the system. The long-time average of any observable $\hat{O}$ can be calculated by considering the trivial time evolution of the eigenstates $|m\rangle$. By expanding the initial state wave function in the eigenstate basis $|\psi(t)\rangle = \sum_m C_m \mathrm{e}^{-\mathrm{i}E_m t/\hbar}|m\rangle$, this leads to

$$\langle\hat{O}\rangle_\infty = \lim_{T\to\infty}\frac{1}{T}\int \mathrm{d}t\, \langle\psi(t)|\hat{O}|\psi(t)\rangle = \sum_m |C_m|^2 O_{mm}\,, \tag{5.1}$$

where we, for simplicity, assumed that the eigenstates are non-degenerate, such that off-diagonal contributions vanish in Eq. (5.1) in the long time average. The long time average Eq. (5.1) defines the "diagonal ensemble" $\langle\hat{O}\rangle_\infty = \mathrm{Tr}[\hat{O}\rho_{\mathrm{diag}}]$, where $\rho_{\mathrm{diag}} := \sum_m P_m\rho_0 P_m$ is determined by the initial state density matrix $\rho_0 = |\psi\rangle\langle\psi|$ and the projection operators onto the eigenstates $P_m = |m\rangle\langle m|$. Note that if a stationary state exists, which we will assume henceforth, its value is given by the diagonal ensemble. Nevertheless $\rho_{\mathrm{diag}}$ can hardly be thought of as a statistical description of the system, since all the information of the initial state is encoded in the overlap-coefficients. One fundamental assumption of statistical mechanics

is that the equilibrium state of the system can be described by only a few thermodynamic variables such as e.g. the mean energy (and particle number). Equilibrium properties of such systems are well described by the canonical (or grand canonical) ensemble. This poses the question, if and how the relaxed state of a closed quantum systems can ever be described statistically.

As discussed in chapter 1, ETH explains the emergence of the microcanonical ensemble from Eq. (5.1) through dephasing of eigenstates and the assumption that the matrix elements $O_{mm}$ are restricted and approximately constant over an energy window $\Delta E$ [18]. These assumptions, however, are commonly violated in integrable systems which leads to the breakdown of the ETH [19]. Extending to these systems, information theory provides a powerful framework for the analysis of emergent statistical phenomena from the microscopic laws governing the dynamics of the system. In particular, the principle of entropy maximization [205, 9, 10] interconnects both of these descriptions by viewing statistical physics as a form of statistical inference dependent on the available information about the system [9]. Although to date no conclusive proof of its validity exists, the approach of sufficiently complex systems to such a maximum entropy state is deeply rooted in our everyday experiences and constitutes one of the fundamental assumptions of statistical physics. One of the most promising approaches for a generalized statistical description, was proposed by Rigol et al. [30] and termed "generalized Gibbs ensemble" (GGE). Maximization of the entropy $S = \mathrm{Tr}[\rho \,\mathrm{Ln}\,(1/\rho)]$ under the constraints inflicted by the integrals of motion leads to the probability distribution [205, 9, 10]

$$\hat{\rho} = Z^{-1}\, \mathrm{e}^{-\sum_m \lambda_m \mathcal{I}_m} \,. \tag{5.2}$$

Here $\{\mathcal{I}_m\}$ is a full set of integrals of motion and the partition function $Z = \mathrm{Tr}[\mathrm{e}^{-\sum_m \lambda_m \mathcal{I}_m}]$ normalizes the density matrix. The Lagrange multipliers (chemical potentials) $\lambda_m$ are determined by the maximization of the entropy under the condition that the average of the respective conserved quantities are set to their correct initial value $\langle \mathcal{I}_m \rangle = -Z^{-1}\partial_{\lambda_m} Z$. One can readily see, that the GGE encompasses the above mentioned ensembles. If the the mean energy is the only conserved quantity, Eq. (5.2) reduces to the well known canonical, or Gibbs, ensemble, leaving as the only Lagrange multiplier the inverse temperature $\beta$. On the other hand, if the projectors $P_m = |m\rangle\langle m|$ are chosen as the integrals of motion, the Lagrange multipliers given by the constraints become $\lambda_m = -\,\mathrm{Ln}\left(|C_m|^2\right)$, and the GGE resembles the diagonal ensemble. These examples alone show that the GGE is formally capable of incorporating the statistical descriptions from only a few conserved quantities to the "quasi-statistical" description given by Eq. (5.1), for which the sum over $m$ has the same dimension as the Hilbert space. Which form of the GGE is applicable certainly depends on the system in question [8].

## 5.2 Coherent Splitting as a Quantum Quench

Coherently split condensates offer an excellent starting point to investigate relaxation and equilibration in closed quantum systems. This far-from equilibrium state can be well isolated and reliably (re)produced in cold atom experiments and therefore renders the study of dynamics of the system possible for vastly different time scales, shedding light on the fundamental relaxation dynamics of isolated many-body systems.

The initial system is a 1D Bose gas in thermal equilibrium at a temperature $T$. The system is split along one of the radial directions (at a time $t = -\tau_s$) by a smooth deformation of the harmonic confinement into a dressed-state DW potential (see [38] and references therein). The decoupling of the two superfluids takes place on a time scale $\tau_d \ll \tau_s$. For energies $E < \hbar\tau_d^{-1}$ correlations along the longitudinal direction can be neglected and the splitting process is analogue to a local beam splitter in optics. This constitutes a rapid change of the systems parameters and can therefore be considered as a quantum quench of the system leading to quasiparticle creation. At the end of the splitting ramp ($t = 0$), the two superfluids are completely decoupled and the subsequent evolution of the system is described by Eq. (2.38) for vanishing tunneling coupling $J$.

In the following we discuss the expected time-evolution and basic theoretical framework for a generic system from the initial to the fully equilibrated state. The relaxation dynamics for a homogeneous and harmonically trapped system are discussed in detail in the subsequent sections Sections 5.3 & 5.4 respectively.

### Initial State

The initial state can be well defined in the limit of a splitting ramp which is fast as compared to the longitudinal dynamics of the system. Herein the initial thermal fluctuations are completely inherited by the symmetric degrees of freedom, while the probability of each of the $N$ atoms to go into either of the two wells is random and uncorrelated. The probability of finding $N_L$ ($N_R$) atoms in the left (right) well is given by a binomial distribution

$$P(N_L; N, p_L) = \binom{N}{N_L} p_L^{N_L} (1 - p_L)^{N_R} , \tag{5.3}$$

where $p_L$ is the probability of an atom being found in the left well and $N_R = N - N_L$. For an evenly split condensate ($p_L = 1/2$) the variance of the atom number difference $\Delta N = (N_L - N_R)/2$ is therefore $\langle \Delta N^2 \rangle = N/4$. In a coarse grained model [135] we can write,

$$\langle \delta\hat{\rho}_r(z)\delta\hat{\rho}_r(z') \rangle = \xi_n(z) \frac{\sqrt{\rho_0(z)\rho_0(z')}}{2} \delta(z - z') , \tag{5.4}$$

due to the absence of correlations in the longitudinal direction. Here $\rho_0$ is the mean density in each of the two condensates. Due to the build up of correlations during a finite splitting, we further included a possible number squeezing $\xi_{\mathrm{n}}(z)$ locally reducing the fluctuations in number difference below that of a coherent state [206, 207]. In the limit $\tau_{\mathrm{s}} \to 0$ for an instantaneous quench of the system we recover the continuous formulation of the above binomial splitting model with $\xi_{\mathrm{n}}(z) \equiv 1$. As a further consequence of the fast splitting as compared to the longitudinal dynamics of the system, the initial phase profile remains rather unchanged during the splitting process and is imprinted onto both condensates [38]. The relative phase profile $\hat{\theta}_{\mathrm{r}}(z)$ is therefore close to zero with the variance determined by the minimum uncertainty state

$$\langle \hat{\theta}_{\mathrm{r}}(z)\hat{\theta}_{\mathrm{r}}(z')\rangle = \xi_{\mathrm{n}}^{-1}(z)\frac{1}{2\sqrt{\rho_0(z)\rho_0(z')}}\delta(z-z') \,. \tag{5.5}$$

For sufficiently high densities in a coarse grained model, the binomial distribution is well approximated by a Gaussian distribution and the above variances completely define the system posterior to the decoupling. The initial state in the relative degrees of freedom is a highly squeezed state, with a huge excess of fluctuations in the relative density and highly suppressed relative phase fluctuations.

### Observables

The above constitutes the simplest model of the splitting process and completely eliminates the dependence on the radial direction. We discuss the validity of this approximations in Section 5.6 in comparison to experimental measurements. Considering for now the binomial splitting, we are able to describe the system, analytically as well as numerically, within the framework of a single or two completely decoupled one-dimensional Bose gases. As stated above, due to the central limit theorem, the initial state has insignificant to no connected higher-order correlations and therefore remains Gaussian at all times. Hence, we are able to analyze the system by use of the simpler periodic correlation functions Eq. (4.18), which for Gaussian fluctuations are determined by the phase variances $\langle \hat{\theta}_{\mathrm{r}}(z,t)\hat{\theta}_{\mathrm{r}}(z',t)\rangle$. By use of the first-order coherence function

$$C(z,z',t) = \left\langle \cos\left(\hat{\theta}_{\mathrm{r}}(z,t) - \hat{\theta}_{\mathrm{r}}(z',t)\right)\right\rangle = \mathrm{e}^{-\frac{1}{2}\left\langle \hat{\theta}_{\mathrm{r}}(z,t)-\hat{\theta}_{\mathrm{r}}(z',t)\right\rangle} \,, \tag{5.6}$$

we simply circumvent the need to correct the phase profile for unphysical jumps across the boundary. We will confirm this approximation later on, numerically as well as experimentally, by analyzing the factorization properties of higher-order correlations.

Within the harmonic approach we can readily calculate the time-dependent variance of the phase difference $\Delta\hat{\theta}(z,z',t) = \hat{\theta}_{\mathrm{r}}(z,t) - \hat{\theta}_{\mathrm{r}}(z',t)$, which for a general state is given by

$$\begin{aligned}\langle \Delta\hat{\theta}(z,z',t)^2 \rangle = \\ \frac{1}{2\sqrt{\rho_0(z)\rho_0(z')}}\Bigg[ \sum_{m=1} \mathcal{B}^1_{m,m}(z,z') \left(2\langle b_m^\dagger b_m\rangle + 1\right) - \left(\mathrm{e}^{-2\mathrm{i}\omega_m t}\, \mathcal{B}^2_{m,m}(z,z')\, \langle b_m b_m\rangle + \mathrm{H.c.}\right) \\ + \sum_{n=2}^{} \sum_{\substack{k=1 \\ k\neq(n-k)}}^{n-1} \mathrm{e}^{-\mathrm{i}\delta\omega^-_{k,(n-k)}t}\, \mathcal{B}^1_{k,(n-k)}(z,z')\, \langle b_k^\dagger b_{n-k}\rangle - \mathrm{e}^{-\mathrm{i}\delta\omega^+_{k,(n-k)}t}\, \mathcal{B}^2_{k,(n-k)}(z,z')\, \langle b_k b_{n-k}\rangle + \mathrm{H.c.}\Bigg] .\end{aligned} \tag{5.7}$$

The first sum represents the diagonal and the latter the off-diagonal contributions of the matrices

$$\mathcal{B}^1_{n,m}(z,z') = F^*_n(z,z')F_m(z,z') \tag{5.8}$$

$$\mathcal{B}^2_{n,m}(z,z') = F_n(z,z')F_m(z,z') \,, \tag{5.9}$$

where $F_n(z,z') := f^-_n(z) - f^-_n(z')$. Both matrices are symmetric under the exchange of the spatial coordinates $z$, $z'$. Additionally $\mathcal{B}^1_{n,m}$ is hermitian and $\mathcal{B}^2_{n,m}$ is symmetric. Based on these properties, the calculations are greatly simplified once a specific geometry (i.e. external potential) of the system is chosen. Further we define the frequency sum and differences as $\delta\omega^\pm_{k,(n-k)} = \omega_{n-k} \pm \omega_k$, emergent with the off-diagonal elements of the $\mathcal{B}$ matrices. We explicitly separated these in Eq. (5.7) as they are often neglected in the literature [208], which is in general not justified for a generic far-from equilibrium state.

### Quasi-particle creation and GGE for weakly interacting Bose gases

In order to introduce physical meaning to the time evolution described by Eq. (5.7) we need to calculate the initial conditions in terms of the quasiparticles for which the time evolution constitutes a simple rotation with frequency $\omega_m$. This amounts to expanding the density and phase fluctuations in the eigen-basis of the new Hamiltonian. The inversion of Eqs. (2.20) & (2.21), using the normalization condition Eq. (2.22), results in the expression for the quasiparticle operators

$$b_m = \int \mathrm{d}z\, \frac{1}{\sqrt{2\rho_0}} \bar{f}^-_m \delta\hat{\rho} + \mathrm{i}\sqrt{\frac{\rho_0}{2}}\bar{f}^+_m \hat{\theta} \,, \tag{5.10}$$

where $b_m^\dagger$ is given by the Hermitian conjugate of Eq. (5.10). The desired quasiparticle correlations are given by

$$\langle b_m^\dagger b_n\rangle = \frac{1}{2}\iint \mathrm{d}z\,\mathrm{d}z'\left[\frac{f_m^-(z)\bar{f}_n^-(z')\langle\delta\hat{\rho}(z)\delta\hat{\rho}(z')\rangle}{[\rho_0(z)\rho_0(z')]^{\frac{1}{2}}} + \frac{f_m^+(z)\bar{f}_n^+(z')\langle\hat{\theta}(z)\hat{\theta}(z')\rangle}{[\rho_0(z)\rho_0(z')]^{-\frac{1}{2}}}\right] - \frac{1}{2}\delta_{m,n} \tag{5.11}$$

$$\langle b_m b_n\rangle = \frac{1}{2}\iint \mathrm{d}z\,\mathrm{d}z'\left[\frac{\bar{f}_m^-(z)\bar{f}_n^-(z')\langle\delta\hat{\rho}(z)\delta\hat{\rho}(z')\rangle}{[\rho_0(z)\rho_0(z')]^{\frac{1}{2}}} - \frac{\bar{f}_m^+(z)\bar{f}_n^+(z')\langle\hat{\theta}(z)\hat{\theta}(z')\rangle}{[\rho_0(z)\rho_0(z')]^{-\frac{1}{2}}}\right]. \tag{5.12}$$

To shorten the notation we dropped the terms containing correlations between the density and phase fields, as they have vanishing contributions for all states considered in this thesis. The remaining correlations are given by the commutation relations of the quasiparticle Fock operators and the Hermitian conjugate of Eqs. (5.11) & (5.12) respectively.

In accordance with the diagonal ensemble, we can calculate the steady state of the system through the long-time average of the observable. As the quasiparticle occupation numbers $n_m = \langle b_m^\dagger b_m\rangle$ are the only time-independent, non-oscillatory contributions to the sum in Eq. (5.7), where now and in the following we will always assume that the spectrum is non-degenerate, the long time average is given by

$$\begin{aligned}\langle\Delta\hat{\theta}(z,z')^2\rangle_\infty &= \lim_{T\to\infty}\frac{1}{T}\int \mathrm{d}t\,\langle\Delta\hat{\theta}(z,z',t)^2\rangle \\ &= \frac{1}{2\sqrt{\rho_0(z)\rho_0(z')}}\sum_{m=1}\mathcal{B}^1_{m,m}(z,z')\left(2\langle b_m^\dagger b_m\rangle + 1\right).\end{aligned} \tag{5.13}$$

This relaxed state can be described by a GGE

$$\hat{\rho}_{\mathrm{GGE}} = \frac{1}{Z}\mathrm{e}^{-\sum_m \lambda_m b_m^\dagger b_m}, \tag{5.14}$$

completely defined by the conserved quasiparticle occupation numbers $\hat{I}_m = b_m^\dagger b_m$. The Lagrange multipliers $\lambda_m$ are given by

$$\lambda_m = \mathrm{Ln}\left(1 + \langle b_m^\dagger b_m\rangle^{-1}\right). \tag{5.15}$$

Since expectation values of conserved quantities can be evaluated at any time, the GGE is fully determined by the initial conditions Eq. (5.11).

Note that while $\hat{I}_m$ are conserved they are neither local nor extensive. It is however always possible to construct local and extensive conserved quantities linearly related to the mode occupations which justifies the Generalized Gibbs state in the form of Eq. (5.14). For a non-interacting theory in the presence of additional symmetries of the dispersion relation the quasiparticle occupation numbers do not form a complete set of conserved charges.

The constraints inflicted on the system by these additional conserved quantities need to be considered in the maximum entropy state and alter the form of the GGE as compared to Eq. (5.14) [8].

While in the harmonic theory the long time average of the phase correlation function Eq. (5.7) is by definition described by Eq. (5.14), the question remains if and for how long the system is actually close to the predictions of this GGE. In other words, does the long time limit of an observable converge to Eq. (5.13). In the thermodynamics limit and in the absence of regularities in the spectrum this is commonly the case. However, as we will see explicitly below for the harmonically confined system, finite size effects and regularities in the spectrum can lead to strong deviations and can prevent the system from reaching the steady state predictions in the long time limit.

#### Long Time Evolution and Non-linear Relaxation

In case of a harmonic system the above calculations would constitute a full discussion of the relaxation dynamics. However, in our system of two coupled quantum wires the GGE Eq. (5.14) is based only on approximately conserved quantities and the system is expected to deviate from the Bogoliubov predictions on larger time-scales. Higher-order corrections in the perturbative expansion couple the symmetric and relative degrees of freedom which leads to a further relaxation of the system driven by physics beyond the harmonic approximation [209, 210, 194, 211]. Considered in terms of the quasiparticles, this long-term relaxation is connected to the breaking of integrability of the harmonic model. While the effect of weak integrability breaking perturbations is a well studied topic in classical systems, culminating in the Kolmogorov-Arnold-Moser (KAM) theorem [23], no general results are available in the quantum regime [32, 24]. The non-linear dephasing of the two condensates constitutes a truly one-dimensional effect which arises due to the coupling of different Bogoliubov modes in higher-order perturbation theory, while the system is still described by the integrable Lieb-Liniger model. The subsequent relaxation is therefore only a manifestation of the fact that Eq. (5.14) is not based on the conserved quantities of the full model [12]. It is an open question whether the system relaxes to a GGE determined by the full Lieb-Liniger model, reduces for all practical purposes to a simple Gibbs ensemble defined by the equipartition of energy, or if e.g. another set of quasi-conserved quantities emerges that determines the statistical properties of the system on intermediate time-scales.

## 5.3 Homogeneous Systems and Prethermalization

After this general introduction we will now specify our system. As a first example we consider the most simple case of a homogeneous condensate with periodic boundary conditions. We

choose the system to be sufficiently large to be able to neglect finite size effects or influences due to the discreteness of the spectrum. These effects, of high interest in themselves, will be discussed in chapter 6.

Let us first evaluate the general equations discussed in the last section for this specific system. Since the bulk density is spatially independent $\rho_0(z) = n_0$, where $n_0$ is the density in a single condensate after the splitting, Eqs. (5.11) & (5.12) together with the orthogonality of the mode functions lead to the only non-vanishing quasiparticle correlations

$$\langle b_k^\dagger b_k \rangle + \frac{1}{2} = \frac{1}{4}\left[\frac{\epsilon_k}{E_k} + \frac{E_k}{\epsilon_k}\right] \tag{5.16}$$

$$\langle b_k b_{-k} \rangle = \langle b_k^\dagger b_{-k}^\dagger \rangle = \frac{1}{4}\left[\frac{\epsilon_k}{E_k} - \frac{E_k}{\epsilon_k}\right] . \tag{5.17}$$

The correlations are dominated by the first term inside the brackets which stems from the binomial density fluctuations. The highly suppressed second term $E_k/\epsilon_k \ll 1$ accounts for the vacuum fluctuations of the phase due to the uncertainty principle. Due to the conservation of the total momentum quasiparticles are created by the quench in correlated pairs of $\pm k$ and the system is therefore in a highly two-mode squeezed state.

The time-evolution of the phase correlation function is given by Eq. (5.7) which upon evaluation for the above initial quasiparticle correlations takes the form

$$\langle \Delta\hat{\theta}(z, z', t)^2 \rangle = \frac{4mg}{\hbar^2 L} \sum_k \left[\frac{\sin(\omega_k t)^2}{k^2}(1 - \cos(k\bar{z})) + \frac{\hbar^2}{4mgn_0}(1 - \cos(k\bar{z}))\right] , \tag{5.18}$$

where we used $\mathcal{B}^1_{k,k} = \mathcal{B}^2_{-k,k} = 2(1 - \cos(k\bar{z}))$ with the distance $\bar{z} = z - z'$. The second term stems from the vacuum fluctuations in the minimum uncertainty state. We neglect these minor quantum fluctuations in the following, which is justified since $\epsilon_k \geq E_k$ and therefore their contribution to the sum is always smaller than the vacuum fluctuations in a single condensate. Further as its contribution is time-independent it merely represents a constant shift of the phase correlation function, slightly decreasing the coherence of the state in accordance with the uncertainty principle. The remaining first term fully determines the dynamics of the system. Astonishingly it is equivalent to the Luttinger-Liquid predictions (c.f. [208, 135, 38]) although Eq. (5.18) is also valid for $\epsilon_k > \mu$, i.e. beyond the linear regime.

The time-evolution is determined by the oscillation of each quasiparticle mode, leading to an initial growth of the phase variance as fluctuations rotate from the density into the phase quadrature. As a result of the different oscillation frequencies $\omega_k$, the quasiparticle modes dephase which leads to a randomization of the phase profile [208]. It is this quasiparticle dephasing that gives rise to the local emergence of relaxed correlations in the system. In case of a common speed of the excitations this randomization traverses the system in a light-cone

like fashion, leading to the emergence of the relaxed state for distances $\bar{z} < 2c_s t$. This can be seen by taking the derivative with respect to time of Eq. (5.18), which in the phononic limit $\epsilon_k = \hbar c_s k$ leads to [208]

$$\partial_t \langle \Delta\hat{\theta}(z, z', t)^2 \rangle = \frac{4c_s}{\lambda_{T_{\text{eff}}}} \Theta\left(\bar{z} - 2c_s t\right) \,, \tag{5.19}$$

with the Heaviside function $\Theta(x) = 1$ for $x > 0$ and zero otherwise[2] and we in foresight defined $\lambda_{T_{\text{eff}}} = 2\hbar^2/(mg)$. The phase variance increases linearly for times $2c_s t \leq \bar{z}$ (for a fixed distance $\bar{z}$) after which the time derivative Eq. (5.19) vanishes and the phase variance is locally conserved (strictly only in the thermodynamic limit, see chapter 6). From the light-cone like time-evolution of the phase variance (5.19) we can immediately infer the emergence of a thermal distribution for the relaxed state of our system. Integrating Eq. (5.19) in time and using the fact that the correlations become stationary at times $t = |\bar{z}|/(2c_s)$ allows us to write the final relaxed state for the phase correlation function

$$C_\infty(\bar{z}) \equiv \exp\left(-\frac{1}{2} \lim_{t\to\infty} \langle \Delta\hat{\theta}(z, z', t)^2 \rangle\right) = \exp\left(-\frac{|\bar{z}|}{\lambda_{T_{\text{eff}}}}\right) \,. \tag{5.20}$$

While we could have gotten this relaxed state by taking the long time average[3] of Eq. (5.18), using this approach the emergence of exponentially decaying two-point correlation functions simply connected to the presence of a sharp light-cone effect [39]. We therefore expect these results to transfer to more complicated systems and geometries, at least up to times where e.g. boundary effects in a finite size system can be neglected.

Comparing the relaxed form of the correlation function (5.20) to the predictions of a thermal state Eq. (2.74) we can identify $\lambda_{T_{\text{eff}}}$ with en effective thermal coherence length defining an effective temperature

$$k_B T_{\text{eff}} = \frac{n_0 g}{2} = \frac{\mu}{2} \,, \tag{5.21}$$

for the relative degrees of freedom [13, 212, 14, 38]. In particular $T_{\text{eff}}$ is independent of the initial temperature $T$ of the system prior to the splitting and the complete system remains in a non-equilibrium state, even after all correlations have taken their quasi-stationary, relaxed form. This effect of the emergence of apparent thermal correlations, long before the system had time to fully equilibrate, was first encountered in the context of heavy-ion collisions and termed prethermalization [34, 35].

We will now show explicitly that the steady state of the system is in the most general case defined by a GGE determined from the conserved quantities. The emergence of the above

[2] More specific we get $\Theta(x) = \frac{1}{2}(1 + \text{sgn}(x))$

[3] Upon neglecting the small quantum contributions (second term) and performing the $k$ integration.

prethermalized state will thereby be related to the reduction of the GGE to an effective Gibbs ensemble. This allows us to connect the phenomenon of prethermalization to the approach of a maximum entropy state determined by quasi-conserved quantities of an underlying near-integrable model. The GGE is defined by its Lagrange multipliers (5.15) determined for the initial state values of the conserved quantities of the system. In the harmonic approximation we found the quasiparticle occupation numbers to define a suitable complete, local, and extensive set of conserved quantities, for which we get the Lagrange multipliers

$$\lambda_k = \mathrm{Ln}\left(1 + \langle b_m^\dagger b_m \rangle^{-1}\right) = \mathrm{Ln}\left(1 + \left(\frac{1}{4}\left[\frac{\epsilon_k}{E_k} + \frac{E_k}{\epsilon_k}\right] - \frac{1}{2}\right)^{-1}\right) . \tag{5.22}$$

These are exact within the harmonic approximation and describe the long-time steady state of the system within the full Bogoliubov theory. We can however, due to the high occupation of quasiparticle modes in the phononic regime neglect the quantum contributions to Eq. (5.22) to get the approximate result

$$\lambda_k \simeq \mathrm{Ln}\left(1 + \frac{4E_k}{\epsilon_k}\right) \simeq \frac{4E_k}{\epsilon_k} = \beta_{\mathrm{eff}}\epsilon_k \, , \tag{5.23}$$

where we expand the logarithm, i.e. taking the Rayleigh–Jeans limit of the Bose-Einstein distribution valid for high occupation numbers, and define the effective, $k$-independent, inverse temperature $\beta_{\mathrm{eff}}^{-1} = k_{\mathrm{B}} T_{\mathrm{eff}}$. Therewith the GGE Eq. (5.14) reduces in the phononic limit to the usual Gibbs ensemble

$$\hat{\rho}_{\mathrm{GGE}} \simeq \frac{1}{Z} \mathrm{e}^{-\beta_{\mathrm{eff}} \sum_m \epsilon_k b_m^\dagger b_m} = \frac{1}{Z} \mathrm{e}^{-\beta_{\mathrm{eff}} H} \, , \tag{5.24}$$

described by just a single Lagrange multiplier[4], the effective inverse temperature of the system corresponding to the conservation of the total energy. The quench therefore leads to an instantaneous equipartition of energy among the different modes.

## 5.4 Harmonically Trapped Systems and Off-Diagonal Correlations

After our discussion of the homogeneous system we now turn our attention to an experimentally more relevant configuration of a harmonic external potential $V(z) = m\omega^2 z^2/2$. We will again first discuss the analytical results within the harmonic theory before comparing them to the numerical simulations of the relaxation dynamics within the full non-linear model.

[4] In the grand canonical ensemble the conservation of the particle number introduces a second Lagrange multiplier $\mu$, corresponding to the chemical potential

Due to the spatial dependence of the bulk density the initial state density-density correlations within the Thomas-Fermi approximation now take the shape of an inverted parabola

$$\langle \delta\hat{\rho}_{\mathrm{r}}(z)\delta\hat{\rho}_{\mathrm{r}}(z')\rangle = \frac{n_0}{2R_{\mathrm{TF}}}\left(1-x^2\right)\delta(x-x') = \frac{n_0}{3R_{\mathrm{TF}}}\left(P_0(x)-P_2(x)\right)\delta(x-x')\,, \tag{5.25}$$

where we used the scaled length $x = z/R_{\mathrm{TF}}$ with the Thomas-Fermi radius $R_{\mathrm{TF}}$ and the peak density $n_0 = \mu/g$. For the last equality, we expressed the inverted parabola through the Legendre polynomials $P_{0,2}$. This is advantageous when calculating the initial state quasiparticle correlations, as the relevant spatial dependence of the mode functions is given by $f_m^{\pm}(z) \sim P_m(x)$. Note that while the mode functions in general contain the spatially dependent terms $(1-x^2)^{\mp}$, these do not influence the correlations of quasiparticles due to the spatially dependent bulk density $\rho_0(z)$ (see e.g. Eq. (5.10)).

Evaluation of the correlations for the above local binomial splitting one is faced with the problem of diverging phase fluctuations at the edges of the cloud $|z| \to R_{\mathrm{TF}}$, when considering the minimum uncertainty state Eq. (5.5). This seeming contradiction is based on the inevitable breakdown of the harmonic approximation near the edges of the cloud. On the other hand, since the mean field density is vanishing, density and phase fluctuations approach their respective values for a vacuum state and hence the phase fluctuations remain finite. They therefore, equivalent to the homogeneous case, raise only minor corrections to the initial correlations within the central part of the cloud. We will hence ab initio neglect the influence of the initial state minimum uncertainty phase fluctuations and confirm the validity of this approximation later on when comparing to numerical simulations of the full model.

Another difference of the harmonically trapped system as compared to the homogeneous condensate is the introduction of another scale $R_{\mathrm{TF}}$ connected to the bulk density, in addition to the chemical potential $\mu$. In the homogeneous system the solutions of the bulk density are smoothly connected by a simple rescaling of the interaction constant $g$. In other words when changing the mean field density $\rho_0$ the equations of motion for the bulk are invariant after a shift in $\mu$. In the harmonically trapped system on the other hand, the additional length scale requires the adjustment of a second parameter. To counteract the halvening of atoms during the splitting process we therefore consider an instantaneous dressing of the longitudinal trapping frequency $\omega \to \omega/\sqrt{2}$, to avoid the excitation of a breathing mode. The mean field density $\rho_0(z)$ in each of the wells consequently remains a stationary solution of the mean field equations, allowing us to continue the usage of the standard Bogoliubov equations discussed in chapter 3.

Before discussing the full time evolution of the phase correlation function we first calculate the steady state predictions described by the GGE. Calculating the quasiparticle

occupation numbers under the above assumptions we obtain

$$n_m = \frac{\mu}{2\epsilon_m}\left[\frac{2}{3}\left(1 - \frac{m(m+1)}{(2m-1)(2m+3)}\right)\right] = \frac{\mu}{2\epsilon_m}\mathcal{A}_m \,, \tag{5.26}$$

where the eigenstates are now labeled by the discrete index $m \in \mathbb{N}\backslash\{0\}$. The factor $\mathcal{A}_m$ is a result of the spatial dependence of the density-density fluctuations (5.25), rapidly approaching the limit $\mathcal{A}_m \to 0.5$ for $m \gg 1$. Direct calculation of the associated Lagrange multipliers (5.15), using again the Rayleigh-Jeans limit for high occupations, leads to

$$\lambda_m \simeq \frac{2}{\mathcal{A}_m \mu}\epsilon_m \underset{m\gg 1}{\to} \frac{4}{\mu}\epsilon_m \,. \tag{5.27}$$

Astonishingly the long time average of correlations is described approximately by a Gibbs ensemble with an effective temperature $k_\mathrm{B}T_\mathrm{eff} = \mu/4$, which dropped by a factor of two as compared to the homogeneous system due to the spatial dependence of the bulk density. In [208] the same effective temperature $\mu/2$ as in the homogeneous system was found as a result of the assumption of homogeneous density-density correlations proportional to the peak density of the trapped system. Therewith, $f_m^{\pm}(z) \sim P_m(x)$ are the only spatially dependent parameters entering the quasiparticle correlations, which together with the orthonormality of the Legendre polynomials leads to similar predictions for harmonically trapped and homogeneous condensates, in particular the only non-vanishing initial quasiparticle correlations $\langle b_m^\dagger b_m\rangle \simeq \langle b_m b_m\rangle = \langle b_m^\dagger b_m^\dagger\rangle$.

The effective temperature Eq. (5.27), while indisputable for time-averaged observables within the above model, raises the question how the discontinuity in temperature can be resolved when approaching the homogeneous limit. Upon taking the thermodynamic limit, $\omega \to 0$ ($\mu = \text{const.}$), the effective temperature Eq. (5.27) does not change, while the system approaches a homogeneous bulk density. We therefore find different effective temperatures for the homogeneous, infinite system based on the way the thermodynamic limit was taken, which is a highly unsatisfactory result. To resolve the apparent inconsistency we now calculate the full time evolution of the phase correlation function to study its approach to the GGE prediction. First note that upon neglecting the minor quantum contributions to the quasiparticle integrals we get

$$\langle b_m^\dagger b_n\rangle \simeq \langle b_m b_n\rangle = \langle b_m^\dagger b_n^\dagger\rangle \,. \tag{5.28}$$

Using Eq. (5.25) the quasiparticle correlations are given by integrals of the form

$$\langle b_m^\dagger b_n\rangle \sim \int \mathrm{d}x\; P_m(x)P_n(x)\left(P_0(x) - P_2(x)\right) \,. \tag{5.29}$$

These integrals, for any value of $n, m$, can be evaluated in closed form resulting in the general expression for the initial state correlations

$$\langle b_m^\dagger b_n \rangle = \begin{cases} \frac{\mu}{2\epsilon_m}\mathcal{A}_m & \text{if } m = n \\ -\frac{2\mu}{3}\sqrt{\frac{(m+1/2)(n+1/2)}{\epsilon_m\epsilon_n}} \begin{pmatrix} 2 & m & n \\ 0 & 0 & 0 \end{pmatrix}^2 & \text{if } m \neq n \end{cases}, \tag{5.30}$$

where $(\dots)^2$ is the square of the Wigner $3j$-symbol given by the second term ($\sim P_2(x)$) of the integrals (5.29). The first term proportional to $P_0(x) = \text{const}$ contributes only to the diagonal part $m = n$, due to the orthogonality of the Legendre polynomials. We therefore find that in general any spatially dependent modulation of the density-density correlations, especially also a local position dependent squeezing $\xi_{\mathrm{n}}(z)$ of the state, will introduce non-vanishing off-diagonal correlations between quasiparticle modes. Evaluating the general form of the time-dependent phase correlation function (5.7), accounting for the fact that for the harmonically trapped system $\mathcal{B}^1 \equiv \mathcal{B}^2$, due to the real mode functions $f^\pm \in \mathbb{R}$, and explicitly taking into account the off-diagonal contributions we find

$$\begin{aligned} \langle \Delta\hat{\theta}(z, z', t)^2 \rangle = & \frac{g\mu}{R_{\mathrm{TF}}} \sum_m \left\{ \frac{2m+1}{\epsilon_m^2} \Delta P_m(x, x')^2 \sin^2(\omega_m t) \mathcal{A}_m \right\} - \left\{ \frac{4(2m+1)(2m+5)}{3\epsilon_m\epsilon_{m+2}} \right. \\ & \left. \begin{pmatrix} 2 & m & m+2 \\ 0 & 0 & 0 \end{pmatrix}^2 \Delta P_m(x, x') \Delta P_{m+2}(x, x') \sin(\omega_m t) \sin(\omega_{m+2} t) \right\}. \end{aligned} \tag{5.31}$$

Here we defined $\Delta P_m(x, x') = P_m(x) - P_m(x')$ to shorten the notation and used the triangular inequality for the Wigner $3j$-symbol to re-arrange the double sum in Eq. (5.7) connected to the off-diagonal contributions. For the considered case of a local binomial splitting of the condensate we find from Eq. (5.31) that the quench introduces non-vanishing quasiparticle correlation between modes with index $m$ and $m + 2$.

To gain some analytical understanding for the time evolution of the phase correlation function, we factor out the contribution of a thermal state with an effective temperature $\mu/2$, corresponding to the first term in Eq. (5.31) with $\mathcal{A}_m \equiv 1$, and define the remainder

$$\delta T_m(x, x', t) = \mathcal{A}_m - \frac{4(2m+5)}{3} \begin{pmatrix} 2 & m & m+2 \\ 0 & 0 & 0 \end{pmatrix}^2 \frac{\omega_m \sin(\omega_{m+2} t) \Delta P_{m+2}(x, x')}{\omega_{m+2} \sin(\omega_m t) \Delta P_m(x, x')}, \tag{5.32}$$

as an effective mode, time, and spatially dependent scaling of this effective temperature. Considering first the thermodynamic limit to see if the inclusion of correlations between the different quasiparticle modes has resolved the problem of the difference in temperature

between the homogeneous and harmonically trapped condensates. For $\omega \to 0$ we can linearize the sinusoidal time-dependence in Eq. (5.32) while the validity of the mode functions $2\epsilon_m < \mu$ can be extended to $m \to \infty$. Significant decay of the phase correlation function occurs at small scaled distances $|x| \ll 1$ and retains dominant contributions only from high $m$ modes. We can therefore Taylor-expand $\Delta P_m(x, x')$ around a variable but fixed $x = x_0$ for which the leading order contributions in $|x' - x_0| \ll 1$ are

$$\Delta P_m(x_0, x') = \begin{cases} \partial_x P_m(x)|_{x=x_0} = -\frac{2\sqrt{\pi}}{\Gamma(-\frac{m}{2})\Gamma(\frac{m}{2}+\frac{1}{2})} & m = \text{odd} \\ \\ \frac{1}{2}\partial_x^2 P_m(x)|_{x=x_0} = -\frac{2^{m-1}\Gamma(\frac{m}{2}+\frac{3}{2})}{\Gamma(m)\Gamma(\frac{1}{2}-\frac{m}{2})} & m = \text{even} \end{cases} . \tag{5.33}$$

Evaluating the mode dependent scaling of the temperature (5.32) within the approximation (5.33) we get $\delta T_m(x, x', t) \to 1$ for $m \gg 1$ and hence the harmonically trapped system in the thermodynamic limit approaches a steady state determined by an effective temperature $k_B T_{\text{eff}} = \mu/2$. Together with the agreement of the thermal state phase correlation function[5] for the harmonically trapped and homogeneous condensates (see Fig. 2.4) we find a consistent effective temperature in the thermodynamic limit.

The above emergence of differences between the conserved quantities in the thermodynamic limit reveals the problem for the harmonically trapped system. It is usually assumed that a steady state exists, which for a finite size system is because of the discreteness of the spectrum not necessarily fulfilled. The convergence of observables to the GGE prediction for most of the time during the evolution is directly connected to the condition that time-dependent oscillatory parts of correlation functions have vanishing contributions in the long time limit. The time-dependence of the phase correlation function (5.7) is given by general integrals of the form[6]

$$\int \mathrm{d}k\, \mathcal{F}(k) \mathrm{e}^{\mathrm{i}(kz+\alpha\omega(k)t)} = \int \mathrm{d}k\, \mathcal{F}(k) \mathrm{e}^{\mathrm{i}\Phi(k,t)} , \tag{5.34}$$

with an arbitrary real function $\mathcal{F}(k)$. For a generic gapped, $k$-dependent frequency $\omega(k)$ vanishing contributions in the long time limit are shown by the stationary phase approximation [213][7]. For a gapless dispersion relation the stationary phase argument does not

[5] For small temperatures the deviations at the edges of the cloud for $|x| \to 1$ are irrelevant as the phase correlation function in the thermodynamic limit is dominated by $|x| \ll 1$

[6] For convenience we will work in the continuum limit

[7] Herein the phase $\Phi(k, t)$ is Taylor-expanded to second order around the saddle-point $k_0$ defined by $\partial_t \Phi(k, t)|_{k_0} = 0$. The integral Eq. (5.34) is then given by

$$\int \mathrm{d}k\, \mathcal{F}(k) \mathrm{e}^{\mathrm{i}\Phi(k,t)} \sim |\mathcal{F}(k_0)| \sqrt{\frac{1}{|\partial_t^2 \Phi(k_0(t), t)|}} \cos\left(\Phi(k_0, t) \pm \frac{\pi}{4}\right)$$

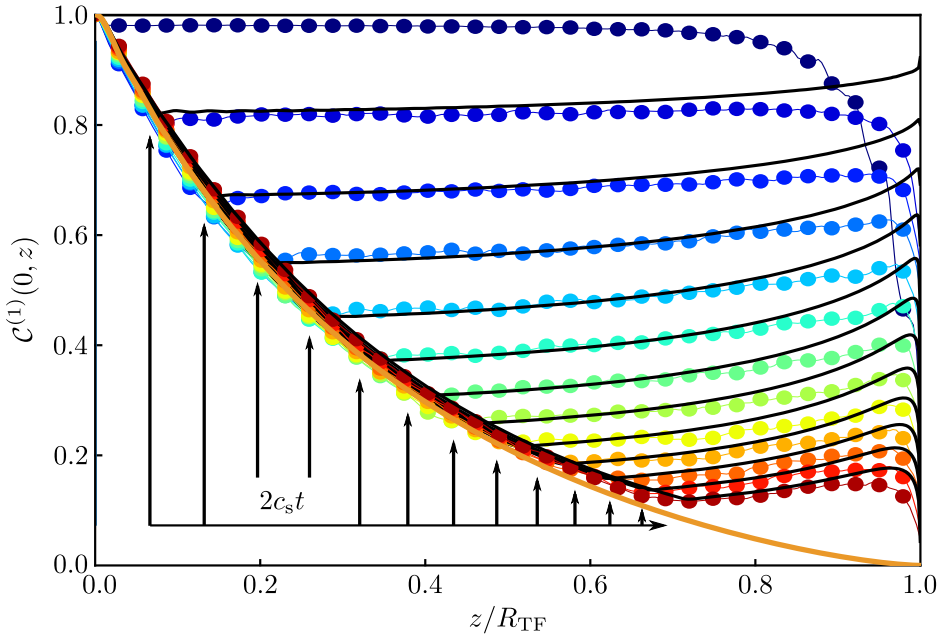


Fig. 5.1 Short time dephasing dynamics for coherently split, harmonically trapped condensates. Depicted is the time evolution of the first order coherence function $C^{(1)}(z,t)$ for the first 12 ms after the local binomial splitting in steps of 1 ms (from blue to red) obtained through simulations of the GPE equation. The parameters are $N2500$ atoms per well, $\omega = 7.5$ Hz, and $T = 0$ in the initial state prior to the splitting. Dephasing of quasiparticle excitations leads to a light-cone like spread of correlations following the local speed of sound $c_s$ in the trapped system (arrows depict the theoretical values). The analytical solution (5.31) is in good agreement with the full non-linear simulation. Notably, correlations inside the light-cone approach a thermal state of temperature $k_B T = \mu/2$ (orange line), which is a factor of two larger than the effective temperature of the GGE (5.27). This additional decrease of correlations is caused by a second light-cone stemming from the off-diagonal quasiparticle correlations caused by the local binomial splitting of the condensate.

straightforwardly apply, however generically the contributions vanish in the long time limit and the system converges to the GGE predictions. In our case of a homogeneous system the decay of these oscillatory terms is connected to the dephasing of quasiparticle modes. In the thermodynamic limit the spectrum is continuous, such that no recurrences occur. For the harmonically trapped system, however, the general form of the time-dependent phase correlation function (5.7) exhibits contributions from the off-diagonal quasiparticle correlations $\langle b_m^\dagger b_{m+2}\rangle$, whose time-dependence is in part determined by the frequency differences $\delta\omega^-_{m,m+2} = \omega_{m+2} - \omega_m$. The remaining off-diagonal contributions evolve with the frequency sums $\delta\omega^+_{m,m+2}$ which are explicitly dependent on $m$ and hence vanish in the long time limit on account of the stationary phase method. Due to the near linearity of the dispersion relation

$\omega_m \sim \sqrt{m(m+1)}$ we find an approximately constant frequency difference $\delta\omega^-_{m,m+2} \simeq \omega$ and the stationary phase approximation is no longer applicable, since $\omega(k) = \text{const}$ and the time dependence can be taken out of the integral. These contributions hence do not vanish in the long time limit and their contribution to the phase variance is of the same order as the conserved quasiparticle occupations. This lowers the effective temperature of the GGE as compared to the homogeneous case. In the thermodynamic limit the frequency of these off-diagonal oscillations approaches zero and the system, after the initial dephasing, shows no sign of recurrent behavior. The approach of the prethermalized state, however, now is not simply connected to the conserved charges of the harmonically trapped system, but new conserved quantities emerge in the limit $\omega \to 0$ connected to the occupation numbers of a homogeneous system.

In Fig. 5.1 we show the time evolution of the first-order coherence function $C^{(1)}(0, z, t)$ for the short time dephasing dynamics over the first 12 ms after the decoupling of the two condensates. We compare the analytical solution (5.31) (black solid lines) to numerical simulations of the full non-linear wave equation for temperature $T = 0$ within the TWA. The initial state is a single Bose gas for which the TWA quantum noise is sampled in the Bogoliubov basis, adding on average half a particle in each mode. The system at $t = 0$ is split coherently, following a local binomial distribution of atoms in the left and right well and the corresponding minimum uncertainty fluctuations of the relative phase, and subsequently the uncoupled condensates are propagated according to the classical equations of motion.

The relative phase between the two condensates is initially almost perfectly correlated, leading to the observed value of $C^{(1)}(0, z) \approx 1$ over the whole extent of the cloud. The slight decrease in the central part and the rapid decay towards the edges of the cloud are the result of the minimum uncertainty phase fluctuations, which in particular lead to a completely random phase between the two condensates once the density approaches zero. Although these contributions are neglected in the analytical equation we find good agreement between the numerical and analytical results, which confirms our previous assumption that also in the case of harmonic confinement phase fluctuations raise only minor corrections to the dynamics of the system.

The system follows the predicted light-cone like spreading of correlations, leading to a decay of $C^{(1)}$ up to a distance $z = 2c_s t$, after which long-range order is still present in the system as can be seen by the constant value of $C^{(1)}$. The light-cone follows the local speed of sound in the trapped system, slowing down towards the edges of the condensate. In the homogeneous system correlations inside the light cone were relaxed to their final steady state predictions. Here, however, we find that off-diagonal contributions lead to a second light-cone that spreads through the system with the same velocity as the diagonal contributions. The correlation function $C^{(1)}$ therefore does not approach the GGE predictions (5.27), but dephases in the short time dynamics towards the final temperature state of the

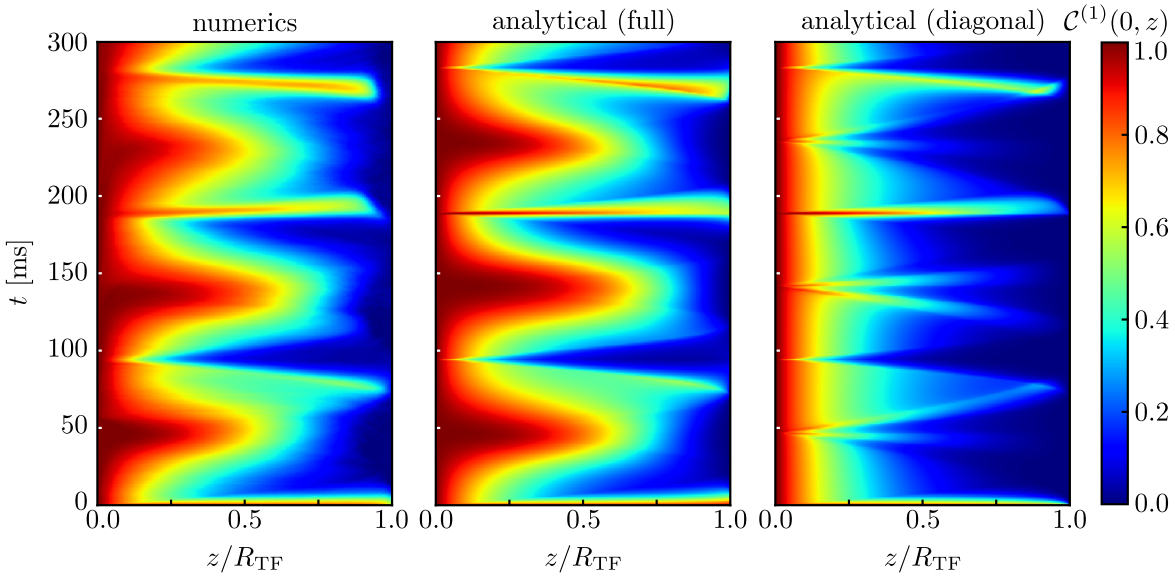


Fig. 5.2 Long time evolution of $C^{(1)}(z,t)$ for the trapped system. The long time evolution reveals strong revivals of phase coherence in the harmonically trapped system, caused by the rephasing of off-diagonal quasiparticle correlations. The analytical solution (5.31) is in good agreement with the full numerical simulation of the GPE equation. For comparison we show the results of [208], assuming constant density-density correlations caused by the splitting process. Therein off-diagonal correlations are absent and the system after dephasing stays close to the GGE predictions. Large recurrences of phase coherence at $t \approx 200, 275$ ms caused by rephasing of the diagonal quasiparticle correlations are visible in all figures.

homogeneous system, given by a temperature $k_{\mathrm{B}}T_{\mathrm{eff}} = \mu/2$ (solid orange line). This shows that also in an inhomogeneous finite size system the local relaxation hypotheses [39, 14] holds for time scale $t \lesssim L/c_{\mathrm{s}}$ below the system size $L$, but may be more complicated than the simple dephasing of uncorrelated quasiparticle modes.

In the limit $\omega \to 0$ this second light cone leads to the system approaching the correct thermodynamic limit. Here on the other hand, the finite trapping frequency leads to periodic recurrences of phase coherence due to the rephasing of off-diagonal contributions. In the long term evolution Fig. 5.2 this rephasing is prominently visible as low frequency oscillations, which lead to a restoration of phase coherence at times $\omega t = (2n+1)\pi/\sqrt{2}$, following from the frequency-differences $\delta\omega_{m,m+2}$. Apart from these off-diagonal contributions, two recurrences of phase coherence are clearly visible at $t \approx 200, 275$ ms. These are caused by the rephasing of the diagonal quasiparticle correlations, dominated by the lowest lying modes (as higher modes approximately approach a linear dispersion relation $\omega_m \sim m$). For comparison we show the results of [208] where homogeneous density-density correlations were assumed, and hence only diagonal quasiparticle correlations are present. Therein, equivalent to the homogeneous case, the system relaxes during the initial dephasing to the GGE predictions

$k_B T_{\text{eff}} = \mu/2$, leading again to a well defined prethermalized state. It is however unclear how such a state could be realized, given the diverging squeezing $\xi_n = (1 - x^2)^{-1}$ towards the edges of the cloud. In the full analytical model, assuming local binomial splitting, the observed large oscillations lead to the predicted decrease of the effective temperature in the GGE by a factor of two for the long time average, and the approach of the prethermalized state for temperature $T = 0$ is only transient.

## 5.5 Experimental observation of a Generalized Gibbs Ensemble

We now turn to the experimental implementation of the splitting process [15]. Our experiment starts with a phase fluctuating 1D Bose gas which is prepared and trapped using an atom chip [64]. The trap frequencies are $\omega_\perp = 2\pi \cdot (2.1 \pm 0.1)\,\text{kHz}$ and $\omega_\parallel = 2\pi \cdot (10 \pm 0.5)\,\text{Hz}$. The initial temperature, atom number, and chemical potential are $T = 30 \ldots 110\,\text{nK}$, $N = 5000 \pm 500$, and $\mu = \hbar \cdot (1.3 \pm 0.1)\,\text{kHz}$ respectively, such that the 1D condition (2.4) is well fulfilled. The coherent splitting of the gas is achieved through smooth deformation of the trap in a dressed state double-well potential by superimposing the static trapping potential with linearly polarized RF radiation with a time dependent amplitude [38, 214, 215]. The splitting ramp is performed in two segments $\tau_1$ and $\tau_2$, where during the first period the longitudinal trapping potential is rapidly changed to its final value $\omega_\parallel = 2\pi \cdot 7.5\,\text{Hz}$. At the end of the splitting ramp the trap has a measured radial frequency of $\omega_\perp = 2\pi \cdot (1.4 \pm 0.1)\,\text{kHz}$. While the longitudinal potential is dressed by approximately a factor of $\sqrt{2}$, the excitation of a breathing mode is inherent to the experimental splitting process due to the finite splitting time. However, since the breathing period is $\approx 75\,\text{ms}$ and symmetric in both condensates it can be neglected for the time scale of the experiment presented in this Section. The decoupling of the two gases happens approximately 3 ms before the end of the splitting ramp within a time period of less than $500\,\mu\text{s}$. The completely decoupled far-from-equilibrium system is afterwards held for a time $t$, after which the system is probed through matter-wave interferometry [13, 14, 215, 212], giving access to the spatially resolved relative phase $\theta_r$. The system has a typical length of approximately $100\,\mu\text{m}$ of which we use the central $60\,\mu\text{m}$ for our analysis. For further details on the experimental implementation see [38].

We start by analyzing the time evolution of the non-translation invariant first order coherence function $C^{(1)}(z, z', t)$ (see Fig. 5.3). The system was coherently split by a slow first ramp $\tau_1 = 30\,\text{ms}$ followed by a fast increase of the RF amplitude during the second stage in $\tau_2 = 12\,\text{ms}$. Shortly after the splitting process the system is almost perfectly phase correlated leading to $C^{(1)}(z, z', 0) \approx 1$ for the entire system. During the course of the evolution the correlations decay in a light-cone like fashion ultimately leading to a

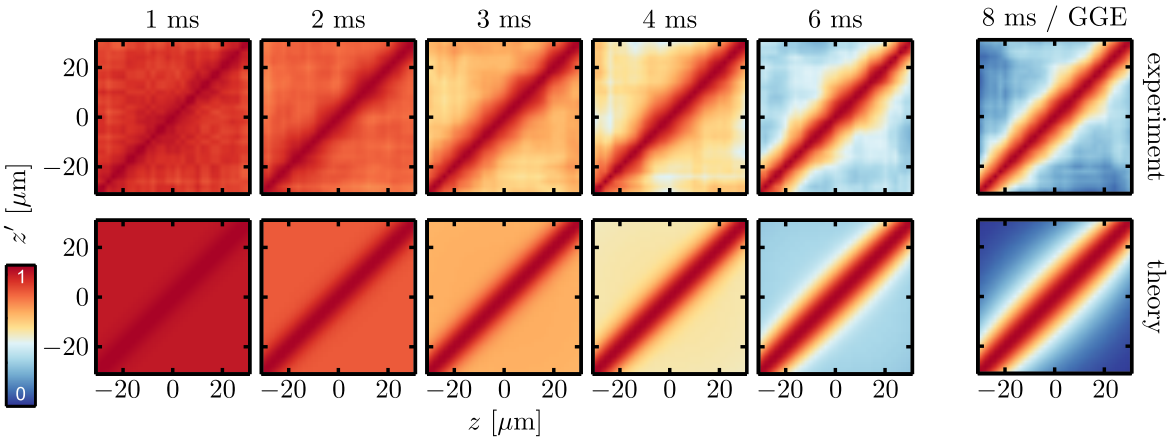


Fig. 5.3 Relaxation dynamics of a coherently split Bose gas to a prethermalized state described by a single temperature. Time evolution of the two-dimensional first-order coherence function $C^{(1)}(z, z', t)$, with the amount of correlation depicted in colors. The evolution shows the described lite-cone like decay of correlations away from the diagonal and a characteristic maximum along the diagonal as each point is perfectly correlated with itself. After $t = 8\,\mathrm{ms}$ the steady state is reached. The experimental observations (top row) are in good agreement with the theoretical predictions assuming a single effective temperature $k_\mathrm{B}T_\mathrm{eff} = \mu/2$. Figure adapted from [15].

quasi-steady state, reached after $t \approx 8\,\mathrm{ms}$. As discussed in the last sections, this state is expected to be described by a GGE with the quasiparticle occupation numbers $n_m = \langle b_m^\dagger b_m \rangle$ as the conserved quantities $\mathcal{I}_m$ of the integrable low-energy effective theory. Fitting the stationary state correlation function with the theoretical predictions of a GGE (5.13) for the harmonically trapped system we find for the low-energy modes a constant effective temperature $k_\mathrm{B}T_\mathrm{eff} = \mu/2$, independent of the initial temperature of the gas before the splitting. Therefore while a GGE in principle Eq. (5.14) reduces in this case to a simple Gibbs ensemble defined by a single effective temperature $T_\mathrm{eff}$. Calculating the full time evolution of the correlation function (5.7), where initially all fluctuations are assumed to be in the density quadrature[8] and we take into account only the diagonal contributions, we find good agreement to the experiment over the complete relaxation period. The emergence of this steady state is due to prethermalization [13, 135, 35–37] which here is described by the dephasing of phononic excitations [36, 216, 198, 135].

To obtain direct experimental signatures of a GGE dependent on multiple distinct Lagrange multipliers we alter the experimental splitting procedure and split the gas by linearly increasing the RF amplitude to its final value in a single 17 ms ramp (corresponding to $\tau_1 = 5\,\mathrm{ms}$). The results of this splitting protocol are presented in Fig. 5.4 and show a clear difference to the previous evolution. While again a light-cone like decay of correlations

[8] This implies $\langle b_m^\dagger b_m \rangle \simeq \langle b_m b_m \rangle = \langle b_m^\dagger b_m^\dagger \rangle$

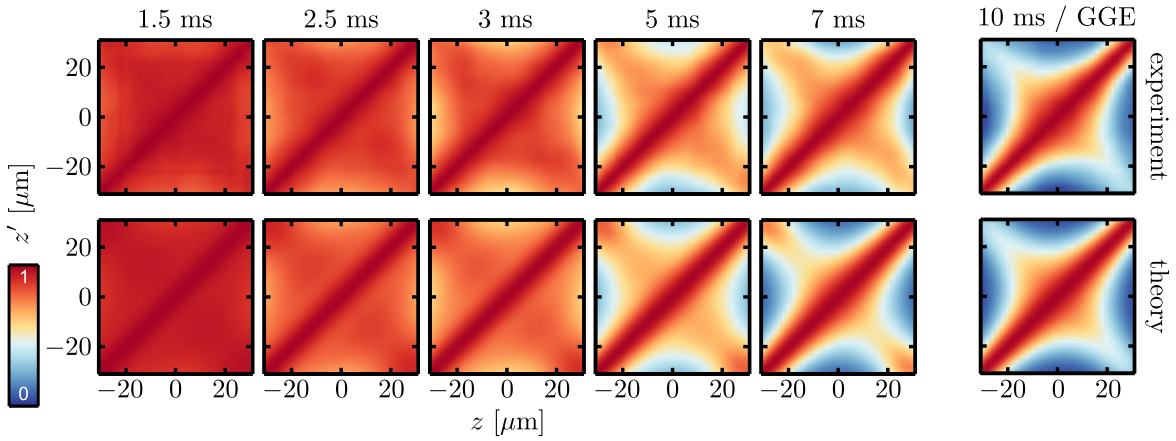


Fig. 5.4 Relaxation dynamics of a coherently split Bose gas to a genuine GGE described by multiple temperatures. Time evolution of the two-dimensional first-order coherence function $C^{(1)}(z, z', t)$, showing an additional maximum of correlations along the anti-diagonal. The experimental observations (top row) are well described by the theoretical model (bottom row) with mode dependent Lagrange multipliers. The quasiparticle occupation numbers for the depicted time evolution are obtained from a fit to the steady state (see Fig. 5.5). The non-translation-invariant state clearly cannot be described by a single temperature. Figure adapted from [15].

is visible during the evolution, a strong maximum remains along the anti-diagonal. This corresponds to enhanced correlations of point $z = -z'$, and reveals that correlations were imprinted outside of the relaxation light-cone. This effect can only arise in finite size or inhomogeneous systems since translation invariance prohibits the emergence of such a state in the thermodynamic limit.

The position of the additional maximum of the correlation function located symmetrically around the center of the longitudinal trap suggests an imbalanced population of quasiparticle modes that are even/odd under mirror reflection with respect to the trap center. Within a first approximation the stationary state can be described by two distinct temperatures (Lagrange multipliers), $\beta_{2m}^{-1} = k_B(T_{\text{eff}} + \Delta T)$ and $\beta_{2m-1}^{-1} = k_B(T_{\text{eff}} - \Delta T)$, for the even and odd modes respectively. A least $\chi^2$ fit to the experimental data yields $k_B T_{\text{eff}} = (0.64 \pm 0.01) \cdot \mu$, $k_B \Delta T = (0.48 \pm 0.01) \cdot T_{\text{eff}}$, and a reduced $\chi_r^2 \approx 6$. In [38] the observed temperature imbalance was found to increase for shorter splitting times $\tau_1$. While significantly improved from the predictions of a single temperature, with fitted $k_B T_{\text{eff}} = (0.38 \pm 0.01) \cdot \mu$ and $\chi_r^2 \approx 25$, more insight can be gained by directly fitting the GGE prediction.

We therefore increase the number of freely fitted modes (starting from the lowest energy $m = 1$) and fit the remaining high energy modes with a single effective temperature. By including 9 + 1 freely fitted parameters in the GGE, where the lowest 9 modes are fitted freely and the remaining high-energy excitations are thermally occupied at a single effective

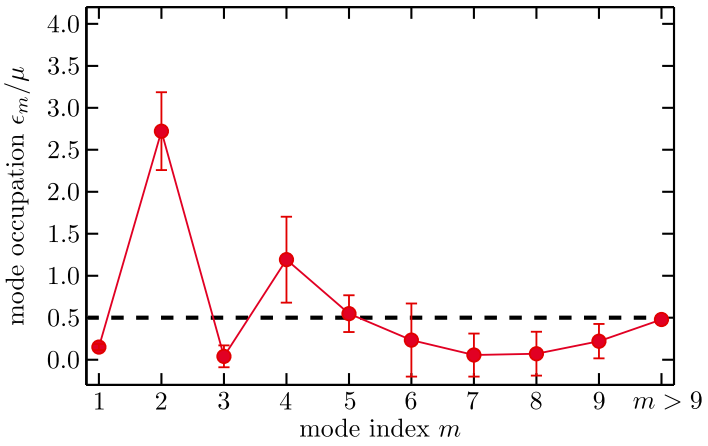


Fig. 5.5 Mode occupations for the GGE state. Occupation numbers $n_m$ of quasiparticle modes with index $m$, determined from a fit with 9 + 1 free parameters applied to the data from Fig. 5.4. The plot clearly reveals how the occupation of the lowest even (odd) modes are increased (decreased) as compared to the single-temperature state from Fig. 5.3 (dashed line).

temperature, we find perfect agreement ($\chi^2_\mathrm{r} \approx 1$) to the experimentally measured steady state (see Fig. 5.4). The fact that only 10 parameters are needed to describe the system is in good agreement with the decreasing influence of high-energy excitations on the phase correlation function and the experimental resolution of the phase profile. This is a beautiful example of statistical inference, which tells us that for the information contained in this specific observable, only a limited number of parameters need to be known out of the infinite set of conserved quantities (Lagrange multipliers) present in the microscopic theory. Interestingly, equivalent to the above prethermalized state the determined mode occupation numbers allow us to describe the full dephasing dynamics of the system.

Notably, our fitting results for the GGE exhibit strong correlations between the different even modes and the different odd modes, respectively. This demonstrates the difficulty in fully and independently determining the parameters of such complex many-body states. In fact, any full tomography of all parameters would require exponentially many measurements. The results thus clearly show the presence of a GGE with at least two, but most likely many more temperatures.

It is important to remember, that the determined GGE is defined through the integrable low-energy effective theory of the system. This includes in particular the conserved quantities $\mathcal{I}_m = \langle b_m^\dagger b_m \rangle$ which are not exactly conserved in the underlying microscopic theory, for which $\mathcal{I}_m$ in general include higher-order operator products [217]. While it is always possible to define complex enough observables which deviate strongly from the predictions of our GGE, the degree to which this reduced ensemble describes the observed steady state of the system is an interesting question. We determined in chapter 4 that deviations to an effective low-energy description can be tested in high precision through higher-order correlation functions. We therefore compare in Fig. 5.6 for both splitting protocols the experimentally measured higher-order correlations $C^{(N)}$ to predictions of the GGE. As previously for the two-point function

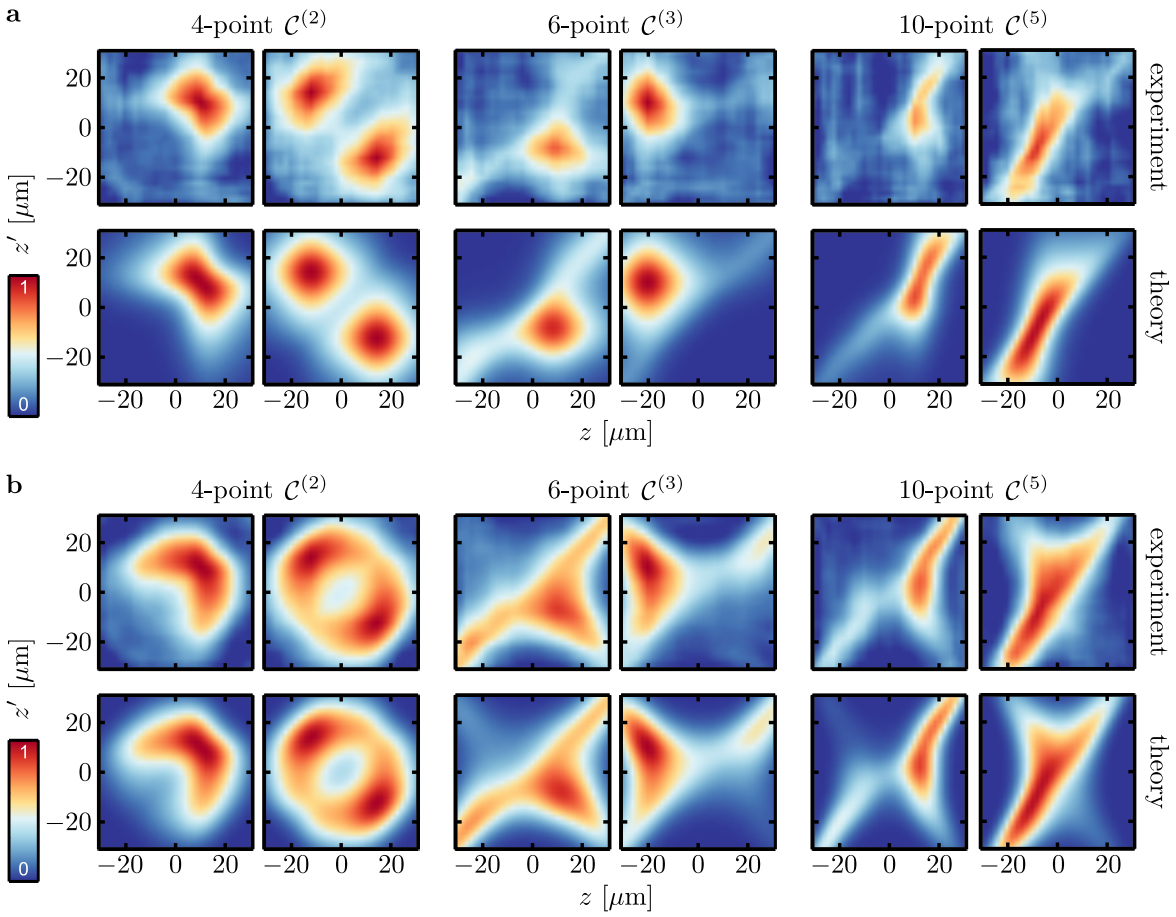


Fig. 5.6 Higher-order correlations for the prethermalized and GGE state. Examples of higher-order 4-, 6-, and 8-point phase correlation functions $C^{(N)}$ for $N = 2, 3$, and 4 (see Eq. (4.18)) for the prethermalized (**a**) and GGE (**b**) state are in good accordance with the theoretical predictions. As the GGE Eq. (5.14) defines a Gaussian theory in terms of the quasiparticles, the observed accordance with the experimental data is equivalent to their complete factorization into two-point correlations Eq. (4.23). This further confirms the description of the steady state in terms of a Gaussian GGE. From left to right, coordinates are $C^{(2)}(z, 10, z', 10)$, $C^{(2)}(z, -12, z', 14)$, $C^{(3)}(z, 10, 10, z', -20, 10)$, $C^{(3)}(z, -8, 8, z', -24, -20)$, $C^{(4)}(z, 4, 10, z', -8, z_2, -22, -18, 10, -4)$ and $C^{(4)}(z, -22, -8, z', -22, -26, -22, z_2, -26, -24)$. All coordinates are given in $\mu$m and were randomly chosen to illustrate the high-dimensional data. Figure adapted from [15].

we find excellent agreement up to 10$^{\text{th}}$ order[9]. Since the GGE per definition does not include correlations between the $\mathcal{I}_m$, and these are defined through the quasiparticle occupation of the harmonic theory, it defines a Gaussian state of the relative phase. Consequently, higher-order correlations calculated with the GGE factorize into one- and two-point functions and all higher-order connected correlations vanish identically. The observed accordance of the

[9] see [38] for additional correlations

experimental correlations to the GGE predictions therefore directly confirms the factorization of experimentally measured higher-order correlations according to Eq. (4.23).

## 5.6 Integrable Dynamics or Emergent Conserved Quantities

The great success of the integrable model in describing the experimental observations bears the question how these results can be brought into accordance with the analytical calculations presented in Section 5.4. Given the quasiparticle occupations determined from the experiment, and the accordance with the observed time evolution, we can evolve the GGE state back in time to determine the initial density-density correlations. For the observed prethermalized state this leads to homogeneous density-density correlations $\langle \delta\hat{\rho}_{\mathrm{r}}(z)\delta\hat{\rho}_{\mathrm{r}}(z')\rangle = (n_0/2)\delta(z-z')$, where $n_0$ is the peak density. This however, cannot be strictly valid as it would entail that near the edges of the condensate density fluctuations exceed the maximum possible level $(n(x)\xi_{\mathrm{h}})^2$, where we consider coarse-grained fluctuations on a length scale of the healing length $\xi_{\mathrm{h}}$. This divergence is not surprising, as it results from the extension of the low-energy description beyond its regime of validity $\epsilon_m \lesssim \mu$. However, as we showed in Section 5.4, the low-lying modes are well approximated by the analytical equations and any deformation of the density-density correlations from a constant value leads to off-diagonal quasiparticle correlations.

As a possible explanation to the above inconsistencies we retain the binomial splitting and study the influence of finite temperature on the dynamics of the system. As discussed in [209, 210, 194, 211] higher-order corrections to the equations of motion lead to a coupling of the common and relative degrees of freedom, which causes further dephasing of the two condensates and hence deviations from the integrable low-energy theory. In [194] the non-linear relaxation of the system was calculated through the dephasing of wave packets caused by random fluctuations in the speed of sound between the two condensates due to thermal fluctuations in the common degree of freedom. We therefore expect, although we like to point out that currently no theory exists describing the relaxation of discrete states in a finite size system, that these effects also to have an influence on the recurrent behavior of off-diagonal correlations, as these rely on an exact relation between the quasiparticle energies.

We hence consider the local binomial splitting of a finite temperature initial state, to determine the influence of this non-linear relaxation on the dynamics of the system. The initial state is created by propagation with the SGPE Eq. (2.51), with a constant value $\gamma = 0.05$, until convergence to the thermal equilibrium state is reached. The system is then coherently split as in Section 5.4, taking into account the minimum uncertainty phase fluctuations. The

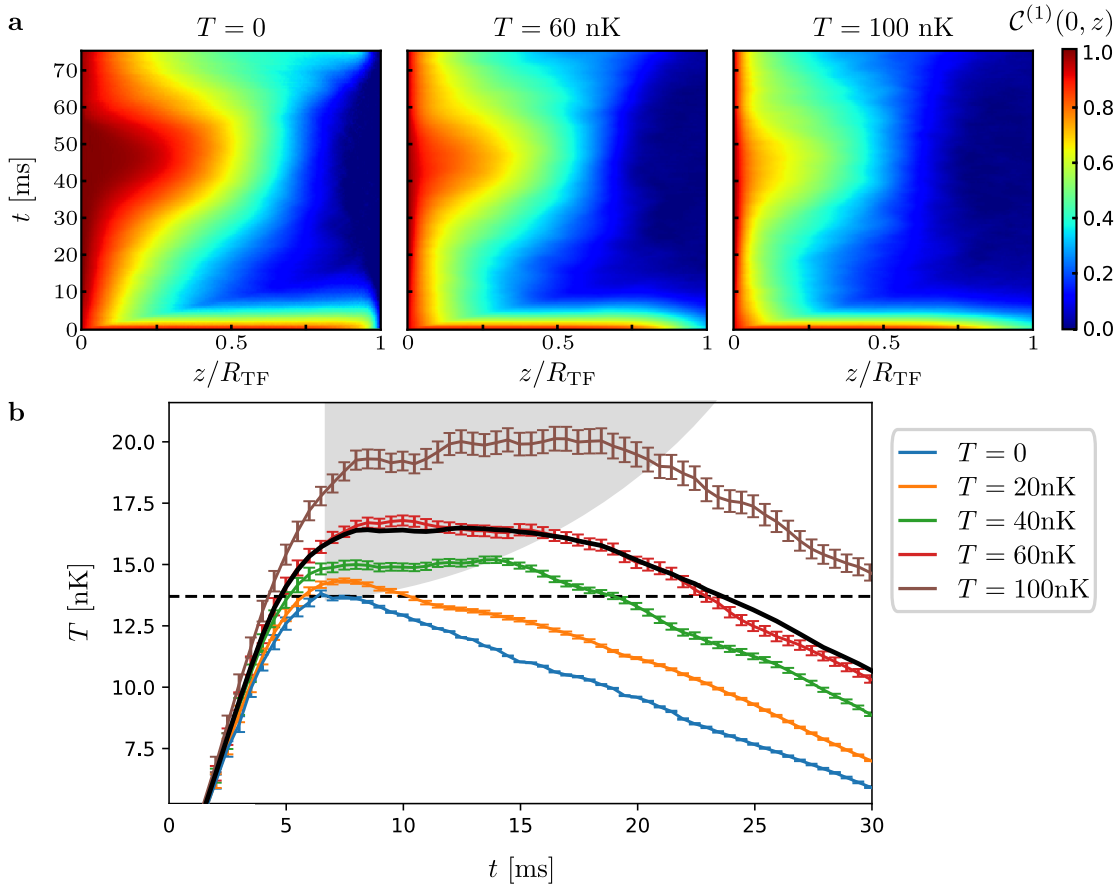


Fig. 5.7 Finite temperature simulations of the binomial splitting model. Simulations of the GPE for the parameters of Fig. 5.1 with an initial state temperature $T = 0 \ldots 100\,\mathrm{nK}$ obtained through evolution with the SGPE (2.51). **a** The time evolution of $C^{(1)}(0, z, t)$ for increasing temperatures shows large damping of the off-diagonal quasiparticle oscillations. For intermediate temperatures a clear plateau emerges in the evolution signaling the approach to a quasi-steady state. **b** Time evolution of the effective temperature obtained by a fit to the first-order coherence function. For $T = 0$ the system approaches the effective temperature $k_{\mathrm{B}}T_{\mathrm{eff}} = \mu/2$ (dashed black line, see also Fig. 5.1) before rephasing of off-diagonal correlations leads to a decrease in temperature. Increasing the temperature in the initial state, a prethermalization plateau emerges, its length (gray shaded area) as well as the effective temperature increasing with the initial temperature before the splitting. The black solid line shows the evolution for the experimental temperature spread.

time evolution of the first-order coherence function for different temperatures is presented in Fig. 5.7. We find a significant damping of the long range oscillations with temperature, showing that off-diagonal correlations experience dephasing beyond the integrable model. Notably, in the short time evolution a plateau emerges, for which $C^{(1)}(0, z)$ is approximately constant. While for higher temperatures non-linear effects become non-negligible even for the short time dynamics, for which high energy modes already show an increased temperature

during the initial dephasing, the long range behavior of the first-order correlation function still shows a clear plateau. Note, in particular, that the conserved quasiparticle occupations in the relative degree of freedom are still determined by the binomial splitting process, and hence would lead to a temperature of $k_B T_{\text{eff}} \approx \mu/4$.

In order to quantify the emergence of this prethermalization plateau, we fit the phase correlation function at each time with the predictions of a thermal state for the harmonically trapped system. For $T = 0$ the system after dephasing reaches the prethermalized state $k_B T = \mu/2$ observed in the experiment, but the off-diagonal contributions quickly lead to a decrease in the effective temperature. For increasing temperatures we find a clear prethermalization plateau emerging. The effective temperature explicitly depends on the temperature of the initial state, which shows that this emerging prethermalization plateau is not simply defined through the conserved quantities of an effective integrable model, but quasi-conserved quantities emerge dynamically in the interplay of off-diagonal rephasing and non-linear relaxation. Taking the average over the experimental temperature spread, reveals an emergent prethermalized state extending up to $t \approx 15 \ldots 20\,\text{ms}$, with a slightly increased temperature as compared to the experimental observations. Interpretation of the experimental observations within this model suggests that additional squeezing, known to arise in realistic splitting protocols [218–220], leads to a a reduction of fluctuations induced by the coherent splitting of the condensates. Since atom number squeezing increases with the local density [221] we expect the initial density-density correlations to be predominantly squeezed in the central part of the trap. This further flattens the density-density correlations, thereby decreasing the off-diagonal contributions (increasing the relative occupation of diagonal elements), which leads to a further damping of the long range oscillations in the PCF. Along this line, it is an open question whether the experimentally observed prethermalized state is a result of dephasing in an integrable low-energy theory or the result of conserved quantities dynamically emerging during the evolution which slow down the dynamics of the system.

Calculating the initial density-density correlations for the observed GGE, we again find along the diagonal diverging correlations near the edges of the condensate, while in the central part of the cloud we find atom number squeezing below the shot noise level. As in the case for the relaxation to a prethermalized state described by a single temperature, limiting the atom number fluctuations at the edges to physically realizable values leads to a reduction of the quasiparticle occupation number by a factor of two, while large correlations between even $2m, 2m+2, 2m+4$ and odd $2m+1, 2m+3, 2m+5$ modes appear in the initial state. Due to the dephasing of off-diagonal correlations these again lead in the short time dephasing dynamics to indistinguishable result for the PCF. Given the reasoning above the same question arises, whether the observed GGE is a result of emergent conserved quantities in the non-integrable model. This shows the difficulty in a full state tomography for inhomogeneous systems.

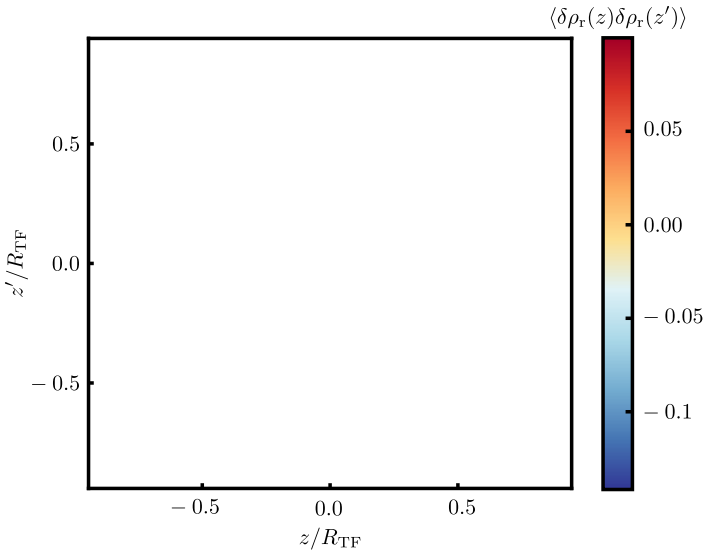


Fig. 5.8 Initial state density-density correlation reconstructed for the GGE of Fig. 5.4. The diagonal part (white area) is masked to show the small off-diagonal correlations present in the initial state density-density correlation $\langle\delta\rho_{\mathrm{r}}(z)\delta\rho_{\mathrm{r}}(z')\rangle$ of the relative density. The observed quasiparticle imbalance is imprinted by the splitting process and already present in the density correlations after the splitting.

Notably, the initial state density-density correlation shows long-range off-diagonal correlations Fig. 5.8, leading to the observed temperature imbalance and the emergence of the GGE. The diagonal contributions are approximately a factor of ten larger. This shows that the imbalance is imprinted by the splitting process. The initial state density-density correlations $\langle\delta\rho_{\mathrm{r}}(z)\delta\rho_{\mathrm{r}}(z')\rangle$ show enhanced correlations for points located symmetrically around the center of the trap, and anti-correlations between the trap center and points towards the edges. These correlations may be caused by a breathing excitation or the dislocated nature of particles in a condensate.

Determining the exact microscopic origin of the observed GGE requires a detailed simulation of the experimental splitting process. In this context, splitting into a double-well potential has previously been simulated using classical field methods or (Multi-Layer) Multiconfigurational Time-Dependent Hartree for Bosons (MCTDHB) [142, 143, 222]. However, a full theoretical model including the longitudinal degree of freedom has so far remained elusive. Classical fields can only account for thermal fluctuations using stochastic methods or determine the non-linear evolution in the TWA, which requires knowledge of the exact initial state Wigner function. While semiclassical simulations here provided detailed knowledge that the observed GGE is not the result of any mean field effects during the splitting[10], all these simulations rely on the binomial splitting model. A self consistent simulation of the coherent splitting process is herein not possible, without a better theoretical understanding of the processes leading to the observed GGE. While MCTDHB has been used to study the creation of squeezing during the splitting of gases containing up to O(100) particles in zero dimensions, a modeling of the experimental splitting process involving

[10]To this end numerous simulations were performed including local and local time dependent decoupling of the condensates, excitation of a breathing oscillation before, during, and after the splitting, and imbalanced condensates.

the 1D direction and thousands of particles would require significantly more self-consistent orbitals and is thus far beyond reach of current computational resources. Consequently, we understand our measurements as an important benchmark for future simulations of quantum many-body systems.

## 5.7 Summary

We demonstrated in this Chapter the emergence of statistical mechanics from the unitary evolution of an isolated many-body systems. Based on the integrable low-energy effective theory, the emergent steady state of the system was defined by the conserved quasiparticle occupations. We observed a genuine GGE exhibiting multiple temperatures by changing the splitting protocol in the experiment. This constitutes an important step in the validation of this generalized statistical description of integrable models and confirms the principle of entropy maximization as the fundamental principle of emergent statistical phenomena.

After a general introduction in the expected evolution of coherently split condensates, we presented a detailed calculation of the systems evolution within the harmonic theory. The evolution of the system was described by the first-order coherence function $C^{(1)}$. Of particular interest was the harmonically trapped system, for which we showed that within a model of local binomial splitting of the gas off-diagonal quasiparticle correlations prevent the system from reaching a true steady state. We connected this breakdown to the regularity of the spectrum, which lead to periodic revivals due to the rephasing of off-diagonal correlations. Comparison to the $T = 0$ simulations of the full non-linear equations of motion within the TWA revealed good accordance with the analytical solutions.

In the following section we analyzed the relaxation of the experimental system by use of the integrable TLL model. For both, the prethermaized state described by a single temperature and the genuine GGE, the full time evolution of the system was well described by the dephasing of the diagonal contributions of quasiparticle modes. Herein, the emergent statistical ensemble was fully defined by the conserved quantities of the integrable model, determined by the experimental splitting process. In the spirit of statistical inference, we showed that for the GGE including only $9 + 1$ parameters was sufficient for an accurate description of the system. While for such a truncated GGE it is in general always possible to define observables that deviate strongly from the ensemble predictions, the question remains if such deviations are practically accessible and therefore if and when such a truncated description is sufficient.

In the last section we reconstructed the initial state density-density correlations from the experimentally measured quasiparticle occupation numbers determined at the steady state. This revealed an apparent problem as correlations diverged near the edges of the condensate,

which in a self consistent reconstruction of the initial state inevitably lead to off-diagonal quasiparticle correlations. Extending the binomial splitting model to finite temperature states, we found that a possible explanation for the observed steady states could be the appearance of dynamically conserved quantities as a result of non-linear relaxation and off-diagonal quasiparticle dephasing. This clearly signals the difficulties in a complete state reconstruction for inhomogeneous finite size systems and highlights the need for the development of exact numerical simulations capable of simulating the experimental splitting process.

# Chapter 6

# Quantum Recurrences

The expectation that a non-equilibrium system evolves towards thermal equilibrium is deeply rooted in our daily experience. So far, in this thesis, while during the relaxation of the system towards such a thermal state complex dynamical processes arose, there was in a sense always a constant direction of time. The system quickly relaxed from some far-from-equilibrium initial conditions towards a state, determined only by a few parameters. From universality far-from-equilibrium to emergent generalized statistical ensembles once such a state is reached, details of the initial configuration the system started with are irrelevant. This reasoning formed the beginning of statistical mechanics [1]. However, as formulated by Poincaré and Zermelo, a finite isolated physical system will recur arbitrarily close to its initial state after a long but finite time [2, 3]. Therefore, although the system appears to have forgotten its initial configuration, the apparently relaxed intermediate state is highly correlated. The reconciliation of these seemingly contradicting statements forms the basis of the emergence of irreversible processes from reversible microscopic mechanics [4].

The above can be transferred to the quantum regime, where already von Neumann formulated a quasi-ergodic theorem for the evolution of the wave function [5]. However, also in the quantum regime, a general recurrence theorem can be proven [6, 7], which immediately follows from the unitary evolution and the discrete energy eigenstates of a finite size system. The equilibration of isolated quantum systems thereby grew into an active field of research [223].

Here we demonstrate that by designing the spectrum of the effective field theory, we are able to observe the recurrence of coherence and long range order in an interacting many-body system containing thousands of particles[1]. This is a striking demonstration of the above

[1]This chapter is based on and contains parts of [224]. I contributed to the theoretical calculations, interpretation of the theoretical results and experimental data, performed numerical simulations, and contributed to writing of the manuscript.

recurrence theorem, where after an initial relaxation to a maximum entropy state, the system returns back close to its initial configuration.

## 6.1 Recurrent Dynamcis in Finite Size Quantum Systems

From a theoretical point of view, it is a well known result that a finite isolated system will never show true relaxation, but always exhibit a return close to its initial configuration. This becomes immediately apparent, when considering the solution to the equations of motion in the energy eigenbasis, where unitary evolution of the wave function is simply a rotation of each energy eigenstate. The frequency is given by the energy eigenvalue $E_n$, and for a discrete set of eigenvalues there will always be a time $t_{\text{rec}}$ for which the wave function returns arbitrarily close to its initial state.

The main challenge to observe such recurrent dynamics, is simply a matter of scales. For small systems, a beautiful example of recurrences is the predictions [225, 226] and observation [227] of collapse and revivals in the Jaynes-Cumming model. Therein interactions of a single atom with a coherent light field lead to the collapse and subsequent revival of finding the atom in the excited state. Further, collapse and revivals were observed for interacting systems of a few atoms trapped in optical lattices [228, 229]. However, if the number of constituents is increased, the time of the recurrence quickly approaches astronomical scales. Since the dimension of the Hilbert space grows exponentially with the number of constituents, the time at which all eigenstates have exactly performed a full rotation, i.e. $E_n t_{\text{rec}}/\hbar = 2\pi n$ with $n$ being an integer number, becomes practically impossible to observe in an actual experiment. This enormous time scale is also the reason that allows us to infer the thermodynamic properties from numerical simulations of a finite size system. The only exception are systems for which the spectrum of the Hamiltonian has a highly commensurate structure, e.g. equidistant energy levels $E_n = E_0 + n\Delta E$ with $n$ a positive integer, or shows a certain degree of regularity, as is for example the case for conformal field theories [8, 230, 231]. We will, however, assume in the following that the microscopic Hamiltonian is sufficiently complex.

Apart from this, there is a second barrier to the observation of quantum recurrences. Assuming for the moment we have found a non-trivial system, which shows a full recurrence of the wave function back to its initial state on an experimentally feasible time scale. While theoretically a well defined problem, from an experimental point of view this raises the question how the recurrence of the system can even be confirmed. Due to the increasing complexity of the Hilbert space, an exponentially growing number of measurements, assuming that these would even be experimentally possible, are needed to determine the exact state of the system. For complex many-body systems this is experimentally not possible and instead one investigates the system through measurements of (local) few-body observables

$\mathcal{O}$. This shifts the question to if and under which conditions the experimental observation of recurrences becomes possible. The system does not necessarily have to return arbitrarily close to its initial configuration, but only has to give the same results under the measurement of certain observables $\mathcal{O}$.

While not a recurrence of the microscopic model in the strict mathematical sense, this approach facilitates the experimental observation of recurrent dynamics in large interacting quantum many-body systems. This definition allows us to interpolate between a full recurrence, where the system returns to its initial configuration for any observable $\mathcal{O}$, and an effective description, where the system only returns close to its initial state under a certain class of observables. The implementation of recurrent behavior in a subset of the Hilbert space thereby permits the detailed study of the underlying microscopic dynamics. By tuning the system to return close to its initial configuration for certain observables, deviations to the predicted recurrence can be measured on time scales far longer than the initial relaxation time of the system. Recurrences thereby provide a clear measurable signal in experiments and thus give valuable insight in the coherent evolution of the full interacting many-body system.

A natural choice for the class of observables $\mathcal{O}$ in a quantum many-body system is to choose them to represent the collective excitations of the underlying field theoretical description. This greatly reduces the complexity, from the infeasible large number of eigenstates in the microscopic description to a much smaller number of populated modes determining the relevant low-energy behavior of the system. By designing the spectrum of these collective excitations to have a commensurate structure, we show that the observation of recurrences in an interacting many-body system containing thousands of particles becomes experimentally feasible.

## 6.2 Experimental Observation of Recurrences

As a model system we study the decay and return of coherence and long range order in CQW. Similar to the system presented in chapter 5, we consider in the following the evolution of the system following a rapid decoupling of the two condensates. However, there are two major differences for the present system.

First, the initial strongly phase correlated state is obtained by evaporative cooling in a dressed double-well potential, with a strong tunneling coupling $J$. As we established in chapter 4 the system in thermal equilibrium is strongly phase locked ($\langle\cos(\theta_r)\rangle \approx 1$) and shows Gaussian statistics, and is therefore very similar to the initial state of coherently split condensates. The difference is that while for the latter the excitations in the relative degrees of freedom, and especially the effective temperature of the relaxed state, are only determined

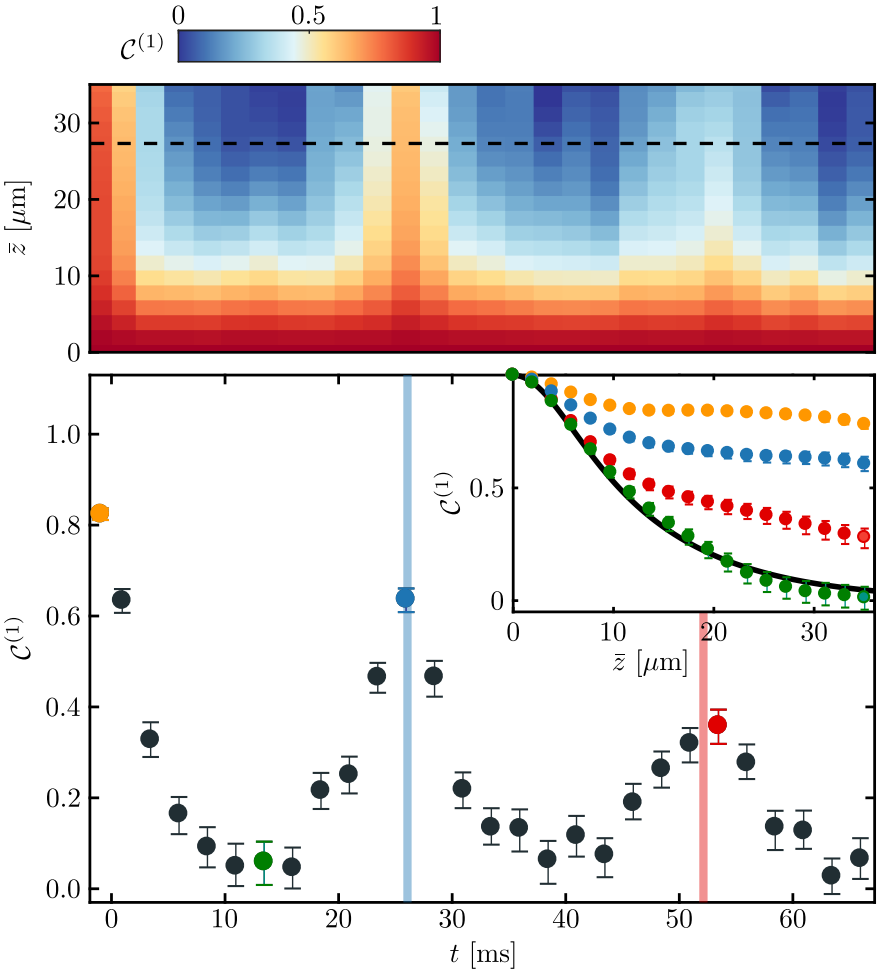


Fig. 6.1 Recurrences of long range order in the evolution following a rapid decoupling of two condensates. The upper panel shows the time evolution of $C^{(1)}(\bar{z}, t)$, averaged over all points $z, z'$ in the central part of the condensate with $\bar{z} = |z - z'|$. The initial strongly phase locked state dephases quickly to a prethermalized state. In the subsequent evolution two recurrences of phase coherence between the two condensates are clearly visible. The lower panel shows the time evolution $C^{(1)}(t)$ for a cut through the correlation functions at $\bar{z}_c = 27.3\,\mu$m (dashed black line in the upper panel). The vertical blue (red) lines are the predicted recurrence times for the first (second) recurrence. The inset shows the spatial dependence $C^{(1)}(\bar{z})$ for different times depicted in color. In between the recurrences (green dots) the system has relaxed to a transient thermal state (black solid line). The error bars represent the 68% confidence intervals obtained by a bootstrapping [202]. Figure adapted from [224].

by the quantum noise of the splitting process the system in thermal equilibrium is dominated by thermal fluctuations of the initial state. This allows us to directly compare the results to numerical simulations suing the SGPE formalism, as we do not have to rely on the local beam-splitter approximation of the splitting process.

Second, instead of the harmonic confinement, the system is now confined to a box-shaped potential along the longitudinal direction. This is achieved by adding hard walls to a very weak harmonic confinement with the help of a blue-detuned optical dipole potential. An exchangeable wire mask blocking a stripe of variable width from the intensity in the central part of the beam, enables to change the length $L$ of the box-confinement. At the walls the potential rises in 3.1 $\mu$m from 10% to 90% of its total height, which is approximately 1.3 kHz. For details on the experimental implementation see [224]. Typical samples have linear density of 70 atoms per $\mu$m, and dependent on the box length 2300 . . . 4800 in each well.

Since we are initially in the strongly phase locked regime, and at this point mostly interested in the revival of phase coherence between the two condensates, we study the evolution of the system through the periodic correlation functions. In particular, we use the spatially averaged first order coherence function $C^{(1)}(\bar{z} = |z - z'|)$, where for the approximately translation invariant system the spatial average is performed over all point $z, z'$ in the central part of the condensate with $|z - z'| = \bar{z}$.

The time evolution of the first order coherence function for a box of length $L = 49\,\mu$m is presented in Fig. 6.1. The system is initially strongly phase correlated showing long range order with $C^{(1)}(\bar{z}) \approx 1$ over the whole central part of the cloud. At $t = 0$ the system is abruptly decoupled and coherence decays in a light cone like fashion due to quasiparticle dephasing. After $t \approx 10$ ms the completely dephased state is reached which is well described by a thermal ensemble (see inset). For a system in the thermodynamic limit $L \to \infty$ or for incommensurately spaced modes this dephased state persists for a long time, showing as discussed in chapter 5 the emergence of statistical mechanics from the unitary evolution of the system. Here on the other hand two partial revivals of phase coherence are clearly visible in the subsequent evolution. The system therefore, after relaxing to a transient thermal like state, shows a recurrence close to its initial configuration, spontaneously restoring long range order in the system. The vertical lines correspond to the theoretically expected revival times, which we examine in the following section.

## 6.3 Theoretical Discussion

The origin of the observed recurrence can be understood by recognizing that long range order, i.e. the observable employed to test the system, is dominated by the long-wavelength low-energy modes of the system. These are expected to be in a first approximation well described by the harmonic approximation. We discussed the general solutions for the time evolution after the decoupling of the condensate in Section 5.2. Here, we consider a box-shaped trapping potential $U(z) = U_0[\Theta(-z) + \Theta(z - L)]$ of length $L$, neglecting the influence

of the finite wall steepness and the deformation of the bulk density close to the boundaries. The latter corresponds to the TF approximation, neglecting the kinetic energy and hence the deformation on a length scale of the healing length. The explicit solutions to the Bogoliubov equations (2.23) for an arbitrary tunneling coupling $J$ then is

$$f^{\pm}_{k,J} = \left(\frac{\epsilon_{k,J}}{E_k + 2\hbar J}\right)^{\mp 1/2} \sqrt{\frac{2}{L}} \cos(kz) \tag{6.1}$$

$$\epsilon_{k,J} = \sqrt{(E_k + 2\hbar J)\,(E_k + 2\hbar J + 2\mu_0)}\,, \tag{6.2}$$

where we chose Neumann boundary conditions $\partial_z \theta_\mathrm{r}\,|_{z=0,L} = 0$ to have vanishing particle flux at the boundary. The discrete states are labeled by the momentum $k = \pi n/L$ with n being an integer number, and $\mu_0$ is the chemical potential in the absence of tunneling coupling $J$. At the time $t = 0$ the tunneling coupling $J$ is quenched to zero and the system evolves according to the uncoupled Hamiltonian. In particular, the time evolution of the first order coherence function is given by Eq. (5.7) with the initial conditions determined by projecting the initial thermal state onto the new basis. Direct calculation for an initial temperature $T$, inserting the modal expansion of the density and phase field in Eqs. (5.11) & (5.12), leads with the orthonormal eigenfunctions (6.1) within the Rayleigh-Jeans limit to the only non-vanishing quasiparticle correlators

$$n_k = \langle b_k^\dagger b_k \rangle = \frac{k_\mathrm{B} T}{2\epsilon_k}\left(\frac{E_k}{E_k + 2\hbar J} + \frac{E_k + 2\mu_0}{E_k + 2\hbar J + 2\mu_0}\right) \tag{6.3}$$

$$m_k = \langle b_k^{(\dagger)} b_k^{(\dagger)} \rangle = \frac{k_\mathrm{B} T}{2\epsilon_k}\left(\frac{E_k}{E_k + 2\hbar J} - \frac{E_k + 2\mu_0}{E_k + 2\hbar J + 2\mu_0}\right), \tag{6.4}$$

where $\epsilon_k = \epsilon_{k,0}$ is the dispersion relation for the uncoupled condensates. The system is again in a highly squeezed state, showing reduced phase fluctuations (first term in the parentheses) and an access of density fluctuations (second term in parentheses). Inserting the quasiparticle correlations in Eq. (5.7) we get the time evolution of the phase variance:

$$\langle \varphi(z, z', t)^2 \rangle = \frac{1}{L n_{1\mathrm{D}}} \sum_{\epsilon_{k,0}>0} \frac{\epsilon_k}{E_k} \left[\cos(z) - \cos(z')\right]^2 \left[n_k + m_k - 2m_k \sin^2(\omega_k t)\right]. \tag{6.5}$$

In the short time evolution this leads to the discussed emergence of a maximum entropy state, described by a GGE, through the dephasing of quasiparticle modes. However, in contrast to the thermodynamic limit $L \to \infty$ where the dispersion relation becomes a continuous function of $k$ it is here discrete, in particular having a finite lowest energy for $k \neq 0$. In the phononic limit the dispersion relation has a highly commensurate structure $\omega_k = c_\mathrm{s} k = n\pi c_\mathrm{s}/L$, which is even equally spaced with $\Delta\omega = \pi c_\mathrm{s}/L$. Therefore after a time $t = 2\pi/\Delta\omega = 2L/c_\mathrm{s}$ all modes have performed an even number of rotations, $\omega_k t \bmod 2\pi = 0$, and the system has

returned to its initial configuration. Half-way to this full recurrence the system rephases to the mirrored state, where all odd quasiparticle modes have performed half integer rotations. As we start initially from an almost flat relative phase profile, and our observable $C^{(1)}$ is insensitive to the transformation $\theta_r(z) \to \theta_r(-z)$, this point is equivalent to the full recurrence. The expected recurrence time for the correlations is therefore

$$t_{\mathrm{rec}} = \frac{L}{c_s} \,. \tag{6.6}$$

Therefore, by designing the spectrum of quasiparticle excitations, the recurrence time for phase coherence in the system is reduced to experimentally feasible timescales. This can be compared, e.g. , to the case of a harmonic confinement, where the mode frequencies $\omega_j = \omega\sqrt{j(j+1)/2}$ are non-commensurate. While partial revivals due to the rephasing of a limited number of modes or the off-diagonal elements appear, the first clear revival happens at $t \approx 3\pi/\omega$. This lies, for typical experimental parameters, on the order of hundreds of milliseconds and observation of these recurrences is not possible due to the further relaxation of the system, driven by physics beyond the harmonic approximation.

For a quantitative comparison to the experiment, it is important to remember that in the quasi 1D regime, radial swelling of the condensate leads to a shift in the speed of sound (see Section 2.1.4). Using the NPSE prediction to account for this effect the speed of sound is given by Eq. (2.36), which for the experimental parameters is typically 20% smaller than the bare value $c_s = \sqrt{n_0 g_{1D}/m}$ predicted by the GPE (see Fig. 2.3). The recurrence times $t_{\mathrm{rec}}$ for the first and second recurrence are the theoretical predictions shown in Fig. 6.1. Note that, while the shift in $c_s$ is due to the limited resolution harder to ascertain in the initial dephasing lite-cone dynamics, it is clearly visible on the longer time scale of the recurrence.

To validate the predicted scaling (6.6) of $t_{\mathrm{rec}}$ with the system size, we present in Fig. 6.2 the recurrence position for varying length $L$ of the box trap. The time axis was rescaled by the theoretical speed of sound to make measurements with slightly different atom numbers comparable. The recurrence times are extracted from the experimental data, by fitting a Gaussian function to each peak in the time dependent first order coherence function $C^{(1)}(\bar{z} = z_c, t)$ for a fixed distance $z_c = 27.3\,\mu$m. The value of $z_c$ was chosen such that the equilibrium correlation function (in between the recurrences) is sufficiently low as to provide a clear signal of the recurrence, while the distance remains in the central part of the cloud even for the smallest system size considered to minimize the influence of boundary effects. The Gaussian shape near the recurrence peak follows from Eq. (6.5) since near the recurrence the sinusoidal time dependence can be Taylor-expanded to second order. The first order coherence function for fixed coordinates $z, z'$ near the recurrence is therefore given by a product of Gaussian functions with $k$-dependent widths, decreasing with temperature. As the product of Gaussian functions is again a Gaussian we can extract the height and position of

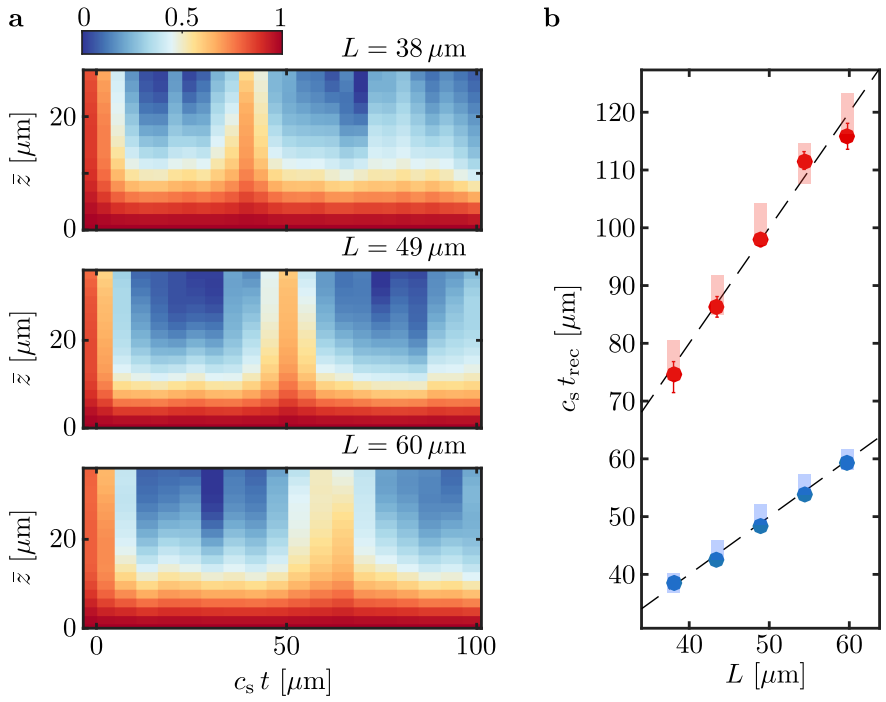


Fig. 6.2 Scaling of the recurrence time with the size of the system. **a** Time evolution of phase correlations for three different box lengths. The time axis is scaled with the theoretical prediction for the speed of sound $c_s$ to make measurements with slightly different atom numbers comparable. **b** Recurrence time for the first (blue) and second (red) recurrence as a function of the box length $L$. The recurrence times are extracted from the correlation function at a distance $\bar{z}_c = 27.3\,\mu$m. The experimental data agrees well with the predicted linear scaling for an ideal box trap (dashed line). The shaded areas are the predictions of a TLL simulation taking into account the experimental imperfections in the trapping potential and the uncertainty in the decoupling time (vertical extent). The error bars represent the 68% confidence intervals obtained by a bootstrapping [202]. Figure adapted from [224].

the recurrence through a Gaussian fit of the first order coherence function $C^{(1)}(z_c, t)$. We find excellent agreement with the predicted linear scaling for the first and second recurrence.

It is important to note, that the observed recurrence of long range order happens globally throughout the whole system. It is therefore related to the properties of the spectrum of quasiparticles, rather than an artifact of light-cone like spreading of correlations in a finite size system. The latter generically leads to peaks and/or minima in two-point correlation functions due to the reflection of the light cone at the boundaries [8, 232]. In contrast to a revival, the appearance of these traversals is position dependent and their amplitude remains exponentially small in the system size. Adopting a quasiparticle picture [39], the difference between traversals and recurrences is depicted in Fig. 6.3. At $t = 0$ at each point in space, the quench produces counter-propagating quasiparticle pairs. For fixed points $z, z'$ this leads to the occurrence of a light cone in the two-point function at time $t_0 = |z - z'|/2c_s$, where $c_s$ is the

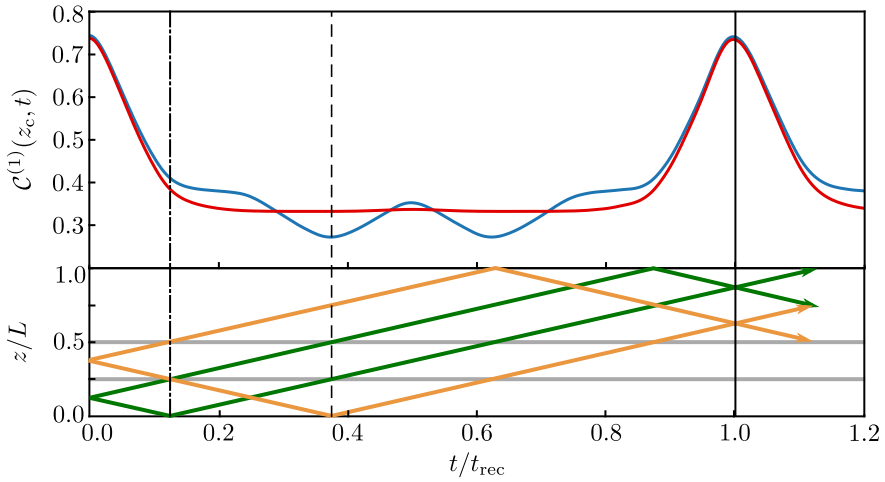


Fig. 6.3 Traversals and recurrences. Time evolution of the phase correlation function in an ideal box trap according to Eq. (6.5) for a cut through the spatially averaged correlation $C^{(1)}(\bar{z}_c, t)$ (red line) and for coordinates $z = L/2$ and $z' = L/4$ (blue line). The vertical lines depict the light-cone (dashed-dotted), the recurrence time $t_{\mathrm{rec}}$ (solid), and the traversal expected for coordinates $z = L/2$ and $z' = L/4$ (dashed line). The traversal is visible as a dip in the correlation for the blue curve. These effects are washed out by the spatial averaging, while the recurrence happens globally and is visible for both curves. The lower panel is a schematic of the time evolution in a quasiparticle picture. Two pairs (orange and green) are created at different positions and the gray solid lines depict the spatial coordinates. The occurrence of the light-cone, traversals, and the mirrored state recurrence are explained through the propagation and reflection of quasiparticles in a finite size system.

propagation velocity of quasiparticles. The first traversal occurs at the time $t_1 = (z + z')/2c_s$. This corresponds to the situation where a quasiparticle pair was created at position $y$ and travels in opposite directions. The left particle gets reflected from the boundary before reaching $z$ at the time $t_1$, while at the same time the right moving particle has moved in a straight line from $y$ to $z'$. In our system the traversals appear as dips rather than a peak in the temporal evolution of the phase correlation function, since the Neumann boundary conditions lead to a phase shift of $\pi$ for excitations reflected from the boundary. Would Dirichlet boundary conditions $\theta_r(0) = \theta_r(L) = 0$ be used instead, the traversals would show up as a maximum. It is clear that this effect can happen generically in any finite size system, as only a quasiparticle pair originating from a single point has to appear at the position $z, z'$. A recurrence requires all quasiparticle pairs to have returned close to their initial position, which therefore happens on a global scale all throughout the system. In the experimental parameter range these traversals are rather small, and their visibility is further diminished by the experimental imperfections of the trapping potential and the finite imaging resolution. We therefore used the spatially averaged correlation function $C^{(1)}(\bar{z}, t)$, for which the traversals are washed out and only global recurrences of phase coherence remain.

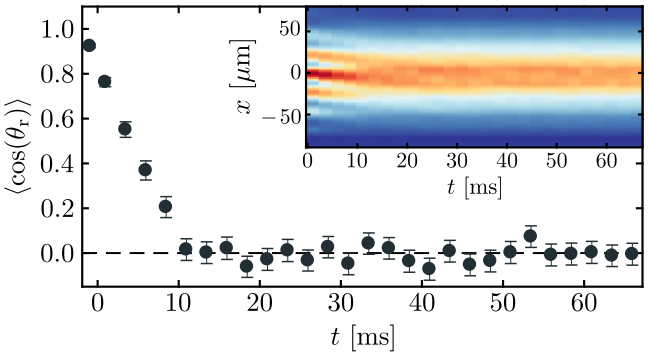


Fig. 6.4 Evolution of the coherence factor. No recurrences are visible due to phase diffusion caused by random atom number fluctuations between the two condensates. This leads to a global phase accumulation and hence averaged interference picture shows no recurrence of high contrast fringes (inset). Figure adapted from [224].

As we stated above, because we designed the system to exhibit recurrent behavior on the level of the low-energy description, not all observables return close to their initial value. This can already be seen on the level of the effective field theory, since e.g. as presented in Fig. 6.4 the time evolution of the coherence factor $\langle\cos(\theta_r)\rangle$ shows no recurrence. It relaxes from its finite value during the initial dephasing time to a value close to zero, where it remains for the remainder of the evolution. This results from small atom number imbalances between the two condensates. The particle number imbalance originates in the thermal fluctuations of the initial state and possible imperfections of the experimental splitting process. This corresponds to a fluctuating population of the $k = 0$ mode, described by the operator $\hat{P}$. Note that even at zero temperature quantum fluctuations lead to a finite spread of the particle imbalance as otherwise the phase operator $\hat{Q}$ diverges. The random nature of particle imbalance in the experiment leads to a constant phase accumulation, or phase diffusion [100], that is different for each realization. Therefore the coherence factor vanishes as the average is performed over a phase with large global fluctuation. This is equivalent to the observation that, while for each experimental realization interference pictures show a return of high contrast fringes, an averaged interference picture shows no revival thereof due to the random spatial offset caused by the accumulated global relative phase (see inset of Fig. 6.4). In contrast the two-point phase correlation function $C^{(1)}$ is insensitive to a global offset of the phase field and recurrences of excitations on top of the field can be observed.

## 6.4 Damping of recurrences

While the recurrences are clearly visible in the experiment and their origin and time $t_{\mathrm{rec}}$ well described within the harmonic theory, the height of the recurrence rapidly decreases, making the observation of a third recurrence infeasible for most experimental parameters. As discussed in Section 5.6, finite temperature effects drive the system beyond the harmonic approximation and lead to complete relaxation between the common and relative degrees of freedom. For a quantitative comparison of the observed damping of recurrences we therefore

focus our attention on the influence of finite temperature in the initial state, and analyze the decay of recurrences for experimental measurements at different temperatures $T$ in a box potential with $L = 49\,\mu$m. The tunneling coupling $J$ is increased accordingly to have comparable results with $\langle\cos(\theta_\mathrm{r})\rangle \approx$ const.

From a theoretical point of view the damping of recurrences in our system can have two distinct origins. First, even within the harmonic theory a perfect recurrence of phase coherence back to its initial value is only expected within the TLL approximation for an idealized box potential within the TF approximation. Any deformation of the quasiparticle dispersion relation from this perfectly commensurate spectrum $\omega_k = c_\mathrm{s}k$ leads to a damping of the recurrence height, as not all modes will perfectly rephase at the time $t_\mathrm{rec}$. These are purely mean-field effects that arise only due to the extension of the low-energy description to energies $\epsilon_k > \mu$ or through experimental imperfections. The dependence on temperature is only indirect through the thermal occupation number of quasiparticle modes.

For the extension of the harmonic theory to the full Bogoliubov dispersion relation, the particle like branch $\omega_k = \hbar k^2/2m$ does not have the same commensurate structure as the phononic part of the spectrum, and hence does not show recurrences for the time $t_\mathrm{rec}$. Since the high energy modes are free particle like excitations, their recurrence time is independent of the bulk density and only determined by the system size and the atomic mass. However, $t_\mathrm{rec} = 2mL^2/\hbar\pi$ grows unfavorably with the system size and for the experimental $L = 49\,\mu$m box already shifts the recurrence of high energy modes to $t_\mathrm{rec} \simeq 2.1$ s. Further, in the transition regime between the phononic and particle like branch non-commensurate frequencies appear, that shift the recurrence to exceedingly long time scales. However, the phase correlation function $C^{(1)}$ is most sensitive to the long-wavelength modes described by the TLL and hence the dephasing of these high-energy modes leads only to a minor constant offset for the correlation function. In addition to this, considering the solutions on top of the exact experimental density profile leads to a small deformation of the spectrum due to the inclusion of the kinetic energy term and the finite wall steepness. These deformations are, however, on length scales much smaller than the system size $L$ and therefore do not strongly influence the long-wavelength excitations dominating the observed recurrence.

The main source of damping within the harmonic theory is caused by the experimentally fluctuating total atom number and particle imbalance between the two condensates. Both of these effects cause a random shift in the speed of sound, which leads to a loss of coherence. For the fluctuations in the total atom number this is merely a statistical effect. The shift in $c_\mathrm{s}$ is global which leads to a random shift in the position of the recurrence $t_\mathrm{rec}$ for each experimental realization. The shape of the coherence function $C^{(1)}(\bar{z}, t)$ near the recurrence is a Gaussian and averaging over realizations with a random displacement of the recurrence peak in time leads to a decrease of the recurrence height. Since the width of the recurrence, i.e. the variance of the Gaussian function, decreases with temperature this effect becomes more

pronounced for increasing $T$. Due to the difference in $c_s$ between the left and right condensate the particle number imbalance, on the other hand, leads to a dephasing of quasiparticles in each individual realization. We discussed in Section 2.2.1 that particle number imbalance, i.e. $\mu_1 \neq \mu_2$, leads to a coupling of the common and relative degrees of freedom. Since, however, the tunneling coupling $J$ vanishes for $t \geq 0$ the two condensates in the left/right basis, decouple independent of the particle number imbalance. Since for a homogeneous system the spatial dependence of the mode functions is independent of the density, we can determine the time dependence of the quasiparticle operators in the relative degree of freedom[2]

$$b_r(k,t) = \frac{e^{-i\bar{c}kt}}{\sqrt{2}}\left[\left(\frac{c_L}{\bar{c}}\right)^{\frac{3}{2}} e^{-i(c_L-\bar{c})kt}\, b_L(k) - \left(\frac{c_R}{\bar{c}}\right)^{\frac{3}{2}} e^{-i(c_R-\bar{c})kt}\, b_R(k)\right]. \tag{6.7}$$

Here we inserted the modal expansion (2.21) of the left and right phase field in $\theta_r = \theta_L - \theta_R$ and factored out the dependence on the mean speed of sound $\bar{c}_s = \bar{c}$. For a balanced splitting $c_L = c_R = \bar{c}$ the time dependence inside the parentheses vanishes and the time evolution reduces to a constant rotation, leading to perfect recurrence to the initial state. For imbalanced condensates the time independent operators $b_{L,R}(k)$ accumulate a relative phase due to the difference in $c_s$, which leads to a decrease of coherence in the relative degree of freedom. While for the typical experimental imbalance spread of $\approx 2\%$ the effect is small on the completely dephased state, its contribution cannot be neglected for the evolution of the recurrence height. Note that this effect is generic in the grand canonical ensemble and will always contribute to the damping of the recurrences.

The second contribution to the damping of recurrences is caused by the non-linear dynamics of the system. While we find a stable recurrence on the level of the effective field theory, the microscopic description of the system is at all times still determined by the full non-linear equations of motion. Processes beyond the harmonic approximation therefore drive the system towards thermal equilibrium. Quasi-particle interactions lead to an irreversible loss of coherence in the system and inevitably lead to damping of the recurrence. The dephasing of completely decoupled condensates having different temperatures for the common and relative degrees of freedom was studied in [194, 211]. However, the theoretical model, describing the loss of coherence in the relative phase through the dephasing of wave packets caused by random fluctuations in speed of sound due to thermal fluctuations in the common degrees of freedom, is only strictly applicable in the thermodynamic limit or for sufficiently high energies. For our system the discretness of the spectrum is essential for the observation of recurrences, and therefore the model provides only a rough order of magnitude prediction for the damping of recurrences. We therefore compare the experiment to finite

[2] We concentrate here on the relevant phononic regime

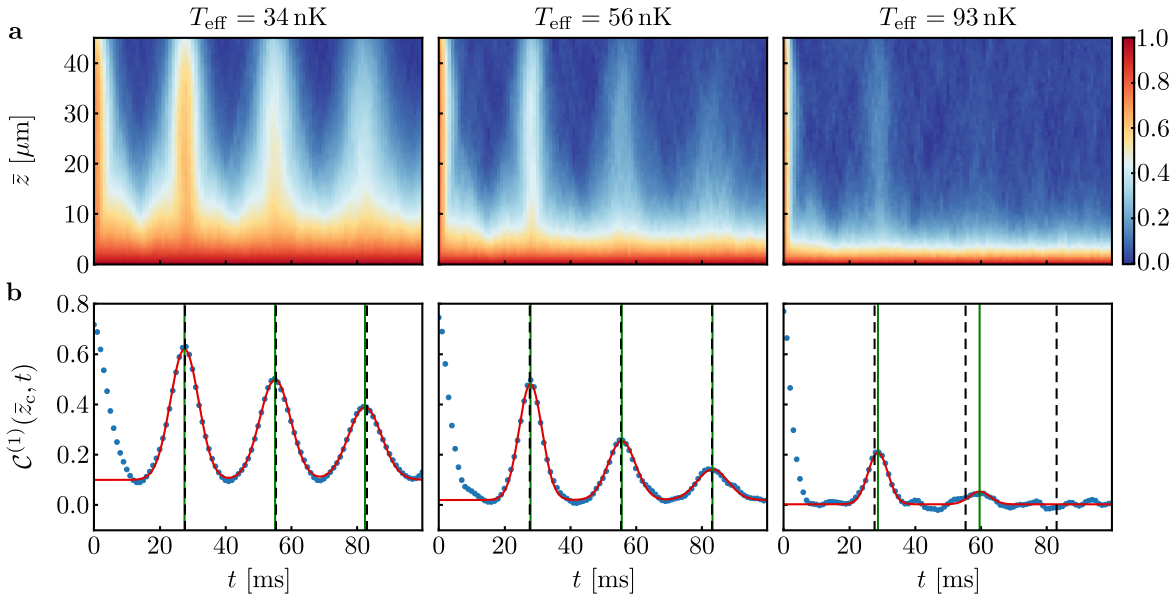


Fig. 6.5 Results of the finite temperature NPSE simulations taking into account the experimental trapping potential and spread of parameters. **a** Time evolution of $C^{(1)}(\bar{z}, t)$ for three different effective temperatures $T_{\mathrm{eff}}$ obtained through a thermal fit to the coherence function in between the recurrences. The damping of the recurrence height with temperature is clearly visible. **b** Time evolution for a cut through the phase correlation function at $\bar{z}_c = 27.3\,\mu$m, taking into account the experimental resolution of the imaging system. Red lines are the result of a multi-Gauss fit to determine the recurrence height and position. The recurrence times $t_{\mathrm{rec}}$ (green lines) are in good accordance with the theoretical TLL predictions for an ideal box taking into account the transverse broadening of the wave function.

temperature numerical simulations of the full non-linear model for the exact experimental trapping potential. We again rely on the SGPE formalism to produce the initial thermal state of the strongly tunnel coupled system. To avoid the excitation of solitons during the condensation process, which in this nearly homogeneous system drastically slow down the approach to thermal equilibrium, we begin the evolution with a finite occupation of the condensate obtained through imaginary time evolution. The system is afterwards evolved with the Lagevin equation (4.29) until convergence to thermal equilibrium is reached. In the experiment the splitting ramp is $\approx 1.9\,$ms, during which the system decouples on a much shorter time scale, such that for the numerical simulations we consider an instantaneous quench in the tunneling coupling $J \to 0$, completely decoupling the two condensates[3]. At the same time the contact to the heat bath is removed, such that, following the quench, the unitary evolution for each condensate is determined by the NPSE (2.33). For a quantitative comparison to the experiment, it is essential to include the additional statistical effects

[3] In the numerical simulations no significant differences were found for a finite splitting time when checked for selected parameters.

contributing to the damping of recurrences discussed above. The particle number imbalance, due to the random nature of the SGPE evolution, is already included in the initial state and agrees well with the experimental observation. We implement the experimental fluctuations of the total atom number through a fluctuating chemical potential $\mu$ for each realization of the SGPE. The total atom number $N$ is sampled from a Gaussian distribution with experimentally determined variance $\sigma_N = 425$ from which, in accordance with the experimental post selection, the central 20% of the distribution are taken for the analysis. The results of the numerical simulations for three different temperatures are shown in Fig. 6.5. In particular, the recurrence times fit well with the harmonic prediction for all temperatures $T$, as long as a recurrence can be detected.

The height of the correlation is measured as compared to the value of the correlation function at the completely dephased state $t = t_{\mathrm{rec}}/2$. We fit, in experiment and numerics alike, a multi-peaked Gaussian

$$f(t) = C_{\mathrm{base}} + \sum_{n\geq 1} C_{\mathrm{fit}}^{(n)} \exp\left(-\frac{(t - n\,t_{\mathrm{rec}})^2}{2\sigma_n^2}\right), \tag{6.8}$$

to the temporal evolution of the correlation function $C^{(1)}(\bar{z}_{\mathrm{c}}, t)$, at the fixed distance $\bar{z}_{\mathrm{c}} = 27.3\,\mu$m. Here $C_{\mathrm{base}}$ is the base line correlation, averaged over the times in between recurrences, $C_{\mathrm{fit}}^{(n)}$ is the absolute height of the $n^{\mathrm{th}}$ recurrence with width $\sigma_n$, and the sum is performed over all detected recurrences showing increased correlations above the base line. From this fit we define the recurrence height

$$H_{\mathrm{rec}}^{(n)} = \frac{C_{\mathrm{fit}}^{(n)} - C_{\mathrm{base}}}{C^{(1)}(\bar{z}_{\mathrm{c}}, 0) - C_{\mathrm{base}}}, \tag{6.9}$$

normalized to the access of correlations in the initial state. The measure is one for a perfect recurrence back to the initial state and zero if no significant correlation above the base line can be detected. For the theoretical phase profiles the finite imaging resolution has to be taken into account by convolution with a Gaussian PSF with $\sigma_{\mathrm{PSF}} = 3\,\mu$m, since the measure (6.9) is not independent of the resolution.

The experimental and theoretical results are compared for the same effective temperature $T_{\mathrm{eff}}$, measured in between the recurrences. For the theoretical calculations $T_{\mathrm{eff}}$ is extracted from a thermal fit to the phase correlation function $C^{(1)}(\bar{z}, t_{\mathrm{rec}}/2)$ and is practically indistinguishable from the initial temperature of the gas prior to decoupling. In the experiment, due to the limited resolution, the temperature is inferred from the full distribution function of the measured contrast $C$ of integrated interference patterns [233, 197, 234, 13, 200, 212]. Specifically, the FDFs of the normalized squared contrast $C^2/\langle C^2\rangle$ for different integration

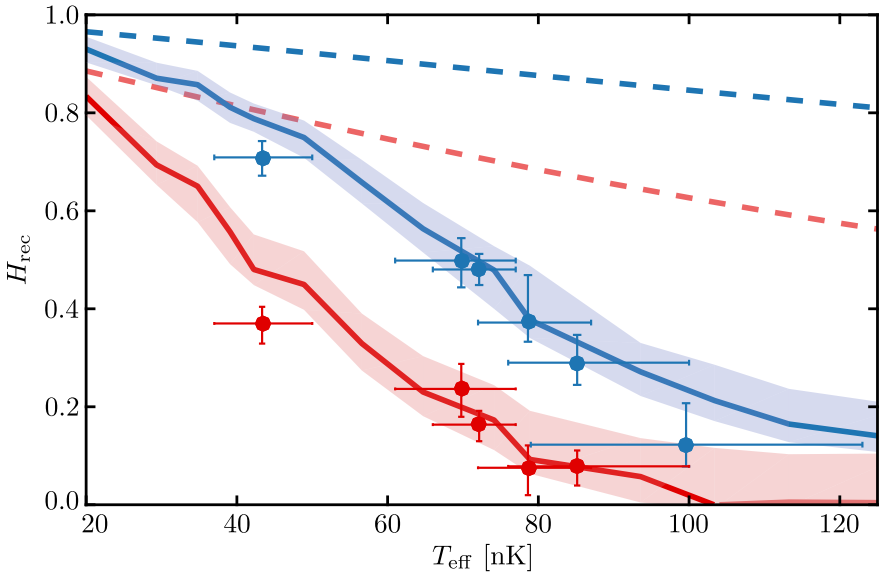


Fig. 6.6 Temperature dependence of the recurrence height. The experimentally determined recurrence height $H_{\mathrm{rec}}$ for the first (blue dots) and second (red dots) recurrence in a box of length $L = 49\,\mu$m for different effective temperatures $T_{\mathrm{eff}}$ are in good agreement with the NPSE simulations of the splitting process (solid lines). In both experiment and numerics, the recurrence height is extracted with a multi-Gaussian fit to the phase correlation function at $\bar{z}_{\mathrm{c}} = 27.3\,\mu$m and the effective temperature is determined at $t = t_{\mathrm{rec}}/2$, in between the recurrences. The shaded area indicates the uncertainty due to the limited experimental statistics ($1\sigma$ deviation). Comparison to the TLL predictions (dashed lines), taking into account the experimental trapping potential and fluctuations in the parameters, reveals that the damping of recurrences is dominated by processes beyond the harmonic approximation.

lengths $s$ are compared to results form simulated phase profiles of the TMF[4] in a $\chi^2$ fit. Notably, the temperatures of the dephased state are systematically higher than the initial temperature determined through the longitudinal density speckle patterns forming in the time-of-flight (TOF) expansion [235, 236]. This suggests that the experimental splitting process adds additional energy, thus increasing the amount of fluctuations in the system. Since an increasing temperature influences the damping of recurrences, we compare all results (experiment and numerics alike) with respect to $T_{\mathrm{eff}}$ determined after the splitting.

In Fig. 6.6 the temperature dependence of the recurrence height for the first and second recurrence is presented for the experimental data and compared to the numerical results of the SGPE and the exact solution within the harmonic theory. The latter is solved numerically (see Appendix B) taking into account the exact mean-field density profile for the experimental trapping potential as well as the spread in the total atom number and atom number imbalance. It is clearly visible that these effects alone cannot account for the experimentally observed

[4]More precise the sampling is performed using the harmonic Ohrnstein-Uhlenbeck process.

damping of the recurrence height. Therefore, already at comparatively low temperatures, the system deviates from the integrable low-energy effective description and quasiparticle interactions lead to the non-linear relaxation of the system towards thermal equilibrium. As the temperature is increased these processes become more relevant leading to stronger deviations between the harmonic theory and the experiment. This non-linear relaxation is faithfully incorporated in the SGPE formalism, which shows very good agreement to the experimental results over a wide range of temperatures. As expected from the semi-classical approximation in the derivation of the SGPE equation, accordance to the experiment improves for higher temperatures.

## 6.5 Summary

Through designing of the dispersion relation in the effective field theory we demonstrated in this chapter that the observation of quantum recurrences becomes experimentally feasible for many-body systems containing thousand of interacting particles.

Based on the immense complexity of the many-body state we argued in the first part, that the experimental observation of recurrences is more suitably defined by a class of observables accessible in experiments. By choosing the observables to reflect the collective degrees of the underling effective field theory, we were able to observe the recurrence of long range order in the evolution of two decoupled one-dimensional Bose gases, long after they have reached an apparent prethermalized state. The experimentally observed recurrence time was in good agreement with the theoretical predictions of the harmonic theory. Noticeably, the radial swelling of the condensate had to be taken into account for an accurate description of the experiment.

Recurrences provided a clear measurable signal during the long time evolution, which we used to study the non-linear relaxation of the system. By comparison of the damping in the recurrence height to numerical simulations of the harmonic and NPSE equations, taking into account the experimental uncertainties and fluctuations, we were able to show that physics beyond the low-energy effective description is non-negligible even for comparatively low temperatures in the initial state. We found good agreement with the numerical simulations of the NPSE, which confirms its validity in the far-from-equilibrium dynamics of Bose gases in the dimensional crossover regime.

# Chapter 7

# Outlook

In this thesis we explored the relaxation of far-from-equilibrium quantum many-body systems through a series of experiments on one-dimensional Bose gases. The topics presented spanned a wide range of phenomena at the heart of the field of non-equilibrium dynamics. Our results demonstrate for the first time various characteristic aspects predicted to emerge during the relaxation of these systems.

In chapter 3 we studied the relaxation of a single Bose gas, which was quenched to the one-dimensional regime by a rapid removal of transversally excited states. Following this cooling quench we found that the system quickly enters a regime dominated by solitonic excitations. While these defects could not be directly observed, we were able to determine their presence through their characteristic impact on the momentum distribution [116, 182]. Based on a model of randomly distributed defects we were able to determine scaling of the defect density with the experimental quench rate and found agreement with the predicted scaling of the inhomogeneous Kibble-Zurek mechanism [165, 77]. Since for the quench rates considered the applicability of the Kibble-Zureck arguments is not strictly fulfilled, our results reveal the preservation of scaling for defect nucleation beyond the Kibble-Zureck regime to strongly quenched far-from-equilibrium systems. Based on the determined increase in the defect density, we explained the observed scaling in the width of the density and momentum distribution, as well as the observed damping of the breathing excitation. Further we found a transition from frequency-doubling to no-doubling for the oscillation of the momentum distribution in a far-from equilibrium system, neither connected to the transition to the ideal gas regime nor the predicted transition in the quasi-condensate regime [178].

We subsequently studied the long time relaxation dynamics following a strong cooling quench and found that the system, before relaxing to a thermal state, shows universal scaling dynamics far-from-equilibrium [40–42, 52, 50]. During this time period we found the evolution of the system, independent of the initial conditions, to be determined by a single universal scaling exponent and function. We connected the presence of this scaling

solution to an emergent conserved quantity, the particle number in the infrared, and its transport to lower wave numbers. Within the model of solitonic defects, we connected the universal scaling dynamics to a dilution of the defect ensemble following a power-law in time. The direct observation of the approach of such a non-thermal fixed point during the relaxation of a far-from-equilibrium quantum many body system constitutes an important step towards the development of a classification of universal behavior far-from-equilibrium, similar to the results of [59] in thermal equilibrium. In this context it is important to note that the observed scaling exponent can not be explained by current theoretical predictions [50, 52], and further studies are necessary to determine the nature of the observed fixed point. Whether an explanation based on the dynamics of solitonic defects, similar to the connection of non-thermal fixed points and vortices in higher dimensions [43–49], or the continuity of scaling exponents based on fractal-dimensions during the approach of the one-dimensional regime, where current understanding predicts vanishing exponents [50] based on the integrability of the model, our findings further the understanding of universal dynamics far-from-equilibrium. The observation of universal dynamics with statistically significant non-zero scaling exponents $\alpha$ and $\beta$ in general is an important step towards the discovery of new non-equilibrium universality classes.

In chapter 4 we examined the equilibrium and near-equilibrium properties of two linearly coupled quantum wires, experimentally realized through a Bose gas in a double-well potential. Through a detailed study of the factorization properties of higher-order correlations we were able to prove that the the relative phase between the two condensates is in thermal equilibrium described by the sine-Gordon model. Analyzing the validity of an effective field theory order by order through the factorization properties of higher-order correlations, presents a statistically significant and unbiased method to determine the relevance or irrelevance of operators [83, 11] and the verification of future quantum simulators [193]. The measurement and evaluation of higher-order correlation functions can easily be generalized to other systems and experimental techniques, e.g. single site detection in optical lattices or generic observables like density, spin, or magnetization. It is further not limited to the quantum regime and can e.g. be transferred to study the onset of non-linear dynamics in classical fluid systems.

We extended the analysis of higher-order correlations to near-equilibrium states. Experimentally, by changing the speed with which the gas was cooled into the double well, non-equilibrium states were found to deviate strongly from the sine-Gordon predictions. Based on the full distribution functions of unbound phase differences we found solitons to be present in the system. Based on simulation of the condensation dynamics using the stochastic Gross-Piteavskii equation we validated the excitation of these topological defects during the initial growth of the condensate. While a strong non-thermal distribution of solitons was found, we showed that fluctuations around these defects thermalized on a

much shorter timescale. This allowed us to determine the near-equilibrium correlations in a model of statistically independent, randomly distributed solitons in a thermal background, for which we found good agreement to the numerical as well as experimental non-equilibrium data. The topological nature of these defects makes the system ideal for future study of the Kibble-Zurek mechanism.

Further we see our results as a crucial step towards the solution of many-body problems via experiments. We showed explicitly that in the case of complete factorization of higher-order correlations one has found the diagonalizing degrees of freedom, effectively solving the many-body problem. In a next step this can be extended to determine the one-particle irreducible correlations, which are fundamental in the theoretical study of quantum and statistical field theory [83]. This would ultimately allow to determine the full (equal-time) quantum effective action [237–239], with the exact, possibly momentum dependent, couplings determined directly through experimental measurements.

In the remaining chapters we concentrated on the dynamics following a rapid decoupling and subsequent relaxation of two strongly phase correlated condensates. Their low-energy effective description, the integrable Tomonaga Luttinger-Liquid model, enabled us to study fundamental principles of statistical physics and their connection to the unitary time evolution of near-integrable quantum-many body systems. In chapter 5 the far-from-equilibrium initial state was prepared by coherently splitting a single condensate into two halves. By changing the experimental splitting protocol, we extended the previous results of the relaxation of the system to a prethermalized state [13, 212, 14, 38, 135, 34–37] and showed that in the most general case the non-thermal steady state is described by a generalized Gibbs ensemble dependent on multiple parameters [15]. Our results are the first direct observation of such a generalized statistical ensemble and provide further evidence for the principle of entropy maximization [9, 10]. Based on the common model of local binomial splitting of the condensate we presented a detailed calculation of the relaxation dynamics in the integrable low-energy effective theory. Our main focus was on the harmonically trapped gas, where we extended previous calculations [208] and revealed the relevance of off-diagonal quasiparticle correlations in the systems evolution. This resolved the apparent problems of the approach to the thermodynamic limit through the emergence of new conserved quantities through the dephasing of off-diagonal quasiparticle correlations. Based on a reconstruction of the initial state from the experimentally measured correlations, we discussed the problems associated with these off-diagonal correlations arising in a self consistent analysis of the systems dynamics within the low-energy description. Through numerical simulations at finite temperature we demonstrated how the intricate interplay of non-linear relaxation [209, 210, 194, 211] and off-diagonal quasiparticle rephasing can lead to a prethermalization plateau, defined through dynamically emerging quasi-conserved quantities. Our results demonstrate the difficulties in achieving a full state tomography for inhomogeneous finite

size systems and reveal the need for the development of new, exact simulation techniques capable of simulating the full experimental splitting process in a self consistent way. Further studies are needed to determine whether the experimentally observed relaxation dynamics are indeed determined by the integrable model or if integrability-breaking contributions to the Hamiltonian lead to a more complex structure for the observed non-thermal quasi-steady state determined by emergent conserved quantities during the evolution. We therefore see our observations as a benchmark for future simulations.

In chapter 6 we demonstrated that by designing the spectrum of the low-energy effective theory describing the system, it is possible to measure quantum recurrences in an interacting many-body system containing thousands of particles. This is a striking demonstration of unitary dynamics and demonstrates the detailed knowledge of the initial conditions that can still be present in the system, but are hidden through the dephasing of eigenstates. The recurrence of long-range order in the system provided a clearly measurable signal during the long time evolution. This enabled us to show that already for moderate temperatures physics beyond the integrable low-energy theory can not be neglected. By splitting the condensate from an initial thermal state in a strongly tunnel coupled double-well potential, a direct comparison to semi-classical field simulations was found to be a good description of the relaxation dynamics. This confirmed the applicability of the non-polynomial Schrödinger equation [128] for the relaxation of far-from-equilibrium one dimensional Bose gases, and further strengthens the results obtained in chapter 5. Future studies of the combined analysis of recurrences and mode occupations will shed light into the fundamental relaxation processes of one-dimensional Bose gases and the influence of integrability breaking contributions. In connection to chapter 4 the study of recurrences of higher-order correlations show great potential in determining the underlying structure of complex many-body Hamiltonians [240], the validity of approximate models [160], and the verification of coherence in quantum simulators [193].

Our results clearly demonstrate the great success and future opportunities cold-atom systems offer in the search for an answer to the fundamental guiding principles of far-from-equilibrium quantum many-body dynamics, which is an open, interesting, and important problem for systems on all scales.

# Appendix A

# Additional Results of Chapter 3

Here we present additional results of the scaling analysis presented in Section 3.3, performed separately for each of the three different initial conditions.

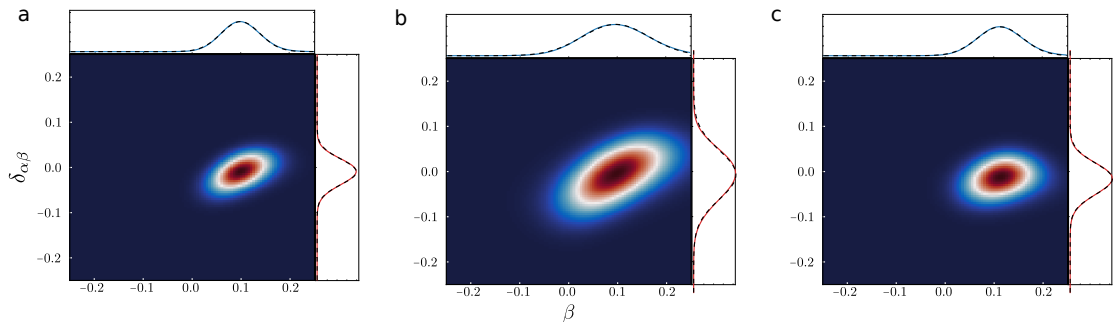


Fig. A.1 Likelihood function of the scaling analysis for different initial conditions. a,b,c correspond to the experimental realizations $1, 2, 3$ of Fig. 3.10

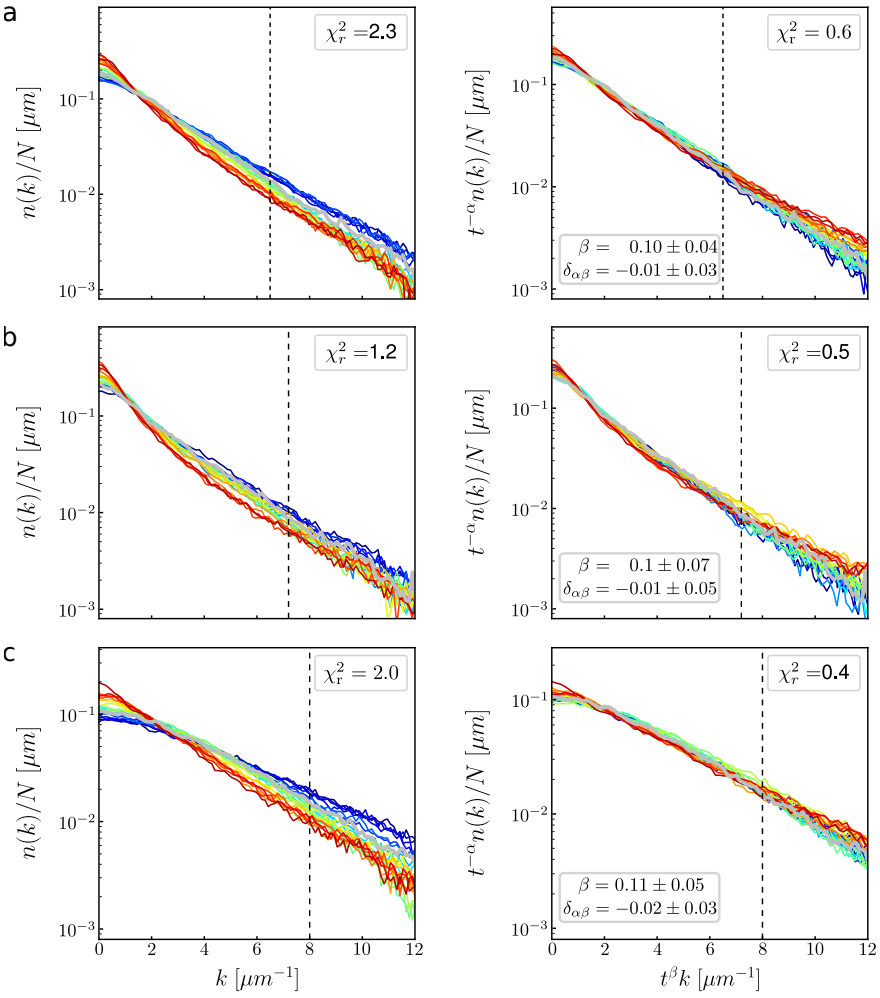


Fig. A.2 Scaling evolution of the momentum distribution for the different initial conditions. a,b,c correspond to the experimental realizations 1, 2, 3 of Fig. 3.10

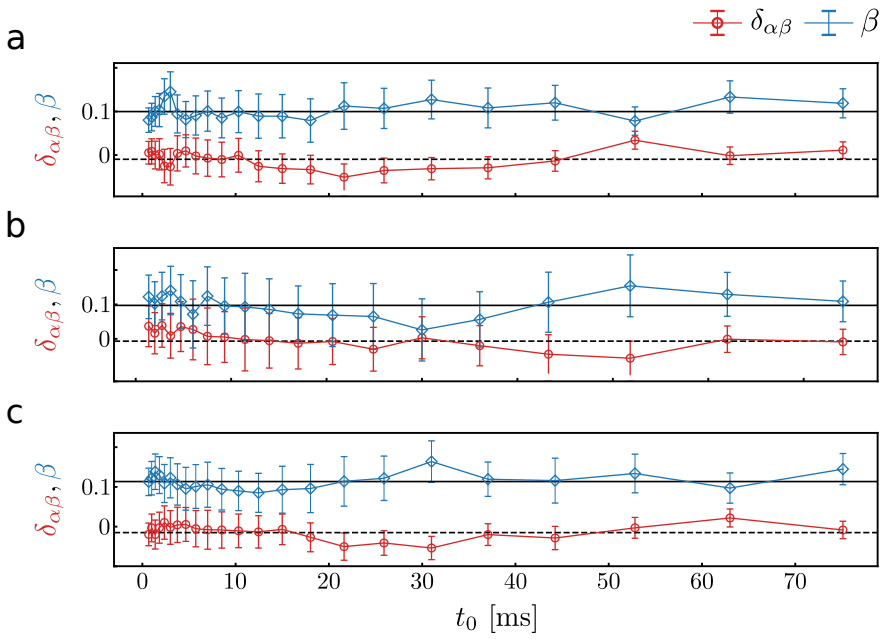


Fig. A.3 Dependence of the scaling exponents on the reference time $t_0$ for different initial conditions. a,b,c correspond to the experimental realizations 1, 2, 3 of Fig. 3.10

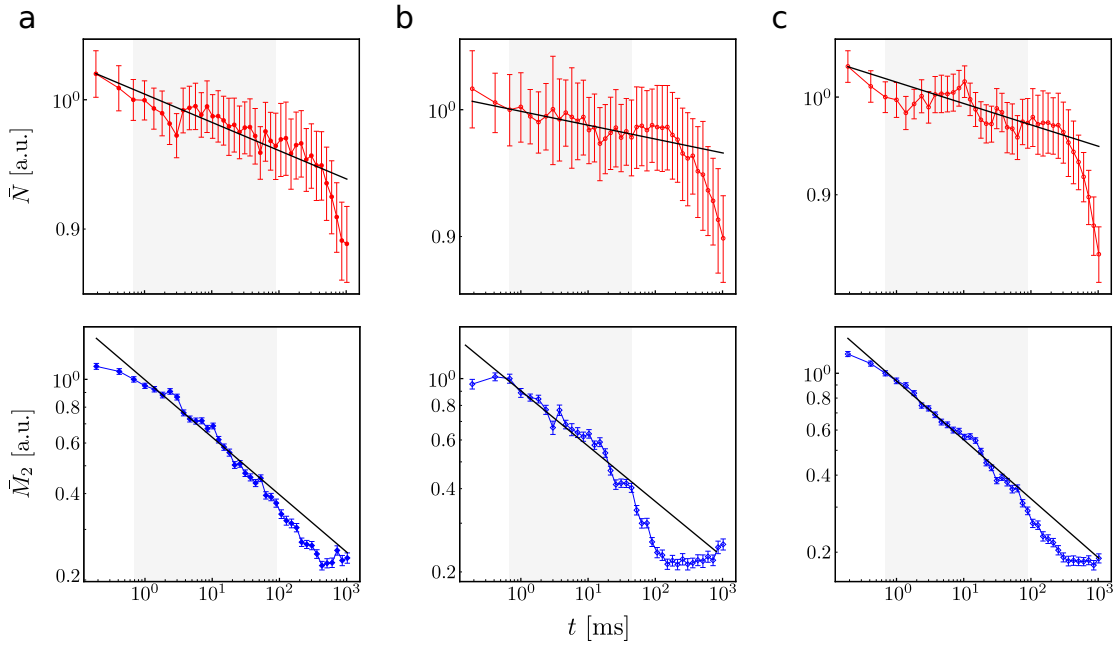


Fig. A.4 Time evolution of global quantities $\bar{N}$ and $\bar{M}_2$ for different initial conditions. a,b,c correspond to the experimental realizations 1, 2, 3 of Fig. 3.10. The solid black lines are the predictions according to the determined scaling exponents $\delta_{\alpha\beta}$ and $\beta$ for each experimental realization.

# Appendix B

# Numerical techniques

Here we give details and practical information on the numerical implementation of the discussed simulations. A large part of this thesis was the development of a classical field library for the simulation of the semi-classical field equations for a single, and two linearly coupled Bose gases.

Based on the close collaboration with experimental physicists, all units in this thesis were given in the international system of units (SI-units). This has during the course of this work also proven to be the most accessible unit system for the input of parameters. Internally, during the solution of the field equations, the classical field equation is brought into a dimensionless form by use of a complete set of dimension-full quantities $\{a_{\mathrm{G}}, m, \hbar, k_{\mathrm{B}}\}$. The grid spacing $a_{\mathrm{G}}$ is hereby the only free adjustable dimension-full parameter and determines the energy cutoff of the numerical simulation. The time spacing is conveniently chosen as $\omega_{\mathrm{G}} = \hbar/ma_{\mathrm{G}}^2$ which sets the numerical factor for the kinetic energy to a constant $1/2$.

The system of linearly coupled quantum wires can be efficiently numerically integrated with the Fourier-Spectral-Split-Step method. Therefore, the Hamiltonian $H = T + V$ is split into the kinetic $T$ and potential $V$ contributions, diagonal in the Fourier and spatial basis respectively. This allows for a fast numerical implementation based on the operator splitting method

$$\begin{aligned}\psi(z, t + \Delta t) &= \mathrm{e}^{-iH\Delta t}\psi(z, t) \\ &= \mathrm{e}^{-i(T+V)\Delta t}\psi(z, t) \\ &= \mathrm{e}^{-iT\frac{\Delta t}{2}}\mathrm{e}^{-iV\Delta t}\mathrm{e}^{-iT\frac{\Delta t}{2}}\psi(z, t) + O(\Delta t^3)\,, \end{aligned} \tag{B.1}$$

where in the last line the Baker-Campbell-Hausdorff formula is used to separate the kinetic and potential operators. Since the kinetic operator is diagonal in the Fourier basis and the operator $V$ is diagonal in real space, fast solution of the equation is possible by use of the Fast Fourier Transform. Thereby, in between each operation one changes from Fourier to

real space (and back) where the respective operators reduce to a simple multiplication. Since this algorithm is based on spectral methods and not on discrete derivatives, it is numerically very stable and further exactly conserves the norm of the wave function (i.e. the particle number). In case of coupled condensates, the hopping term $J$ can be efficiently implemented by absorption in the kinetic energy term $T$. Since this is a static operator the non-diagonal matrix exponential, in the left right field basis, only has to be calculated once during the evolution. The SGPE introduces an additional noise term to the equations of motion but can be implemented in the same way [119]. The code in the course of this thesis was developed in C using the fftw3 [241], GSL [242], and HDF5 [243] libraries. The code is parallelized for multicore architectures with openMP [244]. Apart from the mentioned libraries this code was completely written during the course of my doctoral studies. It has not made public yet, but will most likely be made available including the graphical interface written for ease of use. The code can be obtained upon personal communication and reasonable request.

The simulation parameters are chosen in accordance with the experimental parameters and are given in the main text. Depending on the experimental parameters the numerical gridsize was between $2^{11} \dots 2^{14}$ gridpoints with a gridspacing of $a_{\mathrm{G}} = 0.01 \dots 0.5$. For all presented data independence of the gridcutoff on the numerical results was tested.

## Exact Solution in the Harmonic Approximation

Credit for the idea of solving the harmonic theory in the following way goes to Thomas Schweigler. The algorithm is as follows: We consider the spatially discretized system, where $\varphi$ and $\delta\rho$ are vectors of the discrete lattice model used to approximate the continuous quantum field theory. Since density and phase fluctuations are completely decoupled the density matrix for a thermal state can be written in matrix form as

$$\rho = \frac{1}{Z} \exp\left[-\beta H\right] = \frac{1}{Z} \exp\left[-\beta \begin{pmatrix} \varphi & \delta\rho \end{pmatrix}^{\mathrm{T}} \begin{pmatrix} K & 0 \\ 0 & L \end{pmatrix} \begin{pmatrix} \varphi \\ \delta\rho \end{pmatrix}\right], \tag{B.2}$$

where $\beta = 1/k_{\mathrm{B}}T$ is the inverse temperature, $Z = \mathrm{Tr}\left[\exp(-\beta H)\right]$ is the partition function, and $K, L$ are matrices defined by the discretization of the Hamiltonian $H$. The density matrix is given by a Gaussian multivariate distribution and density and phase variances can be numerically determined in the classical field approximation by inverting the matrices $K$ and $L$. As off-diagonal elements are zero, correlations between the density and phase fluctuations vanish identically. The subsequent time evolution can be readily calculated for this exactly solvable model. The major advantage is the stability of this method for inhomogeneous condensates, for which a direct numerical diagonalization of the Bogoliubov equations is far more time consuming. The mean field density profile is obtained through imaginary time evolution.

# References


[1] L Boltzmann. Weitere Studien über das Wärmegleichgewicht unter Gasmolekülen. *Sitzungsberichte Akademie der Wissenschaften*, 66:275–370, 1872.

[2] H. Poincaré. Sur le probléme des trois corps et les équations de la dynamique. *Acta Mathematica*, 13(1):5–7, 1890.

[3] E. Zermelo. Über einen Satz der Dynamik und die mechanische Wärmetheorie. *Annalen der Physik*, 293(3):485–494, 1896.

[4] D. Ter Haar. Foundations of Statistical Mechanics. *Reviews of Modern Physics*, 27(3):289–338, 1955.

[5] J. v. Neumann. Beweis des Ergodensatzes und des H-Theorems in der neuen Mechanik. *Zeitschrift für Physik*, 57(1-2):30–70, 1929.

[6] P. Bocchieri and A. Loinger. Quantum Recurrence Theorem. *Physical Review*, 107(2):337–338, jul 1957.

[7] Ian C. Percival. Almost Periodicity and the Quantal H Theorem. *Journal of Mathematical Physics*, 2(2):235, 1961.

[8] Fabian H. L. Essler and Maurizio Fagotti. Quench dynamics and relaxation in isolated integrable quantum spin chains. *Journal of Statistical Mechanics: Theory and Experiment*, 2016(6):064002, jun 2016.

[9] E. T. Jaynes. Information Theory and Statistical Mechanics. *Physical Review*, 106(4):620–630, may 1957.

[10] E. T. Jaynes. Information Theory and Statistical Mechanics. II. *Physical Review*, 108(2):171–190, oct 1957.

[11] Michael E Fisher. Renormalization group theory: Its basis and formulation in statistical physics. *Reviews of Modern Physics*, 70(2):653–681, apr 1998.

[12] Marcus Kollar, F Alexander Wolf, and Martin Eckstein. Generalized gibbs ensemble prediction of prethermalization plateaus and their relation to nonthermal steady states in integrable systems. *Physical Review B*, 84(5):054304, 2011.

[13] Michael Gring, Maximilian Kuhnert, Tim Langen, Takuya Kitagawa, Bernhard Rauer, Matthias Schreitl, Igor Mazets, David A. Smith, Eugene Demler, and Jörg Schmiedmayer. Relaxation and Prethermalization in an Isolated Quantum System. *Science*, 337(6100):1318–1322, sep 2012.

[14] T. Langen, R. Geiger, M. Kuhnert, B. Rauer, and J. Schmiedmayer. Local emergence of thermal correlations in an isolated quantum many-body system. *Nature Physics*, 9(10):640–643, sep 2013.

[15] T. Langen, S. Erne, R. Geiger, B. Rauer, T. Schweigler, M. Kuhnert, W. Rohringer, I. E. Mazets, T. Gasenzer, and J. Schmiedmayer. Experimental observation of a generalized Gibbs ensemble. *Science*, 348(6231):207–211, apr 2015.

[16] Josh M Deutsch. Quantum statistical mechanics in a closed system. *Physical Review A*, 43(4):2046, 1991.

[17] Mark Srednicki. Chaos and quantum thermalization. *Physical Review E*, 50(2):888, 1994.

[18] Marcos Rigol and Mark Srednicki. Alternatives to Eigenstate Thermalization. *Physical Review Letters*, 108(11):110601, mar 2012.

[19] Marcos Rigol. Breakdown of Thermalization in Finite One-Dimensional Systems. *Physical Review Letters*, 103(10):100403, 2009.

[20] Toshiya Kinoshita, Trevor Wenger, and David S Weiss. A quantum newton's cradle. *Nature*, 440(7086):900, 2006.

[21] Elliott H. Lieb and Werner Liniger. Exact analysis of an interacting bose gas. i. the general solution and the ground state. *Phys. Rev.*, 130:1605–1616, May 1963.

[22] Elliott H. Lieb. Exact analysis of an interacting bose gas. ii. the excitation spectrum. *Phys. Rev.*, 130:1616–1624, May 1963.

[23] Vladimir Igorevich Arnol'd. *Mathematical methods of classical mechanics*, volume 60. Springer Science & Business Media, 2013.

[24] Jean-Sébastien Caux and Jorn Mossel. Remarks on the notion of quantum integrability. *Journal of Statistical Mechanics: Theory and Experiment*, 2011(02):P02023, 2011.

[25] Hans Bethe. Zur theorie der metalle. *Zeitschrift für Physik*, 71(3-4):205–226, 1931.

[26] Thierry Giamarchi. *Quantum physics in one dimension*, volume 121. Oxford university press, 2004.

[27] Vladimir E Korepin, Nicholay M Bogoliubov, and Anatoli G Izergin. *Quantum inverse scattering method and correlation functions*, volume 3. Cambridge university press, 1997.

[28] Bill Sutherland. *Beautiful models: 70 years of exactly solved quantum many-body problems*. World Scientific Publishing Company, 2004.

[29] Austen Lamacraft. Diffractive scattering of three particles in one dimension: A simple result for weak violations of the yang-baxter equation. *Physical Review A*, 87(1):012707, 2013.

[30] Marcos Rigol, Vanja Dunjko, Vladimir Yurovsky, and Maxim Olshanii. Relaxation in a Completely Integrable Many-Body Quantum System: An Ab Initio Study of the Dynamics of the Highly Excited States of 1D Lattice Hard-Core Bosons. *Physical Review Letters*, 98(5):050405, feb 2007.

[31] Tim Langen, Thomas Gasenzer, and Jörg Schmiedmayer. Prethermalization and universal dynamics in near-integrable quantum systems. *Journal of Statistical Mechanics: Theory and Experiment*, 2016(6):064009, 2016.

[32] Anatoli Polkovnikov, Krishnendu Sengupta, Alessandro Silva, and Mukund Vengalattore. Colloquium : Nonequilibrium dynamics of closed interacting quantum systems. *Reviews of Modern Physics*, 83(3):863–883, aug 2011.

[33] Lev Vidmar and Marcos Rigol. Generalized gibbs ensemble in integrable lattice models. *Journal of Statistical Mechanics: Theory and Experiment*, 2016(6):064007, 2016.

[34] Gert Aarts, Gian Franco Bonini, and Christof Wetterich. Exact and truncated dynamics in nonequilibrium field theory. *Physical Review D*, 63(2):025012, 2000.

[35] J. Berges, Sz Borsányi, and C. Wetterich. Prethermalization. *Physical Review Letters*, 93(14):142002, sep 2004.

[36] Jürgen Berges and Thomas Gasenzer. Quantum versus classical statistical dynamics of an ultracold Bose gas. *Physical Review A - Atomic, Molecular, and Optical Physics*, 76(3):33604, sep 2007.

[37] Thomas Gasenzer, Jürgen Berges, Michael G Schmidt, and Marcos Seco. Nonperturbative dynamical many-body theory of a bose-einstein condensate. *Physical Review A*, 72(6):063604, 2005.

[38] Tim Langen. *Non-equilibrium dynamics of one-dimensional Bose gases*. Springer, 2015.

[39] Pasquale Calabrese and John Cardy. Time Dependence of Correlation Functions Following a Quantum Quench. *Physical Review Letters*, 96(13):136801, apr 2006.

[40] Jürgen Berges, Alexander Rothkopf, and Jonas Schmidt. Nonthermal fixed points: Effective weak coupling for strongly correlated systems far from equilibrium. *Physical review letters*, 101(4):041603, 2008.

[41] Jürgen Berges and Gabriele Hoffmeister. Nonthermal fixed points and the functional renormalization group. *Nuclear Physics B*, 813(3):383–407, 2009.

[42] Christian Scheppach, Jürgen Berges, and Thomas Gasenzer. Matter-wave turbulence: Beyond kinetic scaling. *Physical Review A*, 81(3):033611, 2010.

[43] Boris Nowak, Jan Schole, Dénes Sexty, and Thomas Gasenzer. Nonthermal fixed points, vortex statistics, and superfluid turbulence in an ultracold bose gas. *Physical Review A*, 85(4):043627, 2012.

[44] Boris Nowak, Dénes Sexty, and Thomas Gasenzer. Superfluid turbulence: Nonthermal fixed point in an ultracold bose gas. *Physical Review B*, 84(2):020506, 2011.

[45] Boris Nowak, Jan Schole, and Thomas Gasenzer. Universal dynamics on the way to thermalization. *New journal of physics*, 16(9):093052, 2014.

[46] Maximilian Schmidt, Sebastian Erne, Boris Nowak, Dénes Sexty, and Thomas Gasenzer. Non-thermal fixed points and solitons in a one-dimensional bose gas. *New Journal of Physics*, 14(7):075005, 2012.

[47] Jan Schole, Boris Nowak, and Thomas Gasenzer. Critical dynamics of a two-dimensional superfluid near a nonthermal fixed point. *Physical Review A*, 86(1):013624, 2012.

[48] Markus Karl, Boris Nowak, and Thomas Gasenzer. Universal scaling at nonthermal fixed points of a two-component bose gas. *Physical Review A*, 88(6):063615, 2013.

[49] Markus Karl and Thomas Gasenzer. Strongly anomalous non-thermal fixed point in a quenched two-dimensional bose gas. *New Journal of Physics*, 19(9):093014, 2017.

[50] Isara Chantesana, Asier Piñeiro Orioli, and Thomas Gasenzer. Kinetic theory of non-thermal fixed points in a bose gas. *arXiv preprint arXiv:1801.09490*, 2018.

[51] Boris Nowak, Sebastian Erne, Markus Karl, Jan Schole, Dénes Sexty, and Thomas Gasenzer. Non-thermal fixed points: universality, topology, & turbulence in bose gases. *arXiv preprint arXiv:1302.1448*, 2013.

[52] Asier Piñeiro Orioli, Kirill Boguslavski, and Jürgen Berges. Universal self-similar dynamics of relativistic and nonrelativistic field theories near nonthermal fixed points. *Physical Review D*, 92(2):025041, 2015.

[53] Juergen Berges, Kirill Boguslavski, Soeren Schlichting, and Raju Venugopalan. Universal attractor in a highly occupied non-abelian plasma. *Physical Review D*, 89(11):114007, 2014.

[54] Thomas Gasenzer, Larry McLerran, Jan M Pawlowski, and Dénes Sexty. Gauge turbulence, topological defect dynamics, and condensation in higgs models. *Nuclear Physics A*, 930:163–186, 2014.

[55] Thomas Gasenzer, Boris Nowak, and Dénes Sexty. Charge separation in reheating after cosmological inflation. *Physics Letters B*, 710(4-5):500–503, 2012.

[56] Carlo Ewerz, Thomas Gasenzer, Markus Karl, and Andreas Samberg. Non-thermal fixed point in a holographic superfluid. *Journal of High Energy Physics*, 2015(5):70, 2015.

[57] Makoto Tsubota. Quantum turbulence. *Journal of the Physical Society of Japan*, 77(11):111006–111006, 2008.

[58] Alan J Bray. Theory of phase-ordering kinetics. *Advances in Physics*, 51(2):481–587, 2002.

[59] P. Hohenberg and B. Halperin. Theory of dynamic critical phenomena. *Reviews of Modern Physics*, 49(3):435–479, 1977.

[60] J Berges, K Boguslavski, S Schlichting, and R Venugopalan. Universality far from equilibrium: From superfluid bose gases to heavy-ion collisions. *Physical review letters*, 114(6):061601, 2015.

[61] Steven Mathey, Thomas Gasenzer, and Jan M Pawlowski. Anomalous scaling at nonthermal fixed points of burgers' and gross-pitaevskii turbulence. *Physical Review A*, 92(2):023635, 2015.

[62] Thomas Gasenzer and Jan M Pawlowski. Towards far-from-equilibrium quantum field dynamics: A functional renormalisation-group approach. *Physics Letters B*, 670(2):135–140, 2008.

[63] Immanuel Bloch, Jean Dalibard, and Sylvain Nascimbene. Quantum simulations with ultracold quantum gases. *Nature Physics*, 8(4):267, 2012.

[64] Jakob Reichel and Vladan Vuletic. *Atom chips*. John Wiley & Sons, 2011.

[65] N. D. Mermin and H. Wagner. Absence of Ferromagnetism or Antiferromagnetism in One- or Two-Dimensional Isotropic Heisenberg Models. *Physical Review Letters*, 17(22):1133–1136, nov 1966.

[66] P. C. Hohenberg. Existence of Long-Range Order in One and Two Dimensions. *Physical Review*, 158(2):383–386, jun 1967.

[67] C. J. Pethick and H. Smith. *Bose–Einstein condensation in dilute gases*, volume 9780521846. 2008.

[68] L. P. Pitaevskii and S. Stringari. *Bose-Einstein Condensation*. Clarendon Press, Oxford, 2003.

[69] F. D M Haldane. Effective harmonic-Fluid approach to low-energy properties of one-dimensional quantum fluids. *Physical Review Letters*, 47(25):1840, 1981.

[70] F D M Haldane. 'luttinger liquid theory'of one-dimensional quantum fluids. i. properties of the luttinger model and their extension to the general 1d interacting spinless fermi gas. *Journal of Physics C: Solid State Physics*, 14(19):2585, 1981.

[71] M. A. Cazalilla. Bosonizing one-dimensional cold atomic gases. *Journal of Physics B: Atomic, Molecular and Optical Physics*, 37(7):S1, 2004.

[72] M. A. Cazalilla, R. Citro, T. Giamarchi, E. Orignac, and M. Rigol. One dimensional bosons: From condensed matter systems to ultracold gases. *Reviews of Modern Physics*, 83(4):1405, 2011.

[73] Jesús Cuevas-Maraver, Panayotis G. Kevrekidis, and Floyd Williams, editors. *The sine-Gordon Model and its Applications*, volume 10 of *Nonlinear systems and complexity*. Springer International Publishing, Cham, 2014.

[74] Giuseppe Mussardo. *Statistical field theory: an introduction to exactly solved models in statistical physics*. Oxford University Press, 2010.

[75] L.D. Faddeev and V.E. Korepin. Quantum theory of solitons. *Physics Reports*, 42(1):1–87, jun 1978.

[76] J. F. Currie, J. A. Krumhansl, A. R. Bishop, and S. E. Trullinger. Statistical mechanics of one-dimensional solitary-wave-bearing scalar fields: Exact results and ideal-gas phenomenology. *Physical Review B*, 22(2):477–496, jul 1980.

[77] Adolfo Del Campo and Wojciech H Zurek. Universality of phase transition dynamics: Topological defects from symmetry breaking. *International Journal of Modern Physics A*, 29(08):1430018, 2014.

[78] Thomas WB Kibble. Topology of cosmic domains and strings. *Journal of Physics A: Mathematical and General*, 9(8):1387, 1976.

[79] Tom WB Kibble. Some implications of a cosmological phase transition. *Physics Reports*, 67(1):183–199, 1980.

[80] Wojciech H Zurek. Cosmological experiments in superfluid helium? *Nature*, 317(6037):505, 1985.

[81] WH Zurek. Cosmic strings in laboratory superfluids and the topological remnants of other phase transitions. *Acta Phys. Polon.*, 24:1301–1311, 1993.

[82] Julian Schwinger. On the green's functions of quantized fields. i. *Proceedings of the National Academy of Sciences*, 37(7):452–455, 1951.

[83] Jean Zinn-Justin. *Quantum Field Theory and Critical Phenomena*. Internat. Ser. Mono. Phys. Oxford University Press, Oxford, jun 2002.

[84] Vladimir Gritsev, Anatoli Polkovnikov, and Eugene Demler. Linear response theory for a pair of coupled one-dimensional condensates of interacting atoms. *Physical Review B*, 75(17):174511, may 2007.

[85] HTC Stoof. Coherent versus incoherent dynamics during bose-einstein condensation in atomic gases. *Journal of low temperature physics*, 114(1-2):11–108, 1999.

[86] CW Gardiner, JR Anglin, and TIA Fudge. The stochastic gross-pitaevskii equation. *Journal of Physics B: Atomic, Molecular and Optical Physics*, 35(6):1555, 2002.

[87] D. A. Steck. Rubidium 87 D Line Data. 2013.

[88] M. Olshanii. Atomic Scattering in the Presence of an External Confinement and a Gas of Impenetrable Bosons. *Physical Review Letters*, 81(5):938–941, aug 1998.

[89] Elmar Haller, Manfred J. Mark, Russell Hart, Johann G. Danzl, Lukas Reichsöllner, Vladimir Melezhik, Peter Schmelcher, and Hanns-Christoph Nägerl. Confinement-induced resonances in low-dimensional quantum systems. *Phys. Rev. Lett.*, 104:153203, Apr 2010.

[90] M. Girardeau. Relationship between systems of impenetrable bosons and fermions in one dimension. *Journal of Mathematical Physics*, 1:516–523, nov 1960.

[91] C. N. Yang and C. P. Yang. Thermodynamics of a OneDimensional System of Bosons with Repulsive DeltaFunction Interaction. *Journal of Mathematical Physics*, 10(7):1115–1122, jul 1969.

[92] KV Kheruntsyan, DM Gangardt, PD Drummond, and GV Shlyapnikov. Pair correlations in a finite-temperature 1d bose gas. *Physical review letters*, 91(4):040403, 2003.

[93] DS Petrov, GV Shlyapnikov, and JTM Walraven. Regimes of quantum degeneracy in trapped 1d gases. *Physical Review Letters*, 85(18):3745, 2000.

[94] H Georgi. Effective Field Theory. *Annual Review of Nuclear and Particle Science*, 43(1):209–252, dec 1993.

[95] Alexander O Gogolin, Alexander A Nersesyan, and Alexei M Tsvelik. *Bosonization and strongly correlated systems*. Cambridge university press, 2004.

[96] L. D. Landau. The theory of a Fermi liquid. *Soviet Physics Jetp*, 3(6):920, 1957.

[97] S.-i. Tomonaga. Remarks on Bloch's Method of Sound Waves applied to Many-Fermion Problems. *Progress of Theoretical Physics*, 5(4):544–569, jul 1950.

[98] Daniel C. Mattis and Elliott H. Lieb. Exact Solution of a ManyFermion System and Its Associated Boson Field. *Journal of Mathematical Physics*, 6(2):304–312, feb 1965.

[99] Christophe Mora and Yvan Castin. Extension of Bogoliubov theory to quasicondensates. *Physical Review A*, 67(5):053615, may 2003.

[100] M. Lewenstein and L. You. Quantum Phase Diffusion of a Bose-Einstein Condensate. *Physical Review Letters*, 77(17):3489, 1996.

[101] Gordon Baym and CJ Pethick. Ground-state properties of magnetically trapped bose-condensed rubidium gas. *Physical review letters*, 76(1):6, 1996.

[102] D S Petrov, D M Gangardt, and G V Shlyapnikov. Low-dimensional trapped gases. *Journal de Physique IV (Proceedings)*, 116:5–44, oct 2004.

[103] Eryk Infeld and George Rowlands. *Nonlinear waves, solitons and chaos*. Cambridge university press, 2000.

[104] Roger K Smith. Travelling waves and bores in the lower atmosphere: the 'morning glory'and related phenomena. *Earth-Science Reviews*, 25(4):267–290, 1988.

[105] Linn F Mollenauer, Roger H Stolen, and James P Gordon. Experimental observation of picosecond pulse narrowing and solitons in optical fibers. *Physical Review Letters*, 45(13):1095, 1980.

[106] Panayotis G Kevrekidis, Dimitri J Frantzeskakis, and Ricardo Carretero-González. *Emergent nonlinear phenomena in Bose-Einstein condensates: theory and experiment*, volume 45. Springer Science & Business Media, 2007.

[107] Zakharov V. E. and Shabat A. B. Exact theory of two-dimensional self-focusing and one-dimensional self-modulation of wave in nonlinear media. *JETP*, 34:62, 1972.

[108] K. J. Blow and N. J. Doran. Multiple dark soliton solutions of the nonlinear schrödinger equation. *Physics Letters A*, 107(2):55–58, 1985.

[109] Kevin Geier. Dynamics of vector solitonsin spinor bose-einstein condensates. Master's thesis, Universität Heidelberg, 2017.

[110] Lars Onsager. Statistical hydrodynamics. *Il Nuovo Cimento (1943-1954)*, 6(2):279–287, 1949.

[111] PO Fedichev, AE Muryshev, and Gora V Shlyapnikov. Dissipative dynamics of a kink state in a bose-condensed gas. *Physical Review A*, 60(4):3220, 1999.

[112] Th Busch and JR Anglin. Motion of dark solitons in trapped bose-einstein condensates. *Physical Review Letters*, 84(11):2298, 2000.

[113] V. E. Zakharov and A B Shabat. Interaction between solitons in a stable medium. *Zh. Eksp. Tear. Fiz*, 64(5):1627–1639, 1973.

[114] Yuri S Kivshar and Wiesław Królikowski. Lagrangian approach for dark solitons. *Optics communications*, 114(3-4):353–362, 1995.

[115] Andreas Weller. *Dynamics and interaction of dark solitons in Bose-Einstein condensates*. PhD thesis, 2009.

[116] Sebastian Erne. Characterization of solitonic states in a trapped ultracold bose gas. Diplomarbeit, Universität Heidelberg, 2012.

[117] NG Parker, NP Proukakis, M Leadbeater, and CS Adams. Soliton-sound interactions in quasi-one-dimensional bose-einstein condensates. *Physical review letters*, 90(22):220401, 2003.

[118] BP Anderson, PC Haljan, CA Regal, DL Feder, LA Collins, Charles W Clark, and Eric A Cornell. Watching dark solitons decay into vortex rings in a bose-einstein condensate. *Physical Review Letters*, 86(14):2926, 2001.

[119] Stuart Paul Cockburn. *Bose gases in and out of equilibrium within the Stochastic Gross-Pitaevskii equation*. PhD thesis, University of Newcastle Upon Tyne, 2010.

[120] Tomasz Karpiuk, Piotr Deuar, Przemysław Bienias, Emilia Witkowska, Krzysztof Pawłowski, Mariusz Gajda, Kazimierz Rzążewski, and Mirosław Brewczyk. Spontaneous solitons in the thermal equilibrium of a quasi-1d bose gas. *Physical review letters*, 109(20):205302, 2012.

[121] A Muryshev, GV Shlyapnikov, W Ertmer, K Sengstock, and M Lewenstein. Dynamics of dark solitons in elongated bose-einstein condensates. *Physical review letters*, 89(11):110401, 2002.

[122] J. Armijo, T. Jacqmin, K. Kheruntsyan, and I. Bouchoule. Mapping out the quasicondensate transition through the dimensional crossover from one to three dimensions. *Physical Review A*, 83(2):021605(R), feb 2011.

[123] A. H. van Amerongen, J. J. P. van Es, P. Wicke, K. V. Kheruntsyan, and N. J. van Druten. Yang-Yang Thermodynamics on an Atom Chip. *Physical Review Letters*, 100(9):090402, mar 2008.

[124] J N Fuchs, X Leyronas, and R Combescot. Hydrodynamic modes of a one-dimensional trapped Bose gas. *Physical Review A*, 68(4):043610, oct 2003.

[125] F Gerbier. Quasi-1D Bose-Einstein condensates in the dimensional crossover regime. *Europhysics Letters (EPL)*, 66(6):771, 2004.

[126] I. E. Mazets, T. Schumm, and J. Schmiedmayer. Breakdown of integrability in a quasi-1D ultracold bosonic gas. *Physical Review Letters*, 100(21):210403, 2008.

[127] Austen Lamacraft. Diffractive scattering of three particles in one dimension: A simple result for weak violations of the Yang-Baxter equation. *Physical Review A - Atomic, Molecular, and Optical Physics*, 87(1):012707, 2013.

[128] L. Salasnich, A. Parola, L. Reatto, and a. Parola. Effective wave equations for the dynamics of cigar-shaped and disk-shaped Bose condensates. *Phys. Rev. A*, 65(4):43614, apr 2002.

[129] Tarik Berrada. *Mach-Zehnder interferometry with interacting Bose-Einstein condensates in a double-well potential*. PhD thesis, 2014.

[130] Nicholas K. Whitlock and Isabelle Bouchoule. Relative phase fluctuations of two coupled one-dimensional condensates. *Physical Review A*, 68(5):053609, nov 2003.

[131] Yuki Kawaguchi and Masahito Ueda. Spinor Bose–Einstein condensates. *Physics Reports*, 520(5):253–381, nov 2012.

[132] Markus Karl. *From Quenches to Critical Dynamics and Non-Equilibrium Steady States: Universality in the Dynamics of Low-Dimensional Ultracold Bose Gases*. PhD thesis, 2016.

[133] Marine Pigneur, Tarik Berrada, Marie Bonneau, Thorsten Schumm, Eugene Demler, and Jörg Schmiedmayer. Relaxation to a phase-locked equilibrium state in a one-dimensional bosonic josephson junction. *arXiv preprint arXiv:1711.06635*, 2017.

[134] Pjotrs Grišins and Igor E. Mazets. Coherence and Josephson oscillations between two tunnel-coupled one-dimensional atomic quasicondensates at finite temperature. *Physical Review A - Atomic, Molecular, and Optical Physics*, 87(1):013629, jan 2013.

[135] Takuya Kitagawa, Adilet Imambekov, Jörg Schmiedmayer, and Eugene Demler. The dynamics and prethermalization of one-dimensional quantum systems probed through the full distributions of quantum noise. *New Journal of Physics*, 13(7):73018, jul 2011.

[136] Tim Langen, Thomas Schweigler, Eugene Demler, and Jörg Schmiedmayer. Double light-cone dynamics establish thermal states in integrable 1D Bose gases. pages 1–11, sep 2017.

[137] A Barone, F Esposito, CJ Magee, and AC Scott. Theory and applications of the sine-gordon equation. *La Rivista del Nuovo Cimento (1971-1977)*, 1(2):227–267, 1971.

[138] Bruno Bertini, Dirk Schuricht, and Fabian H L Essler. Quantum quench in the sine-Gordon model. *Journal of Statistical Mechanics: Theory and Experiment*, 2014(10):P10035, oct 2014.

[139] Stefan Kehrein. Flow equation approach to the sine-Gordon model. *Nuclear Physics B*, 592(3):512, 2001.

[140] Sidney Coleman. Quantum sine-Gordon equation as the massive Thirring model. *Physical Review D*, 11(8):2088–2097, apr 1975.

[141] P.B. Blakie†, A.S. Bradley†, M.J. Davis, R.J. Ballagh, and C.W. Gardiner. Dynamics and statistical mechanics of ultra-cold Bose gases using c-field techniques. *Advances in Physics*, 57(5):363–455, sep 2008.

[142] H-D Meyer, Uwe Manthe, and Lorenz S Cederbaum. The multi-configurational time-dependent hartree approach. *Chemical Physics Letters*, 165(1):73–78, 1990.

[143] Ofir E Alon, Alexej I Streltsov, and Lorenz S Cederbaum. Multiconfigurational time-dependent hartree method for bosons: Many-body dynamics of bosonic systems. *Physical Review A*, 77(3):033613, 2008.

[144] Thomas Gasenzer, Jürgen Berges, Michael G Schmidt, and Marcos Seco. Ultracold atomic quantum gases far from equilibrium. *Nuclear Physics A*, 785(1-2):214–217, 2007.

[145] Ulrich Schollwöck. The density-matrix renormalization group. *Reviews of modern physics*, 77(1):259, 2005.

[146] Anatoli Polkovnikov. Phase space representation of quantum dynamics. *Annals of Physics*, 325(8):1790, 2010.

[147] Henry T. C. Stoof. Coherent versus Incoherent Dynamics during Bose-Einstein Condensation in Atomic Gases. *Journal of Low Temperature Physics*, 114(1/2):11–108, 1999.

[148] M. J. Davis, S. A. Morgan, and K. Burnett. Simulations of Bose Fields at Finite Temperature. *Physical Review Letters*, 87(16):160402, sep 2001.

[149] C W Gardiner, J R Anglin, and T I A Fudge. The stochastic Gross-Pitaevskii equation. *Journal of Physics B: Atomic, Molecular and Optical Physics*, 35(6):1555–1582, mar 2002.

[150] Nick P Proukakis and Brian Jackson. Finite-temperature models of bose–einstein condensation. *Journal of Physics B: Atomic, Molecular and Optical Physics*, 41(20):203002, 2008.

[151] S. P. Cockburn and N. P. Proukakis. The stochastic Gross-Pitaevskii equation and some applications. *Laser Physics*, 19(4):558–570, apr 2009.

[152] Chad N. Weiler, Tyler W. Neely, David R. Scherer, Ashton S. Bradley, Matthew J. Davis, and Brian P. Anderson. Spontaneous vortices in the formation of Bose–Einstein condensates. *Nature*, 455(7215):948–951, oct 2008.

[153] Bogdan Damski and Wojciech H. Zurek. Soliton Creation During a Bose-Einstein Condensation. *Physical Review Letters*, 104(16):160404, apr 2010.

[154] S. P. Cockburn, A. Negretti, N. P. Proukakis, and C. Henkel. Comparison between microscopic methods for finite-temperature Bose gases. *Physical Review A*, 83(4):043619, apr 2011.

[155] H. Stoof. Initial Stages of Bose-Einstein Condensation. *Physical Review Letters*, 78(5):768, 1997.

[156] R. a. Duine and H. T. C. Stoof. Stochastic dynamics of a trapped Bose-Einstein condensate. *Physical Review A*, 65(1):013603, 2001.

[157] A. Griffin, D.W. Snoke, and S. Stringari. *Bose-Einstein Condensation*. Cambridge University Press, 1996.

[158] J. A. Krumhansl and J. R. Schrieffer. Dynamics and statistical mechanics of a one-dimensional model Hamiltonian for structural phase transitions. *Physical Review B*, 11(9):3535–3545, may 1975.

[159] H.-P. P. Stimming, N. J. Mauser, J. Schmiedmayer, and I. E. Mazets. Fluctuations and stochastic processes in one-dimensional many-body quantum systems. *Physical Review Letters*, 105(1):015301, jul 2010.

[160] Thomas Schweigler, Valentin Kasper, Sebastian Erne, Igor Mazets, Bernhard Rauer, Federica Cataldini, Tim Langen, Thomas Gasenzer, Jürgen Berges, and Jörg Schmiedmayer. Experimental characterization of a quantum many-body system via higher-order correlations. *Nature*, 545(7654):323–326, 2017.

[161] Stefan Beck, Igor E Mazets, and Thomas Schweigler. Non-perturbative method to compute thermal correlations in one-dimensional systems: A detailed analysis. *arXiv preprint arXiv:1802.06610*, 2018.

[162] Crispin Gardiner. *Stochastic Methods: A Handbook for the Natural and Social Sciences*. Springer, Berlin, 2009.

[163] Dmitry Sergeevich Petrov et al. *Bose-Einstein condensation in low-dimensional trapped gases*. PhD thesis, Universiteit van Amsterdam [Host], 2003.

[164] Michael E Fisher. Phase transitions and critical phenomena. In *Contemporary Physics: Trieste Symposium 1968. Vol. I. Proceedings of the International Symposium on Contemporary Physics*, 1969.

[165] A Del Campo, TWB Kibble, and WH Zurek. Causality and non-equilibrium second-order phase transitions in inhomogeneous systems. *Journal of Physics: Condensed Matter*, 25(40):404210, 2013.

[166] Matthew J. Davis, Tod M. Wright, Thomas Gasenzer, Simon A. Gardiner, and Nick P. Proukakis. Formation of Bose-Einstein condensates. *Applied Physics Letters*, 107(25):252402, jan 2016.

[167] Harald F. Hess. Evaporative cooling of magnetically trapped and compressed spin-polarized hydrogen. *Physical Review B*, 34(5):3476–3479, sep 1986.

[168] Wolfgang Ketterle and N.J. Van Druten. Evaporative Cooling of Trapped Atoms. In *Advances In Atomic, Molecular, and Optical Physics*, volume 37, pages 181–236. 1996.

[169] O. J. Luiten, M. W. Reynolds, and J. T. M. Walraven. Kinetic theory of the evaporative cooling of a trapped gas. *Physical Review A*, 53(1):381–389, jan 1996.

[170] Huang Wu, Ennio Arimondo, and Christopher J. Foot. Dynamics of evaporative cooling for Bose-Einstein condensation. *Physical Review A*, 56(1):560–569, jul 1997.

[171] B. Rauer, P. Grišins, I. E. Mazets, T. Schweigler, W. Rohringer, R. Geiger, T. Langen, and J. Schmiedmayer. Cooling of a One-Dimensional Bose Gas. *Physical Review Letters*, 116(3):1–5, 2016.

[172] Pjotrs Grišins, Bernhard Rauer, Tim Langen, Jörg Schmiedmayer, and Igor E. Mazets. Degenerate Bose gases with uniform loss. *Physical Review A*, 93(3):033634, mar 2016.

[173] E. Witkowska, P. Deuar, M. Gajda, and K. Rzążewski. Solitons as the Early Stage of Quasicondensate Formation during Evaporative Cooling. *Physical Review Letters*, 106(13):135301, mar 2011.

[174] Giacomo Lamporesi, Simone Donadello, Simone Serafini, Franco Dalfovo, and Gabriele Ferrari. Spontaneous creation of Kibble–Zurek solitons in a Bose–Einstein condensate. *Nature Physics*, 9(10):656–660, oct 2013.

[175] Robert Bücker, Aurélien Perrin, Stephanie Manz, Thomas Betz, Ch Koller, Thomas Plisson, Jörg Rottmann, Thorsten Schumm, and Jörg Schmiedmayer. Single-particle-sensitive imaging of freely propagating ultracold atoms. *New Journal of Physics*, 11(10):103039, 2009.

[176] I. Shvarchuck, Ch. Buggle, D. S. Petrov, K. Dieckmann, M. Zielonkowski, M. Kemmann, T. G. Tiecke, W. von Klitzing, G. V. Shlyapnikov, and J. T.M. M. Walraven. Bose-Einstein Condensation into Nonequilibrium States Studied by Condensate Focusing. *Physical Review Letters*, 89(27):2–5, dec 2002.

[177] W. Rohringer, D. Fischer, F. Steiner, I. E. Mazets, J. Schmiedmayer, and M. Trupke. Non-equilibrium scale invariance and shortcuts to adiabaticity in a one-dimensional Bose gas. *Scientific Reports*, 5(1):9820, sep 2015.

[178] I. Bouchoule, S. S. Szigeti, M. J. Davis, and K. V. Kheruntsyan. Finite-temperature hydrodynamics for one-dimensional Bose gases: Breathing-mode oscillations as a case study. *Physical Review A*, 94(5):051602, nov 2016.

[179] Aurélien Perrin, Robert Bücker, S Manz, T Betz, C Koller, T Plisson, T Schumm, and J Schmiedmayer. Hanbury brown and twiss correlations across the bose–einstein condensation threshold. *Nature Physics*, 8(3):195, 2012.

[180] Wolfgang Rohringer, Dominik Fischer, Florian Steiner, Igor E Mazets, Jörg Schmiedmayer, and Michael Trupke. Non-equilibrium scale invariance and shortcuts to adiabaticity in a one-dimensional bose gas. *Scientific reports*, 5:9820, 2015.

[181] Giacomo Lamporesi, Simone Donadello, Simone Serafini, Franco Dalfovo, and Gabriele Ferrari. Spontaneous creation of kibble–zurek solitons in a bose–einstein condensate. *Nature Physics*, 9(10):656, 2013.

[182] Maximilian Schmidt, Sebastian Erne, Boris Nowak, Dénes Sexty, and Thomas Gasenzer. Non-thermal fixed points and solitons in a one-dimensional Bose gas. *New Journal of Physics*, 14(7):075005, jul 2012.

[183] MJ Davis, PB Blakie, AH van Amerongen, NJ van Druten, and KV Kheruntsyan. Yang-yang thermometry and momentum distribution of a trapped one-dimensional bose gas. *Physical Review A*, 85(3):031604, 2012.

[184] S. P. Cockburn, D. Gallucci, and N. P. Proukakis. Quantitative study of quasi-one-dimensional Bose gas experiments via the stochastic Gross-Pitaevskii equation. *Physical Review A*, 84(2):023613, aug 2011.

[185] Glen Cowan. *Statistical data analysis*. Oxford university press, 1998.

[186] Michael E Peskin. *An introduction to quantum field theory*. CRC Press, 2018.

[187] Alexander L Fetter and John Dirk Walecka. *Quantum theory of many-particle systems*. Courier Corporation, 2012.

[188] SS Hodgman, RG Dall, AG Manning, KGH Baldwin, and AG Truscott. Direct measurement of long-range third-order coherence in bose-einstein condensates. *Science*, 331(6020):1046–1049, 2011.

[189] RG Dall, AG Manning, SS Hodgman, Wu RuGway, Karen V Kheruntsyan, and AG Truscott. Ideal n-body correlations with massive particles. *Nature Physics*, 9(6):341, 2013.

[190] Manuel Endres, Marc Cheneau, Takeshi Fukuhara, Christof Weitenberg, Peter Schauß, Christian Gross, Leonardo Mazza, Mari Carmen Bañuls, Lode Pollet, Immanuel Bloch, et al. Single-site-and single-atom-resolved measurement of correlation functions. *Applied Physics B*, 113(1):27–39, 2013.

[191] Gian-Carlo Wick. The evaluation of the collision matrix. *Physical review*, 80(2):268, 1950.

[192] Thorsten Schumm, S Hofferberth, L Mauritz Andersson, Stefan Wildermuth, Steffen Groth, I Bar-Joseph, Jörg Schmiedmayer, and Peter Krüger. Matter-wave interferometry in a double well on an atom chip. *Nature physics*, 1(1):57, 2005.

[193] J Ignacio Cirac and Peter Zoller. Goals and opportunities in quantum simulation. *Nature Physics*, 8(4):264, 2012.

[194] I. E. Mazets and J. Schmiedmayer. Dephasing in two decoupled one-dimensional Bose-Einstein condensates and the subexponential decay of the interwell coherence. *The European Physical Journal B*, 68(3):335–339, apr 2009.

[195] Hagen Kleinert. *Path Integrals in Quantum Mechanics, Statistics, Polymer Physics, and Financial Markets*. World Scientific Publishing Co. Pte. Ltd., 2009.

[196] A.˜N. Shiryaev. *Probability-1*, volume 95 of *Graduate Texts in Mathematics*. Springer, New York, 2016.

[197] Vladimir Gritsev, Ehud Altman, Eugene Demler, and Anatoli Polkovnikov. Full quantum distribution of contrast in interference experiments between interacting one-dimensional Bose liquids. *Nature Physics*, 2(10):705, 2006.

[198] Takuya Kitagawa, Susanne Pielawa, Adilet Imambekov, Jörg Schmiedmayer, Vladimir Gritsev, and Eugene Demler. Ramsey interference in one-dimensional systems: The full distribution function of fringe contrast as a probe of many-body dynamics. *Physical Review Letters*, 104(25):255302, jun 2010.

[199] Anatoli Polkovnikov, Ehud Altman, and Eugene Demler. Interference between independent fluctuating condensates. *Proceedings of the National Academy of Sciences*, 103(16):6125–6129, 2006.

[200] David Adu Smith, Michael Gring, Tim Langen, Maximilian Kuhnert, Bernhard Rauer, Remi Geiger, Takuya Kitagawa, Igor Mazets, Eugene Demler, and Jörg Schmiedmayer. Prethermalization Revealed by the Relaxation Dynamics of Full Distribution Functions. *New Journal of Physics*, 15(7):075011, 2012.

[201] S. Manz, R. Bücker, T. Betz, Ch Koller, S. Hofferberth, I. E. Mazets, A. Imambekov, E. Demler, A. Perrin, J. Schmiedmayer, and T. Schumm. Two-point density correlations of quasicondensates in free expansion. *Physical Review A - Atomic, Molecular, and Optical Physics*, 81(3):031610, mar 2010.

[202] B. Efron and R. Tibshirani. Bootstrap Methods for Standard Errors, Confidence Intervals, and Other Measures of Statistical Accuracy. *Statistical Science*, 1(1):54–75, 1986.

[203] M A Cazalilla and Ming-Chiang Chung. Quantum quenches in the Luttinger model and its close relatives. *Journal of Statistical Mechanics: Theory and Experiment*, 2016(6):064004, jun 2016.

[204] Sidney Coleman. Fate of the false vacuum: Semiclassical theory. *Physical Review D*, 15(10):2929–2936, may 1977.

[205] C E Shannon and W Weaver. *The mathematical theory of communication*. The University of Illinois Press, Urbana, IL, 1947.

[206] Kenneth Maussang, G Edward Marti, Tobias Schneider, Philipp Treutlein, Yun Li, Alice Sinatra, Romain Long, Jérôme Estève, and Jakob Reichel. Enhanced and reduced atom number fluctuations in a bec splitter. *Physical review letters*, 105(8):080403, 2010.

[207] Tarik Berrada, Sandrine van Frank, Robert Bücker, Thorsten Schumm, J-F Schaff, and Jörg Schmiedmayer. Integrated mach–zehnder interferometer for bose–einstein condensates. *Nature communications*, 4:2077, 2013.

[208] R. Geiger, T. Langen, I. E. Mazets, and J. Schmiedmayer. Local relaxation and light-cone-like propagation of correlations in a trapped one-dimensional Bose gas. *New Journal of Physics*, 16(5):053034, may 2014.

[209] S Hofferberth, Igor Lesanovsky, B Fischer, Thorsten Schumm, and Jörg Schmiedmayer. Non-equilibrium coherence dynamics in one-dimensional bose gases. *Nature*, 449(7160):324, 2007.

[210] AA Burkov, Mikhail D Lukin, and Eugene Demler. Decoherence dynamics in low-dimensional cold atom interferometers. *Physical review letters*, 98(20):200404, 2007.

[211] H.-P. Stimming, N. J. Mauser, J. Schmiedmayer, and I. E. Mazets. Dephasing in coherently split quasicondensates. *Physical Review A*, 83(2):023618, feb 2011.

[212] M. Kuhnert, R. Geiger, T. Langen, M. Gring, B. Rauer, T. Kitagawa, E. Demler, D. Adu Smith, and J. Schmiedmayer. Multimode dynamics and emergence of a characteristic length scale in a one-dimensional quantum system. *Physical Review Letters*, 110(9):90405, feb 2013.

[213] Spyros Sotiriadis and Pasquale Calabrese. Validity of the GGE for quantum quenches from interacting to noninteracting models. *Journal of Statistical Mechanics: Theory and Experiment*, 2014(7):P07024, jul 2014.

[214] I. Lesanovsky, S. Hofferberth, J. Schmiedmayer, and P. Schmelcher. Manipulation of ultracold atoms in dressed adiabatic radio-frequency potentials. *Physical Review A - Atomic, Molecular, and Optical Physics*, 74(3):33619, sep 2006.

[215] T. Schumm, S. Hofferberth, L. M. Andersson, S. Wildermuth, S. Groth, I. Bar-Joseph, J. Schmiedmayer, and P. Krüger. Matter-wave interferometry in a double well on an atom chip. *Nature Physics*, 1(1):57–62, oct 2005.

[216] Rafi Bistritzer and Ehud Altman. Intrinsic dephasing in one-dimensional ultracold atom interferometers. *Proceedings of the National Academy of Sciences*, 104(24):9955–9959, 2007.

[217] Pjotrs Grisins and Igor E Mazets. Thermalization in a one-dimensional integrable system. *Physical Review A*, 84(5):053635, 2011.

[218] Tarik Berrada. Mach-zehnder interferometry with interacting bose-einstein condensates in a double-well potential. 2014.

[219] Cédric Bodet. *Dynamics of Quantum Statistical Correlations in Ultracold Bose Gases*. PhD thesis, 2011.

[220] Kaspar Sakmann. *Numerically exact dynamics of the interacting many-body Schrödinger equation for Bose-Einstein condensates: comparison to Bose-Hubbard and Gross-Pitaevskii theory*. PhD thesis, 2010.

[221] Juha Javanainen and Misha Yu Ivanov. Splitting a trap containing a bose-einstein condensate: Atom number fluctuations. *Physical Review A*, 60(3):2351, 1999.

[222] Julian Grond, Jörg Schmiedmayer, and Ulrich Hohenester. Optimizing number squeezing when splitting a mesoscopic condensate. *Physical Review A*, 79(2):021603, 2009.

[223] Christian Gogolin and Jens Eisert. Equilibration, thermalisation, and the emergence of statistical mechanics in closed quantum systems. *Reports on Progress in Physics*, 79(5):056001, 2016.

[224] Bernhard Rauer, Sebastian Erne, Thomas Schweigler, Federica Cataldini, Mohammadamin Tajik, and Jörg Schmiedmayer. Recurrences in an isolated quantum many-body system. *Science*, 360(6386):307–310, 2018.

[225] F. W. Cummings. Stimulated emission of radiation in a single mode. *Physical Review*, 140(4A):A1051—-A1056, nov 1965.

[226] J. H. Eberly, N. B. Narozhny, and J. J. Sanchez-Mondragon. Periodic spontaneous collapse and revival in a simple quantum model. *Physical Review Letters*, 44(20):1323–1326, 1980.

[227] Gerhard Rempe, Herbert Walther, and Norbert Klein. Observation of quantum collapse and revival in a one-atom maser. *Physical Review Letters*, 58(4):353–356, jan 1987.

[228] Markus Greiner, Olaf Mandel, Theodor W. Hänsch, and Immanuel Bloch. Collapse and revival of the matter wave field of a Bose–Einstein condensate. *Nature*, 419(6902):51–54, sep 2002.

[229] Sebastian Will, Thorsten Best, Ulrich Schneider, Lucia Hackermüller, Dirk-Sören Lühmann, and Immanuel Bloch. Time-resolved observation of coherent multi-body interactions in quantum phase revivals. *Nature*, 465(7295):197–201, 2010.

[230] John Cardy. Thermalization and Revivals after a Quantum Quench in Conformal Field Theory. *Physical Review Letters*, 112(22):220401, mar 2014.

[231] Pasquale Calabrese and John Cardy. Quantum quenches in 1+ 1 dimensional conformal field theories. *Journal of Statistical Mechanics: Theory and Experiment*, 2016(6):064003, 2016.

[232] Heiko Rieger and Ferenc Iglói. Semiclassical theory for quantum quenches in finite transverse ising chains. *Physical Review B*, 84(16):165117, 2011.

[233] Anatoli Polkovnikov, Ehud Altman, and Eugene Demler. Interference between independent fluctuating condensates. *Proceedings of the National Academy of Sciences of the United States of America*, 103(16):6125–9, 2005.

[234] S Hofferberth, Igor Lesanovsky, Thorsten Schumm, A Imambekov, V Gritsev, E Demler, and Jörg Schmiedmayer. Probing quantum and thermal noise in an interacting many-body system. *Nature Physics*, 4(6):489, 2008.

[235] S. Manz, R. Bücker, T. Betz, Ch. Koller, S. Hofferberth, I. E. Mazets, A. Imambekov, E. Demler, A. Perrin, J. Schmiedmayer, and T. Schumm. Two-point density correlations of quasicondensates in free expansion. *Physical Review A*, 81(3):031610, mar 2010.

[236] A. Imambekov, I. E. Mazets, D. S. Petrov, V. Gritsev, S. Manz, S. Hofferberth, T. Schumm, E. Demler, and J. Schmiedmayer. Density ripples in expanding low-dimensional gases as a probe of correlations. *Physical Review A - Atomic, Molecular, and Optical Physics*, 80(3):33604, sep 2009.

[237] Christof Wetterich. Quantum dynamics in classical time evolution of correlation functions. *Physics Letters B*, 399(1-2):123–129, 1997.

[238] Christof Wetterich. Time evolution of nonequilibrium effective action. *Phys. Rev. Lett.*, 78:3598–3601, May 1997.

[239] Christof Wetterich. Nonequilibrium time evolution in quantum field theory. *Phys. Rev. E*, 56:2687–2690, Sep 1997.

[240] Johannes Zeiher, Jae-yoon Choi, Antonio Rubio-Abadal, Thomas Pohl, Rick van Bijnen, Immanuel Bloch, and Christian Gross. Coherent many-body spin dynamics in a long-range interacting ising chain. *Physical Review X*, 7(4):041063, 2017.

[241] Matteo Frigo and Steven G Johnson. The design and implementation of fftw3. *Proceedings of the IEEE*, 93(2):216–231, 2005.

[242] Brian Gough. *GNU scientific library reference manual*. Network Theory Ltd., 2009.

[243] Mike Folk, Gerd Heber, Quincey Koziol, Elena Pourmal, and Dana Robinson. An overview of the hdf5 technology suite and its applications. In *Proceedings of the EDBT/ICDT 2011 Workshop on Array Databases*, pages 36–47. ACM, 2011.

[244] Leonardo Dagum and Ramesh Menon. Openmp: an industry standard api for shared-memory programming. *IEEE computational science and engineering*, 5(1):46–55, 1998.